UNIVERSITY OF CALIFORNIA, SAN DIEGO

Impact of Pre-Plasma on Electron Generation and Transport in Laser Plasma Interactions

A dissertation submitted in partial satisfaction of the requirements for the degree

Doctor of Philosophy

in

Engineering Sciences (Aerospace Engineering)

by

Jonathan Lee Peebles

Committee in charge:

Farhat Beg, Chair
Sergei Krasheninnikov
Kevin Quest
George Tynan
David Tytler
Mingsheng Wei

2017

The Dissertation of Jonathan Lee Peebles is approved, and acceptable in quality and form for publication on microfilm and electronically:

Chair

University of California, San Diego

2017

DEDICATION

To my mother and father, who have always been there for me

TABLE OF CONTENTS

LIST OF FIGURES

ACKNOWLEDGMENTS

I would first like to acknowledge my advisor and chair of my committee, Professor Farhat Beg, who has provided valuable guidance throughout my time as a graduate student and a plethora of opportunities to perform experiments at many different facilities and collaborate with other groups and institutions. I would also like to acknowledge Professor Sergei Krasheninnikov who provided the motivation and impetus to perform these experiments as well as theoretical expertise.

Furthermore I would like to thank and acknowledge Mingsheng Wei, who not only allowed me to participate on her experiments conducted on the OMEGA-EP laser at the Laboratory for Laser Energetics, but also provided guidance and drive in finishing papers and this dissertation.

I would also like to acknowledge Christopher McGuffey, Christine Krauland and Shu Zhang for their indispensable help with the experiments on the Texas Petawatt and Titan lasers. Chris in particular helped me greatly in my first terrifying foray in an experimental laser lab. Chris was also instrumental in understanding and implementing proton radiography used in this dissertation, while Christine and Shu performed supporting radiation-hydrodynamic simulations. Finally I would like to thank Alexey Arefiev, who devoted much of his time to teaching and assisting me with the PIC code EPOCH and provided much needed computing time on the Texas Advanced Computing Center and expertise in an unfamiliar area.

I would like to thank my mother and father, who sacrificed so much to make sure their son had every opportunity to succeed. I'm particularly thankful that they encouraged me to choose my own path in college, I guess it turns out I'm more like them than anyone realized. I would also like to thank my big sister Carol, who I've looked up to my whole life and is the standard with which I try to live by.

Additionally I would like to thank my best friends throughout graduate school.

Scott, Seddy, Andrew, Katie and Anthony, damn if it wasn't a fun time! I know I would have lost my mind at some point (maybe around the 2nd year?) if you guys weren't around to keep me sane.

Finally I'd like to thank the love of my life, Sheena, who supports me, loves me and still keeps me grounded when I get too big a head by reminding me of that time we were driving to Julian and I took a wrong turn and drove 30 minutes in the wrong direction towards the Mexican border. Her unconditional support for my choice in post graduate career has meant so much. I look forward to us living and growing together in Rochester this year with our new favorite cat.

Chapter 4 contains some material and figures from "Impact of Pre-Plasma on Fast Electron Generation and Transport from Short Pulse, High Intensity Lasers", J. Peebles, C. McGuffey, C.M. Krauland, L.C. Jarrott, A. Sorokovikova, M.S. Wei, J. Park, H. Chen, H.S. McLean, C. Wagner, M. Spinks, E.W. Gaul, G. Dyer, B.M. Hegelich, M. Martinez, M. Donovan, T. Ditmire, S.I. Krasheninnikov and F.N. Beg, Nuclear Fusion **56**, 016007 (2016). The dissertation author was the primary investigator and author of this paper.

Sections of chapters 4 and 5 are currently being prepared for submission for the publication: "Super-Ponderomotive Electron Generation and Deflection via Self Generated Magnetic Fields", J. Peebles, A. V. Arefiev, S. Zhang, C. McGuffey, J. Park, H. Chen, H.S. McLean, M. Spinks, E.W. Gaul, G. Dyer, B.M. Hegelich, M. Martinez, M. Donovan, T. Ditmire, M. S. Wei, S.I. Krasheninnikov and F.N. Beg, Physical Review Letters (in preparation), (2017). The dissertation author was the primary investigator and author of this material.

Sections of chapter 6 and chapter 7 are currently being prepared for submission for publication of the material. Sections of these chapters are currently being prepared for submission for a publication authored by J. Peebles, C. M. Krauland, C. McGuffey,

P. Forestier-Colleoni, S. Zhang, R. Hua, J. J. Santos, H. Sio, J. Park, H. Chen, H. S. McLean, M. S. Wei, S. I. Krasheninnikov and F. N. Beg. The dissertation author was the primary investigator and author of this material.

Chapters 8 and 9 contains some material and figures from "Investigation of Laser Pulse Length and Pre-Plasma Scale Length Impact on Hot Electron Generation on OMEGA-EP", J. Peebles, M. S. Wei, A. V. Arefiev, C. McGuffey, R. B. Stephens, W. Theobald, D. Haberberger, L. C. Jarrott, A. Link, H. Chen, H. S. McLean, A. Sorokovikova, S. Krasheninnikov, F. N. Beg, New Journal of Physics **19**, 023008 (2017). The dissertation author was the primary investigator and author of this paper.

VITA

2011	Bachelor of Science in Physics, University of California, San Diego
2011	Bachelor of Arts in Economics, University of California, San Diego
2017	Doctor of Philosophy in Engineering Sciences (Aerospace Engineering), University of California at San Diego

PUBLICATIONS

J. Peebles, M. S. Wei, A. V. Arefiev, C. McGuffey, R. B. Stephens, W. Theobald, D. Haberberger, L. C. Jarrott, A. Link, H. Chen, H. S. McLean, A. Sorokovikova, S. Krasheninnikov, F. N. Beg, "Investigation of Laser Pulse Length and Pre-Plasma Scale Length Impact on Hot Electron Generation on OMEGA-EP", New Journal of Physics **19**, 023008 (2017)

J. Peebles, A. V. Arefiev, S. Zhang, C. McGuffey, J. Park, H. Chen, H.S. McLean, M. Spinks, E.W. Gaul, G. Dyer, B.M. Hegelich, M. Martinez, M. Donovan, T. Ditmire, M. S. Wei, S.I. Krasheninnikov and F.N. Beg, "Super-Ponderomotive Electron Generation and Deflection via Self Generated Magnetic Fields", Physical Review Letters (in preparation), (2017)

J. Peebles, C. McGuffey, C.M. Krauland, L.C. Jarrott, A. Sorokovikova, M.S. Wei, J. Park, H. Chen, H.S. McLean, C. Wagner, M. Spinks, E.W. Gaul, G. Dyer, B.M. Hegelich, M. Martinez, M. Donovan, T. Ditmire, S.I. Krasheninnikov and F.N. Beg, "Impact of Pre-Plasma on Fast Electron Generation and Transport from Short Pulse, High Intensity Lasers", Nuclear Fusion **56**, 016007 (2016)

J. Peebles, S. C. Bott, K. Gunasekera, J. Kim, L. Harpster, B. Evans, D. Gomez, O. Paran, C. Peterson, F. N. Beg, "Examination of Bow-Shock Formation in Supersonic Radiatively Cooled Plasma Flows", IEEE Transactions on Plasma Science, vol. 39, no. 11, pp. 2422-2423, Nov. 2011

Y. J. Rhee, S. M Nam, J. Peebles, H. Sawada, M. Wei, X. Vaisseau, T. Sasaki, L. Giuffrida, S. Hulin, B. Vauzour, J. J. Santos, D. Batani, H. S. McLean, P. K. Patel, Y. T. Li, D. W. Yuan, K. Zhang, J. Y Zhong, C. B. Fu, N. Hua, K. Li, Y. Zhang, J. Q. Zhu, I. J. Kim, J. H Jeon, T. M Jeong, I. W. Choi, H. W. Lee, J. H. Sung, S. K. Lee and C. H. Nam, "Spectral tomographic analysis of Bremsstrahlung X-rays generated in a laser-produced plasma", Laser and Particle Beams **34**, 645-654 (2016)

G. J. Williams, D. Barnak, G. Fiksel, A. Hazi, S. Kerr, C. Krauland, A. Link, M. J.-E. Manuel, S. R. Nagel, J. Park, J. Peebles, B. B. Pollock, F. N. Beg, R. Betti, Hui Chen, "Target material dependence of positron generation from high intensity laser-matter interactions", Physics of Plasmas **23**, 123109 Issue 12, (2016)

X. Vaisseau, A. Debayle, J. J. Honrubia, S. Hulin, A. Morace, Ph. Nicolai, H. Sawada, B. Vauzour, D. Batani, F. N. Beg, J. R. Davies, R. Fedosejevs, R. J. Gray, G. E. Kemp, S. Kerr, K. Li, A. Link, P. McKenna, H. S. McLean, M. Mo, P. K. Patel, J. Park, J. Peebles, Y. J. Rhee, A. Sorokovikova, V. T. Tikhonchuk, L. Volpe, M. Wei, and J. J. Santos, "Enhanced Relativistic-Electron-Beam Energy Loss in Warm Dense Aluminum", Physical Review Letters **114**, 095004 (2015)

R. Nora, W. Theobald, R. Betti, F.J. Marshall, D.T. Michel, W. Seka, B. Yaakobi, M. Lafon, C. Stoeckl, J. Delettrez, A.A. Solodov, A. Casner, C. Reverdin, X. Ribeyre, A. Vallet, J. Peebles, F.N. Beg, and M.S. Wei, "Gigabar Spherical Shock Generation on the OMEGA Laser", Physical Review Letters **114**, 045001 (2015)

N. F. Brejnholt, T. A. Decker, R. M. Hill, H. Chen, G. J. Williams, J. Park, J. B. Alameda, M. Fernndez-Perea, M. J. Pivovaroff, R. Soufli, M.A. Descalle, J. Peebles, S. M. Kerr, "Reflective multilayer optic as hard X-ray diagnostic on laser-plasma experiment", Review of Scientific Instruments **86**, 013110 (2015)

W. Theobald, R. Nora, W. Seka, M. Lafon, K. S. Anderson, M. Hohenberger, F. J. Marshall, D. T. Michel, A. A. Solodov, C. Stoeckl, D. H. Edgell, B. Yaakobi, A. Casner, C. Reverdin, X. Ribeyre, A. Shvydky, A. Vallet, J. Peebles, F. N. Beg, M. S. Wei, R. Betti, "Spherical strong-shock generation for shock-ignition inertial fusion", Physics of Plasmas **22**, 056310 (2015)

C. A. Di Stefano, C. C. Kuranz, J. F. Seely, A. G. R. Thomas, R. P. Drake, P. A. Keiter, G. J. Williams, J. Park, H. Chen, M. J. MacDonald, A. M. Rasmus, W. C. Wan, N. R. Pereira, A. S. Joglekar, A. McKelvey, Z. Zhao, S. R. Klein, G. E. Kemp, L. C. Jarrott, C. M. Krauland, J. Peebles, B. Westover, "Measurements of the energy spectrum of electrons emanating from solid materials irradiated by a picosecond laser", Physics of Plasmas **22**, 043113 (2015)

J. R. Fein, J. Peebles, P. Keiter, J. P. Holloway, S. R. Klein, C. C. Kuranz, M. Manuel, R. P. Drake, "Investigation of the hard x-ray background in backlit pinhole imagers", Review of Scientific Instruments **85**, 11E610 (2014)

S. C. Bott, D. M. Haas, R. E. Madden, U. Ueda, Y. Eshaq, G. Collins IV, K. Gunasekera, D. Mariscal, J. Peebles, and F. N. Beg, "250 kA compact linear transformer driver for wire array z-pinch loads", Physical Review Special Topics - Accelerators and Beams **14**, 050401 (2011)

ABSTRACT OF THE DISSERTATION

Impact of Pre-Plasma on Electron Generation and Transport in Laser Plasma Interactions

by

Jonathan Lee Peebles

Doctor of Philosophy in Engineering Sciences (Aerospace Engineering)

University of California, San Diego, 2017

Professor Farhat Beg, Chair

Relativistic laser plasma interactions in conjunction with an underdense pre-plasma have been shown to generate a two temperature component electron spectrum. The lower temperature component described by "ponderomotive scaling" is relatively well known and understood and is useful for applications such as the fast ignition

inertial confinement fusion scheme. The higher energy electrons generated due to pre-plasma are denoted as "super-ponderomotive" electrons and facilitate interesting and useful applications. These include but are not limited to table top particle acceleration and generating high energy protons, x-rays and neutrons from secondary interactions. This dissertation describes experimental and particle-in-cell computational studies of the electron spectra produced from interactions between short pulse high intensity lasers and controlled pre-plasma conditions.

Experiments were conducted at 3 laser labs: Texas Petawatt (University of Texas at Austin), Titan (Lawrence Livermore National Laboratory) and OMEGA-EP (University of Rochester). These lasers have different capabilities, and multiple experiments were carried out in order to fully understand super-ponderomotive electron generation and transport in the high intensity laser regime ($I > 10^{18}$ W/cm^2). In these experiments, an additional secondary long pulse beam was used to generate different scale lengths of "injected" pre-plasma while the pulse length and intensity of the short pulse beam were varied. The temperature and quantity of super-ponderomotive electrons were monitored with magnetic spectrometers and inferred via bremsstrahlung spectrometers while trajectory was estimated via Cu-Kα imaging.

The experimental and simulation data show that super-ponderomotive electrons require pulse lengths of at least 450 fs to be accelerated and that higher intensity interactions generate large magnetic fields which cause severe deflection of the super-ponderomotive electrons. Laser incidence angle is shown to be extremely important in determining hot electron trajectory. Longer pulse length data taken on OMEGA-EP and Titan showed that super-ponderomotive electrons could be created without the need for an initial pre-plasma due to the underdense plasma created during the high intensity interaction alone.

Chapter 1

Introduction

1.1 Motivation of High Intensity Laser Plasma Interaction Research

The goal of this thesis is to investigate the generation of high energy relativistic electrons by a high intensity short pulse laser. These electrons are utilized in a variety of applications including, but not limited to, inertial confinement fusion (ICF) and high energy particle acceleration, which are summarized below.

1.1.1 Inertial Confinement Fusion

Indirect Drive: Over the last half century the ability to generate limitless clean energy via a controlled fusion reaction has been the holy grail of plasma physics. The sheer magnitude of power and efficiency from fusion energy compared to their chemical counterparts can be seen as the difference between conventional and hydrogen bombs. If fusion reactions can be harnessed and controlled, it promises a near limitless supply of energy for the future of mankind. The energy yield from fusing atoms is represented by Einstein's well known equation $E = mc^2$. The fuel used for such reactions are hydrogen and its isotopes, deuterium and tritium since these require the least energy to bind together. Hydrogen fuel, which is the main source of fusion fuel in our sun, is fused into helium and its isotopes which release particles with copious amounts of energy. To achieve the necessary conditions to fuse these atoms, Coulomb forces, which cause the positive charged nuclei to repel each other, must be overcome. When nuclei draw close enough together the attractive nuclear force overpowers the weaker, but longer ranged Coulomb repulsion.

In the sun, immense gravity overcomes the Coulomb force by confining the atoms in close proximity to each other, increasing the likelihood of a fusion reaction. As atoms fuse and give off energy they heat the other fuel, encouraging more fusion reactions. The Earth, not being a giant ball of readily fusible Hydrogen, cannot rely on gravity to achieve fusion. In the most notable fusion demonstration, a hydrogen bomb, the fusion reaction must be generated by imploding the fuel with an atomic (fission) device. This method for generating fusion is obviously untenable for controlled energy production and alternative methods must be tried.

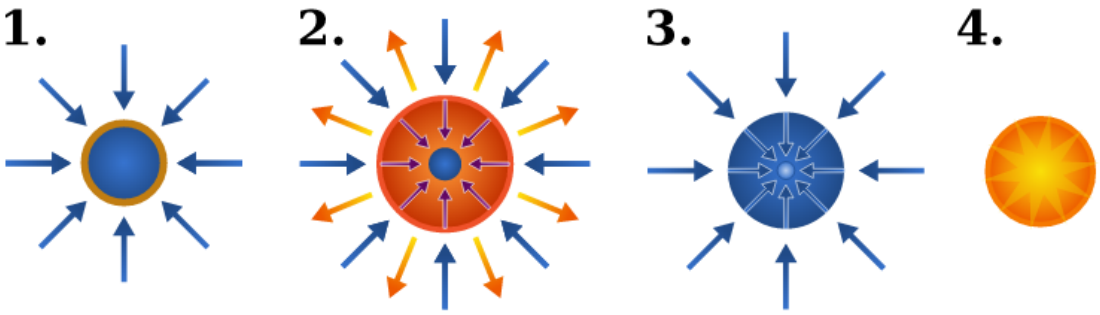

Figure 1.1: Cartoon demonstrating the basic steps of ICF. 1: A fuel pellet is irradiated by either lasers or x-rays. 2: The outer ablator layer (shown as orange in 1) expands due to the incident radiation. 3: Shock waves from the ablator layer's sudden expansion push on the fuel in the core of the capsule, imploding it. 4: The compression of this ablation step brings the fuel to high pressure, density and temperature igniting the fuel, causing thermonuclear burn. High energy alpha particles and neutrons are emitted and cause more fusion reactions in the rest of the fuel.

One large branch of the fusion community studies **inertial confinement fusion (ICF)**, driven by high power laser beams, as a path towards achieving break even fusion yields [1]. The break even result, also known as "ignition" is defined by getting more energy out of the fusion reaction than energy spent in confining it. ICF relies on imploding a small capsule that consists of fuel surrounded by an ablator. The implosion is created by heating the ablator extremely quickly (via lasers or large amounts of x-rays) causing it to expand and drive shock waves to compress the encapsulated fuel. The fuel at the very center reaches high densities (1000 g/cc)

and temperatures which begins a fusion burn. Fusion products created in the initial burn interact with the rest of the fuel and cause more fusion reactions. Initial ICF programs were designed around the principles of direct or indirect drive to achieve ignition. The **direct** drive program compresses the fuel pellet with lasers hitting the ablator surface directly; this method has the downside of introducing significant amounts of drive non-uniformity. Small deviations in beam intensity, focal spot quality and arrangement around the fuel capsule cause instabilities to develop.

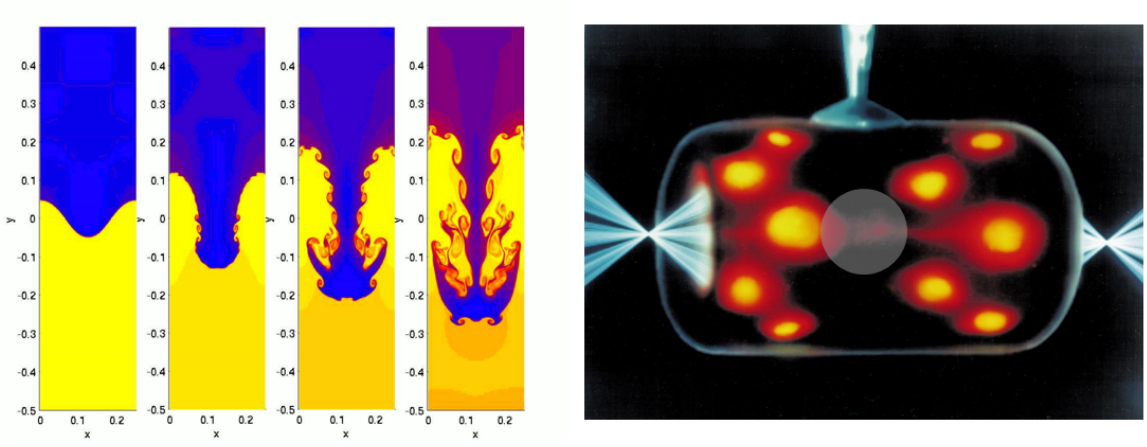

Figure 1.2: Left: Simulations of a single Rayleigh-Taylor instability; a high density fluid, subject to gravity, does not push evenly through the lower density fluid below. When expanded to multiple beams pushing the higher density ablator into the lower density fuel, the instabilities result in uneven compression due to multiple Rayleigh-Taylor instabilities. Right: Image of a hohlraum hit on the interior by several beams generating a warm x-ray bath for the surrounded capsule.

An alternate scheme to this to remove the instabilities caused by non uniform beams is to use a more uniform radiative source to expand the ablator layer, rather than individual laser beams. This technique is called **indirect** drive, where the ablator layer is heated by an x-ray bath that is uniform [2]. This is typically achieved by surrounding the fuel capsule in a hohlraum (German for "cavity") which is a type of high Z material cylinder. The hohlraum is hit by the lasers instead of the capsule and produces an isotropic uniform x-ray "bath" which heats the capsule

uniformly. Difficulties in both direct and indirect drive are caused an instability called the Rayleigh Taylor instability [3]. This originates whenever a denser fluid pushes into a less dense fluid and occurs when the ablator pushes into the fuel. The high density fluid pushes in unevenly and causes large degrees of asymmetry in the imploded fuel causing large reductions in peak density. Increasing the thickness of the ablator layer diminishes this effect, however doing so can reduce the overall effectiveness of a direct drive implosion.

Fast Ignition: One large difficulty that arises in conventional direct or indirect drive ignition schemes is the fact that compression of the capsule and heating the hotspot are coupled processes. Heating the central hotspot during the confinement time of the capsule becomes a difficulty when the two processes are achieved by the same source. An alternate ICF scheme called **fast ignition (FI)** attempts to address this difficulty by separating the compression and heating phases of the interaction [4] [5]. To do so two separate laser systems are used, one to compress the fuel and another to isochorically heat it via energetic particles, which are produced by a high intensity short pulse laser. This method has several benefits in theory. First, by separating the compression and heating phases, conditions are relaxed for obtaining high fusion yields; targets can have uniform density profiles rather than ones tailored to produce a central hotspot when compressed. The relaxed conditions for target design allow for changes to be made to capsule design in order to reduce the Rayleigh Taylor instability. Furthermore the separation between compression and heating laser systems reduces energy required in the driving beams, increasing efficiency and gain. High intensity lasers excel at producing large quantities of high energy particles and two of the most commonly considered FI heating methods use them to generate electrons or protons to deliver energy to the compressed fuel [6]. It is therefore paramount to understand how high intensity beams interact and generate

particles and how those particles propagate in such interactions.

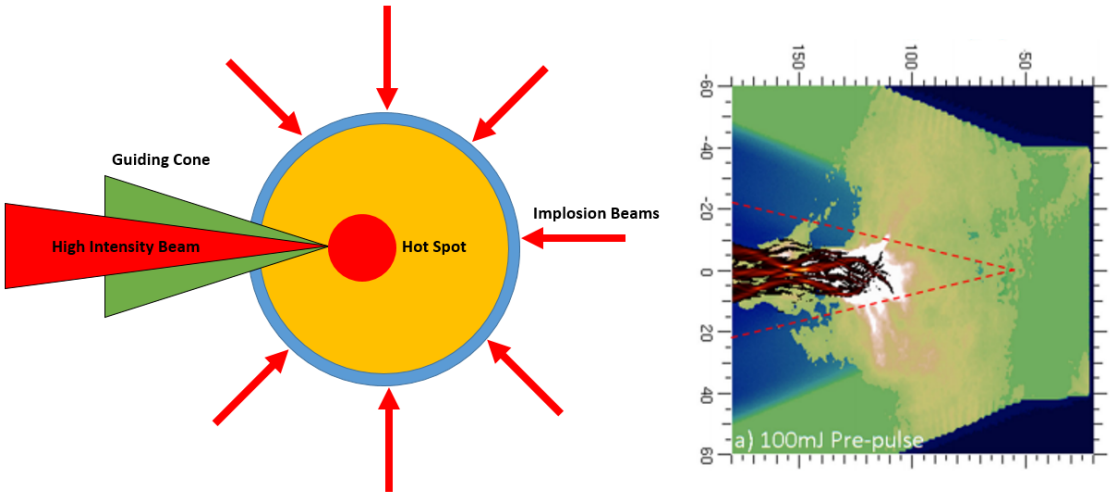

Figure 1.3: Left: Cartoon of the cone guided fast ignition concept. Right: Simulations discussed by A. G. MacPhee demonstrating cone pre-plasma effects on the heating beam.

However, carrying out the 2 stage fast ignition scheme has some difficulties that must be addressed. First the heating beam must be delivered to the compressed fuel. When the fuel is compressed, the region of high density is surrounded by a lower density, but still significant, coronal plasma. This plasma significantly inhibits the propagation of the beam towards the compressed fuel. To work around this problem the fuel capsule is attached to a high Z cone which protects the separate heating beam from the blow off plasma and allows it to propagate unhindered towards the compressed fuel [8]. This cone must be kept intact at the tip when the short pulse arrives to prevent compressed fuel from filling it. However, the cone-capsule target geometry causes a new issue to arise: the laser must now couple to the cone tip and this energy must then be coupled to the compressed fuel. To deliver energy to the fuel, a high intensity laser incident on the cone tip generates 1 - 3 MeV electrons which then couple their energy in the compressed fuel [9] [10]. The generation and transport of such electrons is a large motivation for the initial experiments on which

this dissertation is based. Some issues found in coupling the energy of the electrons have been related to the direction and spread of generated electrons from the cone tip, pre-plasma forming in the cone due to laser pre-pulse and the general coupling efficiency of the laser to electrons and then electrons to the compressed fuel.

Since fast ignition's conception there have been other promising methods to deliver energy to the compressed fuel besides a cone. These include i) boring a hole through the underdense plasma with a high intensity beam and then sending in a second heating beam through the cleared region [4], ii) using protons generated by a thin foil coupled with a cone geometry to heat the core and [6] iii) using counter propagating heating beams [7].

1.1.2 High Energy Particle Sources

High energy electrons play a critical role in accelerating large quantities of protons and ions to high energy, most commonly through the Target Normal Sheath Acceleration (TNSA) mechanism [11]. TNSA is characterized by high energy electrons being accelerated from a metal target via a high intensity beam. These electrons quickly leave the slower ions of the target behind. As the electrons escape they leave behind a positively charged target creating a large electrostatic sheath field around it. Over the longer time scale where ions move, they accelerate in the field's direction outwards, following the electrons.

The energies of protons generated from this mechanism are largely dependent on the electric field on the rear surface of the target. This field relies on large quantities of electrons leaving the target early in time. High energy electrons generated earlier in time are more easily able to escape the target with little resistance. Electrons produced at a later time are impeded and trapped by the sheath field set up by the earlier electrons. Furthermore, the geometry and angle of ejected electrons

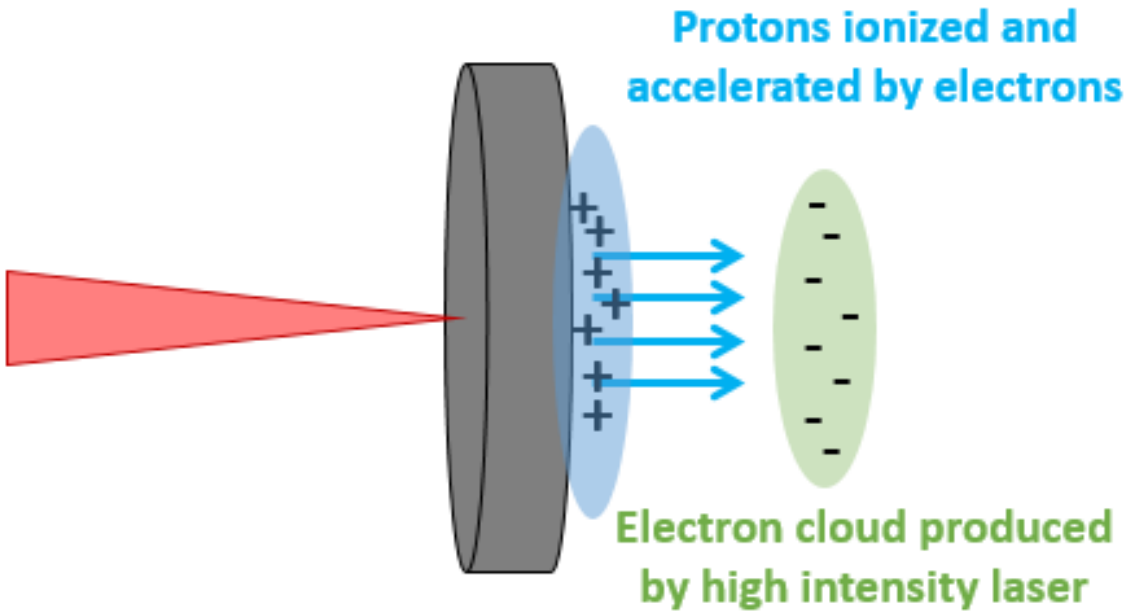

Figure 1.4: Cartoon of TNSA mechanism. Electrons leave the target prior to the ions creating a large field which later accelerates protons off the rear surface of the target.

directly impacts the geometry of the sheath field created. Confining electrons leaving the target with a large magnetic field changes the sheath field significantly enough to drastically alter the transport of high energy ions and protons [12]. Therefore, understanding these aspects of high energy electrons in high intensity laser target interactions is crucial.

Electrons also play a key role in the generation of high energy neutrons [14], x-rays [15]- [17] and gamma rays. When moving through a solid density target electrons interact in two primary ways.

- First the electrons can ionize atoms in the target, often colliding with other electrons, liberating them from their bound states. Other electrons in the atom transition into these newfound free states and emit characteristic x-rays based on the change in bound energy level [13]. This characteristic energy manifests

in specific photon energies and wavelengths based on the Rydberg Formula.

$$\frac{\nu}{c} = \frac{1}{\lambda} = RZ^2\left(\frac{1}{n_1^2} - \frac{1}{n_2^2}\right)$$

In the x-ray spectral range, the most ubiquitous of these series of lines are called Kα x-rays, which are created from the most probable transition from n = 2 to n = 1. These lines are commonly used in diagnostic tools that take advantage of their single wavelength nature.

- Second, the electrons generate bremsstrahlung or "braking radiation". This occurs when electrons effectively collide with the nucleus of an atom and change trajectory and lose energy [18]. The electron emits a photon, which due to conservation of energy, travels in the general direction of the original path of the electron. These x-rays can be of much higher energy than the Kα x-rays and have a much larger spread of energy.

Proton Therapy: As mentioned in the previous section, high intensity lasers are well suited to generate large quantities of high energy particles. The protons and ions generated in such interactions show great promise in being harnessed for proton cancer therapy. Typically radiation treatment of cancer delivers a dosage of photons to the targeted area, disrupting the DNA of the cells, preventing further reproduction [19]. Radiation therapy, due to how it deposits energy in the body, has the downside of harming healthy tissue surrounding the tumor. Protons are valuable in this application since they have a very sharp Bragg peak, the pronounced spike along the Bragg curve, which describes the energy loss of radiation and particles as it travels through matter. A proton will lose small amounts of energy while passing through a material as it excites outer shell electrons. This in turn increases its collisional cross section, resulting in greater energy loss. The end result is the proton

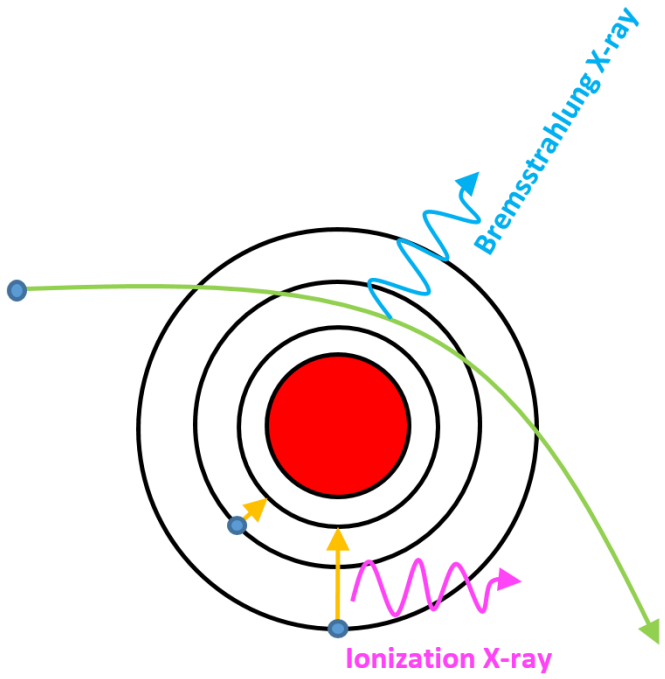

Figure 1.5: Cartoon of two major x-ray emission sources due to hot electrons

quickly loses its energy and deposits it in a very short depth of material. This sharp spike in the Bragg peak means that protons do not harm surrounding tissue nearly as much as other particles when used to treat a tumor.

The main difficulty of course is generating large enough numbers of high energy protons in the first place (if it were easy, we would have done it already!). These protons also need to be **mono-energetic**, since a spread of proton energies results in a broad Bragg peak. An ideal device would generate a mono-energetic beam with a tunable energy in order to zap a tumor at different depths in a body. Cyclotrons and synchrotrons are devices already exist for this purpose but are larger and more expensive than their photon based counterparts. High intensity lasers have been shown to have potential for generating proton and ion beams with the qualities needed for cancer therapy [19]. As the high intensity laser regime continues to be explored, the costs of constructing these lasers becomes cheaper. Using these lasers to generate

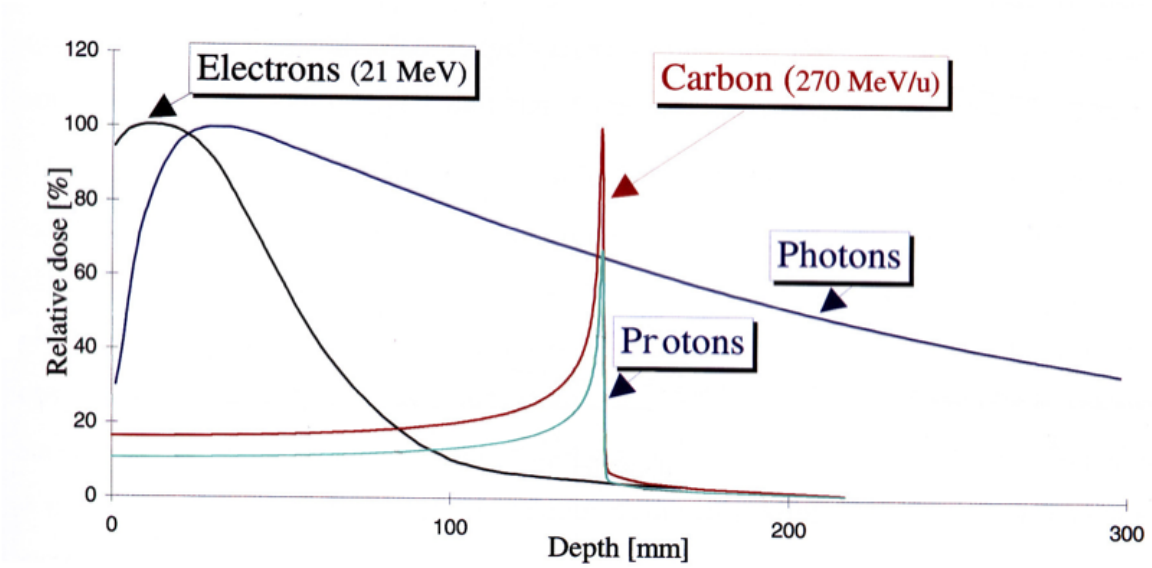

Figure 1.6: Bragg curve chart for various high energy particles [20]. It is notable that the Bragg peak for protons and ions spikes at a very focused location whereas electrons and photons deposit their energy over a much wider range.

protons is still a work in progress however.

Experiments and research have shown [11], [21], [22] that high energy electrons leaving a metal target in a high intensity laser plasma interaction allow for the acceleration of large amounts of protons. The geometry and magnitude of the sheath field used to accelerate protons and ions in TNSA is dependent on the divergence and energy of electrons leaving the target. Therefore in order to understand how to generate large quantities of monoenergetic protons or ions, it is crucial to understand how hot electrons are accelerated and propagated in a plasma.

1.2 Outline of the Dissertation

The dissertation is organized as follows

1. Chapter 1 gives an overview for the applications and motivations for the research performed in the dissertation.

2. Chapter 2 summarizes laser plasma interaction physics mechanisms relevant to the work.

3. Chapter 3 goes into detail on how experiments were carried out, the way each relevant diagnostic works and how the data were analyzed.

4. Chapter 4 describes the layout of the shortest pulse length experiments on the Texas Petawatt laser and subsequent results.

5. Chapter 5 shows 2D PIC simulations carried out using the code EPOCH to more clearly understand the results found in chapter 4. In particular these simulations examine magnetic fields that are created on the target surface during a high intensity interaction.

6. Chapter 6 describes the layout and results from a set of experiments conducted on the Titan laser using a longer pulse length.

7. Chapter 7 describes proton radiography data from the Titan experiment that provided unexpected insight into the complex nature of underdense laser-plasma interactions.

8. Chapter 8 looks into experimental and simulation results for the longest high intensity beam pulse lengths. These experiments took place on the OMEGA-EP laser and simulations examine the impact of beam filamentation on the resulting electrons.

9. Chapter 9 summarizes the whole body of work and describes possible future work, experiments and simulations that could be performed.

Chapter 2
Physics of High Intensity Laser Plasma Interactions

2.1 Overview

The underlaying physics of laser plamsa interactions (LPI) arise from electromagnetic waves impacting large numbers of charged particles. As one of the defining characteristics of a plasma is electrostatic interactions dominating the kinetic interactions of a gas, the use of the strong electromagnetic fields that come with high intensity lasers to impact a plasma yields interesting and unknown physics. These laser fields can be represented by a standard electromagnetic wave:

$$E_0 e^{ikx-i\omega t}\hat{z} \quad and \quad B_0 e^{ikx-i\omega t}\hat{y} \tag{1}$$

When introducing a fundamental charged particle in a plasma (such as an electron) to these oscillating fields several characteristics arise which are demonstrated in the following sections.

2.2 The Vlasov Equation and Conservation Equations

The Vlasov equation is an extremely generalized equation which attempts to capture the position and velocities of all particles within phase space. Phase space is a term that captures the combination of velocity space ($\mathbf{v_x},\ \mathbf{v_y},\ \mathbf{v_z}$) and positional space ($\mathbf{x},\ \mathbf{y},\ \mathbf{z}$). The Vlasov equation begins by capturing and estimating the velocities and positions for all particles in a fixed region of phase space. To do so $f(x, \mathbf{v}, t)$ is denoted as the distribution function for particles with x representing ($\mathbf{x},\ \mathbf{y},\ \mathbf{z}$) and v representing ($\mathbf{v_x},\ \mathbf{v_y},\ \mathbf{v_z}$) to simplify the equation. The number of

particles in the region of phase space can therefore be described by:

$$N_{particles} = \int_{\mathbf{x}}^{\mathbf{x}+d\mathbf{x}} \int_{v}^{v+dv} f(\mathbf{x}, \mathbf{v}, t) d\mathbf{x} d\mathbf{v} \tag{2}$$

The rate of change of the number of particles in this region can be expressed by taking the derivative with respect to time resulting in:

$$\frac{dN_{particles}}{dt} = \frac{df(\mathbf{x}, \mathbf{v}, t)}{dt} d\mathbf{x} d\mathbf{v} \tag{3}$$

This is one way to describe the particles leaving the region in phase space. However another way to describe this is by looking at the flow rate through the edges of a region defined in phase space. Understanding this for physical space is more simple, the flow rate out of the region is the number of particles multiplied by their velocity. Particles flowing out the region on the lower (left) side have a negative velocity and those flowing out of the higher (right) side have a positive velocity. These signs are then reversed for counting particles *leaving* the region rather than entering. This means that when measuring the flow rate across the entire left and right borders representing physical space is defined as $f(\mathbf{x}, \mathbf{v}, t)\mathbf{v}d\mathbf{v}$ for the left and $-f(\mathbf{x} + d\mathbf{x}, \mathbf{v}, t)\mathbf{v}d\mathbf{v}$ for the right. Velocity space is slightly more difficult to understand as a physical picture; a flow rate of particles leaving velocity space is represented by their acceleration, which means that flow of particles out of the top and bottom of the region representing velocity space can be described by $f(\mathbf{x}, \mathbf{v}, t)\mathbf{a}d\mathbf{x}$ and $-f(\mathbf{x}, \mathbf{v} + \mathbf{dv}, t)\mathbf{a}d\mathbf{x}$ respectively.

Putting these particle flows together with the generic rate of change formula of equation 3 and dividing by $d\mathbf{x}$ and $d\mathbf{v}$ we find:

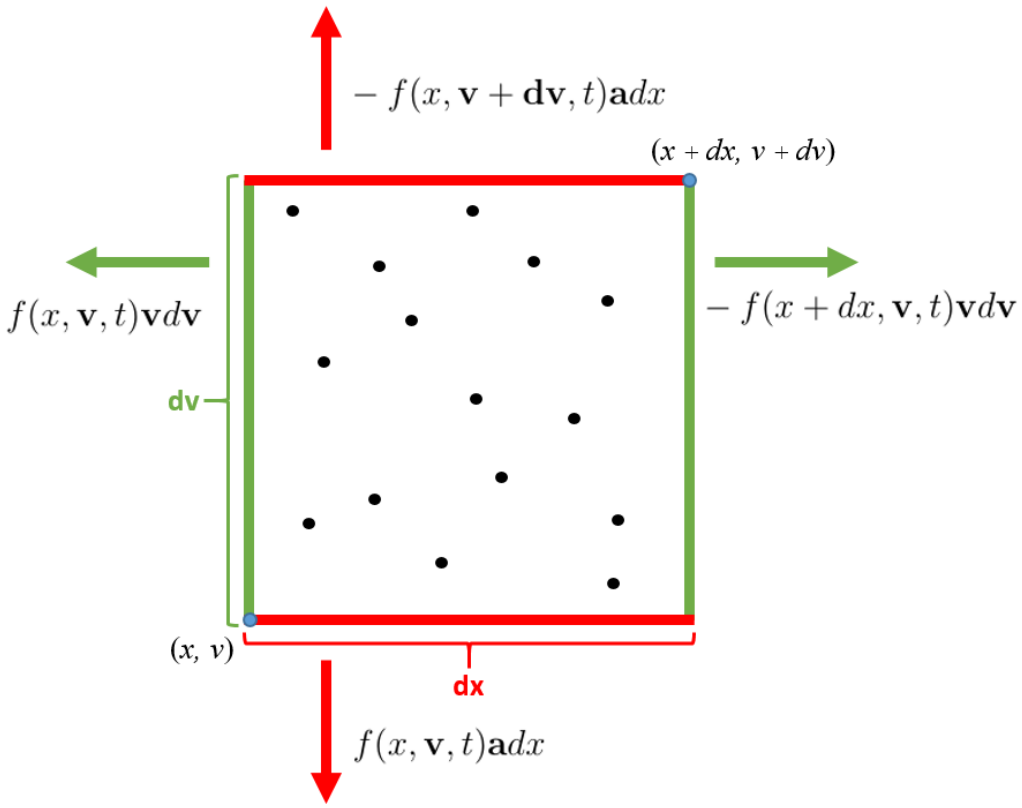

Figure 2.1: A diagram demonstrating how particles are represented in phase space. The horizontal axis represents physical space ($\mathbf{x},\ \mathbf{y},\ \mathbf{z}$) and the vertical axis represents velocity space ($\mathbf{v_x},\ \mathbf{v_y},\ \mathbf{v_z}$). The number of particles leaving through a boundary is represented by negative of the distribution at that location multiplied by the flow rate across the entire border. The flow rate for particles in velocity space is acceleration while for those in physical space it's velocity.

$$\frac{df}{dt} = -\mathbf{v}\frac{f(\mathbf{x}+d\mathbf{x}, \mathbf{v}, t) - f(\mathbf{x}, \mathbf{v}, t)}{d\mathbf{x}} - \mathbf{a}\frac{f(\mathbf{x}, \mathbf{v}+\mathbf{dv}, t) - f(\mathbf{x}, \mathbf{v}, t)}{dv} \tag{4}$$

$$\frac{df}{dt} + \mathbf{v}\frac{df}{d\mathbf{x}} + \frac{d\mathbf{v}}{dt}\frac{df}{d\mathbf{v}} = 0 \tag{5}$$

In terms of electromagnetic behavior in a plasma, the acceleration term from the Lorentz force can be substituted in order to obtain the final equation:

$$\frac{df}{dt} + \frac{d\mathbf{x}}{dt} \cdot \frac{df}{d\mathbf{x}} + \frac{q}{m}\left(E + \frac{\mathbf{v} \times \mathbf{B}}{c}\right) \cdot \frac{df}{d\mathbf{v}} = 0 \tag{6}$$

Considering that the Vlasov equation accounts for the velocity and position of every particle, conservation equations can be derived by taking the moments of the Vlasov equation. The zeroth moment can be taken by integrating the Vlasov equation to create the conservation of mass equation which contains the first moment, velocity. The first moment equation multiplies the Vlasov equation by first moment (velocity) and creates the equation for conservation of momentum which contains the second moment for energy and so on. We can derive these conservation equations as follows:

$$n = \int f(\mathbf{x}, (\mathbf{v}), t) d\mathbf{v} \tag{7}$$

$$n\mathbf{u} = \int \mathbf{v} f(\mathbf{x}, \mathbf{v}, t) d\mathbf{v} \tag{8}$$

Constructing the first moment equation requires averaging the Vlasov equation over velocity:

$$\int \left(\frac{df}{dt} + \mathbf{v} \cdot \frac{df}{d\mathbf{x}} + \frac{q}{m}\left(E + \frac{\mathbf{v} \times \mathbf{B}}{c}\right) \cdot \frac{df}{d\mathbf{v}}\right) d\mathbf{v} = 0 \tag{9}$$

$$\int \frac{df}{dt} d\mathbf{v} = \frac{dn}{dt} \qquad \int \mathbf{v} \cdot \frac{df}{d\mathbf{x}} d\mathbf{v} = \frac{d}{d\mathbf{x}} \cdot (n\mathbf{u}) \tag{10}$$

$$\frac{q}{m}\left(E + \frac{\mathbf{v} \times \mathbf{B}}{c}\right) \int \frac{df}{d\mathbf{v}} d\mathbf{v} \quad \rightarrow \quad \frac{q}{m}\left(E + \frac{\mathbf{v} \times \mathbf{B}}{c}\right) \underbrace{(f(+\infty) - f(-\infty))}_{0} \quad \rightarrow \quad 0 \tag{11}$$

This leads to the conservation of mass equation:

$$\frac{d\rho}{dt} + \nabla \cdot (\rho \mathbf{u}) = 0 \tag{12}$$

The next moment equation is very similar to the one for conservation of mass. By multiplying the integrand by $\mathbf{v}$ and integrating once again returns the conservation of momentum equation:

$$\int \left(\frac{df}{dt} + \mathbf{v} \cdot \frac{df}{d\mathbf{x}} + \frac{q}{m} \left(E + \frac{\mathbf{v} \times \mathbf{B}}{c} \right) \cdot \frac{df}{d\mathbf{v}} \right) \mathbf{v} d\mathbf{v} = 0 \tag{13}$$

$$\rho \left(\frac{d\mathbf{u}}{dt} + \mathbf{u} \cdot \nabla \mathbf{u} \right) = nq \left(\mathbf{E} + \frac{\mathbf{v} \times \mathbf{B}}{c} \right) - \nabla P \tag{14}$$

The two conservation equations are used in a wide range of plasma physics and fluid mechanics (without the Lorentz term) as shown in the following sections.

2.3 Debye Shielding and Length

Debye shielding is a fundamental property of plasmas; similar to a conductor, charges in a plasma can rearrange and move to shield each other's electric field. This leads to the plasma having a quasi neutral quality, where on macroscopic scales a plasma is neutrally charged. How is the "macroscopic" scale defined? To understand this mathematically we can use a test charge example. A test charge placed in a vacuum has a field represented by:

$$E_{test} = \frac{q_{test}}{r^2} \tag{15}$$

To understand how this changes when the charge is placed in a quasi neutral plasma we define the plasma using Poisson's equation:

$$\nabla^2 \phi_{test} = -4\pi e (n_i - n_e) \tag{16}$$

Since protons in a plasma are much more massive than the electrons (2000 times more massive!) it can be safely assumed that they move on much longer time scales than the electrons. We effectively can treat them as stationary when compared to the electrons in the plasma. We can also assume that the electrons have had enough time to come to a thermal equilibrium before bringing in our test charge. We can therefore describe the electron plasma by the equation of motion related to the one derived in the previous section:

$$m_e \frac{d\mathbf{u_e}}{dt} = -e\mathbf{E_{test}} - \frac{\nabla P_e}{n_e} \qquad m_e \frac{d\mathbf{u_e}}{dt} = 0 \tag{17}$$

The equation of motion is equal to 0 from the assumption that the plasma is at thermal equilibrium. Pressure can be described as a combination of density and temperature ($P_e = n_e T_e$) while the electric field can be described by $E_{test} = -\nabla\phi_{test}$. Plugging these into the equation above:

$$e\nabla\phi_{test} = \frac{1}{n_e}(T_e \nabla n_e + n_e \cancelto{0}{\nabla T_e}) = \frac{\nabla n_e}{n_e} T_e \tag{18}$$

Solving this equation for n_e and assuming an initial density of n_0 we find:

$$n_e = n_0 exp(-\frac{q\phi_{test}}{T_e}) \tag{19}$$

which can be plugged into the original Poisson equation describing the plasma:

$$\nabla^2 \phi_{test} = 4\pi e n_0 (exp(-\frac{q\phi_{test}}{T_e}) - 1) \tag{20}$$

The exponential term can be simplified using the Taylor Series expansion, which can be applied to any function that is infinitely differentiable (which an exponential function is). This will effectively turn the exponential term into a sum of terms with different orders of significance.

$$\nabla^2\phi_{test} = 4\pi e n_0\Bigg((1 + \frac{e\phi_{test}}{T_e} + \frac{1}{2}(\frac{e\phi_{test}}{T_e})^2 + ... \xrightarrow{HigherOrder}) - 1\Bigg) \tag{21}$$

Looking only at the 0th and 1st order terms leads to the differential equation:

$$\nabla^2\phi_{test} = 4\pi e n_0 \frac{e\phi_{test}}{T_e} \tag{22}$$

which can be solved to give the characteristic shielding scale length for the test charge as other charged particles move around it:

$$\phi_{test} = \phi_0 exp\Bigg(-x\sqrt{\frac{4\pi e^2 n_0}{T_e}}\Bigg) \qquad where \qquad \lambda_{Debye} \equiv \sqrt{\frac{T_e}{4\pi e^2 n_0}} \tag{23}$$

This Debye length tells us the additional drop off in electrostatic potential at increasing distance from the test charge. In a vacuum the potential from the test particle reduces as $1/r$. While in a plasma, the temperature and density dictate the additional shielding of the particle over distance. The Debye length is essentially a characteristic spatial scale where the quasi neutrality of a plasma becomes apparent.

2.4 Plasma Frequency and Critical Density

The plasma frequency is one of the most fundamental aspects of plasma physics, particularly in how it relates to laser plasma interactions. The plasma frequency is a classification of the Langmuir wave, which is also known as an electron plasma wave. The wave arises as a consequence to small variations in the electron density compared with the ion density. When electrons are slightly displaced in a plasma a small charge imbalance occurs which translates to an electrostatic field.

Due to the conductive nature of plasmas, other electrons respond to this field and are displaced to nullify it. Essentially the information of the original shift in electrons is carried by surrounding electrons outwards forming a wave.

This plasma wave also has an oscillatory component to it. As other electrons are displaced from their equilibrium by the initial change in electric field they gain momentum. This momentum causes electrons to overshoot their equilibrium positions, causing essentially another small change in the electrostatic field. The electrons therefore begin to oscillate around their equilibrium position due to this initial impetus. A physical analogy would be a weight attached to the ceiling by a spring. The initial bump of an electron density displacement is essentially lifting the weight up. When dropping it the weight oscillates about the equilibrium position with simple harmonic motion that is characterized by a frequency.

To show this mathematically we first must consider the three conservation equations from earlier. In addition we must include some assumptions to simplify the problem. The first assumption is that ions move much more slowly to neutralize electrostatic charge than electrons and can be considered stationary. Second we assume that the magnetic field is insignificant to the electric field for the electrons and the thermal pressure term is insignificant. This is essentially an assumption of the electrostatic nature of electron plasma waves. Finally there must be an assumption of how to represent the initial electron density displacement.

$$n = n_0 + n_1 \quad \mathbf{v} = \mathbf{v_0} + \mathbf{v_1} \quad \mathbf{E} = \mathbf{E_0} + \mathbf{E_1} \tag{24}$$

These density, velocity and electric field terms are split into two components, one is the first order component denoted by the subscript 0, which contains the original equilibrium values. The second component is denoted by the subscript 1 which contains the smaller changes caused by the electron density displacement from

the original value. Separating these values into different components is often referred to as perturbation theory.

$$\frac{dn_o}{dt} = \frac{\mathbf{dv_o}}{\mathbf{dt}} = \frac{\mathbf{dE_o}}{\mathbf{dt}} = 0 \tag{25}$$

Density is assumed to be initially uniform and the temperature of ions and electrons is assumed to be 0:

$$\nabla n_0 = \mathbf{v_0} = \mathbf{E_0} = 0 \tag{26}$$

The conservation equations for mass and momentum therefore simplify down to:

$$\frac{dn_e}{dt} + \nabla \cdot (n_e \mathbf{v_e}) = 0 \tag{27}$$

$$\rho\left(\frac{d\mathbf{v_e}}{dt} + \mathbf{v_e} \cdot \nabla \mathbf{v_e}\right) = nq\mathbf{E} \tag{28}$$

With 3 variables and two equations we use Gauss' law to further constrain the system:

$$\nabla \cdot \mathbf{E} = 4\pi e(n_i - n_e) \tag{29}$$

Inputting the perturbed versions of each of the variables and removing terms that are of lower order we can find:

$$\cancelto{0}{\frac{dn_0}{dt}} + \frac{dn_1}{dt} + \nabla \cdot ((n_0 + n_1)(\cancelto{0}{v_0} + \mathbf{v_1})) = 0 \tag{30}$$

$$\frac{dn_1}{dt} + (n_0 + n_1)(\nabla \cdot \mathbf{v_1}) + \mathbf{v_1} \cdot (\nabla(n_0 + n_1)) = 0 \tag{31}$$

Using the distributive property and canceling all terms with first order derivative:

$$\frac{dn_1}{dt} + n_0(\nabla \cdot \mathbf{v_1}) + n_1(\nabla \cdot \mathbf{v_1}) + \mathbf{v_1} \cdot (\nabla n_1) = 0 \tag{32}$$

We can assume that $n_0 >> n_1$ and that therefore terms that include two second order terms such as $n_1(\nabla \cdot \mathbf{v_1})$ are small enough to be negligible compared to $n_0(\nabla \cdot \mathbf{v_1})$.

$$\frac{dn_1}{dt} + n_0(\nabla \cdot \mathbf{v_1}) = 0 \tag{33}$$

Applying the same method to the momentum conservation equation causes it to simplify to:

$$m\frac{dv_1}{dt} = -e\mathbf{E_1} \tag{34}$$

Using the assumption that $n_i = n_e 0$ results in Gauss' equation simplifying to:

$$\nabla \cdot \mathbf{E_1} = -4\pi e n_1 \tag{35}$$

If we assume that the oscillating terms for the variables of the 3 equations above are described by the equation $exp(ikx - i\omega t)$ we find:

$$-\omega n_1 + n_0 k v_1 = 0 \qquad -m\omega \mathbf{v_1} = -e\mathbf{E_1} \qquad k\mathbf{E_1} = -4\pi e n_1 \tag{36}$$

$$\mathbf{v_1} = \left(-\frac{e}{m\omega}\right) * \left(\frac{4\pi e n_1}{k}\right) = -\frac{4\pi e^2 n_1}{mk\omega} \tag{37}$$

$$\omega n_1 - \frac{4\pi e^2 n_0 n_1}{m\omega} = 0 \quad \rightarrow \quad \omega^2 = \omega_{pe}^2 \equiv \frac{4\pi e^2 n_0}{m} \tag{38}$$

The frequency of the electron plasma oscillations ω_{pe} is defined as the plasma frequency and is only dependent on the density of the plasma (n_0) in this case. This is the quality of a plasma which characterizes its response time to a perturbing electric field. If a perturbation's time variation, defined by $t = 2\pi/\omega$ is less than the screening time classified by $t_p = 2\pi/\omega_{pe}$ then the plasma will not be able to respond in time to mitigate the changing electric field. In terms of plasma frequency this relation is inverted, where screening occurs if $\omega < \omega_{pe}$.

This has large consequences in laser plasma interactions as the laser takes the form of an oscillating electric field. We continue to assume the forces from the magnetic field of the laser on electrons are insignificant and using the acceleration of a charged particle we then can calculate the change in current with respect to time. This value is integrated to create a value for current and ω_{pe} is substituted in. We then can use Maxwell's equations to understand the propagation of a beam through a plasma:

$$\mathbf{F} = e(\mathbf{E} + \cancelto{0}{\mathbf{v} \times \mathbf{B}}) \qquad \frac{du_e}{dt} = -\frac{e}{m}\mathbf{E}exp(ikx - i\omega t) \tag{39}$$

$$\mathbf{J} = -neu_e \quad \frac{d\mathbf{J}}{dt} = \frac{\omega_{pe}^2}{4\pi}\mathbf{E} \quad \mathbf{J} = \frac{i\omega_{pe}^2}{4\pi\omega}\mathbf{E} \qquad Where \quad \omega_{pe}^2 = \frac{4\pi e^2 n}{m_e} \tag{40}$$

$$Faraday's\ Law \quad \nabla \times \mathbf{E} = -\frac{1}{c}\frac{d\mathbf{B}}{dt} = -\frac{i\omega\mathbf{B}}{c} \tag{41}$$

$$Ampere's\ Law \quad \nabla \times \mathbf{B} = \frac{4\pi\mathbf{J}}{c} + \frac{d\mathbf{E}}{dt} = \frac{i\omega_{pe}^2}{c\omega}\mathbf{E} - \frac{i\omega\mathbf{E}}{c} \tag{42}$$

Substituting one of Maxwell's equations into the other and using one of the

fundamental properties of plasmas (quasineutrality) we arrive at the dispersion relation (an equation relating wavelength to frequency for a wave) for a laser traveling in a plasma.

$$\nabla \times (\nabla \times \mathbf{E}) = \nabla^2 \mathbf{E} + \nabla(\cancelto{0}{\nabla \cdot \mathbf{E}}) = -\frac{i\omega(\nabla \times \mathbf{B})}{c} \tag{43}$$

$$k^2 \mathbf{E} = \frac{i\omega}{c}(-\frac{i\omega_{pe}^2}{c\omega}\mathbf{E} - \frac{i\omega \mathbf{E}}{c}) \qquad \rightarrow \qquad \boxed{k^2 c^2 = \omega^2 - \omega_{pe}^2} \tag{44}$$

The main importance of this relation is that it tells us how far a laser can propagate in our plasma medium. When $\omega < \omega_{pe}$ then k becomes imaginary and the wave damps and loses energy. This can be visualized physically as the electrons in the plasma not responding quickly enough to the incident light and therefore as an electromagnetic shield preventing further propagation. The limit for the penetration of laser light into a plasma can therefore be altered in two ways. First, plasma frequency is a trait that is mainly dependent on the density of the plasma; by decreasing the density of a plasma, or alternatively, lowering its frequency, a laser can propagate into denser plasma. This also means that for a given wavelength of a laser, there is a characteristic density called the **critical density (n_c)** at which the beam will see the surface as opaque. On the other hand, changing the laser frequency or wavelength will allow a beam to penetrate different levels of plasma, with shorter wavelengths penetrating higher densities.

$$\omega_{pe}^2 = \omega^2 = \frac{4\pi e^2 n_c}{m_e} \quad n_c = \frac{\omega^2 m_e}{4\pi e^2} \quad \omega = \frac{2\pi c}{\lambda} \tag{45}$$

It is important to also note that when the plasma reaches critical density the light wave no longer propagates and a large amount of the light reflects off the surface of the target. Any energy in the light wave that is not absorbed by the plasma must

be reflected to maintain conservation of energy and momentum.

The plasma frequency describes a fundamental time scaling for a plasma's response, and Debye length, a fundamental spatial scaling of a plasma's response. These two qualities together help define what exactly qualifies as a "plasma".

$$\omega_{pe}^2 = \frac{4\pi e^2 n_e}{m_e} = \frac{T_e}{\lambda_{Debye}^2 m_e} \quad Thermal\ Velocity = v_{Th} = \sqrt{T/m} \tag{46}$$

$$\omega_{pe}^2 = \frac{v_{Th}^2}{\lambda_{Debye}^2} \tag{47}$$

This equation best describes the response time ($t \sim \omega_{pe}^{-1}$) of a plasma to recover quasi neutrality in the plasma. If the response time is shorter than the duration of an imposed field change, either by having a very small Debye length, or hot plasma, then the change will be shielded out.

2.5 Ponderomotive Pressure

First we assume the laser field can be best represented by $\mathbf{E} = \mathbf{E}(x)sin(\omega t)$. The dependence of the magnitude of the field on x (the longitudinal direction) primarily represents laser traveling in space. The front of the wave there is a large gradient as the field increases from 0. If electron pressure is neglected the force equation for electrons in this field (treated as a fluid) can be written as:

$$\frac{d\mathbf{u_e}}{dt} + \mathbf{u_e} \cdot \nabla \mathbf{u_e} = -\frac{e}{m}\mathbf{E}(x)sin(\omega t)\hat{\mathbf{y}} \tag{48}$$

Looking at the lowest order of this equation the $u_e \cdot \nabla u_e$ and integrating we gain the equation for simple electron motion as they oscillate in the electric field of the laser:

$$\frac{d\mathbf{u_e}}{dt} = -\frac{e}{m}\mathbf{E}(x)sin(\omega t)\hat{\mathbf{y}} \quad \rightarrow \quad \mathbf{u_e} = \frac{e\mathbf{E}(x)}{m\omega}cos(\omega t)\hat{y} \tag{49}$$

Returning to the full force equation and using the first order velocity we see that the force is dependent on two terms, an oscillating turn and the second order term. Averaging the force over a long period of time we find:

$$\frac{d\mathbf{u_{e-avg}}}{dt} = -\frac{e}{m}\mathbf{E}(x)\langle sin(\omega t)\rangle_t - \frac{e^2}{m^2\omega^2}\mathbf{E}(x)\cdot\nabla\mathbf{E}(x)\langle cos^2(\omega t)dt\rangle_t \tag{50}$$

$$\langle sin(\omega t)\rangle_t = \frac{1}{T}\int_0^T sin(\omega t)dt = \frac{1}{T\omega}(-cos(T\omega) - 1) \tag{51}$$

$$\lim_{T\to\infty}\frac{1}{T\omega}(-cos(T\omega) - 1) = 0 \tag{52}$$

To integrate cos^2 we use the half angle formula to form an easier integral:

$$\langle cos^2(\omega t)dt\rangle_t = \frac{1}{T}\int_0^T \frac{1 + cos(2\omega t)}{2}dt = \frac{1}{2T}\left(T + \frac{1}{4\omega}sin(2\omega T)\right) \tag{53}$$

$$\lim_{T\to\infty}\frac{1}{2T}\left(T + \frac{1}{4\omega}sin(2\omega T)\right) = \frac{1}{2} \tag{54}$$

$$\frac{d\mathbf{u_{e-avg}}}{dt} = -\frac{e^2}{2m^2\omega^2}\mathbf{E}(x)\cdot\nabla\mathbf{E}(x) = -\frac{e^2}{4m^2\omega^2}\nabla\mathbf{E}(x)^2 \tag{55}$$

With the ponderomotive force being:

$$\mathbf{F_{pond}} = -\frac{e^2}{4m\omega^2}\nabla\mathbf{E}(x)^2 \tag{56}$$

It is important to note that this force is not the same as the one in $\mathbf{J} \times \mathbf{B}$ acceleration which scales with what is referred to as "ponderomotive scaling" (shown in the next section). The ponderomotive force represents the push that electrons receive from regions of high field pressure. This force is proportional to the gradient of the electric field squared or the gradient of the intensity of the beam. This causes a beam incident on a plasma to push particles aside, which has implications in how a beam propagates in an underdense plasma, which will be elaborated upon in the self focusing and filamentation sections (2.6.1))

2.6 Defining "High Intensity", Ponderomotive Scaling and J x B Acceleration

To define "high intensity" for lasers we need a parameter that tells us when the relativistic effects of the electron moving in the electric field become significant. To do this we introduce the normalized laser vector potential (a_0). This is defined as the ratio of the momentum from the particle oscillating in the oscillating laser electric field and its rest momentum:

$$F = \frac{dp}{dt} \qquad p_{osc} = \int F dt = \frac{eE}{\omega} \tag{57}$$

$$\boxed{a_0 = \frac{p_{osc}}{m_e c} = \frac{eE_0}{m_e c \omega_L} = \sqrt{\frac{I\lambda^2}{1.37 \times 10^{18}}}} \tag{58}$$

where I is expressed in W/cm^2 and λ is expressed in µm. This is essentially the point where the intensity of the laser becomes relativistically significant, which is the defining characteristic for the "high intensity" regime. Combining this characteristic momentum with the relativistic energy equations we can put them in terms of the laser vector potential:

$$\mathcal{E} = \sqrt{p^2c^2 + m^2c^4} = \gamma mc^2 \quad \rightarrow \quad \gamma = \sqrt{\frac{p^2c^2}{m^2c^4} + 1} \tag{59}$$

Assuming the majority of momentum is from the particle oscillating:

$$p \rightarrow p_{osc} \quad \frac{p_{osc}}{m_e c} = a_0 \quad \rightarrow \quad \gamma = \sqrt{1 + a_0^2} \tag{60}$$

Simply by oscillating electrons with relativistic speeds several new results occur. The first effect is relativistic particles have an increased effective mass, which leads to an induced increase in transparency for the laser penetrating the plasma. This effect redefines the constraint of laser propagation as the *relativistic* critical density. The impact can be shown simply by including the lorentz factor γ in front of the mass term in the critical density equation. This means that high intensity lasers can penetrate even greater densities than their wavelengths suggest.

$$\omega_{pe}^2 = \frac{4\pi e^2 n_c}{m_e} \rightarrow \frac{4\pi e^2 n_c}{\gamma m_e} \qquad n_c = \frac{\omega^2 m_e}{4\pi e^2} \rightarrow \frac{\omega^2 \gamma m_e}{4\pi e^2} \tag{61}$$

The second major impact of having relativistically oscillating electrons in a laser field is that electrons no longer simply oscillate up and down with the laser field. The Lorentz force includes the $\mathbf{J} \times \mathbf{B}$ term which begins to become a prominent force. When electrons travel up or down with the laser field as shown in Fig 2.2, they are pushed via the $\mathbf{J} \times \mathbf{B}$ term in the Lorentz force. At relativistic velocities the J term becomes significant. Electrons oscillating in the electric field of the laser pick up a secondary oscillation due to interaction with the laser's magnetic field. This secondary oscillation caused by the $\mathbf{J} \times \mathbf{B}$ term in the Lorentz force occurs in the laser axis. The electron travels forward but does not gain energy from each cycle unless the laser field symmetry is broken.

The Lawson-Woodward theorem states that there is no net energy gain for

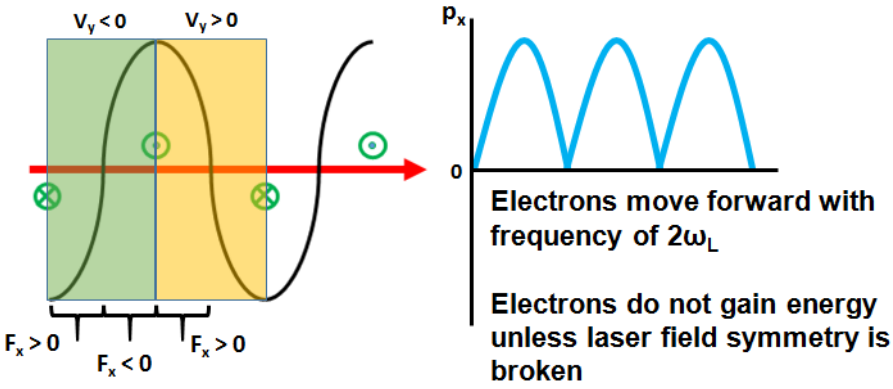

Figure 2.2: Cartoon of J × B acceleration. Electrons oscillating in the electric field of the laser pick up a secondary oscillation due to interaction with the laser's magnetic field. This secondary oscillation caused by the J × B term in the Lorentz force occurs in the laser axis. The electron travels forward but does not gain energy from each cycle unless the laser field symmetry is broken.

relativistic electrons from a magnetic field in an infinite vacuum. This theorem arises from the fact that any energy gained by an electron in the first half cycle is then lost in the next half cycle. The symmetric nature of gaining and losing energy to the laser can be broken by stopping the laser mid cycle which is what occurs when the laser reaches the critical density in a plasma. As the laser pushes an electron forward into the surface of the target, the laser disappears and the electron effectively keeps all the energy it gained. This results in electrons having an energy distribution best described by "ponderomotive scaling" [23]. In the relativistic regime this scaling is derived by using the force equation with an incident wave having a vector potential in the transverse direction that varies in the longitudinal direction. Taking $\hat{z}$ as the longitudinal direction of propagation this means the vector potential is expressed as $\mathbf{A}(z)\hat{x}$. This leads to the following:

$$E = -\frac{1}{c}\frac{d\mathbf{A}}{dt} - \nabla\phi \qquad B = \nabla \times \mathbf{A} \tag{62}$$

$$\frac{d}{dt}\mathbf{p} + \frac{\mathbf{p}\cdot\nabla\mathbf{p}}{\gamma m} = -e\left(\mathbf{E} + \frac{\mathbf{v}\times\mathbf{B}}{c}\right) = e\nabla\phi + \frac{e}{c}\frac{d\mathbf{A}}{dt} - \frac{e}{\gamma mc}(\mathbf{p}\times\nabla\times\mathbf{A}) \tag{63}$$

Looking first at the transverse momentum:

$$\frac{d}{dt}\mathbf{p_t} + \frac{\mathbf{p_l}}{\gamma m}\frac{d}{dz}\mathbf{p_t} = \frac{e}{c}\frac{d}{dt}\mathbf{A} - \frac{e}{\gamma mc}(\mathbf{p}\times\nabla\times\mathbf{A}) \tag{64}$$

$$\nabla\times\mathbf{A} = \frac{d}{dz}\mathbf{A}\hat{y} \qquad \rightarrow \qquad \mathbf{p}\times\nabla\times\mathbf{A} = -\mathbf{p_l}\frac{d}{dz}\mathbf{A}\hat{x} \tag{65}$$

Grouping like terms we find:

$$\frac{d}{dt}\left(\mathbf{p_t} - \frac{e}{c}\mathbf{A}\right) = -\frac{\mathbf{p_l}}{\gamma m}\frac{d}{dz}\left(\mathbf{p_t} - \frac{e}{c}\mathbf{A}\right) \quad \rightarrow \quad \mathbf{p_t} = \frac{e}{c}\mathbf{A} \tag{66}$$

Using this we can examine the longitudinal force equation, which will give us a relation for electrons entering the target:

$$\frac{d\mathbf{p_l}}{dt} + \frac{\mathbf{p}\cdot\nabla\mathbf{p}}{\gamma m} = e\nabla\phi - \frac{e}{\gamma mc}(\mathbf{p}\times\nabla\times\mathbf{A}) \tag{67}$$

We can put this in terms of vector potential by using equations 58 and 60 and using some vector calculus identity reshuffling:

$$\frac{d\mathbf{p_l}}{dt} = e\nabla\phi - m_e c^2\frac{\mathbf{A}\cdot\nabla\mathbf{A}}{\sqrt{1+\mathbf{A}^2}} - m_e c^2\frac{\mathbf{A}\times\nabla\times\mathbf{A}}{\sqrt{1+\mathbf{A}^2}} \tag{68}$$

$$\mathbf{A}\cdot\nabla\mathbf{A} + \mathbf{A}\times\nabla\times\mathbf{A} = \frac{1}{2}\nabla||\mathbf{A}||^{\mathbf{2}} \tag{69}$$

$$\frac{1}{2}\nabla\mathbf{A}^2 = \frac{1}{2}\nabla(1+\mathbf{A}^2) = \frac{1}{2}\nabla(\sqrt{1+\mathbf{A}^2})^2 = \sqrt{1+\mathbf{A}^2}\;\nabla\sqrt{1+\mathbf{A}^2} \tag{70}$$

$$\frac{\mathbf{A}\cdot\nabla\mathbf{A}+\mathbf{A}\times\nabla\times\mathbf{A}}{\sqrt{1+\mathbf{A}^2}}=\nabla\sqrt{1+\mathbf{A}^2} \tag{71}$$

$$\mathbf{F_{pond}}\equiv\frac{d}{dt}\mathbf{p_l}=e\nabla\phi-m_0c^2\nabla\sqrt{1+\mathbf{A}^2}=e\nabla\phi-m_0c^2\nabla(\gamma-1) \tag{72}$$

Since γ increases with $\mathbf{E}$ we can see that at large gradients of the electric field the force is maximized. This essentially means that in regions with highest intensity, the light pressure from the laser pushes electrons and imparts large amounts of energy. The energy distribution often used with such scaling laws is a simple exponential decay function, where the ponderomotive temperature is used as the decaying slope. Using $a_0=\mathbf{A}$ this slope is derived from the force law above and is described by:

$$k_bT_{pond}(MeV)=m_ec^2\left(\sqrt{1+a_0^2}-1\right)=m_ec^2\left(\sqrt{1+\frac{I\lambda^2}{1.37\times10^{18}}}-1\right) \tag{73}$$

2.6.1 Vacuum Heating

Vacuum heating is a laser absorption mechanism that occurs when both a high intensity laser is incident at an angle on a target and a sharp density discontinuity or gradient is present [24]. This mechanism depends largely on the reflection of the incident laser and therefore only takes place near the relativistic critical density. When the laser is incident on the target at an angle it can encounter a small region of electrons that can be pulled away from the target. Electrons are pulled out of the surface of the target every laser cycle forming a cloud of electrons. At the surface some of these electrons can be accelerated back into the target by the laser all within one laser cycle. These electrons reenter the target with a different phase absorbing

energy from the laser.

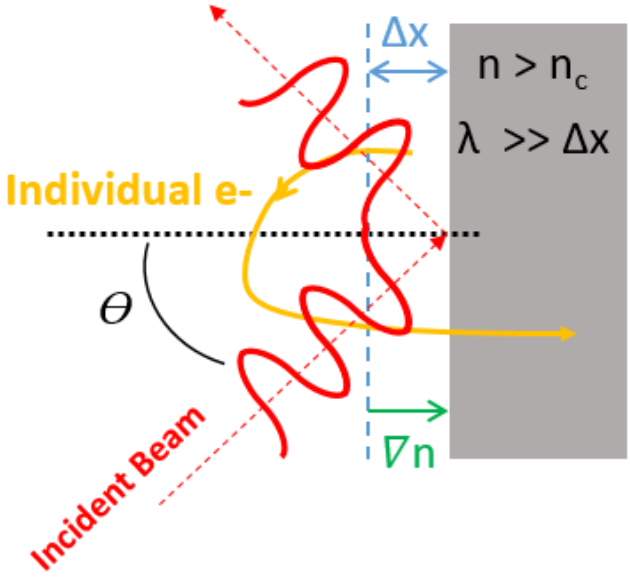

Figure 2.3: Cartoon of vacuum heating. An angled beam pulls electrons out of the target a small amount causing an oscillating electric field on the surface of the target. Electrons absorb and gain some laser energy before being sent back into the target.

As the electrons reenter the target each cycle, an oscillating field is created along the surface. This induced electric field can further accelerate and decelerate the electrons sent back into the target. The absorption of the laser energy as the electrons are removed is a function of angle relative to the target surface, but simply it scales as $cos^{-1}(\theta)$. Not all of the electrons drawn out by vacuum heating are accelerated back into the target. The majority of electrons that move far enough away from the target surface become part of the the underdense plasma that expands in high intensity interactions.

2.6.2 Resonance Absorption and Inverse Bremsstrahlung

Another form of laser energy deposition in plasma is called Resonance Absorption. Resonance absorption arises when a linearly polarized light is incident on a target surface at an angle [25]. The electric field of the laser field pushes and pulls

small amounts of electrons on the surface of the target since the electric field is no longer perpendicular with the target surface. This results in a small electron density perturbation corresponds to a small electrostatic oscillation due to changes in density along the perturbation path that is propagated in the form of an electron plasma wave.

$$\mathbf{E} = E_x\hat{x} + E_y\hat{y} \quad \epsilon_p = 1 - \frac{\omega_{pe}^2(x)}{\omega^2} \tag{74}$$

Using Poisson's equation we can show that an angled beam on a charge neutral plasma with a density gradient results in a resonance wave

$$\nabla \cdot (\epsilon\mathbf{E}) = 0 \quad \nabla \cdot \epsilon\mathbf{E} = \epsilon\nabla \cdot \mathbf{E} + \nabla\epsilon \cdot \mathbf{E} \tag{75}$$

$$\nabla \cdot \mathbf{E} = -\frac{1}{\epsilon}\frac{d\epsilon}{dx}E_x \quad \rightarrow \quad \frac{d\epsilon}{dx} = -\frac{2\omega_{pe}}{\omega^2}\frac{d\omega_{pe}}{dx} \tag{76}$$

We can see that the charge separation that occurs depends on the change in plasma frequency with respect to the longitudinal direction. Since plasma frequency primarily depends on density at this point we can say that resonance absorption occurs primarily at regions with a sharp density gradient, particularly at critical density. This effect is similar to, but affects a much larger region than vacuum heating. Whereas vacuum heating accelerates electrons very close to the surface of the target, resonance absorption creates plasma waves in density gradients that do not need to be close to critical density.

While it appears that this effect would only take place when the laser is obliquely incident on the target, this effect actually occurs in non-angled incidence cases as well. The primary cause of this is target deformation that occurs via ponderomotive pressure outlined in section 2.5. When the target is deformed significantly

the effective incidence angle of the laser is no longer normal and resonance absorption can occur.

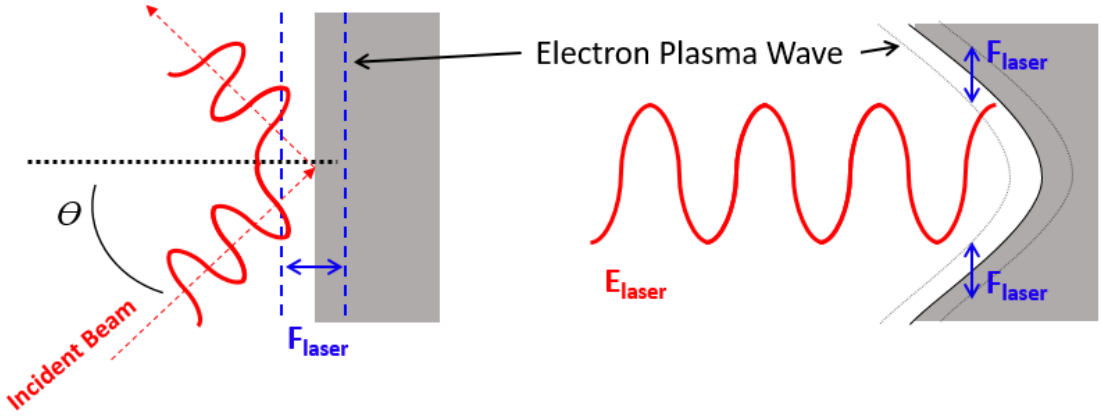

Figure 2.4: Diagrams describing two aspects of resonance absorption. On the left an angled beam has an electric field component in the direction of a gradient in the density profile of the target. The field oscillates electrons in and out of the target and the density gradient causes this to generate an electron plasma wave. This effect is dependent on the beam having non normal incidence on the target and can be achieved by impacting a target that is cavitated by ponderomotive light pressure.

Another laser absorption effect that occurs is inverse bremsstrahlung heating [26]. As was described in chapter 1, bremsstrahlung, or "braking radiation" occurs when energetic electrons are deflected in coulomb collisions with other particles. Conservation of momentum and energy results in the ejection of an x-ray photon as a result. Inverse bremsstrahlung is a somewhat deceiving name, which implies x-rays are absorbed into electron motion. In reality inverse bremsstrahlung occurs when electrons oscillate with the beam, these electrons then collide with other electrons or ions. Since electrons oscillating in phase with the beam do not permanently absorb energy, the electron ion collisions cause the energy of the laser to be absorbed by the plasma.

It is important to note that for the work in this dissertation, as intensity of the laser increases resonance absorption and inverse bremsstrahlung energy deposition

fractions are reduced. While not completely gone, they play a less significant role than $\mathbf{J} \times \mathbf{B}$ acceleration, vacuum heating and pre-plasma acceleration mechanisms outlined in the following section.

2.7 What is a Pre-Plasma and Amplified Spontaneous Emission

A pre-pulse in a laser arises from a process known as Amplified Spontaneous Emission (ASE) [27]. This is a separate but similar mechanism to Amplified *Stimulated* Emission, which is the basis light generation in all lasers (after all LASER is an acronym for Light Amplification by Stimulated Emission of Radiation). In lasers, a gain medium is usually some form of doped glass or gas which is excited by large amounts of electrical power. The gain medium's energy levels determine its fundamental wavelength described by $E_2 - E_1 = \Delta E = h\nu$. When a photon with the characteristic wavelength passes through the medium it stimulates its electrons to drop in energy state, emitting an identical photon with the same wavelength and phase.

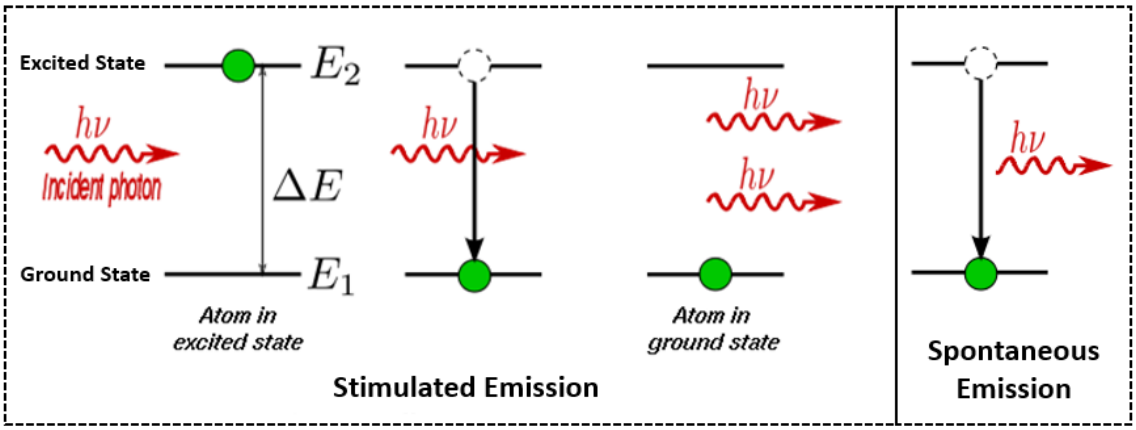

Figure 2.5: Schematic outlining the process of amplified spontaneous emission; an excited gain medium emits an identical photon to the one that passes though it. Spontaneous emission is a process on the right where a photon is emitted randomly with no original incident photon.

While the vast majority of lasing energy occurs from this stimulated emission, electrons raised to higher energy levels by charging the gain medium can spontaneously drop to lower ones resulting in photon emission. These photons do not have the same phase and are less controllable than those from stimulated emission. This emission then passes through the amplification chain of the laser, generating an ASE pre-pulse. In typical lower intensity lasers a pre-pulse has insignificant intensity to do anything. This is often represented by a contrast ratio number, which is the ratio of main pulse intensity to pre-pulse intensity. Typical intensity contrasts range from $10^5 - 10^8$, however, for beams with high main pulse intensities, this results in pre-pulses with enough intensity and energy to significantly ionize material.

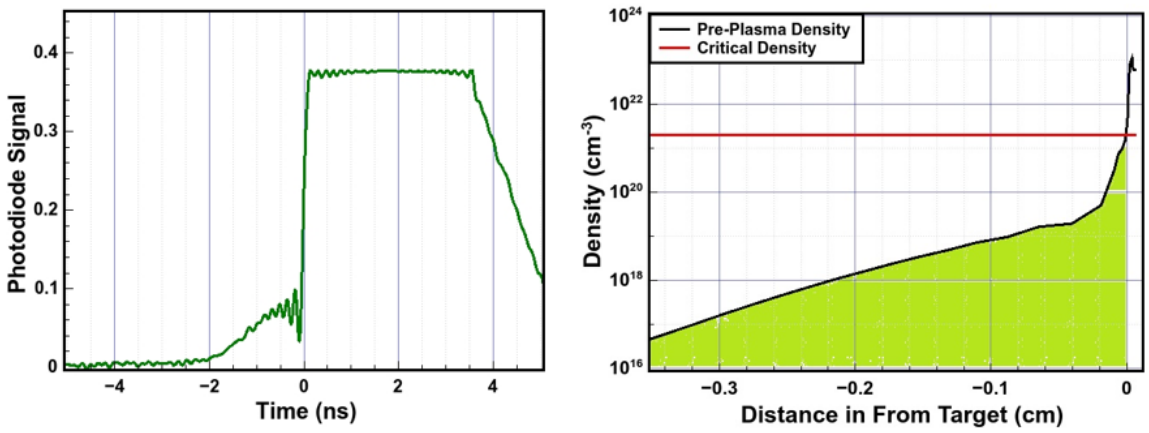

Figure 2.6: Left: A oscilloscope trace of a measured pre-pulse on a shot next to a higher intensity nanosecond scale beam (which saturates the photodiode). Right: Simulation results predicting the pre-plasma density profile for a given pre-pulse.

Since the pre-pulse typically arrives several nanoseconds prior to the main beam of the laser, in high intensity laser plasma interactions the pre-pulse pre-ionizes the target surface. The pre-plasma results changes the qualities of the target that the main beam interacts with. Rather than interacting with a flat surface, the laser passes through several millimeters of underdense plasma. This pre-plasma has been shown to severely change how a laser propagates and the quality of the electrons

generated from such a beam.

2.8 Laser Propagation in Pre-plasma

2.8.1 Self Focusing and Filamentation

One significant feature for laser propagation in pre-plasma is relativistic self focusing. This trait of relativistic beams arises from the ponderomotive force discussed in the previous section. A key component to this effect is that the index of refraction of plasma is dependent on the plasma's dielectric constant:

$$n_{index} = \frac{c_p}{c} = \sqrt{\frac{\mu_0 \mu_p \epsilon_0 \epsilon_p}{\mu_0 \epsilon_0}} \rightarrow \sqrt{\epsilon_p} \tag{77}$$

Since ω_{pe} includes the relativistic mass term we notice that as the electrons become more relativistic in higher fields, the index of refraction increases as well. Ponderomotive pressure from the beam in regions of higher intensity also pushes plasma away resulting in lower densities where the laser is most intense. Since ω_{pe} scales with density, this introduces another change that further increases the index of refraction in the region of highest intensity. These two effects combined produce a plasma with a lensing effect due to the change in index of refraction.

$$\epsilon_p = 1 - \frac{\omega_{pe}^2}{\omega^2} \rightarrow 1 - \frac{\omega_{pe}^2}{\gamma \omega^2} \sim 1 - \frac{n}{\sqrt{1+I}} \qquad \uparrow I \ \downarrow n \rightarrow \uparrow n_{index} \tag{78}$$

The lensing effect of self focusing is also an unstable equilibrium. As the beam focuses more, the intensity increases and the changes in density and intensity become more severe. This instability combined with random fluctuations in the plasma or beam leads to the filamentation instability. Here individual fluctuations cause portions of the beam to self focus differently and split into different components called filaments. The result of the filamentation is the beam changing from a single uniform

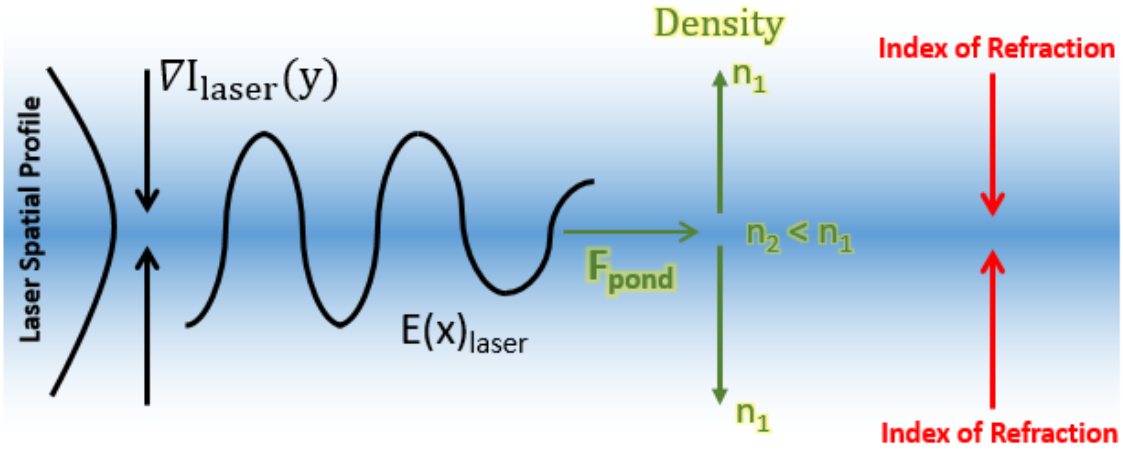

Figure 2.7: Diagram showing how self focusing develops in underdense plasma. A laser is typically more intense at the center of the spot and ponderomotive pressure pushes plasma away from the laser. These two aspects combine and increase the index of refraction of the plasma resulting in a lensing effect that focuses the beam.

spot into multiple uneven spots. These filaments can also be deflected and focused into different directions independent of each other. The random nature of these two instabilities causes large repeatability issues for experiments with pre-plasmas.

2.8.2 Magnetic Field Growth and Collimation of Relativistic Electrons

While electric fields that form on the surface of the target, such as those in the TNSA acceleration mechanism, play a large role in electron dynamics, self generated magnetic fields from electrons traveling as a current also have a large impact on electron trajectory. The magnetic fields that develop from a current from accelerated electrons can be readily understood by Maxwell's equations (Ampere's law and Gauss' law for no magnetic monopoles):

$$\nabla \times \mathbf{B} = \mu_0 \mathbf{J} \tag{79}$$

However the need for charge and current neutralization results in the initial

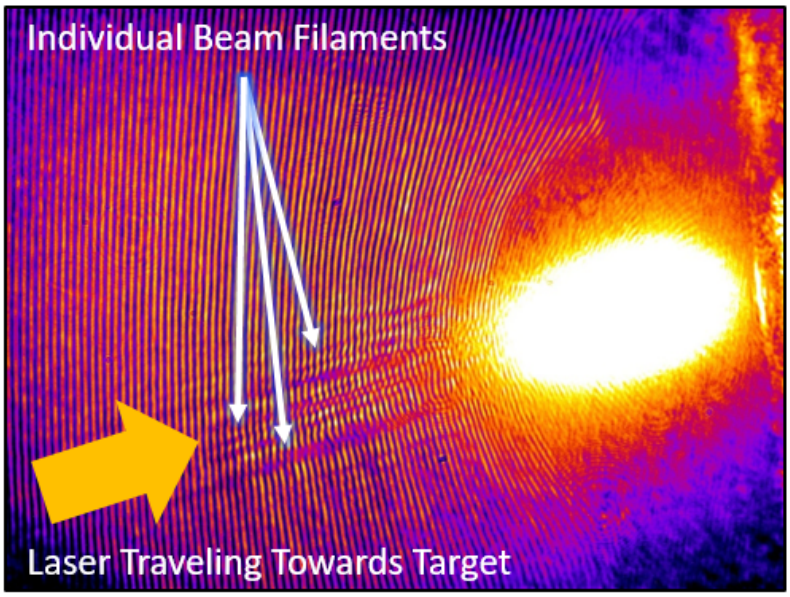

Figure 2.8: Interferogram image showing a laser incident on a target originating from the bottom left corner of the image. The density fluctuations due to the beam splitting into several filaments and pushing aside underdense plasma are visualized.

current creating a return current response in the opposite direction. However, this return current generally comes from cold electrons in the solid target and can be seen as cold and collisional (hence resistive).

$$\mathbf{J}_{return} = \frac{\nabla \times \mathbf{B}}{\mu_0} - \mathbf{J}_{initial} \tag{80}$$

Using Ohm's law to describe the return current, we can plug it into Faraday's law of induction to show:

$$\mathbf{E} = \eta \mathbf{J}_{return} \qquad \frac{d\mathbf{B}}{dt} = -\nabla \times \eta \mathbf{J}_{return} \tag{81}$$

$$\frac{d\mathbf{B}}{dt} = \nabla \times \eta \mathbf{J}_{initial} - \nabla \times \frac{\eta}{\mu_0}(\nabla \times \mathbf{B}) \tag{82}$$

The magnetic field growth in high intensity laser plasma interactions therefore

primarily depends on the magnitude of the fast electron current and the resistivity of the background plasma or material. To understand the effect on electrons accelerated by a cylindrical beam, the easiest treatment is to think of them as a large cylindrical current density traveling forward with the beam. Since currents in the same direction attract each other via an azimuthal magnetic field, hot electron streams tend to collimate if given a long propagation distance. However, in the presence of a return current, the collimating magnetic field is dissipated and deflected.

2.8.3 $\nabla N \times \nabla T$ Magnetic Fields

Magnetic fields also arise due to gradients in temperature and density in the plasma. The so called "Biermann Battery" field develops from an electron pressure that develops which is a product of temperature and density gradients in a plasma. Electrons flow from regions of higher electron pressure and generate an electromotive force which in turn creates a toroidal magnetic flux. We can begin to describe this process by using the equation of motion for electrons with the pressure term included.

$$nm_e\left(\frac{d}{dt}\mathbf{v_e} + \mathbf{v_e}\cdot\nabla\mathbf{v_e}\right) = -n_e e\left(\mathbf{E} + \frac{\mathbf{v_e}\times\mathbf{B}}{c}\right) - \nabla P_e - \nu_{ie} m_e(\mathbf{v_e} - \mathbf{v_i}) \tag{83}$$

Since the mass of electrons is small compared to the other terms we can drop the left hand side of the equation and the collision term to 0. The equation then simplifies to:

$$\mathbf{E} = -\frac{P_e}{n_e e} - \frac{\mathbf{v}\times\mathbf{B}}{c} \tag{84}$$

Which can then be plugged into Faraday's law (equation 4):

$$\frac{d\mathbf{B}}{dt} = \nabla \times (\mathbf{v} \times \mathbf{B}) + \nabla \times \left(\frac{c \nabla P_e}{n_e e} \right) \tag{85}$$

Using the vector identity

$$\nabla \times (\psi \mathbf{A}) = \psi(\nabla \times \mathbf{A}) + (\nabla \psi) \times \mathbf{A} \quad where \quad \psi = n_e^{-1} \; and \; \mathbf{A} = \nabla P_e \tag{86}$$

and by chain rule

$$\nabla n_e^{-1} = -\frac{\nabla n_e}{n_e^2} \tag{87}$$

$$\frac{d\mathbf{B}}{dt} = \nabla \times (\mathbf{v} \times \mathbf{B}) - \frac{c}{n_e^2 e} \left(\nabla n_e \times \nabla P_e + \cancelto{0}{\psi(\nabla \times \nabla P_e)} \right) \tag{88}$$

Since pressure is a function of temperature with $P_e = n_e k_b T_e$ we can rearrange the final term as:

$$\frac{c}{n_e^2 e} \left(\nabla n_e \times \nabla P_e \right) = \frac{c k_b}{n_e^2 e} \left(\nabla n_e \times n_e \nabla T_e + \cancelto{0}{\nabla n_e \times T_e \nabla n_e} \right) \tag{89}$$

The Biermann Battery term in typical environments close to 0 since pressure is usually a function of density and their gradients are often parallel. However in the high intensity regime, temperatures and densities often become decoupled resulting in the creation of large magnetic fields proportional to $-\nabla n_e \times \nabla T_e$. The resulting magnetic fields have enough strength to inhibit and deflect electrons passing through the region.

2.9 The Potential Well Heating Mechanism

2.9.1 Development of the Potential Well

The development of significant electrostatic potential well is one of the most significant consequences to electron generation and transport in pre-plasma. When a high intensity laser is incident on a significant pre-plasma a large degree of charge

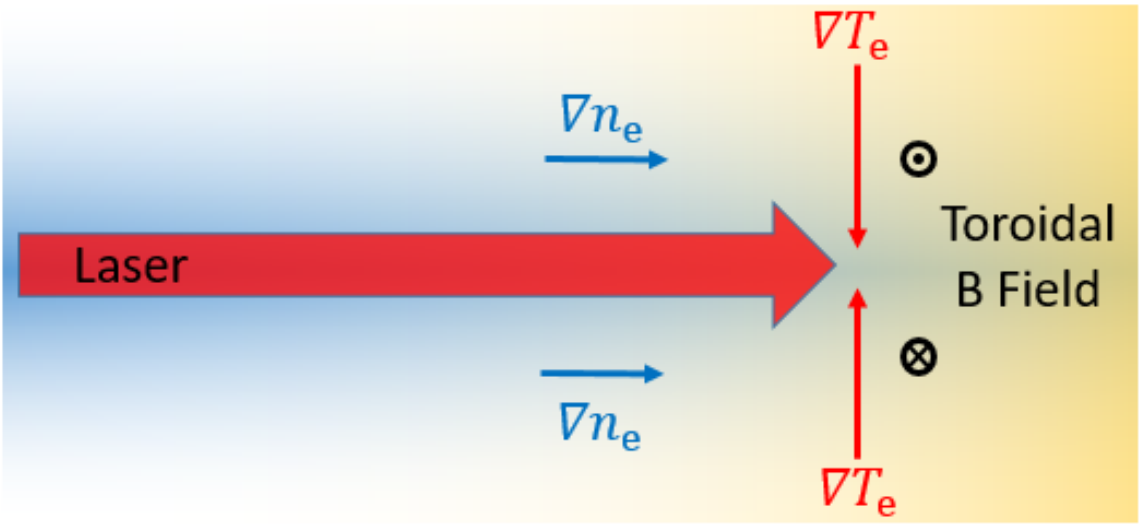

Figure 2.9: Cartoon of major components of magnetic field generation via the Biermann Battery effect. Plasma temperature increases closer to the center of the laser in the region of high intensity while plasma density increases as the laser gets closer to the target.

separation occurs since electrons react to the incident light much more quickly than ions. This manifests in two ways, first a density shelf develops at the critical density of the laser, as the laser pressure pushes plasma forward until it reflects at the critical density. Second, the swift response of electrons leaving the region of greatest laser absorption results in the development of a large electrostatic potential well. This well manifests as an electric field in the longitudinal (laser propagation) direction and heats electrons significantly in two ways.

2.9.2 Stochastic Heating

Stochastic heating occurs where the laser is reflected near the critical density. The light from reflection combines with the incident light creating a standing wave where the electric and magnetic fields oscillate only with respect to time. The standing wave and reflecting wave cause the electrons that are trapped in the region with the electrostatic potential to become dephased from the incident beam [29], [30]. One

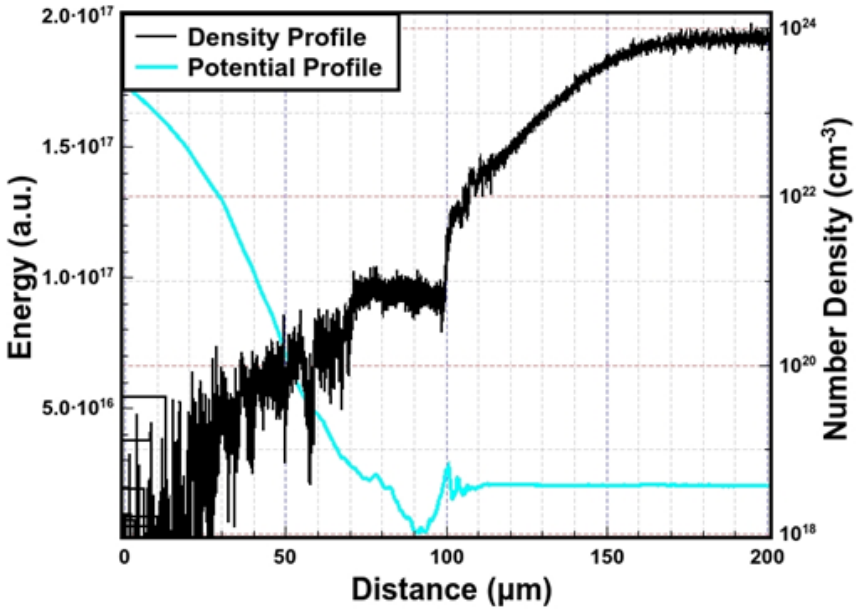

Figure 2.10: 1D simulation results showing the resulting density profiles of a beam incident on a simple exponential scale length pre-plasma. In black the density profile shows how a small density shelf can be created by the beam pushing electrons away up to the critical density. In blue the expansion of the electrons quickly results in a large charge separation creating an electrostatic potential well that traps future electrons.

effect of this is that the symmetry described previously by the Lawson-Woodward theorem is broken and energy can be gained by the electron. The standing wave and reflected waves can cause the electron to travel in an effectively random direction and not in line with the polarization of the beam. The stochastic nature of the electron is mostly independent from the incident beam and therefore the electron can be accelerated via $\mathbf{J} \times \mathbf{B}$ forces further while keeping its stochastic energy gain.

Z. M. Sheng demonstrated in 1D PIC simulations that when the two counter propagating pulses are of equal intensity, longitudinal momentum gained by the electrons is symmetric around zero [30]. However, as the reflected wave decreases in intensity, this symmetry is eroded and the motion of electrons go preferentially forward in momentum space. A counter propagating pulse with $\sqrt{I} = 1/30$ the incident beam

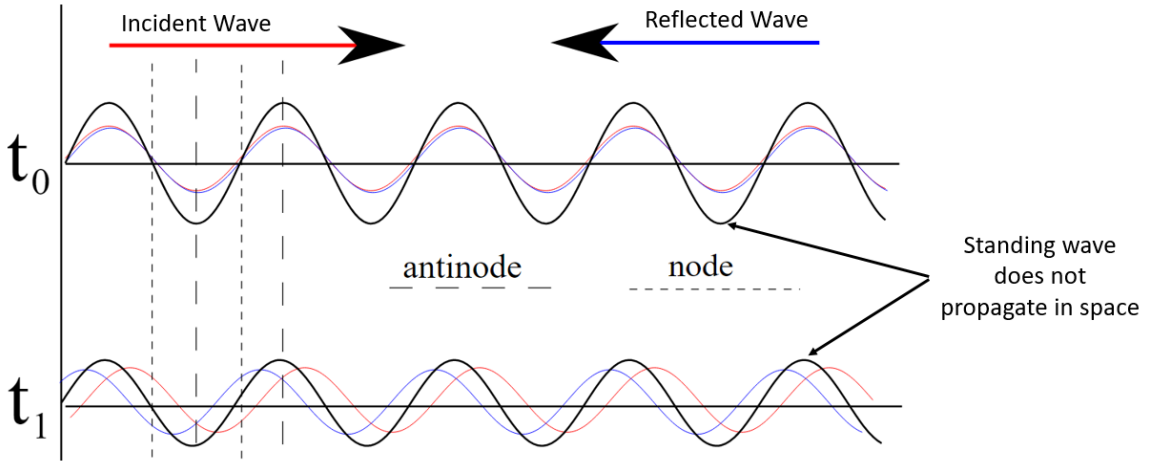

Figure 2.11: Diagram of the formation of a standing wave due to reflected light. The standing wave allows the typical symmetry of the $\mathbf{J} \times \mathbf{B}$ force to be broken in the pre-plasma instead of at the target surface. Electrons can gain momentum in unanticipated directions from the standing wave and be further heated by the incident beam after asymmetry is broken.

produced a nearly 4 fold increase in maximum electron energy. Electrons were shown to gain the majority of their energy by the transverse electric field of the laser. These electrons are eventually propagated in the forward direction via the Lorentz force. However, this stochastic heating was greatly decreased when the counter-propagating pulse simulation was brought into 2D simulations.

These results were compounded upon by A. Kemp [29] and B. Paradkar [31] who used 1D 3 velocity PIC simulations to characterize the time scale and degree to which this stochastic heating takes place. These results showed that the majority of super-ponderomotive electrons that make up the hot electron tail are heated in the long underdense pre-plasma, with densities between $0.01-0.1n_c$. The potential which traps the electrons develops over roughly 170 fs; electrons lock phase with either the incident or counter propagating beam and gain energy. The asymmetry of the well as shown in Fig 2.9 leads to electrons preferentially escaping the well in the forward going direction.

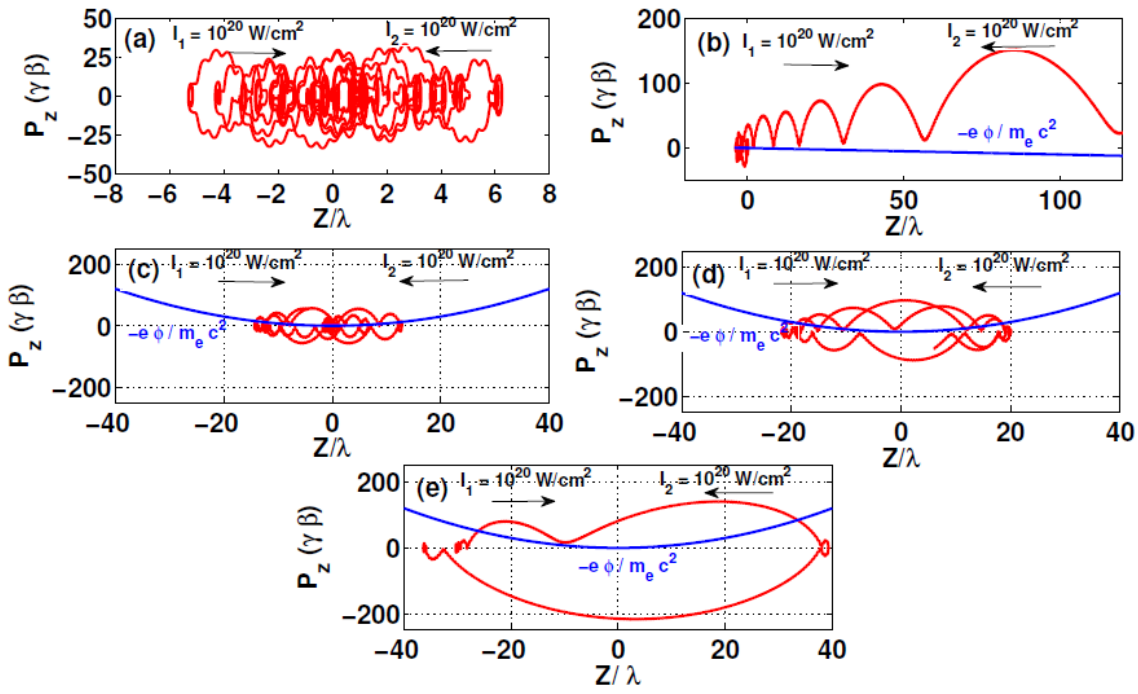

Figure 2.12: Phase space trajectories for electrons in the presence of different potential wells [31]. (a) has no potential, (b) has a constant field in one direction, (c), (d) and (e) are with the same symmetric potential well but with different starting locations.

B. Paradkar further built upon this work with an exploration of an infinitely tall V shaped potential well to examine how electrons are heated [32] using only the forward going wave. Assuming the center of the well is placed at z = 0 an electron would be pushed up the well slightly by the laser, then eventually would move back down the well and travel up the other side. Each pass through the well allows the electron to gain energy from the laser. The electron Using the Z momentum and energy equations, along with the assumption of a constant longitudinal electric field an expression for the trajectory of an electron can be produced:

The significance of the potential well for stochastic heating is two fold. First, the right edge of the well near the target causes some electrons to move backwards slowly into regions with large amounts of reflection and stochastic heating. The second is that the left side of the well in the under dense pre-plasma feeds in cold electrons

to be trapped and heated. These effects cause electrons heated by stochastic heating to have energy greater than ponderomotive scaling predictions. These electrons are generated somewhat close to the target surface on the critical density shelf and scale with quantity of pre-plasma (characterized by an exponential scale length) and pulse length.

$$\frac{d\gamma V_z}{dt} = -\frac{1}{2\gamma}\frac{da^2}{dz} - E_z \qquad \frac{d\gamma}{dt} = \frac{1}{2\gamma}\frac{da^2}{dt} - E_z V_z \tag{90}$$

Assuming the plane wave has a form of a(t-z) (where z is normalized to c) and combining the two equations and integrating:

$$\gamma(1 - V_z) = \delta_0 + E_z(t - t0 - z) \tag{91}$$

Where δ_0 is a constant found by using the known condition for when the electron crosses the boundary at z = 0, and $E_z = 0$. Describing V_z in terms of local time for the electron ($\tau = t - z$ in the normalized wave scheme)

$$V_z(\tau) = \frac{dz}{d\tau} = \left(\left[\frac{\gamma_\perp(t_0 + \tau)}{\delta_0 + E_z\tau} \right]^2 - 1 \right) \Big/ 2 \tag{92}$$

The energy gained from a single "bounce" inside the potential well (where passing the center z = 0 point is denoted by times τ_0 and τ_1) can be then described by:

$$\Delta\mathcal{E}(\tau_1 - \tau_0) = \frac{1}{2}\int_0^{\tau_1 - \tau_0} \frac{d(\gamma_\perp(t_0 + \tau))^2}{d\tau}\frac{1}{\delta_0 + E_z\tau}d\tau \quad \propto \quad \frac{a_0^2}{E_z} \tag{93}$$

These results signify that significant heating of electrons can occur within the potential well without any counter propagating beam. The amount of energy gained from traveling through the potential well is a function of the distance that the well covers. The longer the distance, the more time that the electron has to gain energy

from the beam. For electrons in a vacuum accelerated by a plane wave, the maximum energy gain is approximately $m_e c a_0^2/2$, while electrons in accelerated via the potential well have an energy proportional to a_0^2/E_z.

2.9.3 Direct Laser Acceleration

Direct laser acceleration is a separate pre-plasma/electrostatic potential heating effect that typically occurs farther away from the target surface than stochastic heating. It relies on the electron dephasing from the laser far from the critical surface and being accelerated asymmetrically by the laser field once dephased and was outlined by A. P. L. Robinson [33] To show this we first must show the case without the longitudinal electric field. First we list the equations of motion from the Lorentz force given that the laser is traveling in the x direction with B in the y direction.

$$\frac{dp_x}{dt} = ev_z B_y \qquad \frac{dp_y}{dt} = 0 \qquad \frac{dp_z}{dt} = eE_z - ev_z B_y \tag{94}$$

$$\mathcal{E} = \frac{1}{2} m\mathbf{v}\cdot\mathbf{v} \quad \rightarrow \quad \frac{d\mathcal{E}}{dt} = m\mathbf{v}\cdot\frac{d\mathbf{v}}{dt} = \mathbf{v}\cdot\mathbf{F} \tag{95}$$

$$\frac{d\mathcal{E}}{dt} = mc^2\frac{d\gamma}{dt} \quad \rightarrow \quad \frac{d\gamma}{dt} = \frac{q\mathbf{v}\cdot\mathbf{E}}{mc^2} = -\frac{ev_z E_z}{mc^2} \tag{96}$$

By conveniently describing the incident light wave as a vector potential $\mathbf{A} = (0, 0, A_0 cos(\omega_L \tau))$ we can rearrange using:

$$\mathbf{E} = -\frac{d}{dt}\mathbf{A} \qquad \mathbf{B} = \nabla\times\mathbf{A} \quad \rightarrow \quad E_z = -\frac{d}{d\tau}A \quad B_y = \frac{1}{c}\frac{d}{d\tau}A \tag{97}$$

Where $\tau = t - \frac{x}{c}$ is the phase of the wave and $\frac{d\tau}{dt} = 1 - \frac{v_x}{c}$. Using the equation of motion for p_z we find:

$$\frac{dp_z}{dt} = e\frac{d}{d\tau}A - \frac{ev_x}{c}\frac{d}{d\tau}A \tag{98}$$

$$\frac{dp_z}{dt}\frac{dt}{d\tau} = \frac{dt}{d\tau}\left(e\frac{d}{d\tau}A - \frac{ev_x}{c}\frac{d}{d\tau}A\right) = \frac{dt}{d\tau}\cancel{\left(1 - \frac{v_x}{c}\right)}^{1} e\frac{d}{d\tau}A \tag{99}$$

$$\frac{dp_z}{d\tau} = e\frac{d}{d\tau}A \quad \rightarrow \quad p_z = eA \quad Integral\ of\ motion\ 1 \tag{100}$$

Where an integral of motion is a description of a a value is constant in phase space. In this case, traveling along p_z in phase space has a constant value of eA. We use this along with the expressions E_z and B_y in the conservation of energy and x momentum equations to obtain two more integrals of motion for x and gamma:

$$v_z = \frac{eA}{\gamma m} \quad \frac{dt}{d\tau} = \gamma \quad \rightarrow \quad \frac{dp_x}{dt} = ev_z B_y = \frac{e^2 A}{\gamma mc}\frac{d}{d\tau}A = \frac{e^2}{2\gamma mc}\frac{d}{d\tau}A^2 \tag{101}$$

$$\frac{dp_x}{dt}\frac{dt}{d\tau} = \frac{dp_x}{d\tau} = \frac{dt}{d\tau}\frac{e^2}{2\gamma mc}\frac{d}{d\tau}A^2 = \frac{e^2}{2mc}\frac{d}{d\tau}A^2 \tag{102}$$

$$p_x = \frac{e^2 A^2}{2mc} \quad Integral\ of\ motion\ 2 \tag{103}$$

This integral of motion is tied to the earlier energy gain equation for $\mathbf{J} \times \mathbf{B}$ acceleration in section 2.3. It leads to the maximum energy gain for electrons without the longitudinal field to be characterized by $m_0 c^2 A^2/2$. Continuing by combining the equations for conservation of longitudinal momentum and gamma we find:

$$\frac{d\gamma}{dt} = -\frac{ev_z E_z}{mc^2} = \frac{ev_z}{mc^2}\frac{d}{d\tau}A \quad \rightarrow \quad ev_z\frac{dA}{d\tau} = mc^2\frac{d\gamma}{dt} \tag{104}$$

$$\frac{dp_x}{dt} = ev_z B_y = \frac{ev_z}{c}\frac{d}{d\tau}A = mc\frac{d\gamma}{dt} \quad \rightarrow \quad \frac{d}{dt}\left(\gamma - \frac{p_x}{mc}\right) = 0 \tag{105}$$

Integrating this equation and choosing the constant carefully results in:

$$\gamma - \frac{p_x}{mc} = R \quad where \quad R \equiv 1 \quad Integral\ of\ motion\ 3 \tag{106}$$

The dephasing rate of R is chosen to be 1 for simplicity in this case. This rate is essentially the rate at which the phase of the laser wave changes at the electron's location with respect to proper time τ. A dephasing rate that is 0 is to say that the particle is moving completely in phase with the wave. All of these results are standard for the electron in an electromagnetic wave, however when a constant longitudinal electric field is introduced a few significant changes occur.

$$\frac{dp_x}{dt} = eE_o + ev_z B_y = eE_o + mc\frac{d\gamma}{dt} \tag{107}$$

$$\frac{d}{dt}\left(\frac{p_x}{mc}\right) = \frac{eE_o}{mc} + \frac{d\gamma}{dt} \quad \rightarrow \quad \frac{-eE_o}{mc} = \frac{d}{dt}\left(\gamma - \frac{p_x}{mc}\right) = \frac{dR}{dt} \tag{108}$$

This shows that a longitudinal electric field that traps electrons, providing a force towards the target decreases the dephasing rate. This can be used in conjunction with the momentum equation in the x direction.

$$\frac{d\tau}{dt} = 1 - \frac{v_x}{c} \quad R = \gamma - \frac{p_x}{mc} = \gamma - \frac{\gamma m v_x}{mc} = \gamma - \frac{\gamma v_x}{c} \tag{109}$$

$$\frac{d\tau}{dt} = \frac{R}{\gamma} \quad p_z = \gamma m v_z = eA \quad \rightarrow \quad v_z = \frac{eA}{\gamma m} \tag{110}$$

$$\frac{dp_x}{dt} = eE_o + \frac{ev_z}{c}\frac{d}{d\tau}A = eE_o + \frac{e^2A}{\gamma mc}\frac{d}{d\tau}A = eE_o + \frac{e^2A}{\gamma mc}\frac{dt}{d\tau}\frac{d}{dt}A \tag{111}$$

$$\frac{dp_x}{dt} = eE_o + \frac{1}{R}\frac{A}{mc}\frac{d}{dt}A \quad \boxed{p_x = eE_o t + \frac{1}{R}\frac{A^2}{2mc}} \tag{112}$$

This equation demonstrates the clear effect of the electrostatic potential in the longitudinal direction. When comparing the two cases there are two differences to the change in momentum in the longitudinal direction. First the electron is affected directly by the potential in the eE_o term. However, much more significantly a new factor is introduced to the original integral of motion for p_x which is the factor of $1/R$. It is immediately clear that if the dephasing rate decreases significantly the energy and momentum gained by electrons in the x direction increases dramatically.

This effect essentially means that while the electrostatic potential might impart a slight bit of energy to the electron, the majority of the energy gain comes from the electron traveling more in phase with the laser and encountering an asymmetric balance in the laser field as a result. It makes sense that the electrostatic force is not the main driver as the potential well that traps electrons close to the target surface would decelerate electrons close to the target as much as accelerate them far away.

2.10 Previous Experiments Examining Pre-Plasma Impact

Initial experiments looking into the effect of pre-plasma on electron generation and transport were conducted with respect to fast ignition target geometries. A particular experiment which demonstrated this was that performed by T. Ma et al. [59]. This experiment demonstrated that in the cone target case total conversion into 1-3 MeV electrons produced by $\mathbf{J} \times \mathbf{B}$ forces was reduced significantly. Another outcome was greater coupling to a hotter temperature component in the electron spectrum that

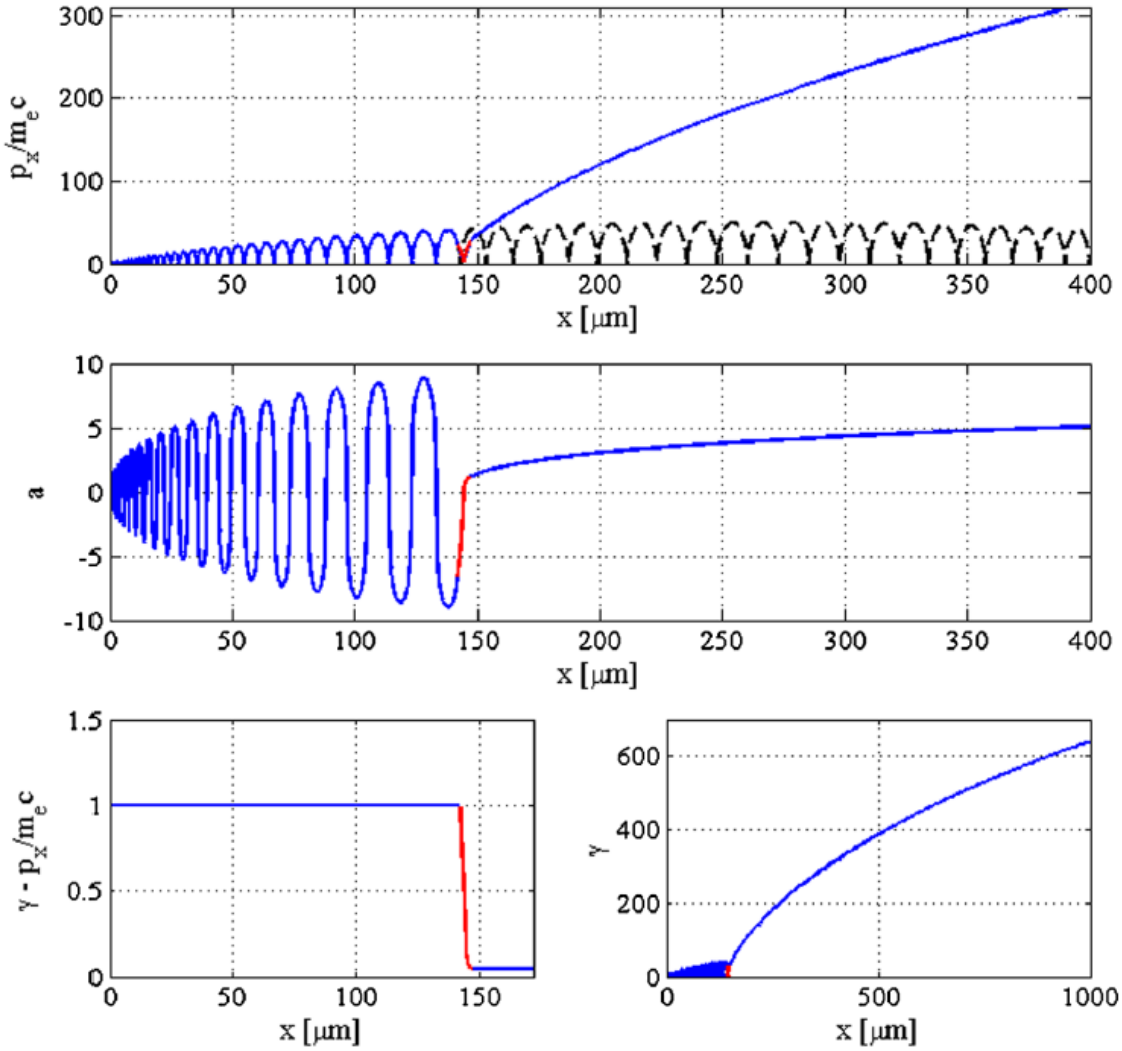

Figure 2.13: Simulation results conducted by A. P. L. Robinson [33] who demonstrated this DLA effect via simulation. Here we see how the electron is accelerated primarily by $\mathbf{J} \times \mathbf{B}$ forces until it reaches a large electrostatic potential shown in red. This drops the corresponding dephasing rate (bottom left) which causes a large jump in electron energy well beyond the limits of $\mathbf{J} \times \mathbf{B}$ acceleration.

also increased in temperature. These electrons were not of great interest to the study as 1-3 MeV electrons that scaled ponderomotively are the drivers for fast ignition and these higher energy electrons would simply pass through the target. It should also be noted that this experiment utilized the cone geometry; while this target was

a good comparison for fast ignition schemes, it is difficult to understand some of the basic underlaying processes for pre-plasma with complicated geometry. Furthermore, this experiment took place on the Titan laser (0.7 ps, 10^{19} W/cm^2) with a secondary beam used to generate different levels of pre-plasma. It must be kept in mind that the case with least amount of pre-plasma still is a significant amount compared to other laser systems that have been developed with higher contrast ratios. The minimum amount of energy in a pre-pulse for Titan is 17 mJ, easily enough to ionize several microns scale length of pre-plasma. This intrinsic pre-plasma was overlayed by another controlled pre-plasma created by a separate low intensity long pulse beam. Another aspect of this experiment is that the hot electron temperature was inferred by the Cu-Kα x-rays that were generated inside the wire target by electrons that made it through the target into the wire. In the context of this experiment this makes complete sense since the goal was to understand the type of electrons that would make it into the compressed fuel capsule rather than understanding the processes within the pre-plasma itself. However, to fully understand the nature of hot electrons on these experiments, direct measurements of electrons are extremely important since inferring electron qualities from Kα x-rays alone is prone to error and only applies to a small energy range of electrons.

Further experiments were conducted by K. Tanaka et al. [35] (with further PIC analysis performed by H. Cai et al. [36]) and T. Yabuuchi et al. [37] utilized a planar target geometry and along with a controlled long pulse beam to generate a pre-plasma. In the Tanaka experiment Kα x-rays were once again used to gauge the temperature change in electrons due to the increased pre-plasma. The results using the GEKKO XII laser system showed similar results to T. Ma's Titan experiment, which is reasonable considering experimental parameters were very similar (0.5-1.0 ps pulse length with $I \sim 10^{18} - 10^{19}$ W/cm^2). A two temperature spectrum was

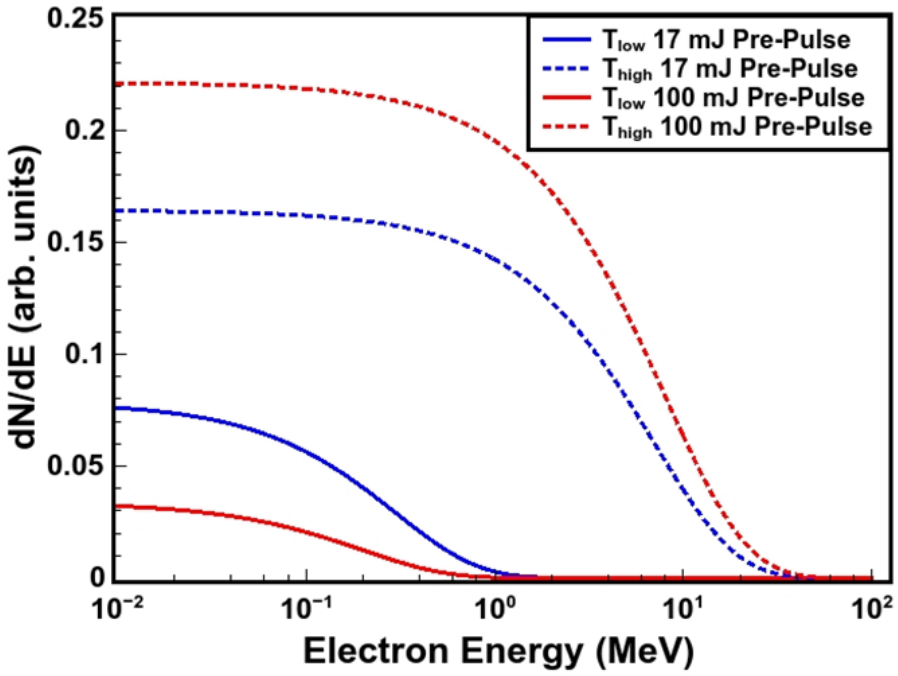

Figure 2.14: Inferred components of the electron spectra from T. Ma's experiment with cone wire geometry on the Titan laser. As pre-pulse increased from 17mJ to 100mJ the conversion efficiency of laser energy to lower energy 1-3 MeV electrons was decreased while the temperature and coupling to higher energy electrons greatly increased. These measurements were inferred by Cu-Kα measurements taken on the wire that was attached, which was heated by electrons that emitted from the cone tip.

inferred from a Kα measurement of a buried fluor layer in the planar target, similar to that used in T. Ma's experiment. As pre-plasma increased, the second temperature component appears to become hotter and have slightly increased coupling, while the lower temperature component decreases in temperature and coupling.

T. Yabuuchi's experiment at the GMII laser facility at ILE Osaka University finally used a few different approaches to understand the generation and transport of hot electrons in the target. Similar to other experiments, a 12 J, 400-600 fs beam with a nominal intensity of $I = 2 \times 10^{18}$ $/mathrmW/cm^2$ was incident on a planar foil target with a buried copper fluor layer. An injected pre-plasma was created with a 1.5 J, 500 ps beam sent 200 ps in advance to the short pulse. A magnetic electron

spectrometer was introduced, and the use of a x-ray crystal imager on a planar geometry setup allowed clear tracking of electron trajectories. Direct measurements of electrons and their energy clearly demonstrated that the introduction of pre-plasma causes a second hotter temperature component to arise in the electron spectrum (Fig 2.15). Direct electron measurement showed that without pre-plasma, the maximum energy of electrons measured by the magnetic spectrometer was around 1 MeV, in line with ponderomotive scaling predictions. When the pre-plasma was introduced the maximum energy shot up to over 8 MeV.

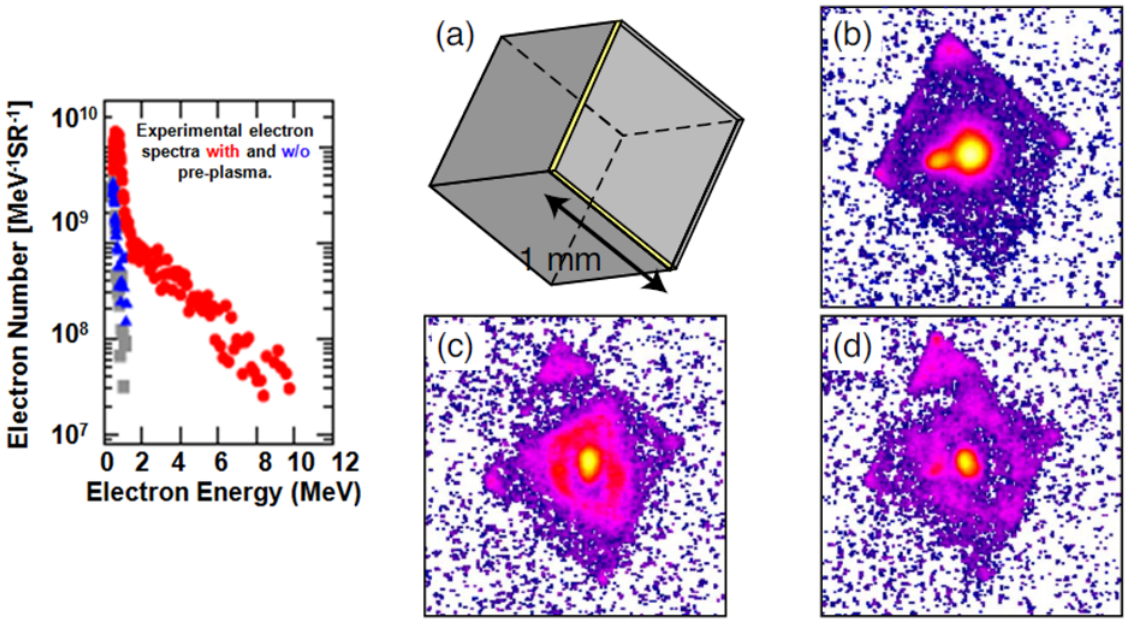

Figure 2.15: Left: Magnetic spectrometer results for T. Yabuuchi's experiment on the GMII laser. The electron spectrum for a shot with an injected pre-pulse is shown in red which demonstrates the distinct 2 temperature nature of the electron spectrum with pre-pulse [37]. Right: 3 sets of Cu-Kα imager data with increasing levels of injected pre-plasma in cases b-d. These images demonstrate how electron trajectory changes significantly along with temperature.

Even shorter pulse length experiments were conducted by K. A. Ivanov [38]. This experiment used a beam with a peak intensity of around $1-2\times10^{18}$ W/cm^2 and had a variable pulse length of 45 and 350 fs. In this experiment an underdense plasma was created on solid target surface by a short spike pre-pulse timed 12.5 ps prior to

the main pulse and inferred hot electron production by placing x-ray scintillators in the reflection direction. The changes in the electron spectrum are difficult to attribute directly to the pre-plasma in this experiment since intensity appeared to vary between 7×10^{17} and 2×10^{18} W/cm^2 for comparable results. Increases in x-ray (and therefore electron) temperature can be attributed to both increases in intensity and pre-plasma and it is difficult to separate the two. The lower intensity data is strictly out of the high intensity regime which could have a large impact on the resulting electrons.

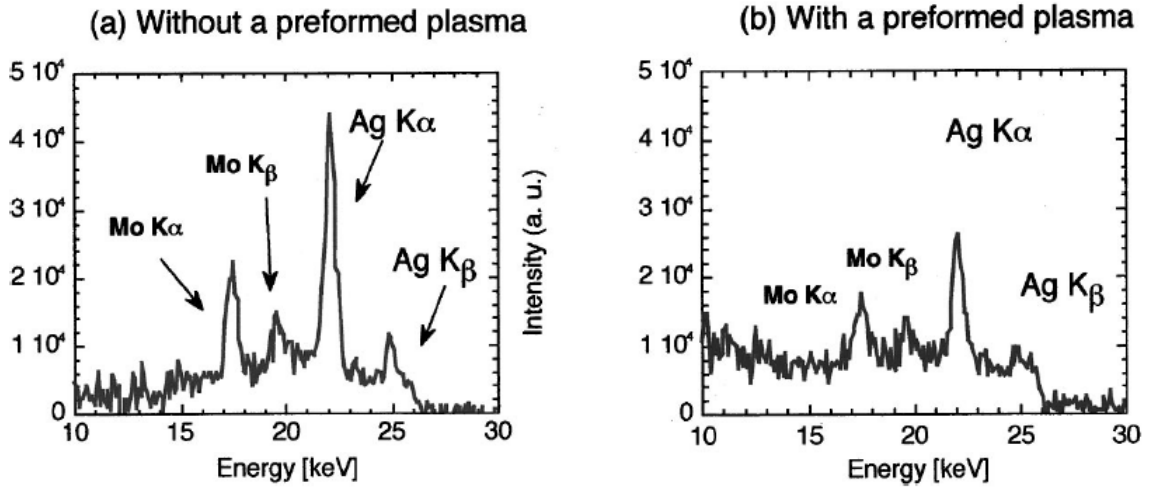

Figure 2.16: Change in x-ray signals for a high intensity laser plasma interaction with and without a pre-plasma in K. Tanaka's experiment [35]. It is difficult to infer precise changes to the electron spectra and trajectory by only using Kα and Kβ magnitudes and ratios.

Another fs pulse length experiment was conducted by C. Gahn who used a helium gas jet to create an underdense plasma with a maximum density of 4×10^{20} $/mathrmcm^{-3}$, which was shot by a 2×10^{18} W/cm^2, 200 fs beam [39]. Electrons were measured by magnetic electron spectrometer, similar to T. Yabucchi's experiment. Rather than comparing cases with and without pre-plasma like in other experiments this experiment examined how a change in beam intensity would change the spectrum of electrons generated. Supplemental 3D PIC simulations showed that higher energy electrons were more collimated and that higher energy electrons are

much more collimated than their low energy counterparts. These also showed that the electrons gained most of their energy from the transverse electric field rather than the longitudinal one suggesting DLA was the primary cause of electron acceleration in the large underdense plasma.

A noticeable trend in these experiments is all of them have a very short pulse length, in the sub ps regime. With respect to fast ignition schemes the pulse lengths are often orders of magnitude less than those that would be used on a full scale fast ignition experiment. Furthermore the intensities for many of these experiments is only slightly above the order of magnitude for relativistic laser plasma interactions. An experiment that was performed in parallel with this work was conducted by L. Willingale et al. which used OMEGA-EP's long pulse high intensity capabilities to look at super-ponderomotive electron generation for longer pulse lengths [40]. The 10 ps pulse was incident on a completely underdense target generated by shooting a metal foil by a low intensity beam. The expanding plasma was hit by the 10 ps high intensity OMEGA-EP beam perpendicular to the direction of expansion such that the beam only interacted with underdense plasma and not the foil target. Using magnetic electron spectrometers and proton radiography these experiments showcased the channel that forms from the intense beam punching through the underdense plasma and measured large quantities of super-ponderomotive electrons guided in the channel direction. These electrons have implications for fast ignition as the channel can potentially guide lower energy electrons, though the higher energy electrons waste laser energy into potentially preheating the fuel.

These experiments have a few gaps in terms of regime. Most experiments were performed on lasers that were either very short pulse with borderline relativistic intensities, or on lasers with intensities suited for fast ignition studies. How electron generation and transport changes with $> 10^{20}\ W/cm^2$ beams (more typically used

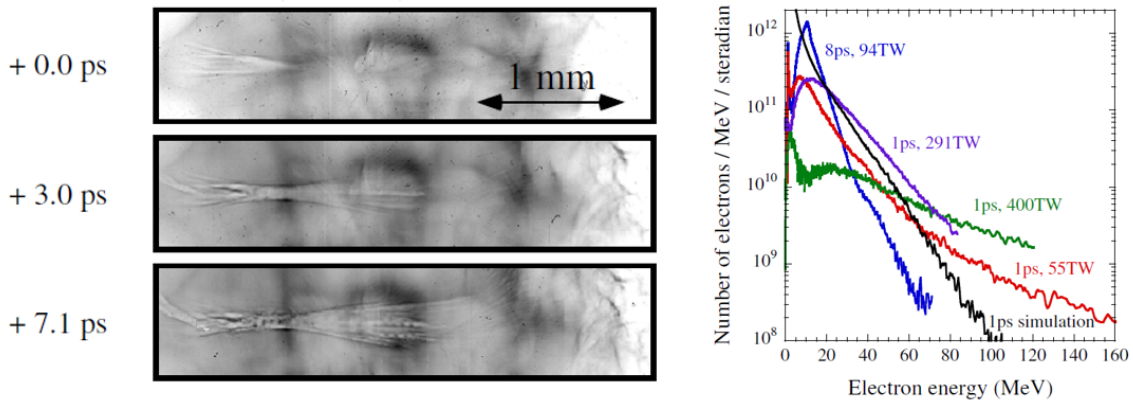

Figure 2.17: Results from L. Willingale's experiment on OMEGA-EP [40]. Left: proton radiographs showing extensive beam filamentation with beam focusing and self focusing. Right: Multiple results from a magnetic electron spectrometer showing changes in the electron spectrum based on beam intensity and pulse duration (1 and 8 ps)

in ion/proton acceleration experiments) is less studied. Research has also been concentrated on the lower temperature "ponderomotive scaling" electrons which would be useful in fast ignition while the super-ponderomotive electrons accelerated in the pre-plasma receive less interest. In a fast ignition context, these super-ponderomotive electrons are detrimental and much work goes into trying to remove them instead of create them. Some diagnostic challenges are showcased in the previous experiments, electrons are often diagnosed indirectly by x-rays. These x-rays do not adequately capture the 10-100s MeV electrons generated in higher intensity pre-plasma interactions and also does not measure their trajectory. Target type was also extremely varied, with the most basic experimental targets consisting of an underdense plasma (i.e. gas jet), while extremely complicated targets used a cone geometry.

2.11 Previous Simulation Work Examining Pre-Plasma Impact

Pre-plasma's impact on electron generation and transport has been extensively examined with particle-in-cell simulations. These can best be split into two categories, those looking at ponderomotive scaling electrons and those looking at the source and acceleration mechanisms of super-ponderomotive electrons.

Of large significance to the fast ignition community was the work conducted by A. G. MacPhee, which simulated a high intensity beam incident on a cone filled with pre-plasma [41]. These simulations attempted to replicate conditions inside a cone for a fast ignition experiment with high pre-plasma and used a 10^{20} W/cm^2 laser incident on a copper cone. It found that the pre-plasma significantly impacted beam propagation and electron energy and trajectory. In terms of forward going electrons, which would theoretically couple to the compressed fuel, it was found that 2-4 MeV ponderomotive scaling electrons were directed away from the forward going direction. This was caused by the beam filamenting into multiple smaller beams and these resulting filaments self focusing into a trajectory away from the forwards going direction. This results in electrons being generated far from the cone tip which would lead to poor coupling to compressed fuel.

Further cone geometry simulations were conducted by A. J. Kemp. These simulations did not include an underdense plasma, but they did examine the resulting plasma expansion of a high intensity beam incident on a solid cone for several ps [42]. Since a full scale fast ignition experiment would require a beam duration of several tens of ps it was important to understand how the surface of the target evolved over the entire duration of the high intensity laser pulse. Kemp showed that significant perturbations grow in the target surface as the laser impacts it non uni-

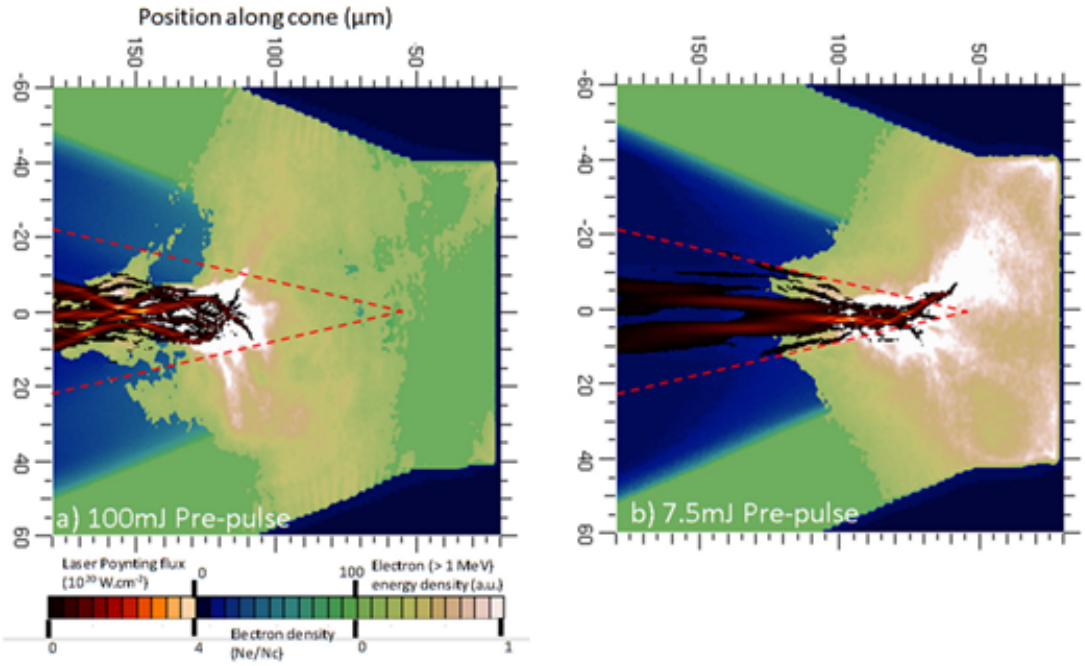

Figure 2.18: Simulation results of a beam incident on a copper cone filled with underdense plasma. Electron flux is shown in white and green while beam pointing is shown in red. The red trace of the actual position of cone walls shows that the beam filaments and stops far before the solid surface. Electrons are generated in the walls of the cone rather than in the cone tip.

formly. These perturbations become unstable and cause the incident laser to generate electron beams in certain locations more favorably. Instead of a uniform spread of electrons, the electrons also become filamented and do not necessarily travel in a forward direction. These simulations also demonstrated that for longer pulse beams, an underdense plasma forms during the laser pulse due to the target self heating. This plasma significantly increased the temperature and quantity of super-ponderomotive electrons, likely acting much like a pre-plasma does for other interactions.

Two main sources of super-ponderomotive electron generation and transport have been posited by simulations Z. Sheng [29], B. Paradkar et al. [30], A. Krygier [43], A. P. L. Robinson et al. [33] and A. Arefiev et al. [44]. B. Paradkar demonstrated using 1D PIC simulations that stochastic heating (seen previously in section 2.6.2)

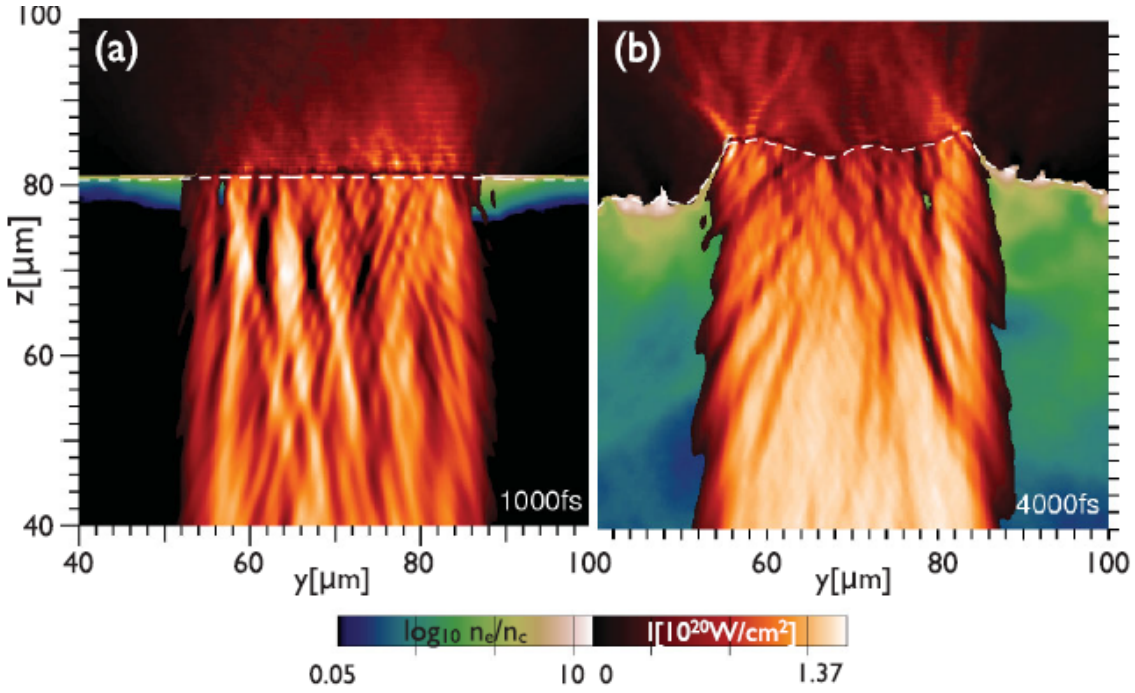

Figure 2.19: Simulation results by A. Kemp which use a beam with a variety of pulse lengths incident on a clean cone without pre-plasma. The underdense plasma and uneven surface of the cone wall leads to uneven electron generation and propagation.

occurs in an electrostatic potential well that develops in the pre-plasma. The well traps electrons which are affected by both the incident and reflected beams. These simulations were conducted for a wide intensity range of 10^{19}, 10^{20} and 10^{21} W/cm^2 for a ~ 0.5 ps pulse and 3 single scale length exponential pre-plasma density profiles. Electrons heated by this potential well are estimated to gain energy proportional to $1 + C(a_0^2/E_z) + \beta a_0$ where C and β are factors depending on beam intensity and pre-plasma scale length. This is much more than the ponderomotive proportional energy gain of $\sim a_0^2/2$.

The other simulations are in regard to another source of super-ponderomotive electrons. These are created by Direct Laser Acceleration (DLA) (which is explained in more detail previously in 2.6.3) which is another product of the longitudinal electrostatic potential that arises in a pre-plasma. Simulations showcasing this effect have been performed in 1-3D PIC simulations with various levels of pre-plasma and

pulse length. Most work surrounding this effect, such as in the 3 publications listed, examine shorter sub ps pulse length scenarios with higher intensities in line with the capabilities of new high intensity laser systems such as the Texas Petawatt. A. Krygier's publication also showcases the role of the magnetic field in injecting cold electrons into the DLA region; this mechanism of loop-injected direct acceleration is called LIDA. Further simulations that have recorded DLA for longer pulse lengths have been shown by L. Willingale et al. These simulations corresponded to the previously mentioned experiment on OMEGA-EP verified the acceleration of these electrons in the channel through underdense plasma over a longer period of time.

2.12 Defining Ponderomotive and Super-Ponderomotive Components of an Electron Spectrum

As shown in section 2.6, electrons accelerated near the surface of a target by a relativistic beam gain an energy that is best described by ponderomotive scaling. This represented by a single slope exponential decay spectrum with a characteristic slope temperature $k_b T_{Hot} = m_e c^2(\sqrt{1+a_0^2}-1)$. Furthermore, the predicted maximum energy gain for an electron in vacuum in a high intensity plane wave is best represented by $\mathcal{E}_{max} = m_e c^2(a_0^2/2)$ [45]. Using these characteristics, for the purpose of this dissertation **"ponderomotive scaling electrons"** refers to a portion of the electron spectrum that is best represented by a single slope temperature and have energy approximately less than the maximum energy gain of an electron in a vacuum. These electrons are accelerated via $\mathbf{J} \times \mathbf{B}$ and vacuum heating as listed in previous sections.

"Super-ponderomotive electrons" as we define them, must therefore have two defining characteristics. One, their temperature must vastly exceed $m_e c^2(a_0^2/2)$. Two, the super-ponderomotive electrons should not conform to the slope temperature of ponderomotive scaling electrons. In many papers and in this dissertation this is

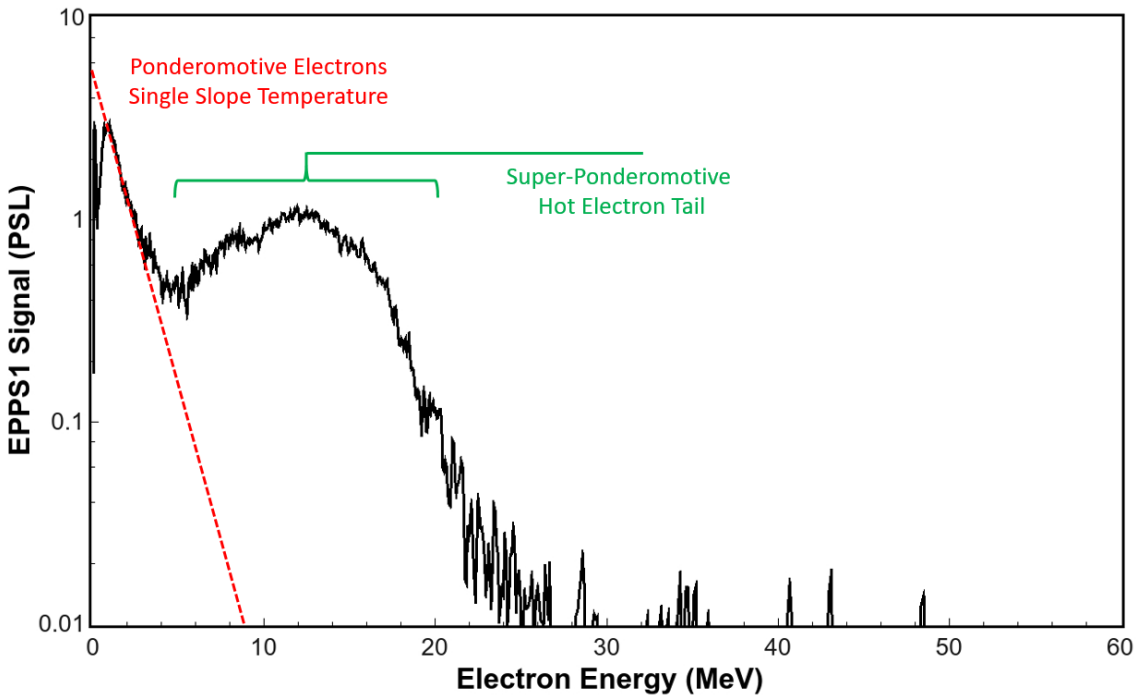

Figure 2.20: Example of an electron spectrum demonstrating the differences between ponderomotive scaling electrons and the super-ponderomotive hot electron tail.

referred to as a **hot electron tail**, where the super-ponderomotive electron spectra conform more closely with characteristic slope temperatures that are much higher. These are highlighted in Fig 2.20, which shows a clear two component electron spectrum where higher energy electrons do not conform at all to a single slope electron decay pattern.

Chapter 3
Experimental Design and Parameters

3.1 Overall Experimental Goals

The overall goal for the experiments described in this thesis is to examine the impact of pre-plasma on electron generation and transport over a wider range of beam pulse lengths, pre-plasma scale lengths and beam intensities than previously explored. To carry this out each experiment has the following characteristics:

- A high intensity ($I > \ 10^{18}$ W/cm^2) short pulse beam. This beam will be used for the main interaction to generate and heat electrons. The pulse length should be varied from hundreds of picoseconds to several picoseconds to examine the evolution of hot electrons for longer pulses.

- A low intensity (10^{11} W/cm$^2 < I < 10^{13}$ W/cm^2) long pulse beam. This beam should be several nanoseconds long and will be used to generate a controlled pre-plasma. To do this it must be carefully timed to arrive prior to the arrival of the short pulse beam. This low intensity beam should also cover a wide spot in order to create a one dimensional "injected" pre-plasma. This 1D pre-plasma aids interpretation of the results and simplifies the setup and analysis of simulations following the experiment.

- A simple planar metal target. The target should be planar in order to allow the interaction with the pre-plasma to be better understood and diagnosed compared to target geometries such as cones. The target is metal in order to provide a large solid density material that also glows with x-ray emission for diagnostic purposes and comparison to other experiments.

- Finally diagnostics should specialize in measuring hot electrons in the 1-100+ MeV range in order to characterize the impacts caused by pre-plasma. These diagnostics should be kept consistent between different experiments to allow closer comparisons between datasets.

3.2 Diagnostics

Most diagnostics use a recording device that are in 3 categories: image plates (IPs), charge-coupled devices (CCDs) and radiochromic film (RCF).

The majority of diagnostics used in the experiments presented, record their information on IPs, which consist of a coated phosphor layer attached to a magnet. The phosphor layer is comprised of a combination Cl, Br, I and Eu^{2+} which is excited to Eu^{3+} when energetic particles interact with the IP. The Eu^{3+} state is held until exposed to a HeNe laser used in most IP scanner systems. The laser excites the trapped electrons causing the phosphor to emit blue light as the Eu drops back to 2+. The light is then collected and amplified via a photomultiplier tube (PMT), and then digitized by the scanner. This information along with the scanning parameters are stored in PSL units, a consistent standard across scanning devices. This unit takes into account the various parameters and scanner settings used in the scan.

$$PSL = \left(\frac{Resolution(\mu m)}{100}\right)^2 \times \frac{4000}{sensitivity} \times 10^{(\frac{5*Signal}{65535}-0.5)} \tag{113}$$

The IPs are then "wiped" by being exposed to an intense light source for 20 minutes. The phosophor also slowly decays back to the 2+ level over time without illumination, however the rate at which it transitions decreases to small levels after 20 minutes. Therefore all IPs are scanned at consistent times 20 minutes after exposure in order to reduce uncertainty from signal drop due to the time of scan. The major caveat of most IP based diagnostics is that they are inherently time integrated, but

they have major advantages in spatial resolution (10-25 µm), reusability, dynamic range (5 orders of magnitude) and flexibility (IPs can be cut into nearly any shape for any diagnostic, the magnet layer allows for easy placement).

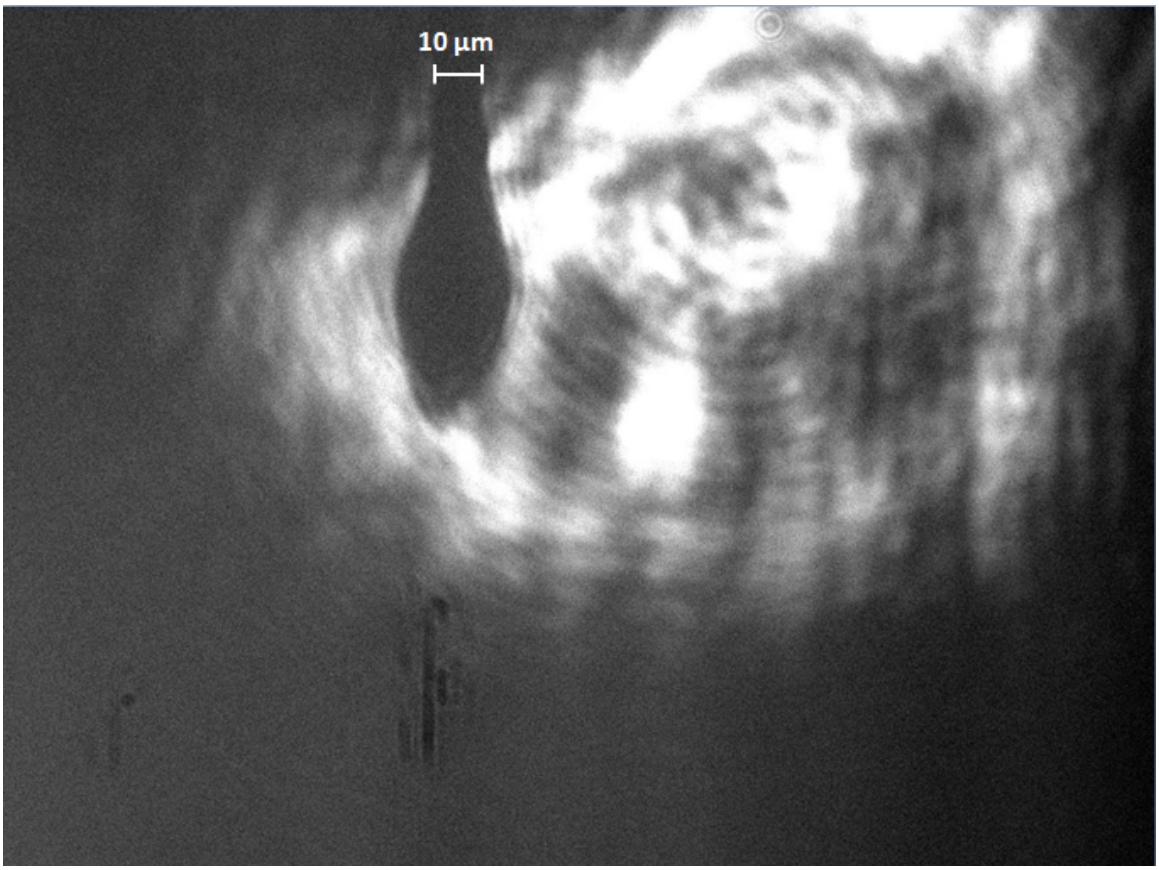

Figure 3.1: Example of a CCD looking at the shadow of a 10 µm against a defocused beam via a series of imaging optics.

CCDs offer many positives that fill in image plate short comings. Common to cameras and other light sensing tools they are time resolved and are used in more roles than just diagnostics. For this dissertation CCDs are used primarily in alignment of diagnostics and lasers. CCDs function by storing incident photons as a charge on a semi-conductor. These photo electrons are then shifted to a single channel and turned into a serialized data stream. The sensitive nature of the CCD chip reduces its flexibility as a diagnostic tool, as even minimal exposure to a laser plasma interaction pulse will permanently burn a mark on the semiconductor chip. Furthermore, the

electromagnetic pulse which takes the form of a large x-ray burst, which occurs on most experimental shots, has a tendency to fry electrical equipment. In particular devices with long unshielded wires, connected to sensitive electrons, can pick up a large current from the EMP and break.

Radiochromic film is a piece of film, typically coated in plastic or polyester that changes color when exposed to ionizing radiation and does not require any kind of physical or chemical post processing treatment. The sensitive layer is typically comprised of a polymer, which when exposed to radiation, changes into a dye polymer. After exposure the dyeing of the sensitive layer slows and becomes fixed quickly, usually within 24 hours. These pieces of film are extremely useful in collecting high energy proton and ion data. Since these particles have a very pronounced Bragg peak, meaning as they pass through material they deposit their energy in a very small depth range, it is possible to use multiple layers of film to differentiate between particles of different energy. Many different film types exist with varying levels of sensitivity. Those used on the experiments in this dissertation in order from most sensitive to least sensitive are EBT-3, MD-V2 and HD-810.

3.2.1 A Note About Error

Error comes in many forms in the experiment and it is important to distinguish between the different types of error in order to have any confidence in measurements taken on each experiment. The two most significant categories of error encountered in this work are **diagnostic error** and **experimental error**.

Diagnostic error represents the accuracy of a measurement taken by a diagnostic. When a measurement is taken by a diagnostic it must be asked: “”how certain is it that this information is what the diagnostic saw on the experiment?”. This is primarily governed by how many data points are collected and the signal to noise of those data points. In the case of image plate diagnostics, diagnostic error can

potentially be extremely low, each pixel measured on an image plate by the scanner is essentially another observation. These pixels may have a degree of standard deviation, or background signal which reduces the signal to noise ratio leading a degree of uncertainty in the measurement. Additionally if signal levels on the image plate are on the same order as the noise, diagnostic error increases. In the results graphs shown in later chapters the diagnostic error is represented by the error bars.

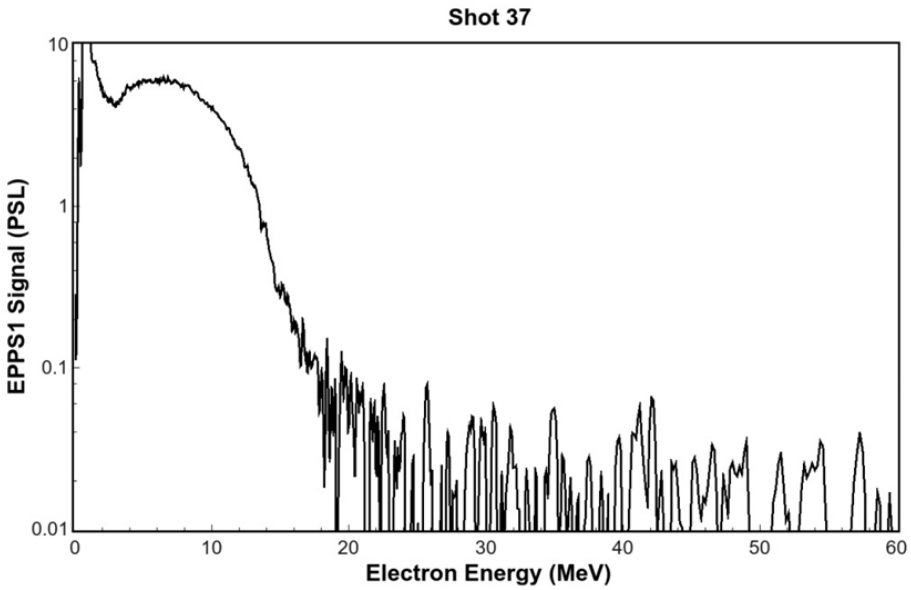

Figure 3.2: Lineout data in PSL taken from the EPPS diagnostic. It is clear from the high energy data that the noise threshold is around 0.03 PSL where actual signal becomes indistinguishable from noise.

Experimental error essentially captures everything else on the experiment and a large portion of it is commonly referred to as "shot to shot variation". These are sources of error that are near impossible to account for on every experiment in a quantitative manner. The number of parameters that can affect an experimental result is staggering; a full accounting is nearly impossible and no experiment in the real world is perfect. Some examples of this for a typical experiment are: quality of the laser spot, quality of the laser pulse length, amount of intrinsic pre-pulse, uniformity

of the target surface, laser energy transmission rates for every optic and debris on the main parabola and target positioning. Making measurements for each of these variables is often impossible on a shot. For example: measuring spot quality on a full power laser shot is often done prior to the beam hitting the main parabola and any imperfections on the parabola will not be captured or noticed. Even if certain variations are measured, understanding the degree to which they change the end result is also difficult. Rather than trying to account for all of these small sources of error on the experiment, this error combated for by amassing statistics and using the same experimental parameters for multiple shots. As the number of shots for a given set of parameters increases, confidence of the overall result increases for the entire dataset. Essentially if shot to shot variation is considered the noise for the entire data set, reducing error must be done by conducting more observations or more shots.

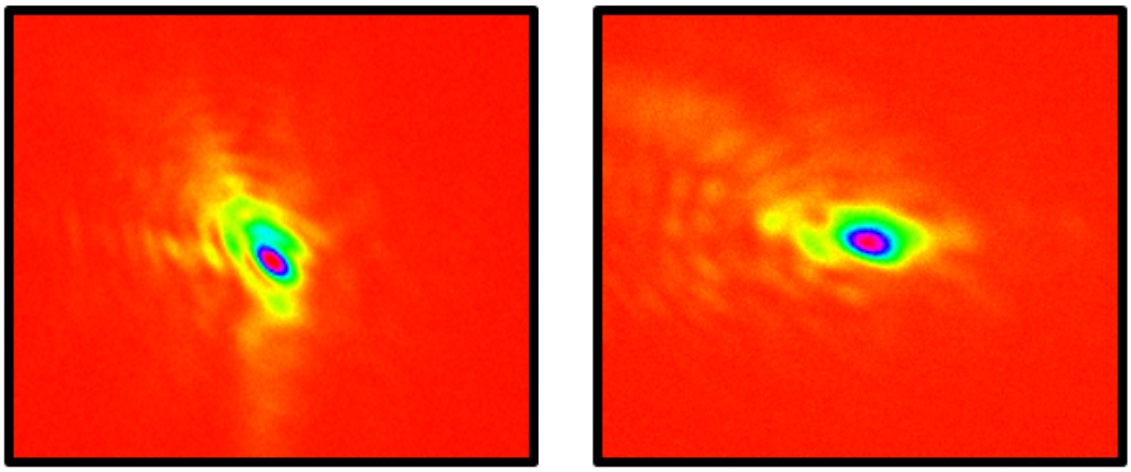

Figure 3.3: Images of a source of shot to shot variation: changing laser focal spot quality. Spot quality can change between shots simply due to heat in the beam amplifiers causing distortions in the beam as it passes through air or slight shifts to the parabola. Realignment of the main parabola is done between shots to achieve the best quality, but changes in focal spot shape and quality are omnipresent.

3.2.2 Alignment Procedure and Beam Characterization

The beam alignment procedure is one of the most important parts of performing experiments in the lab. Two beams are typically used in alignment, a continuous wave (CW) beam, which is low intensity beam, and an OPCPA beam (Optical Parametric Chirped Pulse Amplification), which as the name suggests, arrives in short pulses at higher intensity at a frequency of around 1-10 Hz. The OPCPA is essentially the short pulse beam with significantly less amplification, and is the most accurate representation of the spot position and quality that will be seen on a full shot. The OPCPA due to its chirped nature has higher intensity than the CW and it must be used carefully (lest it fry the target or alignment objectives before the experiment). The typical procedure to align beams for the experiments of this dissertation is as follows:

1. Designate a target chamber center (TCC) and place an alignment target slightly smaller than the anticipated beam size there. The target mount should have stages with a minimum of 3 degrees of motion (x, y, z) with an angular degree of motion as well.

2. Send the CW beam through the chamber out of focus hitting the alignment target. This creates an image/shadow of the target.

3. Pipe this beam out to a CCD via optics system involving a microscope objective and lenses. The objective is ideally looking directly down the path of the laser. This beam transmission system must be placed on a stage in order to move expensive objects like objectives out of the way on actual shots.

4. Adjust the distance of the microscope objective so that the shadow image of the target on the CCD comes into focus. This means that the working distance of the objective is accurately placed to view the target plane.

5. The image out of the microscope objective is what the laser the target "sees" in its plane, therefore the parabola can be adjusted to bring the beam into focus.

6. Typically beams have a large amount of astigmatism, especially during initial alignment. This is shown by a + or a × pattern as a result of one plane (horizontal or vertical) having a different focus from the other. Fixing this problem requires shifting the parabola on one axis (horizontal axis for + shape, vertical for ×) which shifts the focus position. This is then compensated for by adjusting the tip-tilt of the parabola to bring the laser back to the target location.

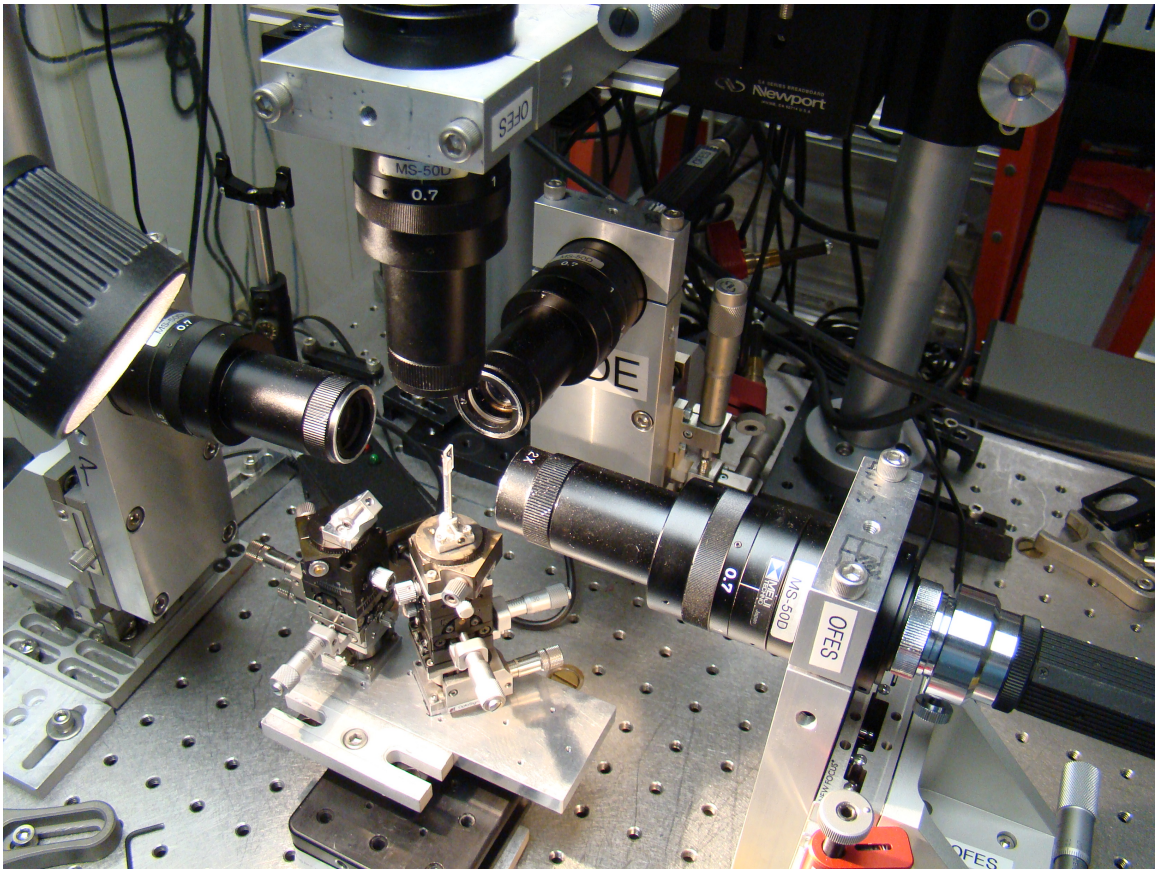

Figure 3.4: Alignment jig of the Titan laser, 4 CCDs are used to pinpoint the position of an aligned target outside the chamber. This or a similar apparatus was used in aligning targets for several experiments.

7. Now that the CW beam is at best focus it's time to double check the OPCPA best focus, which will be close to, but not exactly where the best focus for the CW is. The target should be removed slightly before switching and **filtering on the beam before entering the chamber should be increased**. The OPCPA can easily reach ionization intensities despite its low energy due to its chirped nature and will actually ionize the air at full power resulting in a popping sound. If the target happens to be in place at this time that popping sound will be the target vaporizing! This light can also burn the CCD and microscope objective if not careful.

8. A balance between filtering upstream and filtering in front of the CCDs must be used in order to have enough light to focus the beam, but not enough light to cause burn problems. After this is complete, turn off the OPCPA and return the target to its original location where it would be hit by the laser.

9. Pump down the chamber to vacuum and tweak the OPCPA alignment under vacuum. Focus alignment is best done when the chamber is at vacuum since the chamber and everything attached to it shift and bend under vacuum. Make sure when doing this that the weight in the chamber from diagnostics and equipment is as it will be when the shot is performed. A diagnostic weighing 20 lbs sitting on the chamber floor will significantly change the parabola's precise alignment.

10. Now that the beam is aligned a real target should be inserted. To align targets easily most experiments at smaller facilities use an external alignment jig outside the chamber. The target, which is on a kinematic mount, is removed from the chamber and is placed on another mount outside with a 2-3 objective system. These fixed objectives look at the target along the 3 axes of motion and are used to mark a position in space. Since the alignment target is set to be at

the laser's best focus, the best focus location is transferred to a position in the alignment jig. This allows for more convenient, quicker alignment.

11. Now that the location of best focus is known on the external jig, remove the alignment target and place in a real target and adjust the target stage to align the surface with the marked location of best focus. When the target is placed back inside the chamber, it should be aligned to the best focus of the laser.

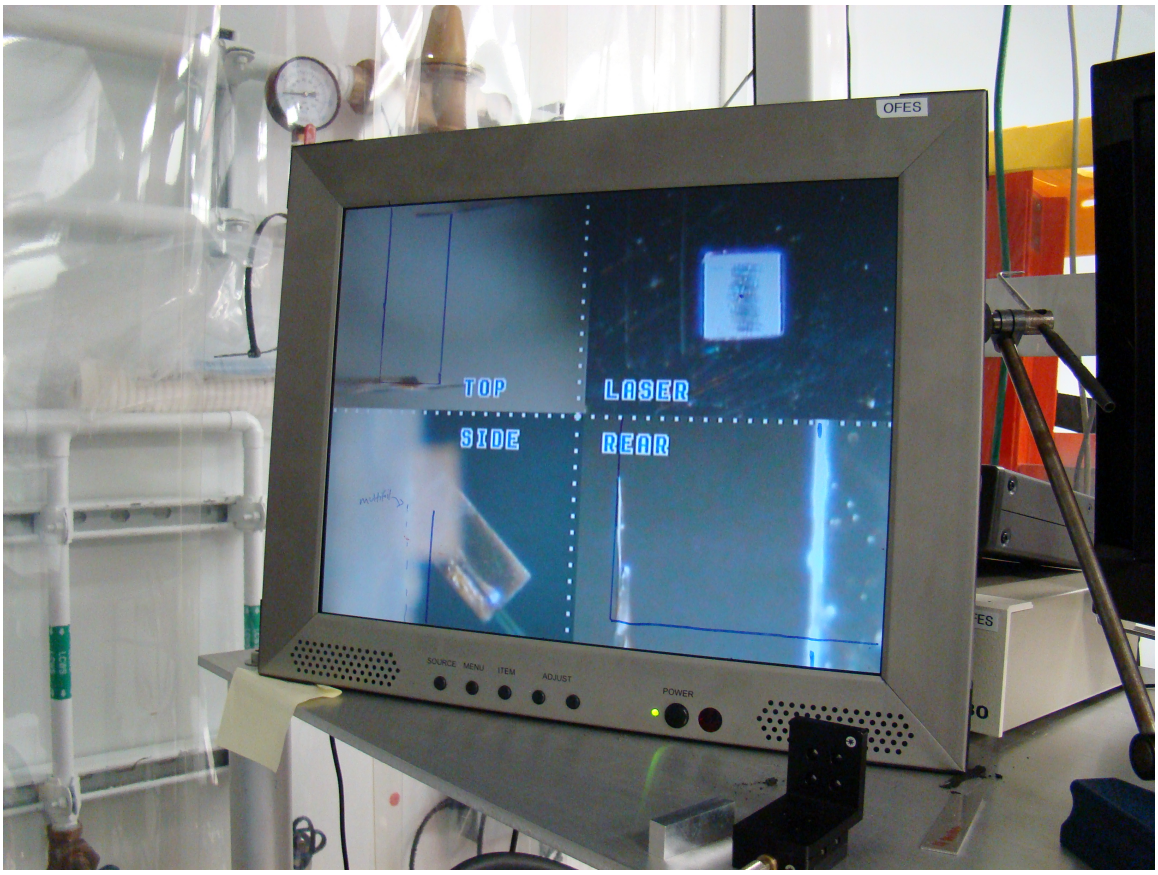

Figure 3.5: Images from the 4 CCDs on the alignment jig. The laser CCD shows where the laser would hit on the target if the target were in the chamber. The target is also in focus in this image indicating that the beam would be at best focus when hitting the target.

This alignment procedure assumes that the parabola and target return to their respective positions as the chamber is pumped down and vented repeatedly. This

means that after the best focus location is obtained and transferred to the external jig best focus alignment does not necessarily need to be performed again. However, it is common on laser systems that the position of the beam varies slightly over time due to factors like humidity and temperature. For example: experiments on TPW best focus alignment under vacuum was performed every morning to account for any shift overnight. This daily alignment found very little change from day to day giving confidence in a repeatable setup on that laser.

3.2.3 Electron Proton Positron Spectrometer (EPPS)

The electron proton positron spectrometer (EPPS) is a simple diagnostic that relies on a large magnetic field to deflect charged particles into an image plate. The particles enter the diagnostic through a small $1mm^2$ pinhole directly from the target and are immediately deflected by a strong magnetic field. Particles with greater energy have a larger gyroradius when encountering this field, and can therefore travel further before being deflected sufficiently into the image plate [46]. These spectrometers are each designed and calibrated to a dispersion, which specifies where particles of different energy deposit their energy along the IP. As oppositely charged particles deflect in different directions, an image plate is placed on each side of the incoming particle beam with one side used for electrons and the other for positrons, and to a lesser extent, protons.

Signals, usually read in PSL, are then converted into electron counts via a calibrated dispersion shown in Fig 3.7. The EPPS used on the experiments presented has an electron energy range of 5-150 MeV with a resolution of 0.05 - 1 MeV. Resolution decreases at higher energies due to energy bin size increasing per pixel. Electrons with sub 5 MeV energies are deflected too close to the pinhole to accurately measure due to noise from other sources. Electrons with higher energies can make it through

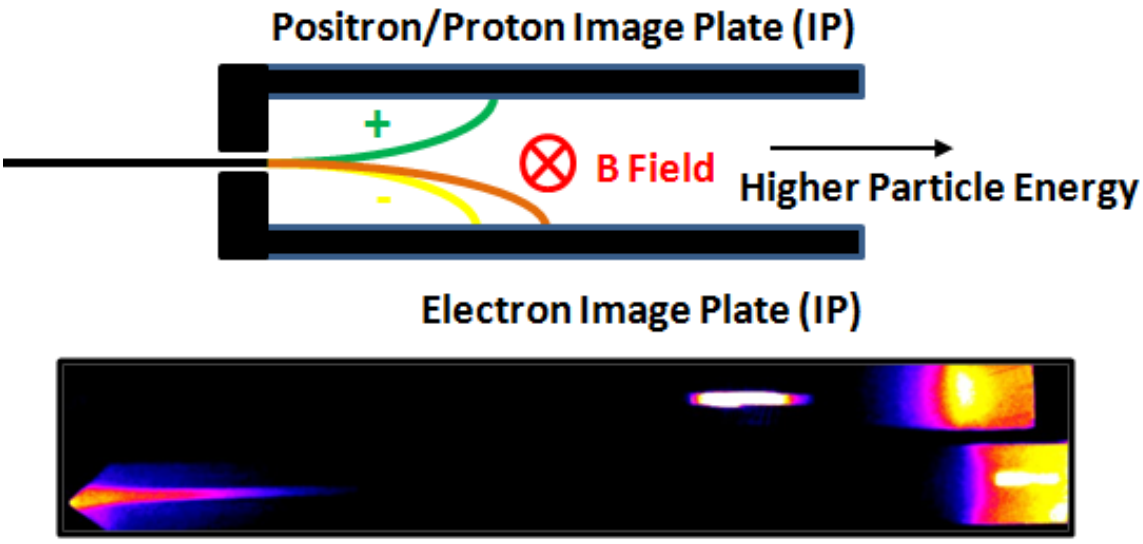

Figure 3.6: Simplified cartoon of EPPS. Charged particles enter the small pinhole and a magnetic field discriminates them based on charge and energy. In actuality the image plate holders inside the walls of the diagnostic are curved/bowed in order to reduce noise from the pinhole and achieve a more friendly dispersion range for electrons. Below is raw image plate data from the two image plates from the spectrometer. The positive side above shows a thick oversaturated proton signal in a small region on the IP while the negative side below shows the streakier signal from electrons.

the entire detector before impacting the image plate.

To turn PSL on the image plate into an electron spectrum, a lineout of the image is taken. The lineout is typically averaged over the width of several pixels in order to reduce noise. Two other lineouts are also taken at the top and bottom of the image plate. These areas are out of the way of the pinhole and their results are averaged together in order to construct a background signal that is subtracted from the main signal. The main signal is typically very noisy in lower energies (1-5 MeV) due to proximity of the pinhole and can usually be disregarded for spectrum characterization.

The spectrum is multiplied by the dispersion relation shown above and divided by the width of each energy bin. Another constant, a conversion from PSL to electron count, is also used to obtain a raw spectrum called $\frac{dN}{dE}$. The units for the spectrum are $counts * MeV^{-1} * SR^{-1}$. The SR^{-1} (steradian) is key distinction to make when

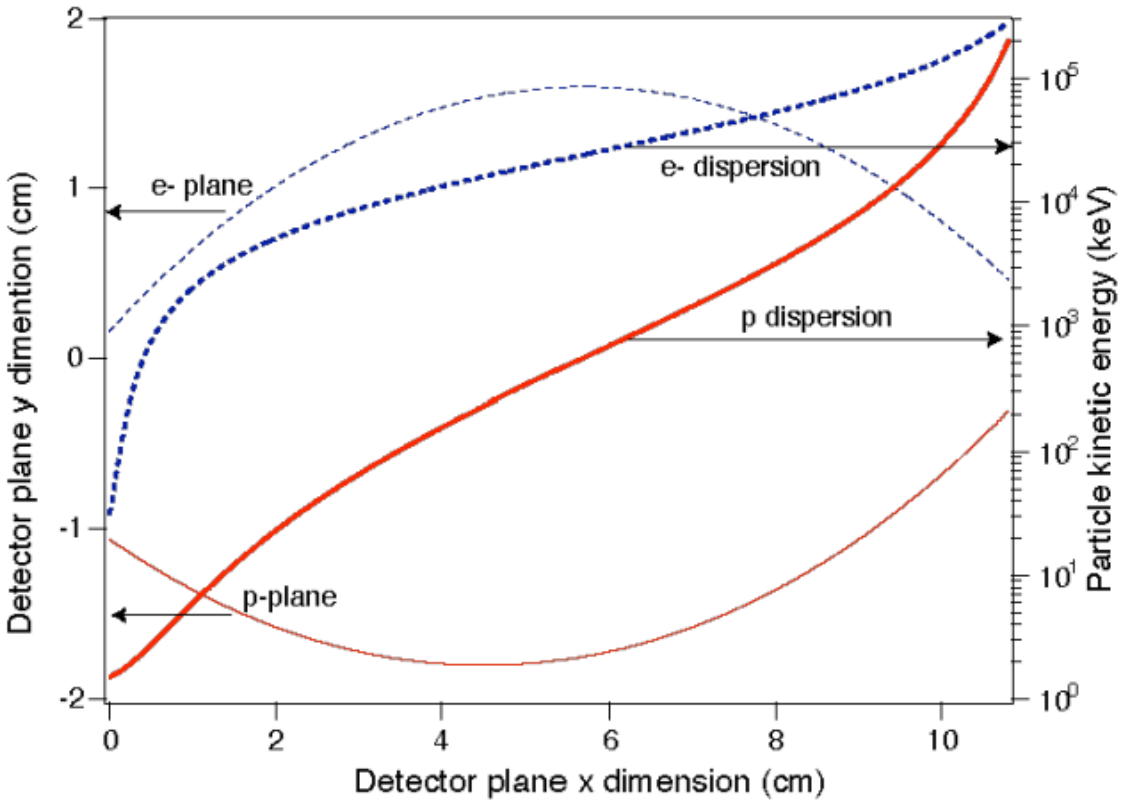

Figure 3.7: Actual dispersion and image plate curvature of an EPPS used on experiment. This dispersion shows how the EPPS is best suited to measure electrons from 1-100 MeV. Note that the positive side captures a wider range of proton energies in the same space resulting in a concentrated signal. [46]

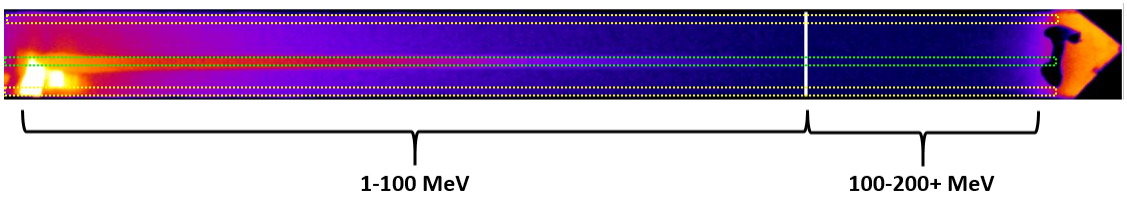

Figure 3.8: Image of electron EPPS image plate data and areas where lineouts are taken for measuring the electron spectrum. The main signal is taken in the lineout circled in green. In yellow, two background signals are measured and subtracted from the main signal. The unequal dispersion of the diagnostic is demonstrated by showing that 80% of the image plate measures 1-100 MeV electrons while the other 20% measures 100-200 MeV. This reduces resolution for measuring higher energy electrons.

comparing EPPS results to results from simulations. This takes into account the fact that the EPPS only takes a small angular sample of the electrons and does not

measure all electrons. This should be kept in mind when comparing raw numbers with simulation numbers, since simulations have the ability to essentially collect all particles.

This highlights another important feature of the EPPS, the small pinhole and acceptance angle of the diagnostic. The only electrons measured by the diagnostic are those on a direct path from the target to the pinhole. Therefore the EPPS is a good diagnostic to measure electrons that spread isotropically but fails at measuring those that have a high variability in their direction from shot to shot.

Several methods are used to characterize data from EPPS. The first of these is converting the image plate data into a $\frac{dN}{dE}$ spectrum. Often $\frac{dN}{dE}$ is characterized by a single slope temperature T_{Hot} for an exponential decay fitted curve represented by:

$$\frac{dN}{dE} = Aexp(-\mathcal{E}/kT_{Hot})$$

However, this type of fitting assumes that the electron spectrum is of a similar shape. Super-ponderomotive electrons of interest to this work often cannot be characterized by an exponential slope as the value can drastically change depending on where the slope is taken. An example comparing experimental data is shown in figure 3.9. In one case an exponential slope temperature is a decent characterization of the spectrum shown in blue. However the spectrum in red clearly has a secondary electron component that has a slope which changes significantly depending on where it is measured.

To characterize spectra with non exponential shapes we introduce the Half Maximum Integrated Energy (HMIE) value, which is represented by this equation:

$$\sum_{n=1MeV}^{\mathcal{E}_{\mathbf{HM}}} \frac{dN}{d\mathcal{E}}(\mathrm{n})(\mathcal{E}_n - \mathcal{E}_{n-1}) = \frac{1}{2}\sum_{n=1MeV}^{100MeV} \frac{dN}{d\mathcal{E}}(\mathrm{n})(\mathcal{E}_n - \mathcal{E}_{n-1})$$

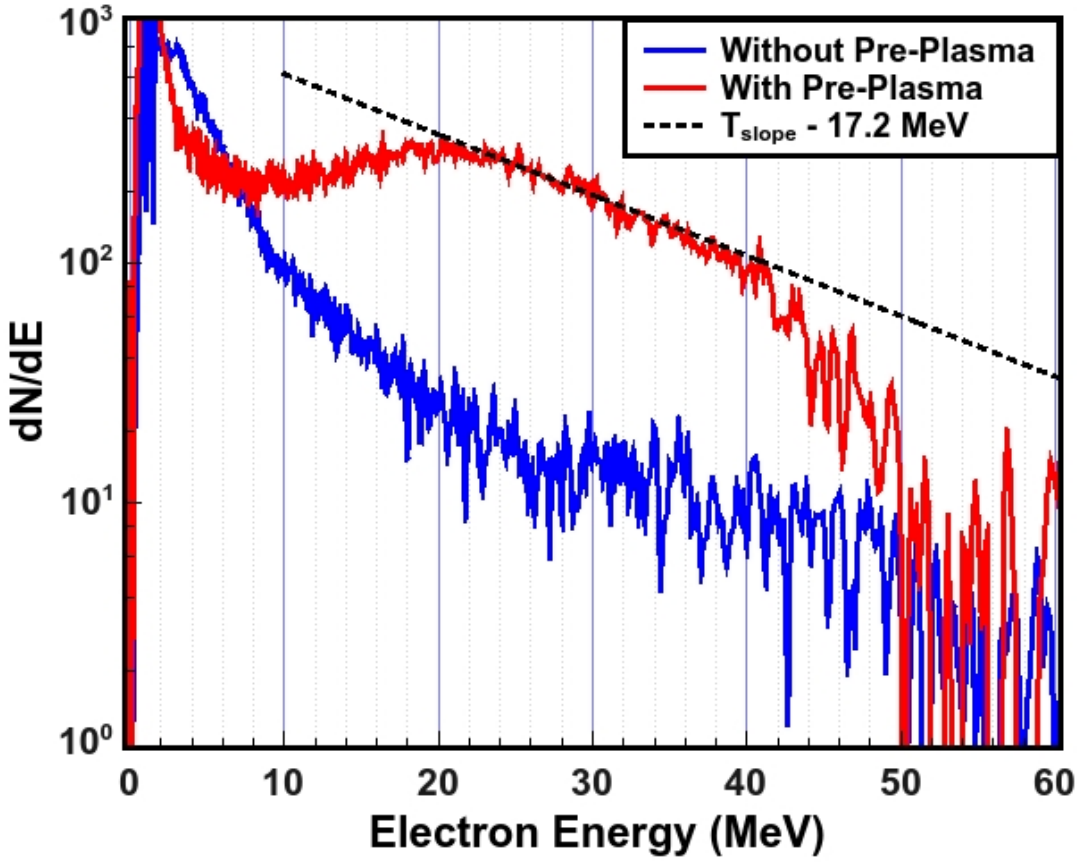

Figure 3.9: Two electron spectra; the one in blue can be characterized by an exponential slope temperature whereas the one in red cannot. In this case the electron spectra are characterized by the HMIE value.

The HMIE value represents the point where 50 percent of the total energy is contained in electrons above or below this energy. This gives a good representation of different groups of electrons without using a somewhat arbitrary slope. The HMIE value is calculated by multiplying each electron by its energy, integrating this value and finding where half of this value is represented on the energy axis.

3.2.4 Bremsstrahlung Spectrometer (BMXS)

The bremsstrahlung spectrometers (BMXS), sometimes referred to as "cannons" (for reasons still unknown to me, they look like bricks) are stacked filter image plate spectrometers [47]. Image plates and metal filters are stacked in alternating

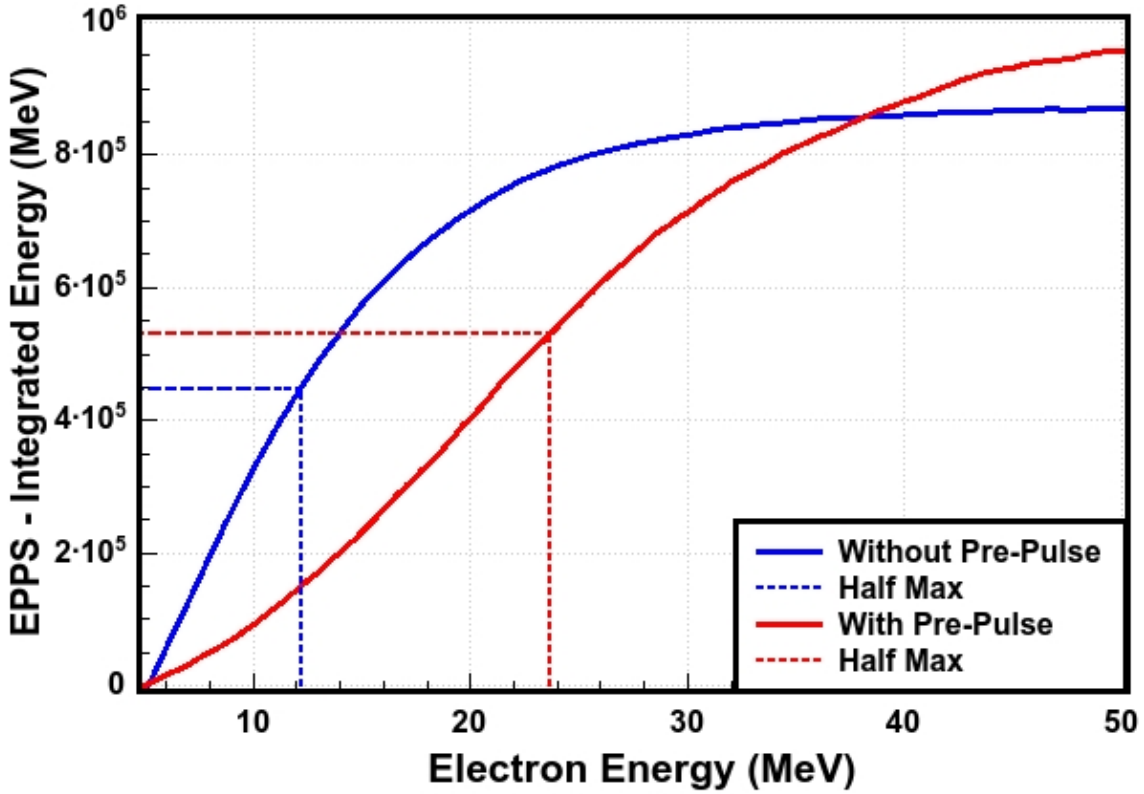

Figure 3.10: Integrated energy plot of the two electron spectra from the previous figure. The blue line has a much lower HMIE value (12.3 MeV) compared to the red line (23.8 MeV). The values indicate that the red spectrum derives a larger proportion of its total energy from higher energy electrons than the blue spectrum.

order in a 1 inch container; towards the front of the diagnostic are filters made of metals with lower Z (Al, Cu) whereas later filters are comprised of higher Z materials such as Au or Pb of increasing thickness. The stacked nature of these filters allows the discrimination of x-ray energies between image plates, which are called channels. Channel 1 corresponds to the first image plate behind a 100um Al filter, which registers x-rays with energy as low as 10 keV. In the back, channel 15, is behind all 14 of the other filters and the 15th filter which is a block of lead 5.6 mm thick. Channel 15 therefore measures x-rays with a minimum energy of 800 keV.

In addition to the stacked filters, two other components are part of the BMXS, a long, 7 inch, Pb collimator, and a magnet, not unlike the one used in the EPPS used to divert electrons. All components have an aperture of 0.5 in diameter and are aligned with direct line of sight to the target.

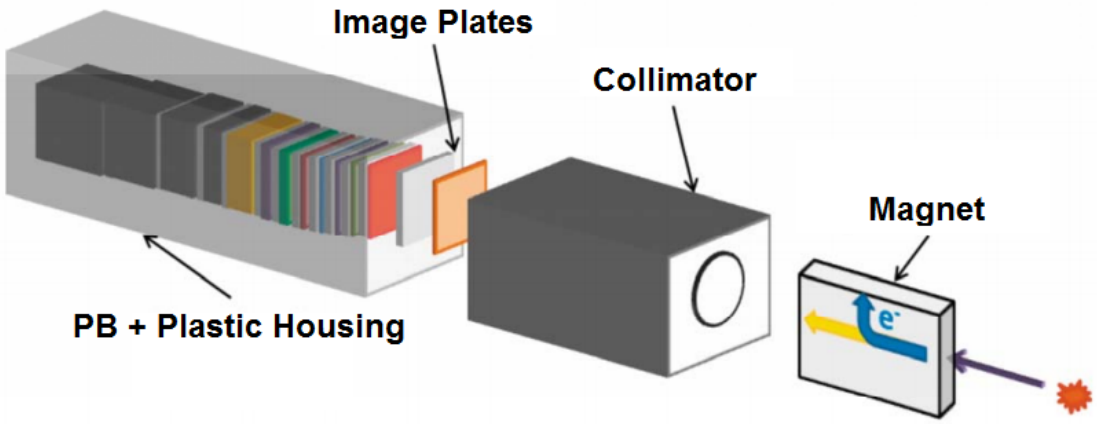

Figure 3.11: Schematic of BMXS. X-rays directly from the target travel through the 0.5" collimator and deposit their energy on several image plates behind metal filters. A magnet is placed in front of the target to deflect electrons so they are not counted on the spectrometer. [47]

While the BMXS directly measures bremsstrahlung radiation from a shot, it's main purpose is indirect. Bremsstrahlung radiation energy, coupling and direction is directly related to the electrons that are "braking" to generate it. Therefore it

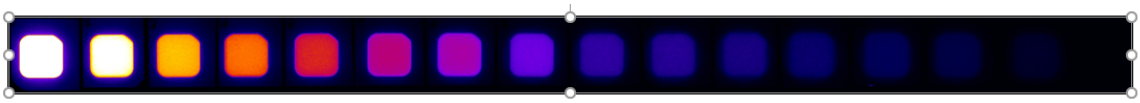

Figure 3.12: Raw image plate data from a single BMXS arranged from channel 1 on the left to channel 15 on the right.

is possible to use bremsstrahlung spectra measured from multiple angles to infer characteristics about the electron spectra. The x-rays discernible with the BMXS translate to an electron energy range of 30 keV to 5 MeV. This makes it an excellent complement to the EPPS for two reasons. First, the BMXS examines electrons that have collided and deposited energy into the target, whereas the EPPS primarily sees electrons that have deposited little to no energy in the target. Second, the BMXS is very good at measuring electrons regardless of angle since they look at x-ray emission which is more isotropic. A pencil beam of electrons will probably not be measured by EPPS, but the x-rays generated will have a greater spread which can be measured by the BMXS.

Multiple spectrometers are placed at different angles with respect to the rear normal of the target in order to infer qualities (temperature, total energy and angular divergence) of the electron source. The Monte-Carlo code package ITS is used to simulate x-rays generated by the target (Target Response Matrix, TRM) given an incident electron spectra. These x-rays are then sent into a simulated response of the diagnostic (Cannon Response Matrix, CRM) to generate a synthetic diagnostic signal for each image plate channel, which is then compared to the experimental result. The electron spectra inputed are relativistically corrected Maxwell-Boltzmann distributions centered on temperature (T_{hot}) with a given energy coupling (η) and divergence angle (θ).

$$\mathbf{BMXS}(r, T_{hot}, \eta, \theta) = \mathbf{CRM}(r)^{*}\mathbf{TRM}^{*}\frac{\mathbf{dN}}{\mathbf{dE}}(T_{hot}, \eta, \theta) \tag{114}$$

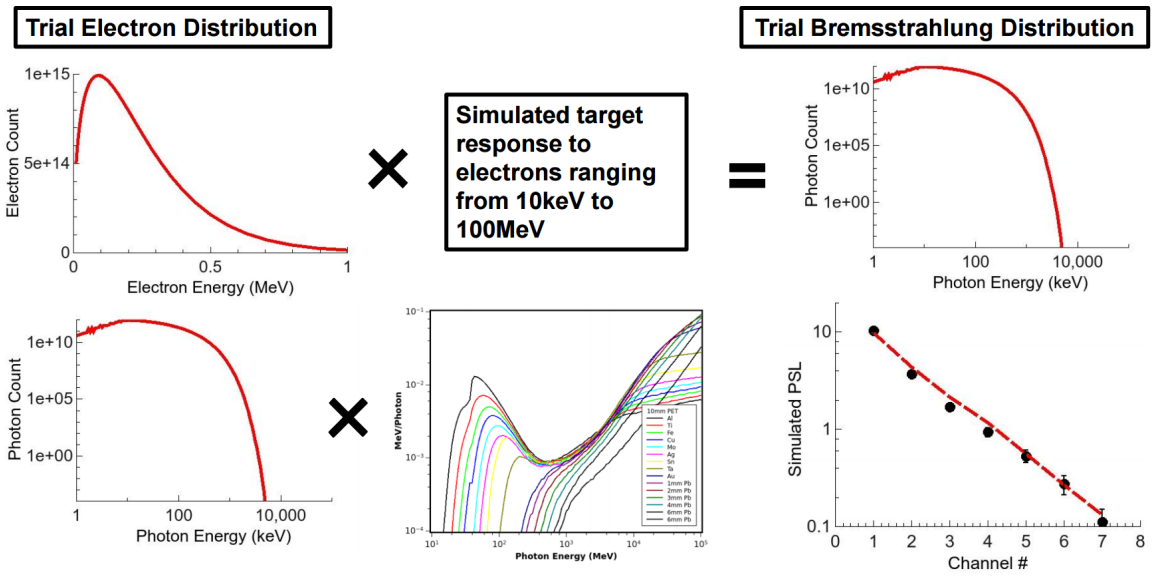

Figure 3.13: Methodology for analyzing BMXS results. From left to right: First a trial electron distribution with specified temperature, total energy and angular distribution is introduced into the target. Multiplying this incident beam with the TRM results in an x-ray spectrum with different angular components. The x-ray signal along the line of sight for the detectors is then multiplied by the CRM leading to a synthetic set of BMXS signals which can be compared to data. This process is repeated with many temperatures, total energies and angular distributions.

Turning image plate signals into actual data is achieved by using ImageJ image analysis software and creating a circle that contains roughly 50% of the central signal region. A measurement of averaged value over the area is taken along with standard deviation. This is performed for each individual image plate for each BMXS. Image plates tend to have a signal minimum of 0.003 PSL where any signal at or below this value is lost in the noise. When fitting BMXS results spectrometers with signals below this value will be automatically ignored and not included in the fit. Similarly on occasional experiments the first channel of data will receive higher amounts of background signal from other sources besides the interaction and is sometimes ignored.

Calculating error for these results is therefore a complicated process. Error for the diagnostic results (conversion efficiency and temperature) is calculated as a percentage based on a number of factors. First is the degree to which the synthetic

data matches the actual data on experiment. This value is represented by the Chi-Squared value of the fit, which uses the standard deviation of the measured signal as an error term. A typical "good fit" value for Chi-Squared is less than 1. Synthetic BMXS results that are outside of the measured value by 1 standard deviation heavily increase the percentage error in the results. This percentage is also influenced by how much a change in a single parameter changes the overall fit. This percentage is dependent on target geometry and what parameters are being changed. For example a case where changing the temperature of the incident electron spectrum from 0.5 to 0.6 MeV raises the Chi Squared value from 1 to 2 would result in significant error bars for the inferred temperature value of 0.5 MeV, whereas if the Chi Squared value only changed from 1 to 1.1 the error bars for inferred temperature would be smaller.

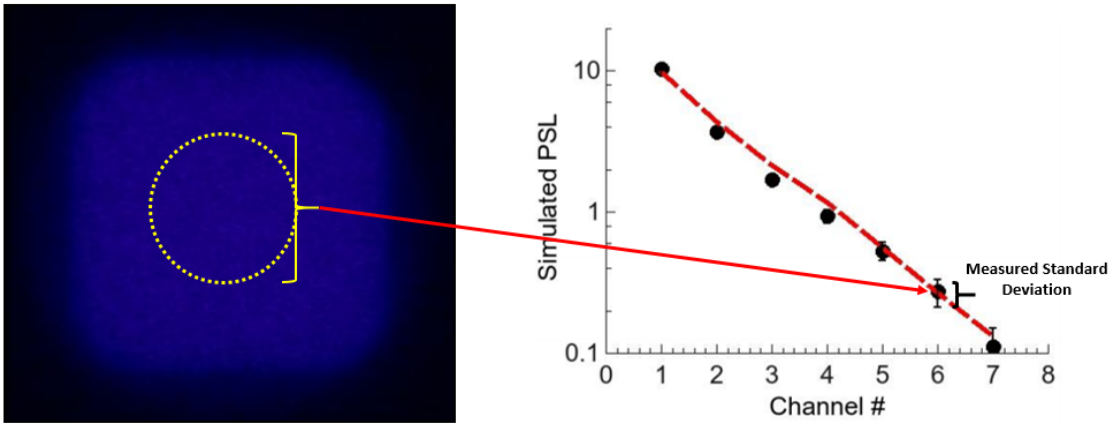

Figure 3.14: Example of individual data point measurement and error on BMXS. The mean of the encircled area of a higher energy channel often has comparable signal to the variance from un-uniformity in the region. Channels 2 and 3 have synthetic spectrum (shown in red) that is outside the region of mean +/- standard deviation resulting in a larger Chi-Squared value.

There are few difficulties that arise from the BMXS. Primarily if multiple sources of bremsstrahlung x-rays are present it is very difficult to decouple the x-rays of one source from another due to their more isotropic nature. Each target typically generates x-rays from multiple temperature spectra which have different angles and

conversion efficiencies. Doubling the number of sources doubles the number of fitting parameters (T_{Hot}, η, θ) for the synthetic result. This can be compounded further if multiple temperature distributions are considered. There are 4096 possible spectra to fit in the case of a single temperature fit with 16 possible values for each parameter. However, a two temperature double target case has nearly 3×10^{14} possibilities. In these cases some manual tweaking of possible parameter windows should be done to narrow down the number of possible values.

Another difficulty arises from the manual labor nature of the diagnostic. Each BMXS contains of 15 1" image plates, which must be individually placed on the scanner in the dark while wearing gloves (due to lead filtering). Since multiple spectrometers are often fielded this leads to sometimes 60 image plates being scanned each shot. Logistically this results in the BMXS being the slowest part of a shot cycle if only one set of image plates is available.

3.2.5 Cu-Ka Spherical Crystal Imager (SCI)

The spherical crystal imager (SCI) for Cu-Kα x-rays utilizes copper present in a target to image hot electron excited copper K-shell fluorescence emission. The K-shell emission, whose cross section maximized for electrons with 3 times the binding energy of 8.06 keV, is focused by a spherical Bragg crystal onto an image plate. This results in a magnified spatial image of the electrons passing through the copper layer of the target [48]. This information therefore contains the position and quantity of hot electrons at a point in space, which is extremely valuable in inferring laser electron coupling and electron trajectory.

A Bragg crystal used as the Cu-Kα reflecting surface is a specialized lattice structure where atoms are separated by specific values. The specialized spacing between the layers of atoms in the crystal allow it to act as a reflector for a select

bandwidth of incident wavelengths. The Bragg angle and lattice spacing used to generate the constructive interference reflection in such crystals is defined by:

$$n\lambda = 2dsin(\theta_{Bragg}) \tag{115}$$

Where n is the harmonic of light reflected (usually set to 1 for maximum signal) and d is the spacing between the crystal lattices. Often these characteristic x-rays are described in terms of energy $\mathcal{E}$ rather than wavelength. To find the Bragg angle for these x-rays can be expressed in terms of energy by:

$$\lambda = \frac{hc}{\mathcal{E}} \quad \rightarrow \quad \theta_{Bragg} = \frac{180}{\pi} sin^{-1}\left(\frac{n\lambda}{2d}\right) = 57.3 * sin^{-1}\left(\frac{6.2 \times 10^{-7}}{\mathcal{E}d}\right) \tag{116}$$

To help setup an imaging system the Bragg crystal constraint is combined with the constraints of an imaging system. Assuming that the crystal is a spherical optic, with a focal length = $R_c/2$ (where R_c is the radius of the sphere of the optic), the lensmaker's equation and law of cosines can be used to help fix the crystal's position depending on the distances between the target and the crystal d_o, the target and the image plate L and the crystal and the image plate d_i.

$$Lensmaker's\ Equation: \quad \frac{1}{d_i} + \frac{1}{d_o} = \frac{2}{R_c} \tag{117}$$

$$Law\ of\ Cosines: \quad d_i^2 + d_o^2 - 2d_i d_o cos(\theta_{Bragg}) = L^2 \tag{118}$$

The magnification of the image created is defined as $\frac{d_i}{d_o}$. An additional aspect of crystal and image plate placement that must be kept in mind is the relative position of the crystal to the target, as this determines the view that the crystal has of the

region of interest. The final necessary piece for the diagnostic to function is a beam block, which stops energetic particles from the target directly saturating the image plate detector. All of these features require a delicate balance to set up on experiment. In particular x-ray wavelengths with very small Bragg angles often have difficulties with setting up a system such that light from the crystal reaches the detector, but light from the target is blocked.

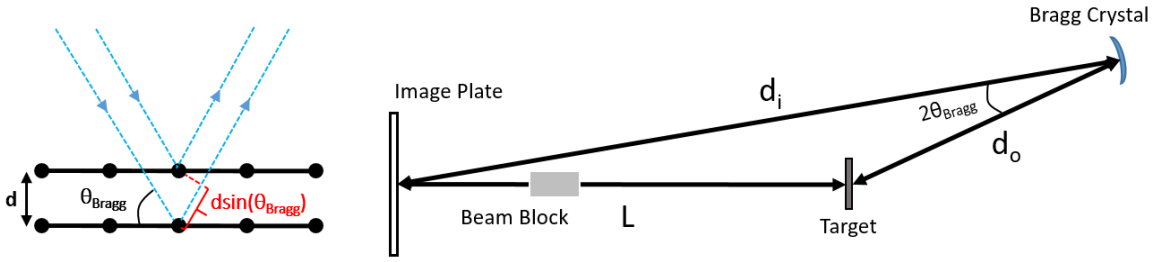

Figure 3.15: Left: Crystal lattice structure of a Bragg crystal which reflects a specific wavelength of light constructively. Right: SCI setup relative to target and imaging system using a spherically shaped Bragg crystal.

While spatial images of electrons passing through a layer in the target are extremely valuable, the images do not allow for the resolution of electron energy, as the K-shell emission cross section maximized for electrons with 3 times the binding energy of 8.06 keV. However the images do not allow for the resolution of electron energy, as any electron with greater than 8.06 keV energy can generate Kα emission. Cu-Kα emission has been shown to be most responsive to total electron count passing through the copper layer and is not largely dependent on the energy of the stimulating electrons, so long as their mean energy is much higher than the binding energy of copper [48], [49]. This introduces uncertainty in inferring the trajectory of high energy electrons in experiments due to their lower number, since there is no guarantee that higher energy electrons follow the same trajectories as lower energy ones.

3.3 Proton Radiography

Proton radiography is a diagnostic technique which utilizes high energy protons in order to characterize electric and magnetic fields. To achieve this, large quantities of protons are typically produced by a high intensity laser incident on a thin metal foil. As described in section 1.1.2 the TNSA interaction generates copious amounts of high energy protons with wide energy range. These protons pass through the region of interest and are deflected by magnetic and electric fields. In the case of our experiments the radiography target, or **side-lighter** was placed facing perpendicular to the main target and region of interest.

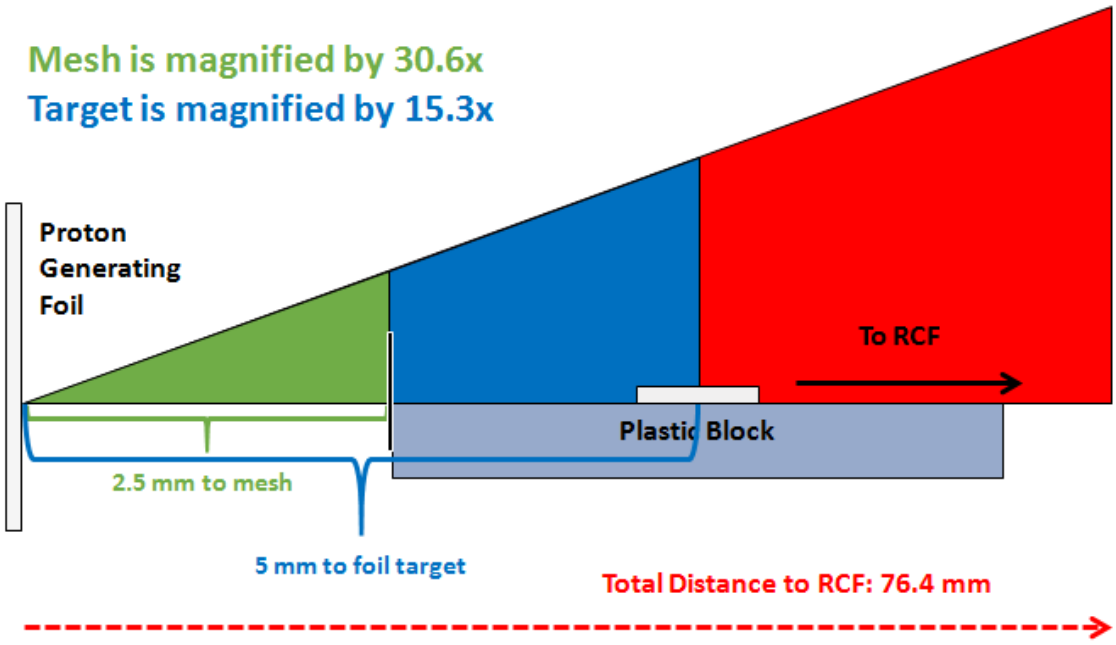

Figure 3.16: Cartoon of example of proton radiography setup using numbers measured on experiment. Depending on placement of target, mesh, foil and RCF stack magnification of various features change on film.

After the protons pass through the region of interest they deposit their energy on a stack of **radiochromic film (RCF)**. The film stack is constructed of multiple layers of film, with differing levels of sensitivity. Taking advantage of the very specific

Bragg peak deposition for protons, in addition to the wide range of energy that TNSA generated protons have, the RCF stack is able to discriminate protons passing through the interaction region earlier in time than those later in time. High energy protons (with say 20 MeV energy) travel faster and interact with fields in the region of interest at an earlier in time than low energy protons (say 1 MeV). These high energy protons travel further in the film stack and deposit the majority of their energy in a specific layer of film. Therefore proton radiography can be used to have some level of time resolution of fields in the interaction.

A few details are required in order to fully utilize proton radiography. A reference mesh is often required between the proton source and region of interest in order to ensure that the features seen on the radiographs are a result of fields in the main interaction instead of oddities in the sidelighter interaction. If a feature of proton deflection is measured on the film but the mesh pattern is unaffected it is likely that whatever mechanism caused the deflection happened before the protons interacted in the main region of interest.

Furthermore, the time resolution of each film changes based on the energy of the protons. Discriminating between low energy protons results in very poor time resolution between film layers; as the table shows there is nearly 100 ps difference between the film layers looking at the lowest energy electrons while the time resolution improves to nearly 1 ps for the highest energies. Therefore when timing the proton beam the goal is to time the highest energy protons to coincide with the time of the interaction of interest in order to have the best time resolution.

Analyzing proton radiographs for useful information is an ongoing field of research. To do so several computationally intense simulations are often required. Typically back of the envelope calculations are often used to characterize fields. These involve measuring the size of regions where protons of certain energies are absent and

RCF Recipe 2	Proton Min Energy (MeV)	Travel Time (ps)	Δt (ps)
JLF Al Foil (25um)	-	-	
H1	1.5	300.92	99.26
H2	3.35	201.66	30.32
H3	4.65	171.34	15.78
H4	5.65	155.56	10.98
H5	6.55	144.58	8.46
H6	7.4	136.12	11.85
M1	8.9	124.27	9.45
M2	10.45	114.82	6.65
M3	11.8	108.17	4.82
E1	12.95	103.35	3.7
E2	13.95	99.65	3.15
E3	14.9	96.50	2.87
E4	15.85	93.63	2.35
E5	16.7	91.28	2.18
E6	17.55	89.10	2.03
E7	18.4	87.07	1.67
E8	19.15	85.40	1.57
E9	19.9	83.83	
Al Plate (100um)	-	-	

Figure 3.17: Proton radiography energy/flight time table cross referenced with peak deposition energy for each film layer. This table was constructed by C. McGuffey for the experiment on the Titan laser. For example, film H6 has maximum deposition from 7.4 MeV protons, which have a corresponding flight time from generation to the region of interest of 136.12 ps. The different letters in front of each film layer represent different types of film with different sensitivities. Time resolution between each layer of film is not constant and tends to increase for later timed pieces of film that correspond to lower energy protons.

calculating the minimum amount of impulse required to change a proton's trajectory to such a degree. This calculation requires some assumptions, such as geometry of the deflecting fields and whether or not the primary deflecting field is magnetic or electric or both. It is therefore very difficult to gain quantitative field data from radiograph

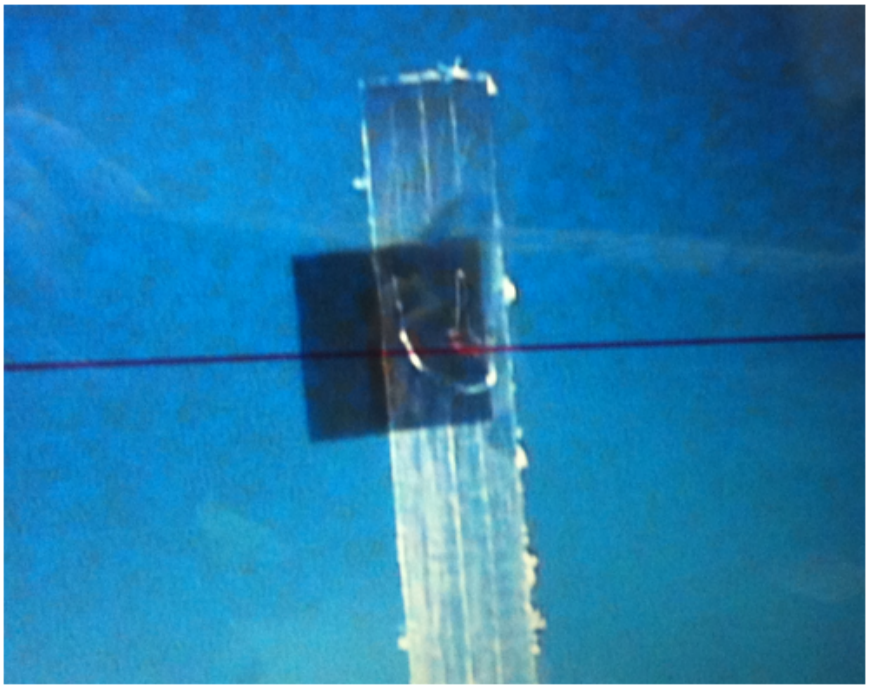

Figure 3.18: Image from the point of view of the side-lighter target. The main foil target can be barely seen through the super-fine mesh in front. Beam and target alignment must be extremely precise or else the plastic leading edge from the main target canll block the surface of the foil target.

images and they are often used to supplement other diagnostics. To fully simulate a proton radiograph, a computationally complex 3D PIC simulation of the interaction region is required, then a batch of energetic protons must also be simulated in 3D transversing the original simulation. The exiting trajectories of these protons must be then extrapolated to the imaging surface to create a synthetic radiograph that can be compared to the one on experiment.

3.4 Target Design

The targets for these experiments were designed with the knowledge they would be used at several different facilities and with the diagnostics listed above. A metal target made primarily of aluminum was chosen in order to have a solid density component with enough matter after the pre-pulse hit. Aluminum also has sufficiently

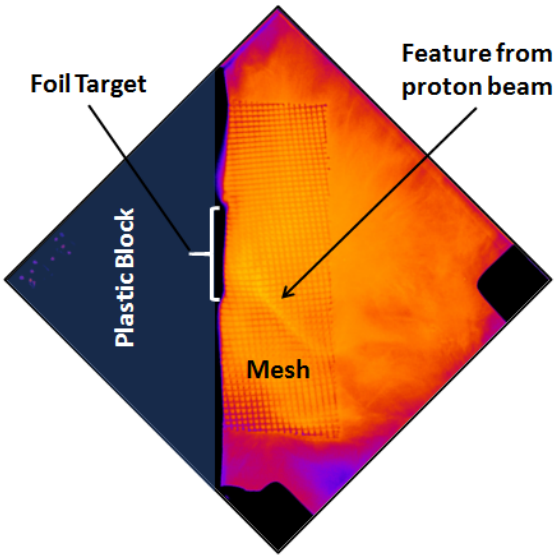

Figure 3.19: False color reference proton radiography image with no main beam interaction. Some features are seen in the radiography image which are due to imperfections in the generated proton beam.

high Z to generate significant amounts of bremsstrahlung which is measured BMXS. Aluminum foil targets have also been used in prior experiments by T. Yabuuchi [37] and using similar targets allow for a better comparison. The metal foil has a copper layer sandwiched in between the aluminum which acts as a tracer layer for hot electrons. Copper will emit prodigious amounts of Cu-Kα x-rays and can be used to trace electron trajectories via the SCI diagnostic. The copper must be placed at such a depth that dynamics on the front surface of the target do not impact the copper layer.

Finally the metal foil is attached to a 1 mm thick plastic block. Beyond being a convenient mounting point and aid to target alignment, the block provides a layer of material which helps inhibit electron refluxing [50]. When electrons leave the rear surface of the foil target they generate large fields as seen in TNSA, which can cause other electrons later in time to turn around and pass through the target again in the opposite direction. If these electrons pass through the copper layer, they essentially

are double counted on the SCI diagnostic and provide erroneous information. The plastic block helps provide some material to inhibit these refluxing electrons before they hit the copper layer a second time. The entire target block is then mounted on a 3 mm diameter aluminum stalk which can be placed in a drill chuck or other device for easy insertion and removal.

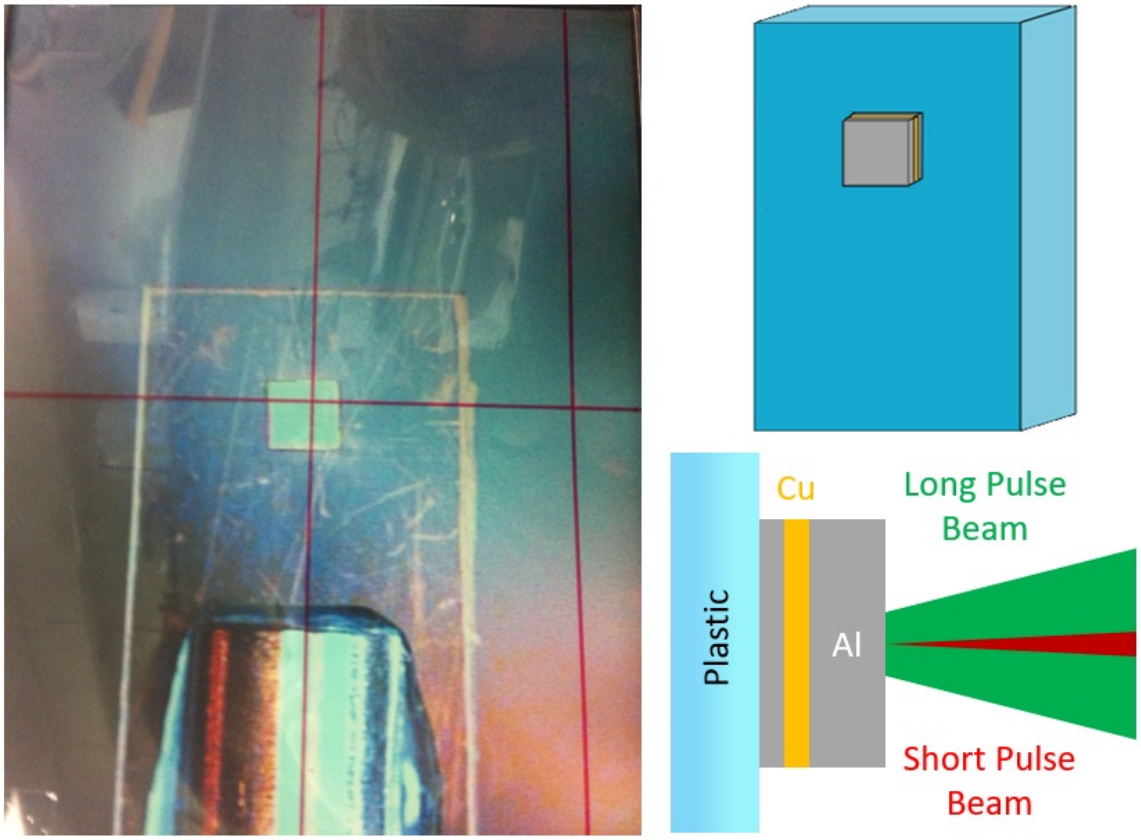

Figure 3.20: Left: Magnified image of actual target attached to aluminum stalk. Top right: Cartoon version close to scale. Bottom right: Cartoon (plastic not to scale) showing layers of the metal foil target. Al-Cu-Al-Plastic thicknesses were 60-20-20-1000 µm respectively.

For proton radiography targets a simple 7 µm metal titanium metal foil is used. These were attached to an extruded glass fiber and aligned to be normal to the main metal foil target. To get the most time resolution out of the proton radiography setup, a 5.5 mm separation between the two targets was chosen. Ideally this would allow

picosecond resolution for the best radiography frames without being close enough to disrupt the main interaction. In the first attempts at proton radiography the proton generating target and main target were attached to the same apparatus made from glass capillaries glued together. This required extreme precision in manufacture since the alignment of both targets are coupled and occur simultaneously when when attached. Furthermore the alignment of a double target on a single apparatus meant that the beams must by definition be aligned to the targets since the relative position between the targets must be fixed. This in contrast with other experiments where the target can be moved to the beam. After an experiment the difficulties in aligning such a target resulted in the change to two separate independent target stalks and mounting systems. This system saved shot time and removed the requirement to realign both beams prior to each shot.

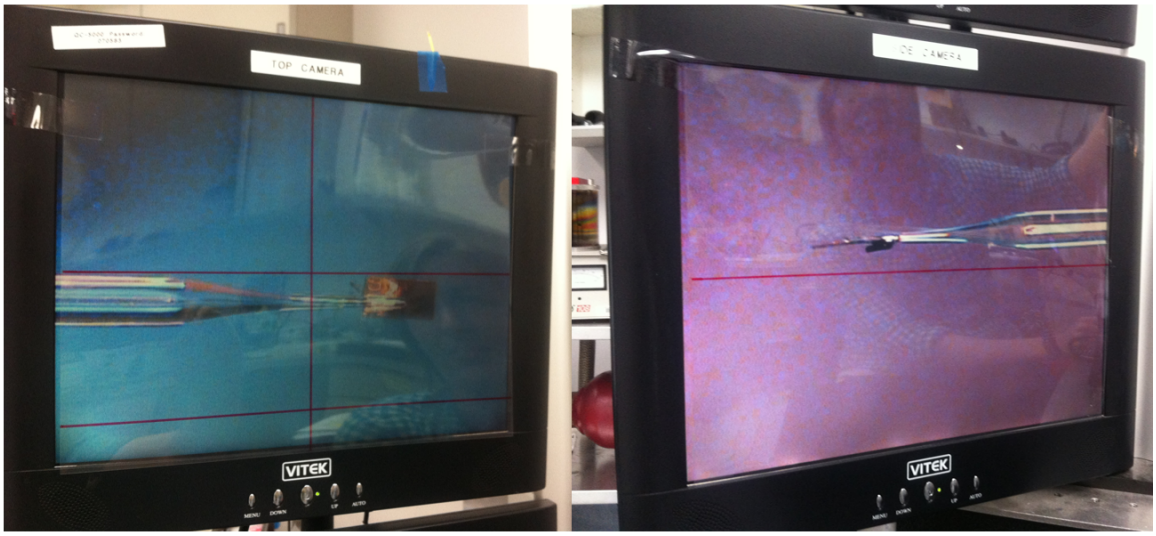

Figure 3.21: Proton target qualification images taken using the assembly station at General Atomics. Proton generating targets for radiography were created by attaching a thin 7 µm foil to an extruded glass capillary. If you look closely you can see the reflection of C. Krauland who helped greatly in their qualification.

Each target (both main and sidelighter) is cataloged and assigned a grade of good, fair, or bad and photographs of each target were taken. Attempts on experiment

were made to ensure that at least each group of shots in a data set had at least one shot with a good target. Target assembly, metrology and images were primarily performed on a robotic arm, vacuum chuck system provided by General Atomics.

3.4.1 EPOCH and PIC Codes

PIC or Particle-in-Cell codes are the primary form of kinetic particle interaction modeling in the high intensity beam community. These codes are defined by having a fixed mesh grid of cells and populating the simulation box with "macro particles". These macro particles are used to represent large quantities of actual particles by using a weighting system. Using these macro particles and their momenta, electric and magnetic fields are calculated for each mesh point. These mesh points are then used in the pusher part of the code which uses the recorded fields to calculate the force on the macro particles. The particles are moved accordingly on the timestep of the simulation and the process begins again.

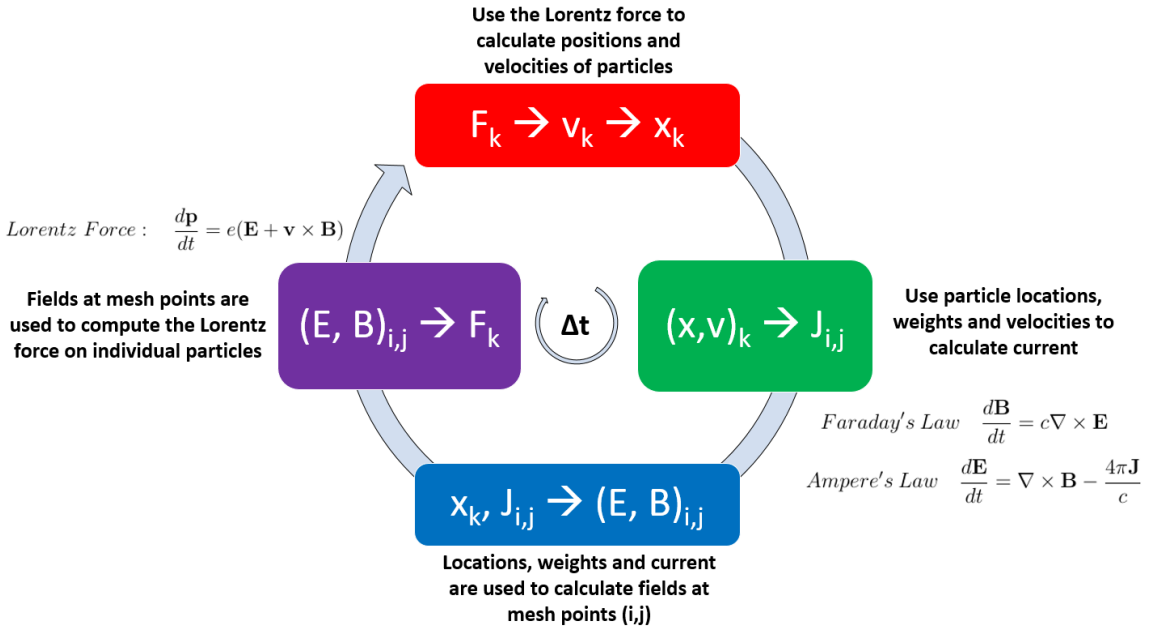

Figure 3.22: PIC code computation cycle

PIC codes have the potential to be incredibly accurate since at their heart they're calculating the Lorentz force trillions of times. A PIC code would approach a nearly completely accurate simulation as resolution increases and as the number of macro particles approach the number of actual particles. Difficulties arise from using assumptions to ease the number of calculations to make it reasonable to compute, without tarnishing the results. These changes take the form of changing grid resolution, time resolution and number of macro particles. Further reductions to computation cost come from reducing the number of dimensions used in the simulation; a 1D simulation that takes minutes would take days in 2D with the same resolution and possibly months or years in 3D. In order to obtain good results the PIC code must also follow the Courant-Friedrichs-Lewy (CFL) condition which places a restriction on time and space resolution:

$$CFL\ condition: \quad \Delta t \sum_{i=1}^{n} \frac{v}{\Delta x} \leqslant 1 \quad where\ n\ is\ the\ number\ of\ dimensions \tag{119}$$

This condition ensures that the cell size is not so small that information traveling velocity v can traverse two cells in one timestep. In our case the information can take the form of an electromagnetic wave traveling at c. The CFL condition arises from how PIC codes work: a point in the grid-space has a finite range of influence and finite domain of dependence. The domain of dependence represents the fact that single points only use information in a limited range in calculations. Therefore if this condition is broken, information can propagate beyond this domain in a single time step. This essentially translates to a loss of information and the simulation becomes unstable. The result of this is if time resolution is decreased (that is Δt goes up) and the total number of time steps decreases, then the size of each cell must increase as well to keep the simulation stable.

EPOCH is the PIC code used in this work and is an explicit multidimensional code [51]. The timesteps from EPOCH are automatically scaled to be compliant with the CFL condition depending on spatial resolutions specified. Simulations were run on the University of Texas at Austin super computer. Time and expertise was generously granted by A. V. Arefiev for this work. Output files are downloaded and analyzed with the data visualizer VisIt (from Lawrence Livermore National Laboratory) and Matlab.

Chapter 4
Short Pulse Length: Texas Petawatt Experiments

4.1 First TPW Experiment Parameters

The first set of experiments examined the very shortest interaction pulse lengths of 150 - 600 fs. Two experiments were conducted on the Texas Petawatt laser (TPW), which features a beam that can have a variable pulse length (with 150 fs being best compression) with an energy of 120 J. The f/3 parabola allows the beam to be focused to a diameter of < 10 µm achieving intensities of 3×10^{20} W/cm^2 for the experiment. An attempt was made to keep intensity constant as pulse length was varied by deliberately requesting lower energy for shorter pulse length shots. The short pulse beam was incident on the target at a 22 degree angle to ensure that reflected light did not strike the parabola and reflect up the beam line and damage optics.

To create the injected pre-plasma a probe beam was utilized as a **long pulse**, which is split off from the main beam and separately amplified with a booster amplifier. This beam had a nominal intensity of 2×10^{12} W/cm^2 and had a pulse length of 2 ns. The beam was timed to arrive 4 ns prior to the arrival of the short pulse beam, leaving a 2 ns gap for plasma to continue to expand off the target surface. The long pulse was periscoped in through the chamber and injected just prior to the parabola, where a small section of the main short pulse beam was blocked. The probe beam was sent coincident on the main target with the parabola and alignment was adjusted via mirrors outside the chamber. The small initial diameter of the probe beam (1 cm) causes the best focus of the long pulse beam to be much larger than that of the short pulse beam. This calculation, using the effective numerical apertures of both beams, shows how the smaller diameter of the probe beam restricts its smallest spot

size (w_0).

$$\frac{Entrance\ Diameter}{Parabola\ Focal\ Length} = NA \sim \frac{\lambda}{\pi w_0} \tag{120}$$

Therefore, by using the same parabola the short pulse beam can be focused to a smaller, high intensity spot due to its large entrance diameter ($\sim$ 25 cm) while the long pulse beam is focused collinearly into a low intensity spot due to its smaller entrance diameter ($\sim$ 1 cm). The long pulse spot was roughly a 25 x 50 µm oval that was overlaid with the short pulse beam. On the experiment this beam was timed with respect to the main beam by a photodiode with roughly 0.1 ns of error.

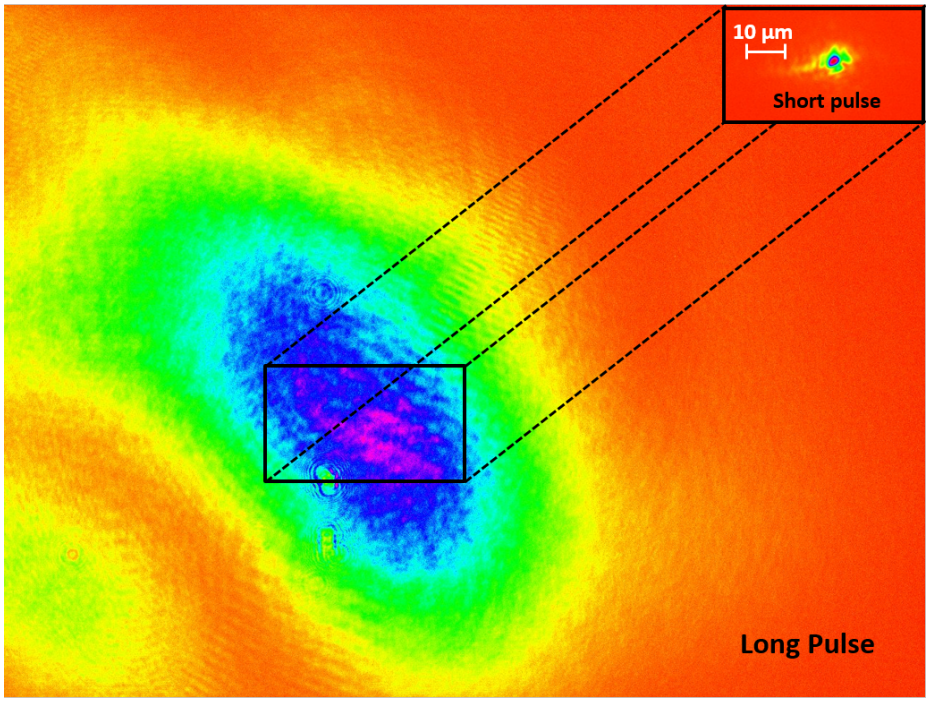

Figure 4.1: Alignment beam images from the long and short pulse beams. On the experiment the long pulse is moved via 1 inch turning mirrors to overlap with the short pulse spot.

Two experiments were conducted at TPW with similar setup and parameters. The first preliminary experiment only examined short pulse lengths of 150 fs. This

experiment also attempted to introduce a split beam capability to the TPW facility and use part of the laser energy for proton radiography. To achieve this a portion of the short pulse beam was picked off with a 4 inch mirror placed in the beam. This portion of the beam, called the side lighter, was sent to a "trombone" variable delay stage which is used to time the picked off portion of the beam relative to the main beam. This delay stage can be moved backwards or forwards to introduce different amounts of delay between the beams. Timing these beams precisely is very difficult with this method as there is no way at TPW to precisely measure the time difference between the two pulses on a picosecond time scale beyond measuring the distance the light travels by hand. The side lighter was focused with a 6 inch off axis parabola (OAP) to hit a separate target facing perpendicular to the main target to generate large quantities of protons. The proton target was placed 5 mm away from the main target and the RCF stack is placed 3 inches away on the other side.

Another important aspect of the TPW experiments was the level of intrinsic pre-pulse. For the first experiment the level of uncontrolled ASE on TPW was significant and generated a scale length of pre-plasma (estimate in Fig 4.7). Therefore this experiment compares the impact of different levels of pre-plasma on electron production rather than comparing cases with and without pre-plasma entirely. As shown by previous work ([31], [52]), different scale lengths of pre-plasma should still yield different results in the number and energy of super-ponderomotive electrons.

The difficulty in using the two beam method arises in target and beam alignment and focus. In order to align the two perpendicular beams for the two targets, two objectives facing separate target planes must be fielded. These are placed on a large stage with over 100 cm of travel so that they can be removed before each shot. These beams are piped out to two separate CCDs outside the chamber with a series of mirrors, lenses and filters. As shown in the actual experimental photo,

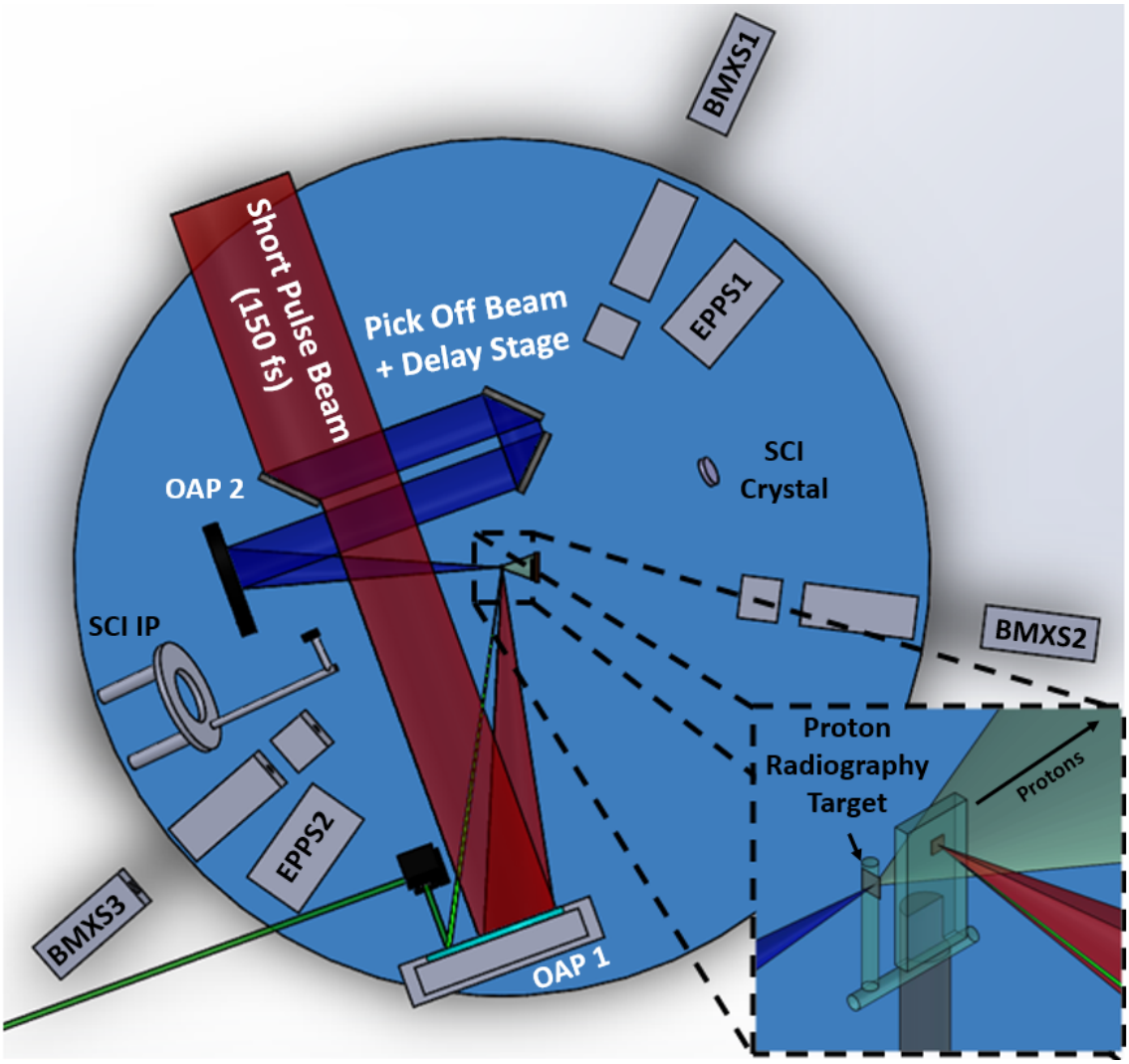

Figure 4.2: Rough chamber layout schematic of the first, preliminary experiment on Texas Petawatt. In blue the picked off portion of the main beam (red) goes towards a secondary proton radiography target. The thin beam in green is the probe beam acting as an injected pre-pulse.

this actually takes up a large amount of chamber space and restricts the placement of diagnostics. Furthermore, the necessity of having a collimator and magnet for the BMXS means that there was not enough chamber space to place the entire BMXS inside the chamber. Therefore the BMXS had to be aligned according to the limited port apertures around the chamber, with the collimator and magnet placed inside the

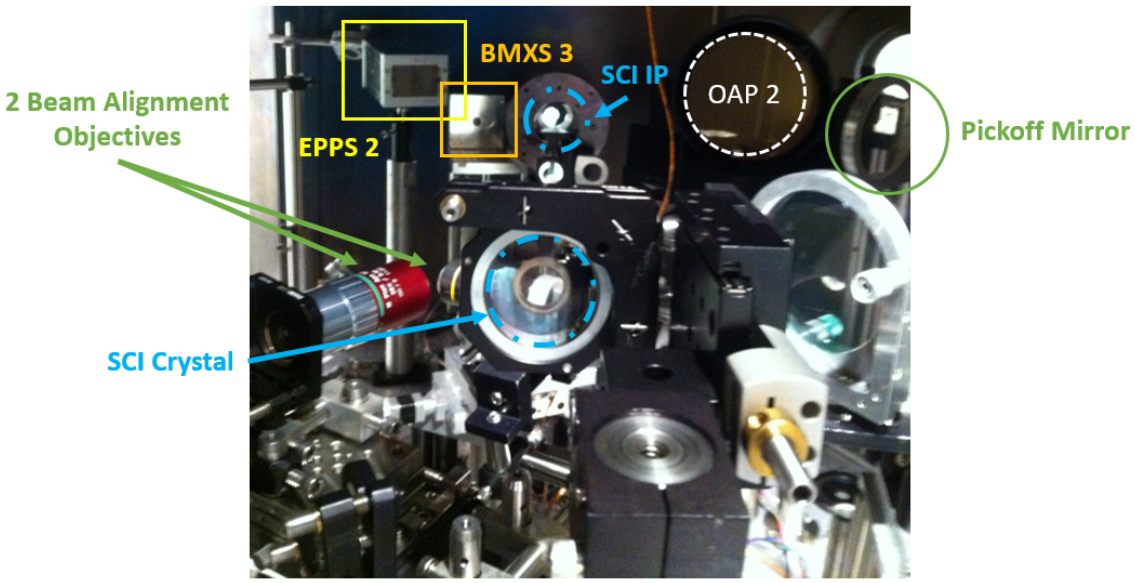

Figure 4.3: Photo of part of the TPW experimental setup, which demonstrates how precious chamber real estate is! Shown are the 2 alignment objectives which pipe the alignment light out of the chamber via mirrors and lenses, the SCI crystal which reflects Cu-Kα emission to the image plate across the chamber, the front facing EPPS2 and BMXS3, the beam periscope just next to EPPS 2 bringing the probe beam to the main parabola (not shown) and part of the pick off system which is focused with OAP 2.

chamber, and the image plate spectrometer placed outside of port windows.

A further restriction at the TPW facility is the requirement of a blast shield for the target. It has been noted that the violent interaction of larger targets (such as our 1 mm thick plastic ones) has been known to cause target fragments to fly off through the gate valve and into the compressor and pose a damage risk to the very expensive gratings. Other material can also fly off, ricochet off the chamber wall and damage the main parabola (also expensive). A blast shield was designed and machined custom for the experiment, with port holes for each diagnostic. This did limit the ability to change the location of some diagnostics reducing their flexibility.

Arranged around the chamber were the diagnostics outlined in chapter 3. These included 3 BMXS, 2 EPPS and SCI. These diagnostics were difficult to ar-

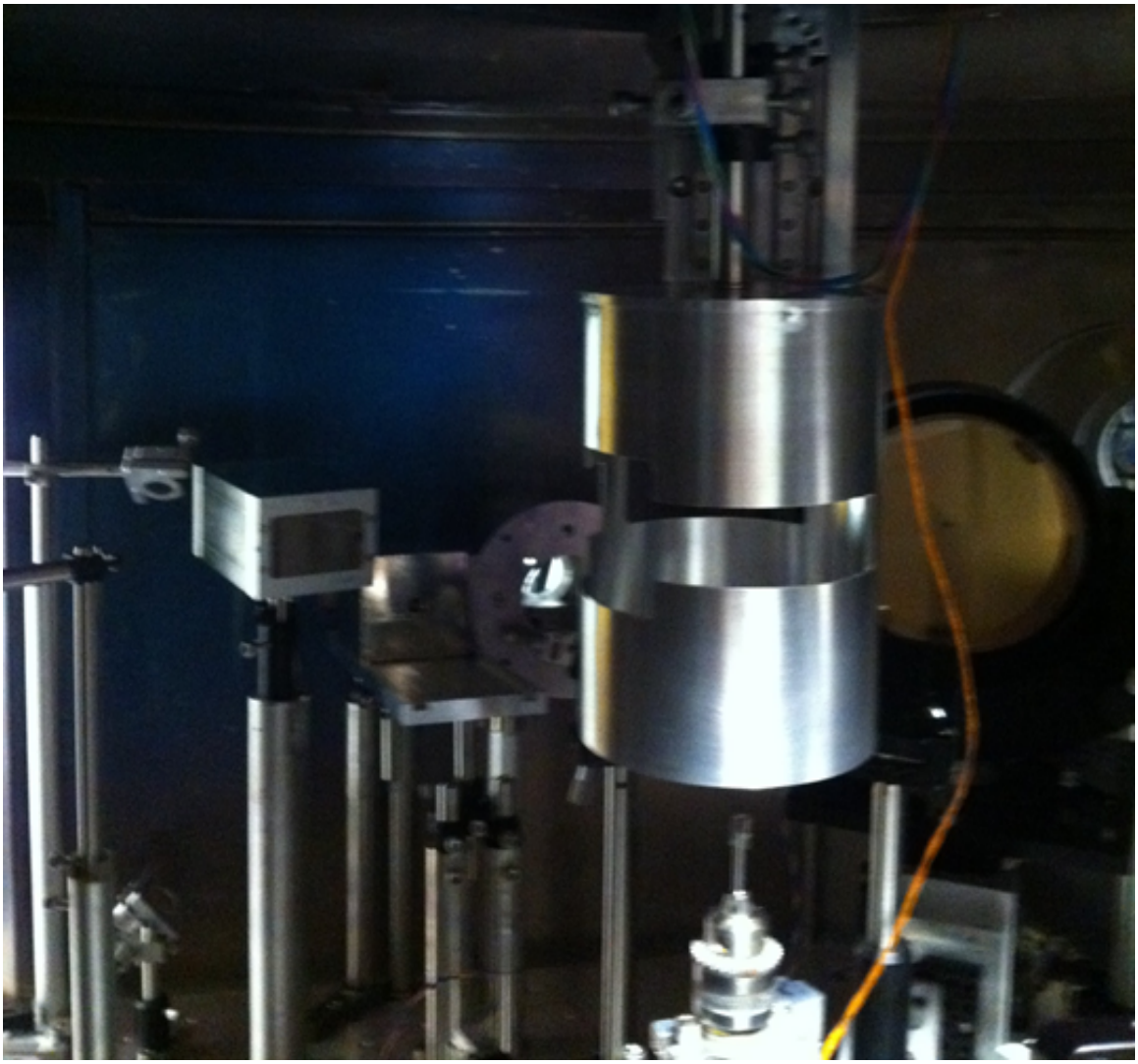

Figure 4.4: Blast shield machined to specification for the experiment. It is shown here attached to a motor which is raised and lowered for each shot. The large aperture on the left is for the 2 inch square RCF stack.

range optimally as space had to be arranged with the alignment system in place and retracted. The exact layout and position of the diagnostics are listed in the table below:

	Azimuthal Angle (deg)	Azimuthal Angle (rel to target)	Polar Angle (deg)	Distance (cm)	Pixel Size	IP Type
SCI	43	21.22	11	32	25um	BAS-MS (white)
EPPS1	31	9.22	0	44	100um	SR (blue)
EPPS2	202	180.22	0	46		
BMXS1	-3	-24.78	0	93	100um	BAS-MS (white)
BMXS2	62	40.22	0	94.5		
BMXS3	213	191.22	-11	86.8		

Figure 4.5: Specific diagnostic distances and angles for the TPW experiment

4.2 TPW Experimental Results

A series of 20 data shots, along with several calibration shots, were conducted over the course of the first TPW experimental campaign. SCI data collected helped confirm the presence and impact of the injected pre-plasma. Fig 4.6 gives an example of data taken; a large spot of fluorescence is seen in the outline of the target where Cu is present. Most electrons are generated at a point close to the critical density and spread forward in a cone towards the fluor layer. The Cu-Kα measurements were characterized by measuring a circle containing 80% of the signal, while taking the crystals azimuthal and polar angles relative to the target into account (resulting in a slight oval shape when overlaid on the scanned image plate). From shots taken without injected pre-plasma, the electron trajectories can be extrapolated using the Cu-Kα spot. The bulk of electrons were generated roughly in a 75 half angle cone. The radius of the Cu-Kα spot for all data shots is plotted in Fig. 4.6 and shows that when the 2 ns long pulse beam was introduced, the radius of the Cu-Kα spot increased by 20-40%. This suggests that the interaction region for the main short pulse beam was likely pushed away from the target surface. If it is assumed that the electron spectras angular dependence remains the same with and without pre-pulse in this regime, the change in spot size is consistent with moving the source of electrons roughly 25 µm away from the target surface (Fig 4.6 bottom).

This critical density pushback estimate is further supported by 1D HYADES

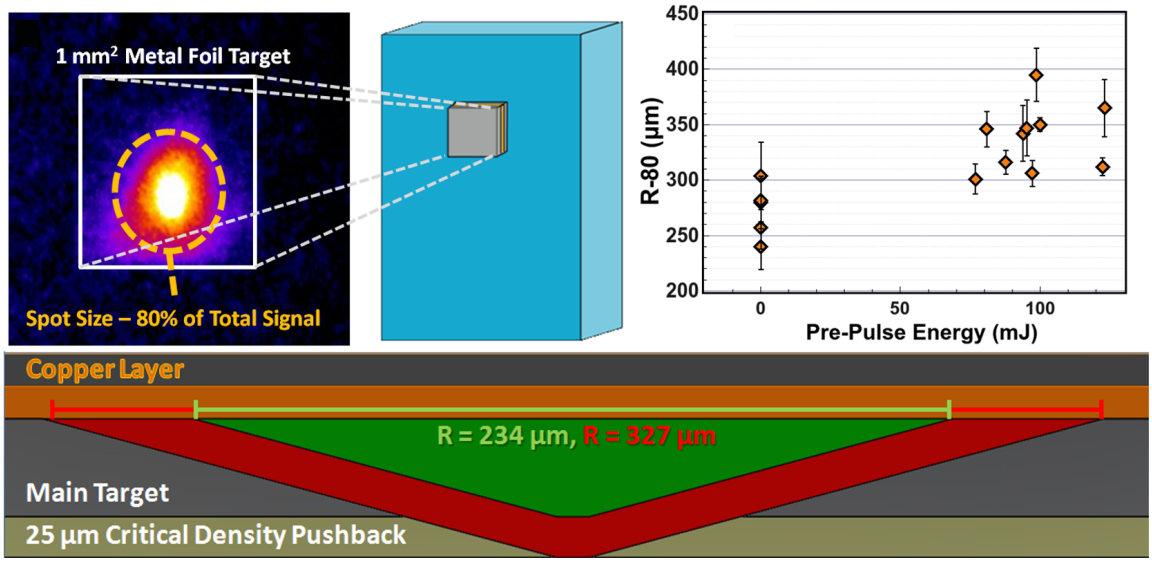

Figure 4.6: Top Left: Image taken of Cu-Kα via Spherical Crystal Imager (SCI). The spot of fluorescence indicates distribution of electrons. The solid box indicates the borders of the target. Top Right: Measurements of the radius of the Cu-Kα spot encompassing 80% of the signal. Increasing the pre-pulse energy resulted in an increase in spot size, indicating that the interaction region was pushed away from the target surface. Error was estimated from the background signal that was subtracted from the image plate. Bottom: Diagram demonstrating the effects of pre-pulse pushing the critical density and interaction region away from the target by 25 µm. Generated electrons must travel further in order to impact the copper layer and generate x-rays, which allows them to spread out more.

simulations which estimated the density profile in two pre-pulse cases in our experiment. As shown in Fig 4.7, with the intrinsic 20 mJ, 4 ns pre-pulse only, the critical density is estimated as being 58 µm away from the original target surface. When the injected pre-pulse (100 mJ, 2 ns) was included with the intrinsic, the critical density is pushed back to 88 µm. This shift in critical density of 30 µm helps account for the results seen with the SCI.

While the SCI data confirms the laser-plasma interaction is impacted by the presence of pre-plasma, the electron spectrometers showed little to no change when the long pulse was introduced. An example of data taken (with and without the injected pre-pulse) from the rear facing electron spectrometer is presented in Fig 4.8.

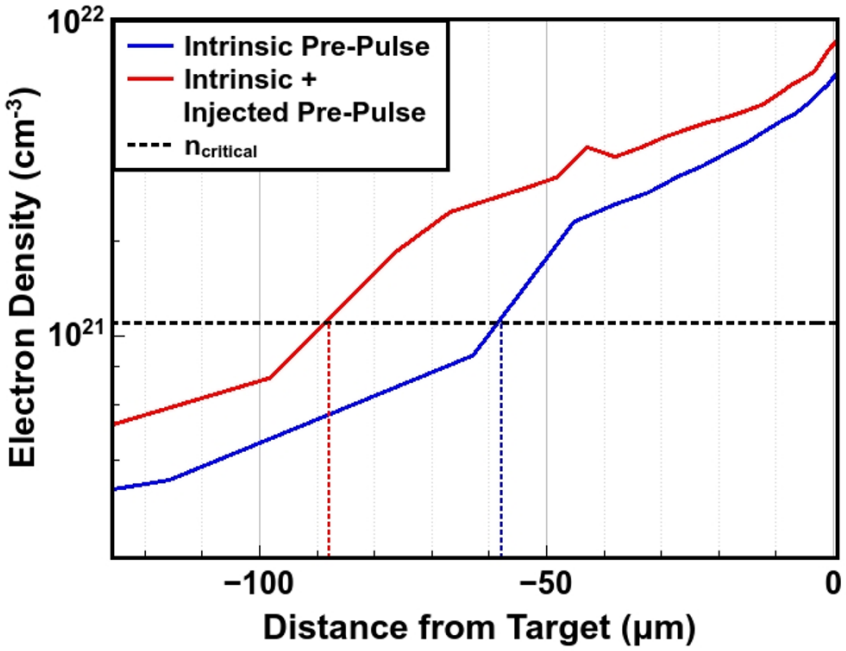

Figure 4.7: Density profiles from 1D HYADES simulations comparing intrinsic pre-pulse only (blue) with combined intrinsic and injected pre-pulse (red). The difference in the position for estimated n_{crit} is over 30 µm, which accounts for the change in SCI signal size.

The slope temperature of the electrons in these two shots were close, approximately 4.6 MeV, which is similar to what is predicted by a ponderomotive scaling at the expected intensity (4.9 MeV). Fig 4.8 shows data set of the entire experiment with respect to the injected pre-pulse beam energy. Electron slope temperatures for the no pre-pulse case varied from 3.5 to 6.9 MeV over the course of the experiment, likely due to shot to shot variation in laser energy and target alignment. Cases with pre-pulse had a similar, though slightly lower range of 2.0 to 5.0 MeV and with no cases with pre-pulse exceeding the average temperature seen without pre-pulse. A key aspect to this data is the clear single slope nature of the electron spectra. Previous experiments demonstrated that the super-ponderomotive electron component measured by a magnetic spectrometer manifests as a two temperature spectrum. While the slopes of the spectra change shot to shot, they are all a single

temperature in line with ponderomotive scaling. The HMIE electron spectrum data also supports these trends.

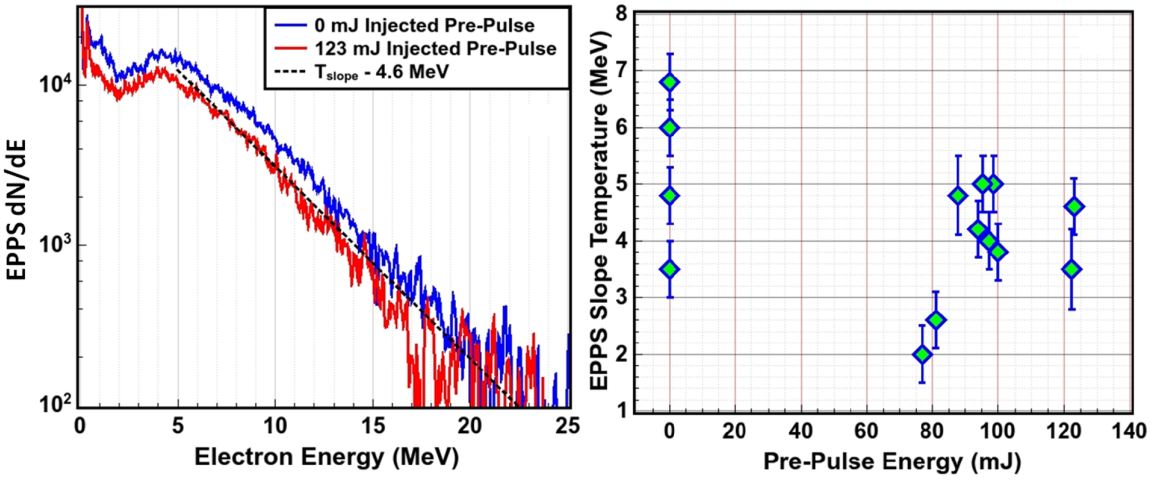

Figure 4.8: Left: EPPS data of two shots taken with and without the injected pre-pulse. The characteristic slope temperature of both shots is nearly identical, and slightly below what is predicted by ponderomotive scaling. Right: All EPPS slope temperature data shows little to no impact from the addition of pre-pulse.

The main takeaway from the first TPW experiment appears to be that for extremely short pulse lengths of 150 fs, no super-ponderomotive electrons are measured. This is somewhat surprising considering that prior experiments such as those conducted by T. Yabucchi et al. [37] demonstrated super-ponderomotive electron production for 500 fs pulses. Furthermore, shorter pre-pulse experiments by K. A. Ivanov [38] and C. Gahn [39] inferred some electron temperature shift from the addition of pre-plasma. Comparing these findings would suggest either that super ponderomotive electrons require a minimum pulse length in order to be produced in large enough quantities to be measured, or that our small apertured EPPS diagnostic is missing the measurement every time. It was also possible that having a large intrinsic pre-pulse could have an unforeseen impact on the results. These issues were kept in mind when designing the second experiment on TPW, which included an additional EPPS facing the front target surface, BMXSes, a variable pulse duration and a higher

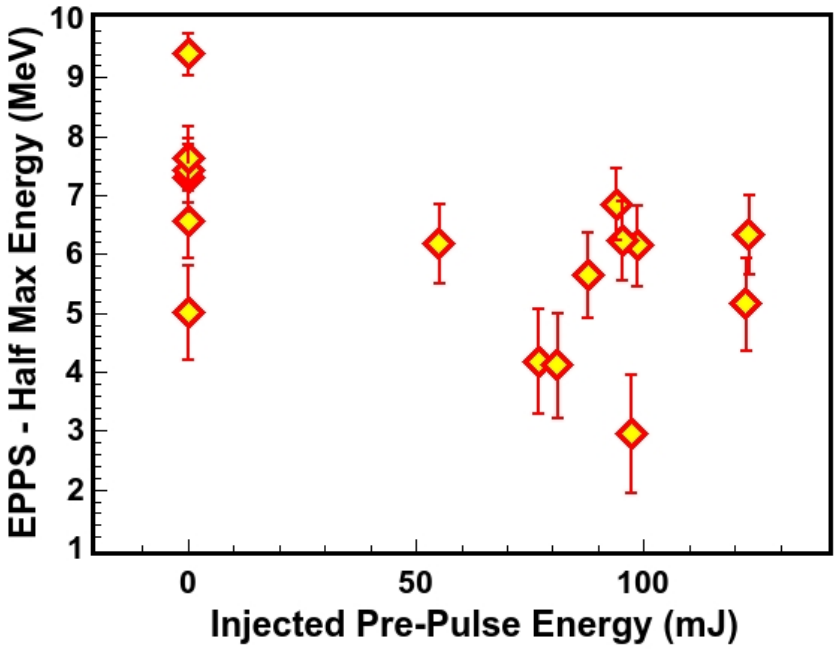

Figure 4.9: HMIE results from EPPS for the first TPW experiment mirroring the slope temperature results. No hot electron tails were measured with the injected pre-plasma.

contrast beam with reduced intrinsic pre-pulse.

Unfortunately many of the other diagnostics on the experiment failed to operate properly. The proton radiography, which introduced severe restrictions on several diagnostics was the main culprit. While some proton radiographs were collected, total laser energy delivered was much lowered than advertised. This resulted in an inadequate number of high energy protons to consistently examine the interaction region. The low number of protons also made it difficult to have a significant time resolution in the radiographs resulting in single images taken with large variances in time. The energy dumped into the secondary target had another effect; it severely impacted the level of signal generated on some of the diagnostics, particularly the BMXS's and the EPPS facing the front surface of the sidelighter target. BMXS signal in high energy channels was dominated by the proton radiography target signal and the EPPS was

poorly calibrated to receive signal from both the proton target and the main target.

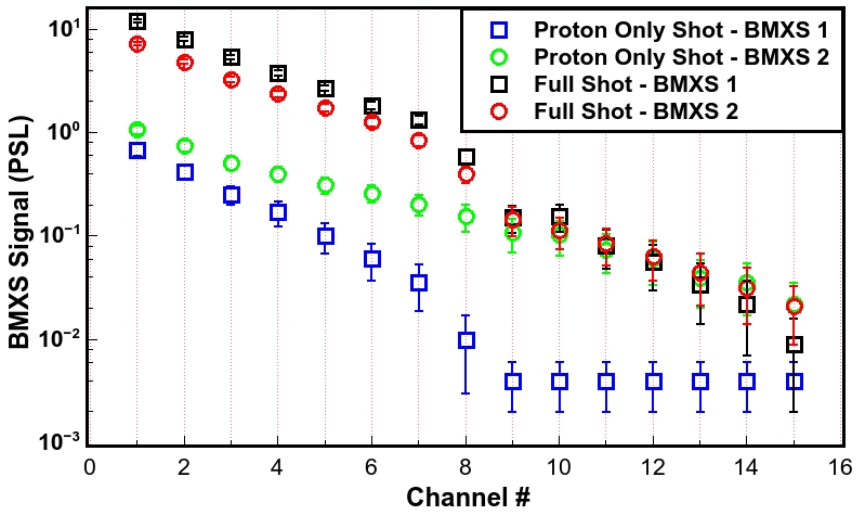

Figure 4.10: High energy bremsstrahlung signal on one BMXS is dominated by signal from the proton radiography target rendering it difficult to diagnose electrons in the main target.

The resulting proton radiographs, if timed properly, with a large quantity of high energy protons, seemed to suggest some proof of a potential forming on the surface. Radiographs taken early in time with the highest energy protons showed a slight decrease in proton signal just in front of the target indicating an electric potential generated by an electron trapping potential well. This potential was bordered by a region of higher proton signal where the protons were presumably deflected. This proton deficiency indicates a potential well for electrons since a potential that traps electrons would deflect the radiograph protons away.

While proton radiographs are promising, they provide too poor resolution close to the surface of the target to be definitive and ruin much of the data on other diagnostics on the TPW platform.

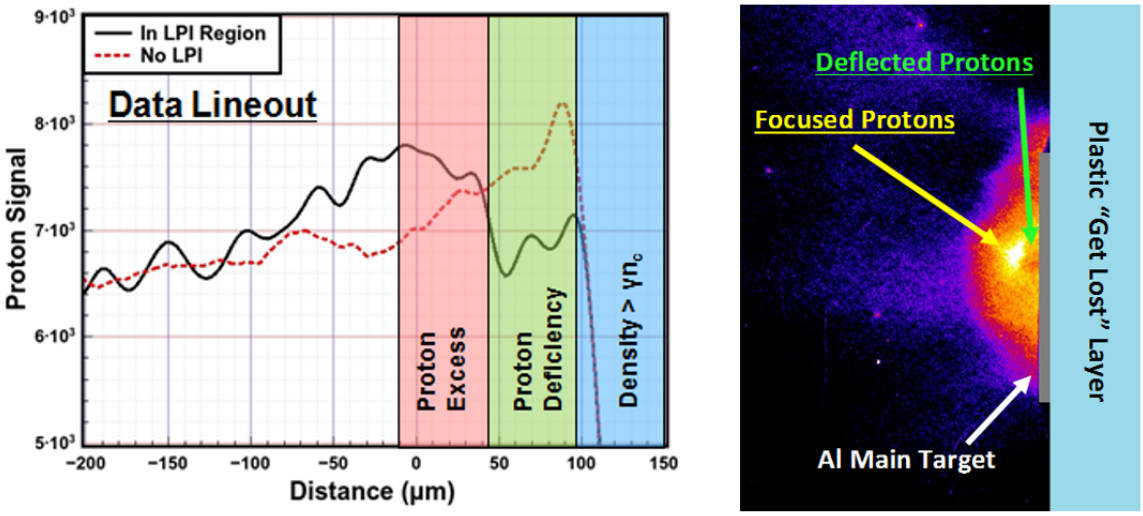

Figure 4.11: Proton radiograph and corresponding lineout in the region of interest. The radiograph lineout is compared between cases with and without the short pulse interaction beam. We can see that there is a large proton deficiency when there is a short pulse beam interacting with the pre-plasma which indicates a large potential well that would trap electrons.

4.3 Second TPW Experiment Parameters

A second follow up experiment was conducted on the TPW laser, which took advantage of a laser contrast upgrade in order to confirm and expand on findings in the first experiment. In the preliminary experiment TPW had an intensity contrast level of 10^6 which rendered an **intrinsic** pre-pulse with significant intensity. This intrinsic pre-pulse introduced uncertainty in the amount of pre-plasma that was formed with the long pulse beam. The first experiment therefore compared different levels of pre-plasma with the long pulse beam rather than comparing cases with and without pre-plasma. Since previous simulations showed that super-ponderomotive electron temperature scales somewhat with level of pre-plasma the long pulse beam it was still useful to perform this experiment with the reduced contrast.

Proton radiography caused too much complication on the first experiment and

energy levels at TPW were not sufficient to consistently use proton radiography as a diagnostic tool. This, along with its ability to dominate diagnostic results, encouraged us to remove this part from the second experiment. This allowed for use of the entire beam for the main interaction. We could therefore keep intensity consistent with the first TPW experiment, but extend the pulse length from 150 to 600 fs. Removal of the extra off axis parabola, trombone delay stage and secondary target alignment system allowed for more leeway in diagnostic placement, though BMXS and SCI were still limited by the physical constraints of the chamber.

Furthermore, in the second experiment, main beam contrast was greatly improved by 2 orders of magnitude, reducing the intrinsic pre-pulse energies far below that of the long pulse. Here, work from the first experiment was double checked with the high contrast beam and expanded upon by increasing the pulse length. Additional diagnostic improvements were made, such as using an EPPS with a more suited calibration facing the front surface of the target in the beam reflection direction. The rest of the diagnostics were primarily arranged in order to look at electrons from the rear surface of the target. The specific distances and angles relative to the back surface are listed in the table below:

4.4 Second TPW Experiment Results

As a check, the results from the first TPW experiment at 150 fs were verified for the new high contrast beam. Intensities between the two experiments were kept the same though improvements to scanning equipment allowed for the resolution of lower signals on the EPPS. The results, shown in figure 4.14 verified that for 150 fs, no significant super-ponderomotive electron component was measured with the injected pre-pulse. It is clear that after over 30 shots with 150 fs pulse length that no amount of pre-plasma dramatically effects the super-hot electron spectrum from the rear of the target.

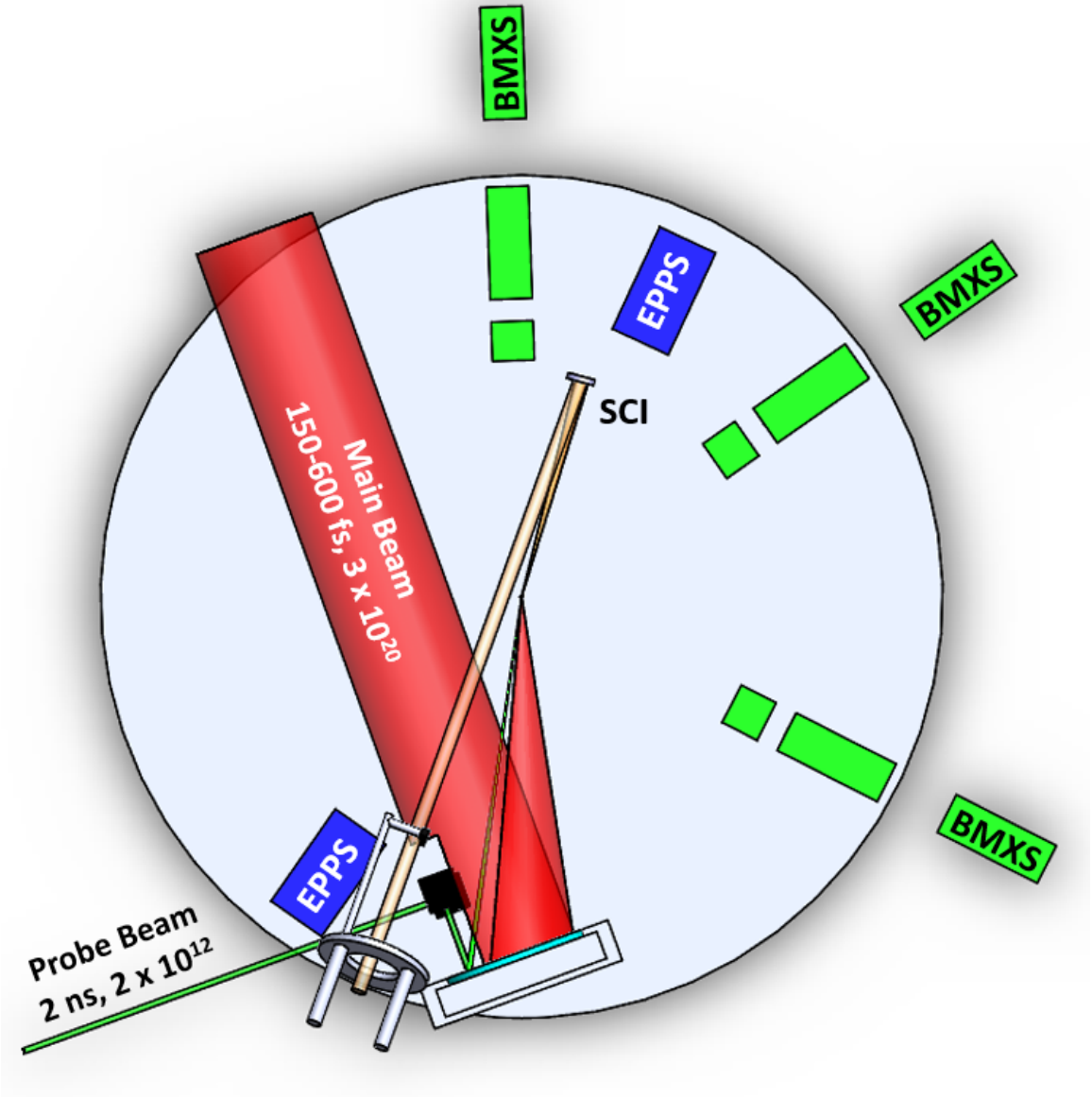

Figure 4.12: Initially planned layout for the second TPW experiment. Some rearrangement was made from the first experiment in order to better capture the effects of the main interaction.

While no additional hot electron population was measured off the rear surface of the target, the EPPS facing the front surface of the target at the beam's reflection angle measured a clear secondary hot electron component. The electrons on the whole for the front facing EPPS are lower energy than those measured on

	Azimuthal Angle (deg)	Azimuthal Angle (rel to target)	Polar Angle (deg)	Distance (cm)	Pixel Size	IP Type
SCI	48	26.22	12.7	32.3	25um	BAS-MS (white)
EPPS1	21.78	0	0	43	100um	SR (blue)
EPPS2	205	183.22	0	55.5		
BMXS1	-2	-23.78	0	92.5	100um	BAS-MS (white)
BMXS2	15	8	0	93		
BMXS3	90	68.22	6.83	92.5		

Figure 4.13: Specific diagnostic distances and angles for the TPW experiment

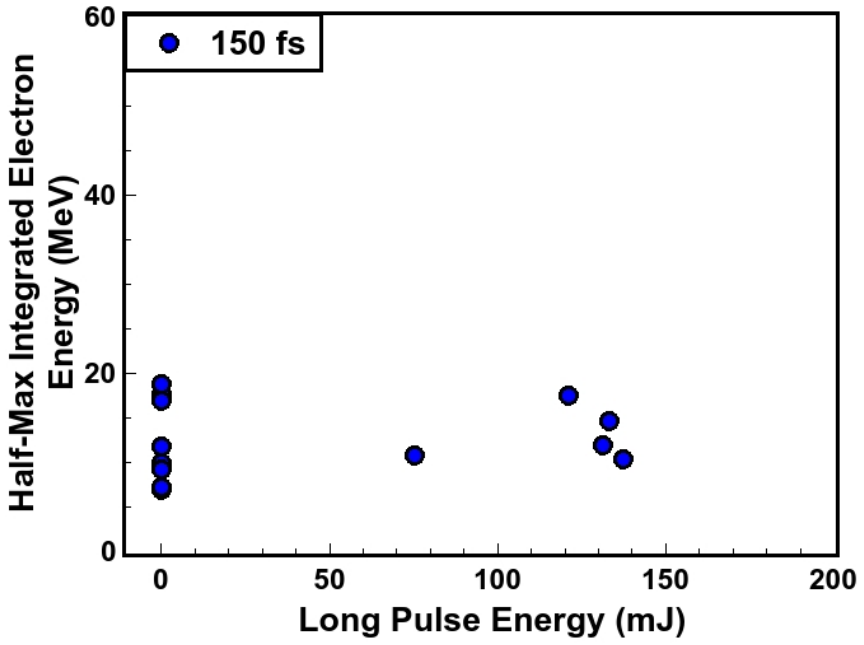

Figure 4.14: HMIE results from the EPPS facing the rear surface of the target for 150 fs pulse lengths. No notable hot electron tails were measured.

the rear side, but the trend is clear and the secondary hotter electron component is measured with nearly 100% consistency. The slope temperatures for these backwards going electrons appears not to change significantly, however the quantity of electrons measured increase by an order of magnitude when pre-plasma in introduced. This shift also corresponds to a significant increase in HMIE, which nearly doubled in most cases.

When extending the short pulse length to 450 fs trends from the EPPS continued (Fig. 4.15). No hot electron tails were measured with the injected pre-plasma out

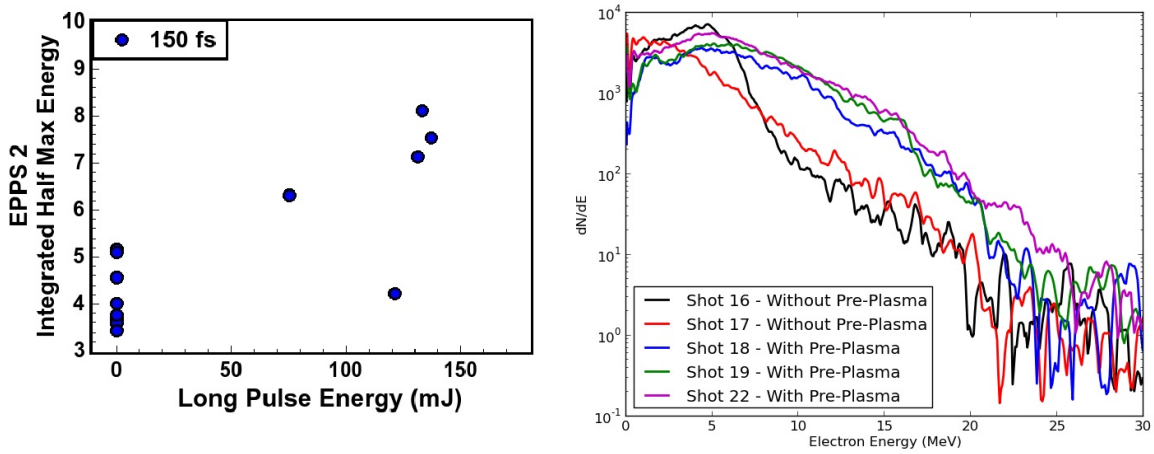

Figure 4.15: HMIE results from the EPPS facing the front surface of the target for 150 fs pulse lengths. On the right are several individual spectra showing the different shape when pre-plasma was introduced.

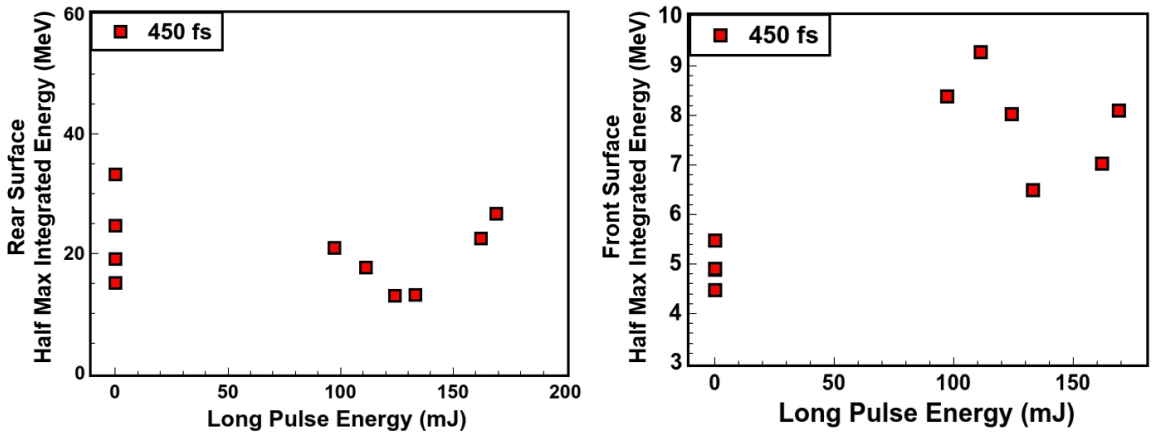

Figure 4.16: HMIE results for rear facing (left) and front facing (right) EPPS for shots with 450 fs pulse length.

the back of the target, but more hot electrons were once again measured out of the front surface of the target. This was somewhat unexpected as 450 fs is very close to the regime where prior experiments measured super-ponderomotive electrons under similar conditions.

Finally when extending the pulse length to 600 fs a significant change was measured for the electron spectra out of the rear of the target. On 3 out of 9 shots

with the long pulse beams a significant component of super-ponderomotive electrons was measured, with energies of nearly 200 MeV. When comparing these spectra to a spectrum without the super-ponderomotive component it is clear that electrons below 50 MeV are suppressed.

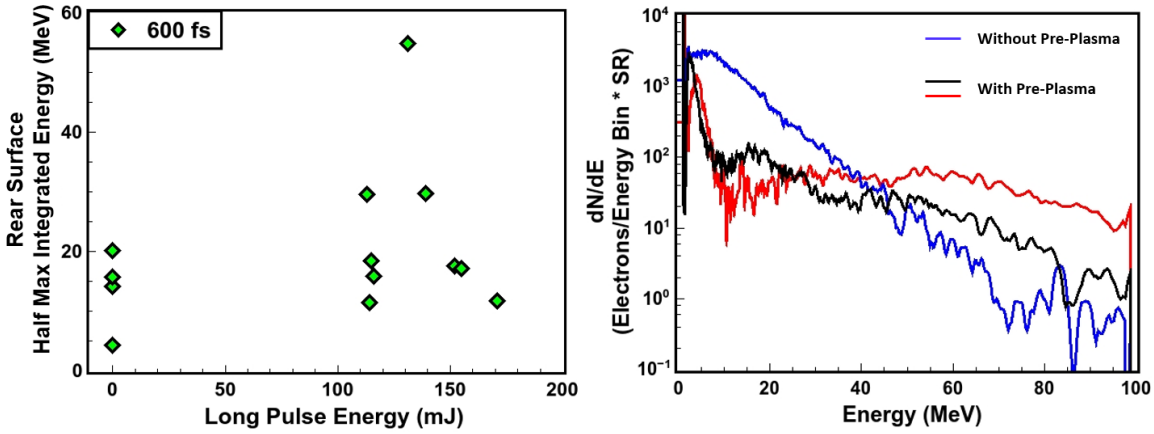

Figure 4.17: Left: HMIE results for rear facing EPPS for 600 fs pulse length. 3 of the 9 shots with the long pulse had significant super-ponderomotive electron components. Right: spectra for 3 600 fs shots. The lines in red and black are 2 shots where a hot electron tail was measured, some electrons were measured with up to 200 MeV energy

When comparing the spectra directly that the super-ponderomotive components are not simply "added" to the original single temperature ponderomotive scaling electron spectrum. Rather some large change happens on these shots which causes a large shift in the entire measured spectrum. When examining what was unique about these 3 shots, the beam and target qualities appear to be on par with the other 600 fs shots with the long pulse.

Therefore, the generation of super-ponderomotive electrons appears to be based on shot to shot variation in the 600 fs case. The most likely answer for this seemingly random behavior can be traced to the EPPS diagnostic itself. The EPPS's small pinhole results in an extremely small acceptance angle for measured electrons. If the super-ponderomotive component of the electron spectrum is non isotropic it

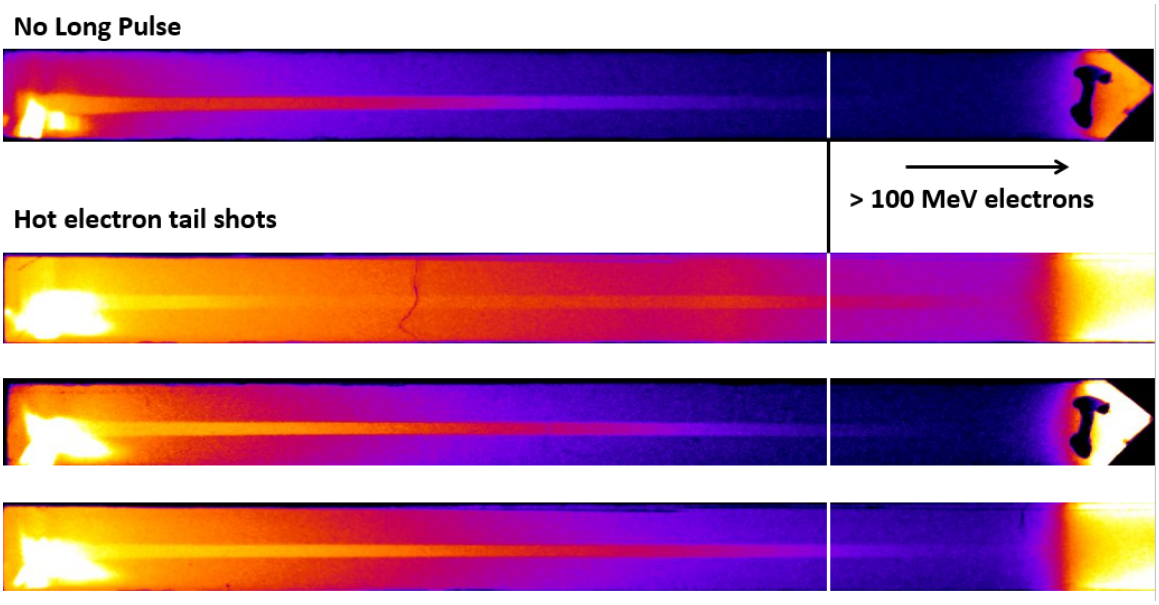

Figure 4.18: Direct image plate data of EPPS from all 3 shots with the hot tail. The white lines indicate 100 MeV and electrons with nearly 200 MeV energy will reach the end of the readable area on the spectrometer. Note: color scale is not identical across all image plates but changed to show highest energy signal the clearest.

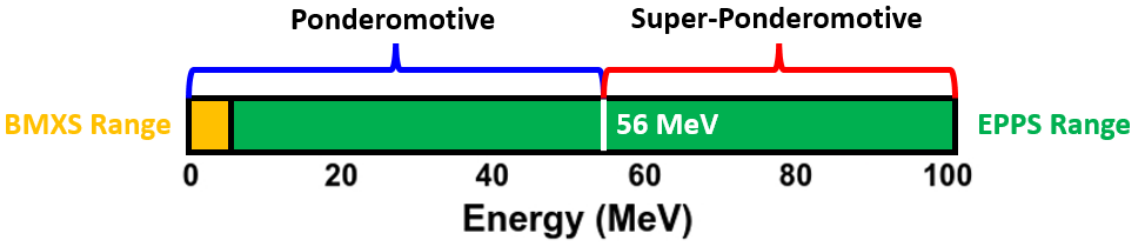

Figure 4.19: Diagnostic energy ranges compared to heating mechanisms for TPW intensities.

is possible, or even extremely likely that it will miss the diagnostic. Increasing the pulse length therefore has 1 of 2 effects: either a pulse length > 500 fs is required for any super-ponderomotive acceleration, or as pulse length increases, directionality changes, sending more super-ponderomotive electrons in the direction of the detector.

It was hoped that by using the BMXS, some of the uncertainty of the small EPPS pinhole would be alleviated. However, since TPW's intensity is extremely high,

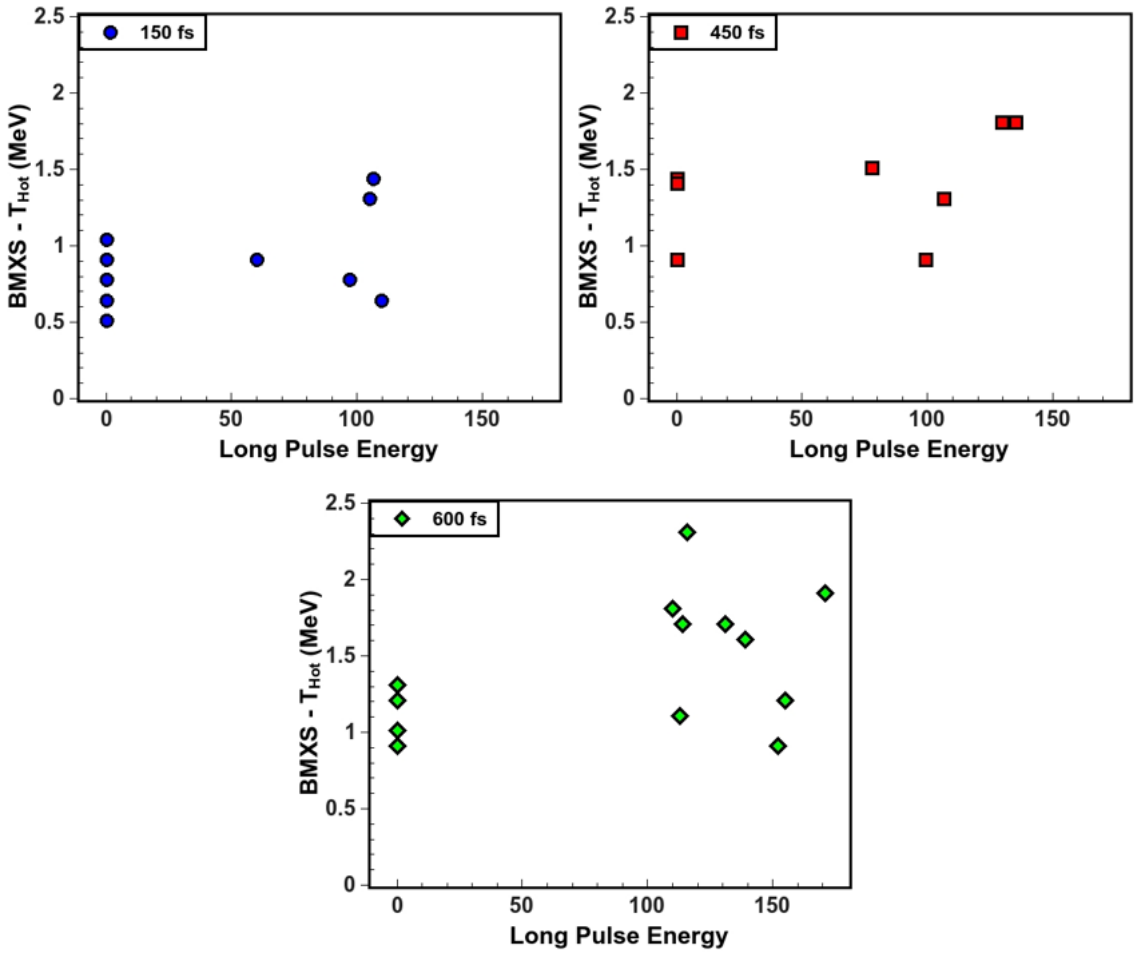

Figure 4.20: Slope temperature of electrons used in BMXS analysis for all 3 pulse lengths for TPW.

ponderomotive scaling electron energies far exceed the limits of the diagnostic. This means that any trends measured with BMXS are difficult to attribute to a physical mechanism in the beam since the BMXS examines electrons between 100 keV - 5 MeV and ponderomotive electrons can reach up to 56 MeV. So while the BMXS appears to show similar trends to the EPPS in that temperatures increase with pre-plasma only for 600 fs pulses, it must be said that the BMXS is only looking at a very small component of the ponderomotive scaling portion of the electron spectrum.

This chapter contains some material and figures from “Impact of Pre-Plasma

on Fast Electron Generation and Transport from Short Pulse, High Intensity Lasers", J. Peebles, C. McGuffey, C.M. Krauland, L.C. Jarrott, A. Sorokovikova, M.S. Wei, J. Park, H. Chen, H.S. McLean, C. Wagner, M. Spinks, E.W. Gaul, G. Dyer, B.M. Hegelich, M. Martinez, M. Donovan, T. Ditmire, S.I. Krasheninnikov and F.N. Beg, Nuclear Fusion **56**, 016007 (2016). The dissertation author was the primary investigator and author of this paper.

Sections of this chapter are currently being prepared for submission for the publication: "Super-Ponderomotive Electron Generation and Deflection via Self Generated Magnetic Fields", J. Peebles, A. V. Arefiev, S. Zhang, C. McGuffey, J. Park, H. Chen, H.S. McLean, M. Spinks, E.W. Gaul, G. Dyer, B.M. Hegelich, M. Martinez, M. Donovan, T. Ditmire, M. S. Wei, S.I. Krasheninnikov and F.N. Beg, Physical Review Letters (in preparation), (2017). The dissertation author was the primary investigator and author of this material.

Chapter 5
Exploring TPW Experimental Results with 2D PIC Simulations

The goal of the simulations below is an attempt to understand the super-ponderomotive electron data from the shortest pulse length experiments. This data showed that at pulse lengths shorter than 450 fs, no super-ponderomotive electrons were measured. As pulse length was increased to 600 fs super-ponderomotive electrons were measured inconsistently. PIC simulations can help explain the reason why super-ponderomotive electrons are measured for longer pulse lengths as well as shed light on why the measurement of such electrons is so inconsistent.

Initial simulations performed in previous work used a few assumptions about initial conditions. In these works a sin squared temporal laser pulse profile was used and pre-plasma density profiles are estimated as a single exponential slope, characterized by a number called the pre-plasma scale length [31]:

$$n_{pre-plasma} = \frac{n_{solid}}{1 + exp\left[- \left(\frac{x - x_{crit}}{L_{ScaleLength}} \right) \right]}$$

This density profile has the benefit of having a scalable amount of pre-plasma material within a region of the target that can be reasonably simulated by a PIC code. However, experimental techniques such as angular filtered reflectometry (AFR) [53] and interferometry using short wavelength beams are able to probe and measure actual pre-plasma densities on some experiments. The results from these diagnostics are corroborated with 1 and 2D radiation hydrodynamic simulations. These results show a significant departure from the original single slope density profile, instead they show that pre-plasma is best estimated by at least two exponential slopes: a steep

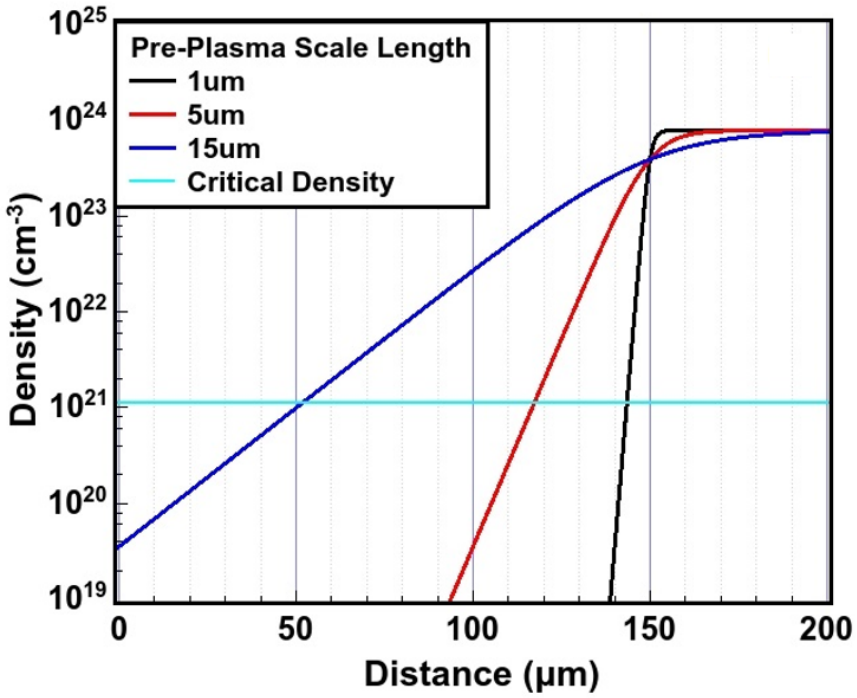

Figure 5.1: 3 exponential decay density profiles represented by 3 scale lengths of pre-plasma. In previous work 10-15 µm scale lengths are considered very large pre-plasmas, while 1 µm would be considered essentially as little pre-plasma as reasonably possible.

initial slope from solid to critical density and then a second, much longer slope. These results also showed that the secondary slope can also often have larger scale lengths than 15 µm with significant amounts of plasma extending several hundred microns.

This change in pre-plasma density profile could greatly affect the propagation of the laser through the plasma before it hits the target. Therefore in all simulations pre-plasma is estimated by 2D rad-hydro simulations and density probe diagnostics such as AFR and interferometers.

Initial simulations were performed in 2D (with x as the direction of beam propagation) with the following parameters:

- An initial pre-plasma density profile of $n = \frac{7.85e23}{1+exp(-(x-150)/1.0)} + \frac{2.5e21}{1+exp(-(x-150)/30.0)}$ where solid density is placed near 150 µm.

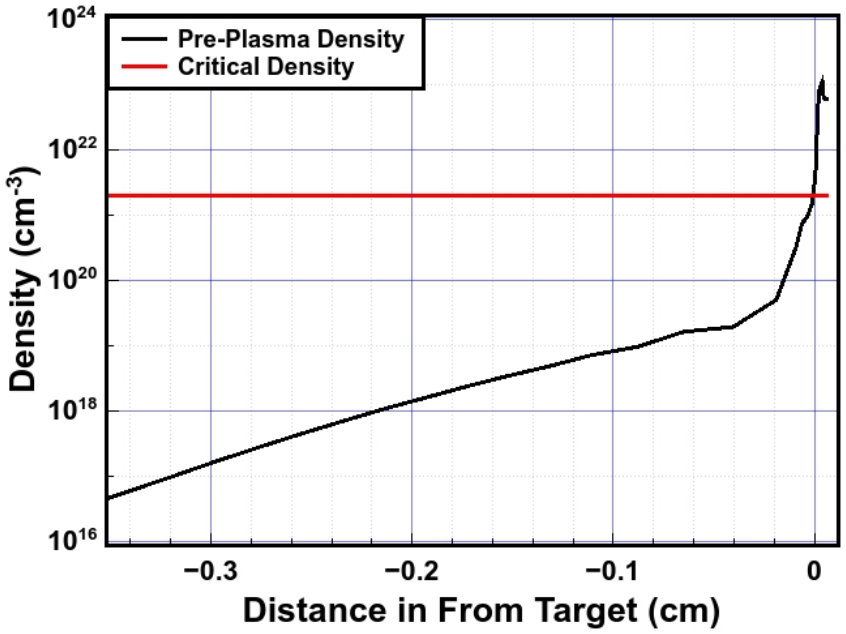

Figure 5.2: Pre-plasma density profile estimated by 2D FLASH rad-hydro simulations for injected pre-plasma on TPW.

- The no pre-plasma case assumes a density profile simply of $n = \frac{7.85e23}{1+exp(-(x-150)/1.0)}$
- The size of the entire simulation box is x = 250 µm, y = 60 µm with $\Delta x = 40$ cells/µm and $\Delta y = 10$ cells/µm
- The pulse shape is represented by $sin^2(\frac{\pi t}{t_0})$ where t_0 is the pulse length.
- Electrons are measured 30 µm inside the target in the forward going direction and 30 µm in front of the target for electrons going backwards.
- Plasma is treated as "fully ionized" where the density is comprised of a balance of electrons and aluminum ions with +13 charge and 1/13 the density.
- The resolution of these simulation was 30 cells/µm in the x (laser) direction, 15 cells/µm in the y direction and the box was 250 µm long in the x direction and

60 µm in the y direction. When initializing there were 10 macroparticles per cell for electrons and 5 for ions.

The first results of these simulations using these parameters for pulse lengths of 150, 450 and 600 fs were surprising. When looking at electrons traveling in the forward direction inside the target it was found that 150 fs gave very different results from the longer pulse lengths. It is expected that when pulse length is increased from 150 fs, that the spectrum in the 150 fs case would be a subset of the longer pulse cases. However the 150 fs case has the highest energy electrons measured and a very different spectrum shape (Fig 5.3). Going from 150 to 450 fs most electrons above 140 MeV disappear. The difference between the 450 and 600 fs cases was closer to what was anticipated. The maximum energy of measured electrons without pre-plasma is on par with what is expected from ponderomotive scaling and conforms more closely with a one temperature profile. A beam of intensity $3e20$ W/cm^2 generates electrons with an approximate maximum energy of 56 MeV using the maximum energy estimate of $mc_e^2(\frac{a_0^2}{2})$.

The question must be asked, what causes such a change in electron spectra for the shortest pulse case? The strange result from the 150 fs simulation arises from the incorrect assumption that a $sin^2(\frac{\pi t}{t_0})$ profile is a good estimate for a laser profile. While the $sin^2(\frac{\pi t}{t_0})$ profile can somewhat accurately reproduce actual laser profiles of picosecond pulse lengths, when the pulse length is shortened to 150 fs the rise time of the beam becomes unreasonably fast. When compared to actual measurements of pulse profiles on laser systems like TPW, shown in Fig 5.4, $sin^2(\frac{\pi t}{t_0})$ becomes unrealistic and a new profile must be constructed.

It is notable that while the 150 fs results make little sense in the context of the experiment, that does not mean that the simulations were wrong or unphysical. An actual laser with a quick rise time could potentially accelerate electrons to energies

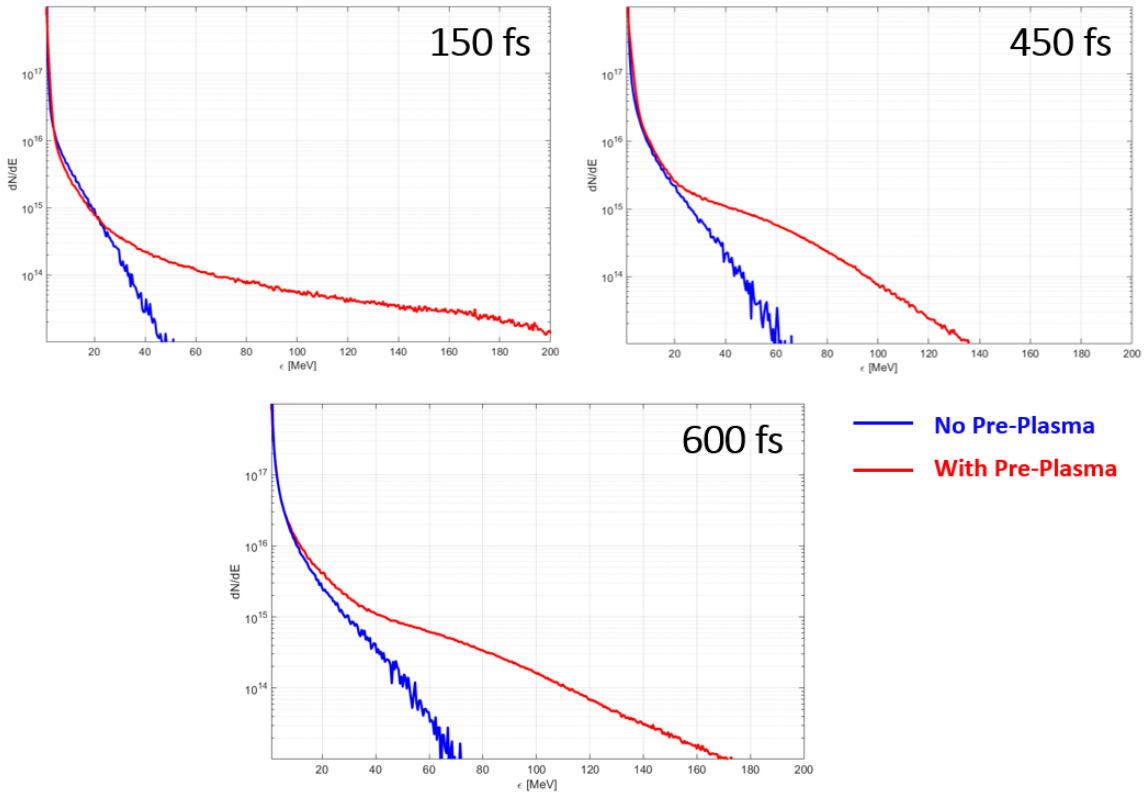

Figure 5.3: Electron spectra in the forward direction with and without pre-plasma in the 150, 450 and 600 fs pulse length cases plotted on the same scale. While the 450 fs case appears to be a subset of the 600 fs case the 150 fs case is markedly different. In all cases without pre-plasma no significant number of super-ponderomotive electrons were measured and maximum electron energy was around 60 MeV.

seen in the simulation. To examine the point at which the acceleration transitions from the fast rise regime (sin squared 150 fs profile) to the slow rise one (sin squared with pulse length $>$ 450 fs), several simulations were conducted with varying rise times. To do this a tunable rise time gaussian function was chosen as the laser profile; rise times of 50, 70 and 90 fs were tested. The rise time of 50 fs was slightly slower than the sin squared profile but the most comparable.

The results of the rise time test confirm that steep rise times of the laser are the culprit for the inconsistent 150 fs results in the simulations. The 50 fs gaussian rise is similar in result to the 150 fs sin squared pulse with 10^{13} 200 MeV electrons. The 70

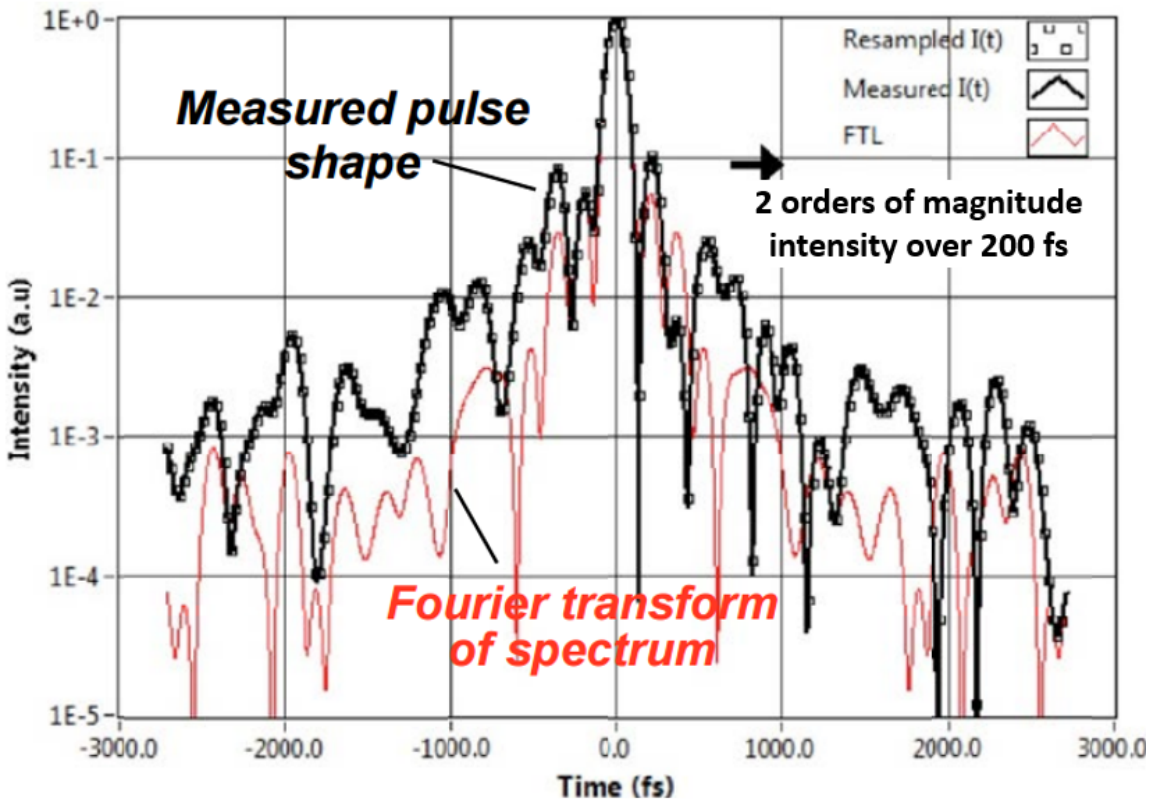

Figure 5.4: Actual pulse shape measurements from TPW show that rise time can be estimated as a rise of 2 orders of magnitude of intensity in 200 fs. This means that for the best compression 150 fs pulse on experiment is better described by a rise and fall over approximately 400 fs with most of the energy contained in 150 fs. [54]

and 90 fs gaussian rise pulses produce spectra more in line with the 450 and 600 fs sin squared simulations, with 10^{13} 140 MeV electrons. The overall shape of the spectra also shows the telltale "bump" that is a signature of pre-plasma heated electrons. This bump has been notable in previous pre-plasma heating experiments and simulations seen in section 2.10, and helps verify that the 450 and 600 fs simulations were closer to the experiment. These results mean that future simulations examining pre-pulse in the short pulse length regime should be profiled with a gaussian pulse shape. The rise time of 70 fs is chosen as it most accurately represents the actual rise time measured on TPW when comparing the rate at which the intensity rises and falls.

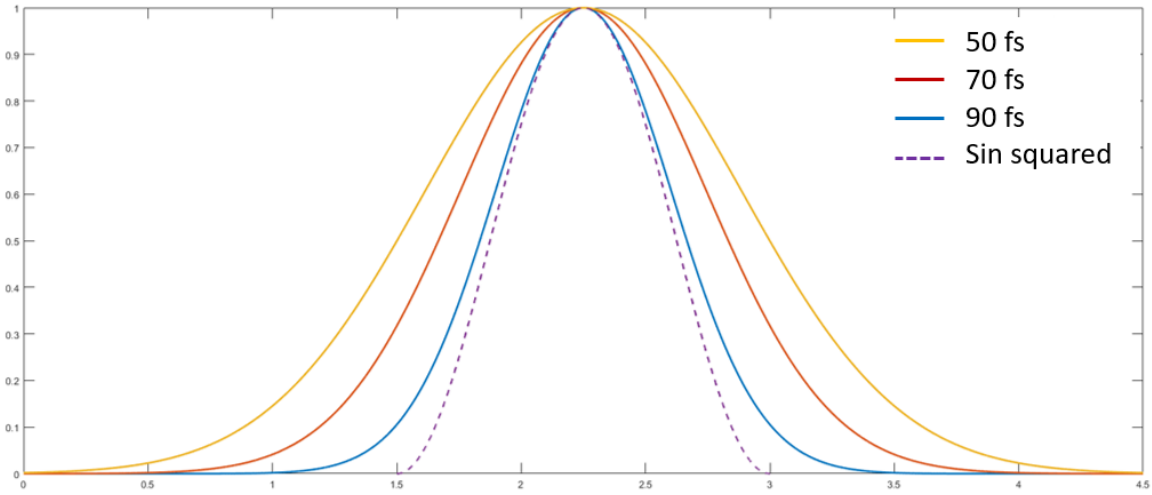

Figure 5.5: Several different gaussian laser profiles with different rise times compared to the sin squared profile.

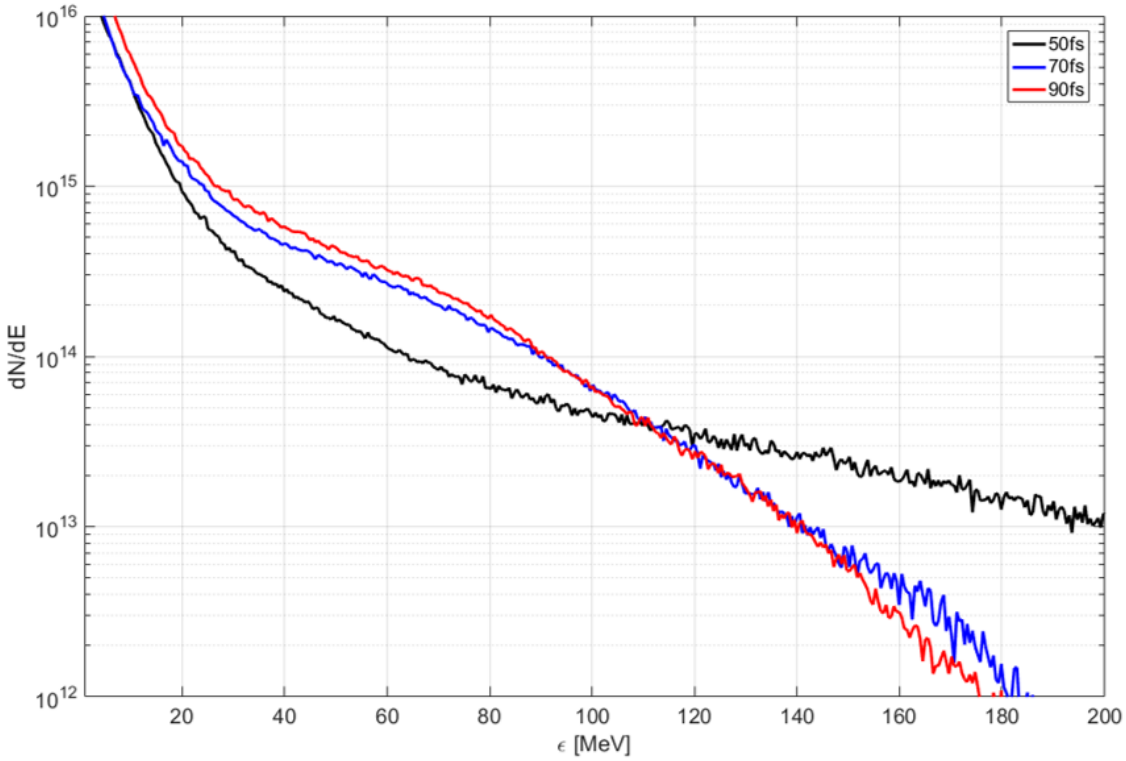

Figure 5.6: Results from different gaussian rise times. The 50 fs rise time laser clearly lies in a different regime from the longer rise time pulses. The longer rise time pulses generate results more consistent with the 450 and 600 fs pulses tested before.

For simulations of longer pulse lengths seen on 450 fs and 600 fs experiments the 70 fs gaussian rise time was used in conjunction with a flat top pulse. Since the rise and fall of this pulse is essentially a 150 fs in itself, the flat top added on is the difference between the longer pulse length and 150 fs. Hence a 450 fs pulse would be estimated by a 300 fs flat top sandwiched by a 70 fs rise and fall. Actual measurements of pulse shape are not available for the 450 and 600 fs at TPW and so this best guess assumption must be made.

When applying the new pulse profiles for all 3 pulse lengths, the spectra change significantly again. It is clear that the sin squared pulse shape had unintended side effects for longer pulses as well. In the 600 fs case a sin squared profile has a longer ramp up to peak intensity than new 70 fs gaussian ramp. We can see when plotting the new spectra that the differences between 450 and 600 fs are almost negligible whereas there's nearly an order of magnitude difference in the number of high energy electrons when compared to the 150 fs spectrum. Some of this effect is simply due to having more energy over a longer period of time generating more electrons. However the smaller difference between 450 and 600 fs cases show the disparity in number of electrons for the 150 fs case cannot be accounted for by changes in energy alone. Some difference must occur between the 150 fs and 450 fs cases.

While the simulation results using the new pulse shape are consistent when compared with each other, they do not completely replicate what was measured on the experiment. In the experiment super-ponderomotive electrons were only measured for pulse lengths of 600 fs and were only measured on a small portion of shots. When the super-ponderomotive electrons were not measured, the spectra appeared very similar to the no pre-plasma case. There are a few possibilities that can explain this discrepancy. First, it could be that for shorter pulse lengths unanticipated 3D effects, not captured by the 2D simulations, come into play, reducing pre-plasma

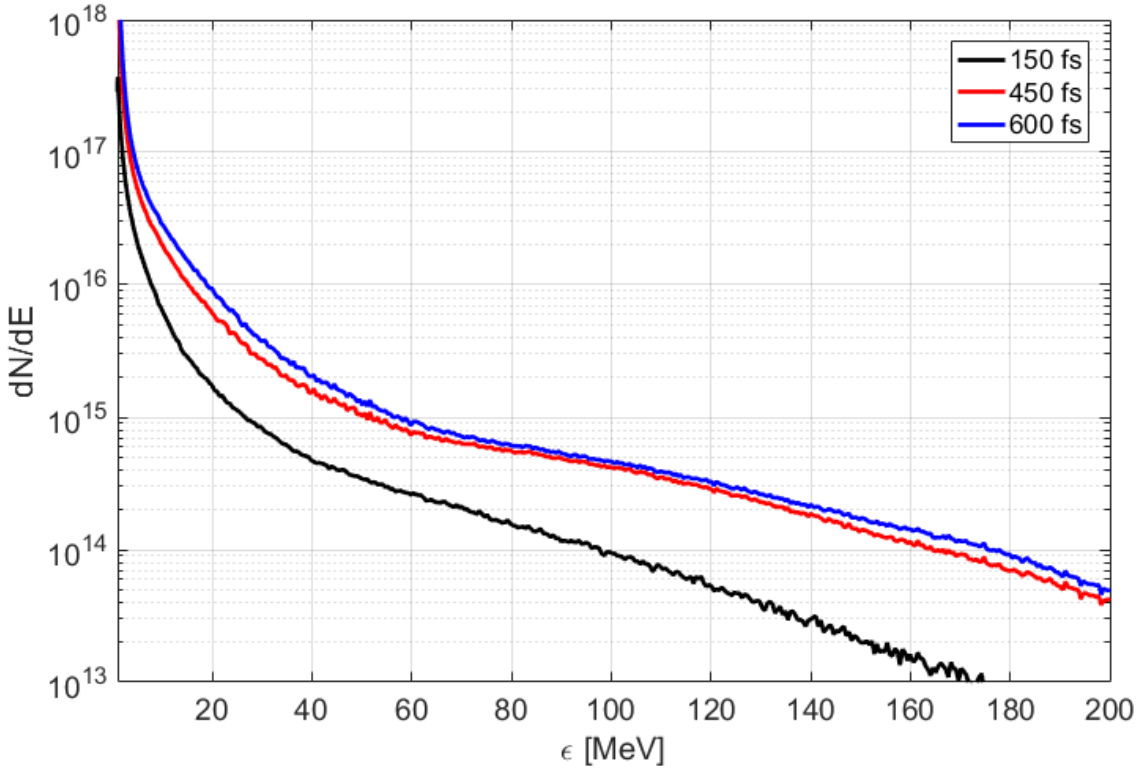

Figure 5.7: Results from different new pulse profiles for 3 pulse lengths: 150, 450 and 600 fs. A quicker rise to peak intensity with peak intensity held for a longer duration increases number of super-ponderomotive electrons significantly compared to the sin squared pulse length case.

heating effects for 450 fs pulses. Second, the probe measurement in the EPOCH code measures all electrons crossing an invisible plane, it could be that these electrons are too diffuse in number to measure, or are directed away from the diagnostic on the experiment.

Testing the effects of 3D on pre-plasma heating is straightforward; a sample 150 fs case was run in 3D and compared with the 2D result. Parameters such as density and laser profiles were held the same but resolutions and particles per cell were changed in order to account for the massive computing times of 3D simulations. The resolution of the 3D run was 10 cells/µm (x) 5 cells/µm (y) and the particles per cell was reduced to 1 for ions and 4 for electrons. The size of the simulation box was

decreased to 100 µm by 20 µm with 10 µm of solid density material. The extraction plane was moved to just inside the surface in order to accommodate the smaller box. Due to the changes to the box size and extraction plane position, a 1 to 1 comparison of electron count cannot be made, the resulting electron spectrum is can be compared to the 2D case in terms of shape and slope. The electron count decreases from $2 * 10^9$ to $2 * 10^7$ for 50 to 150 MeV in the 3D case, while in the 2D case the slope is a little shallower (a hotter slope temperature) decreasing from $3.5 * 10^{14}$ to $2 * 10^{13}$ over the same energy range. While 3D effects do appear to decrease super-ponderomotive electron temperature it appears that measurable quantities of super-ponderomotive electrons are still accelerated and measured in the extraction plane.

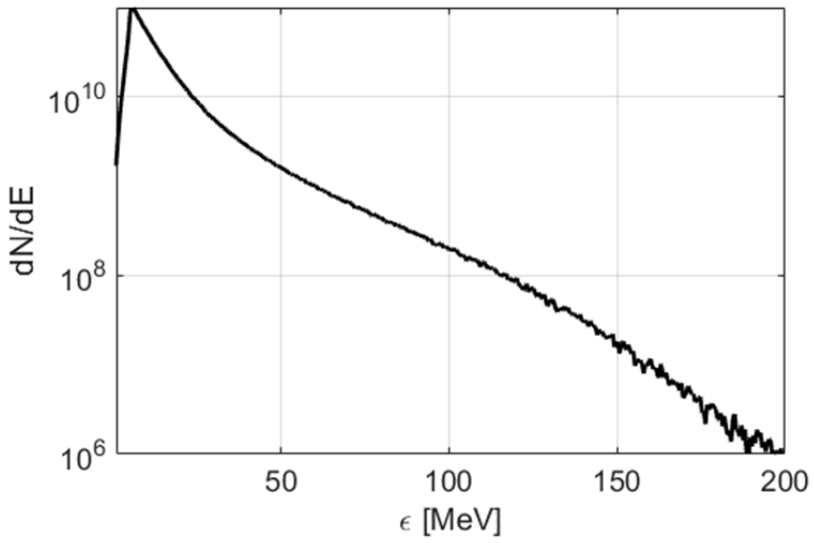

Figure 5.8: Electron spectrum output from the 3D test case. General slope and shape are very similar to the 2D case

In order to examine the directionality of electrons, using the extraction plane/probe functionality of EPOCH to gauge the directionality of the electrons is a difficult task since it only provides information in one plane of space. The best way to visualize

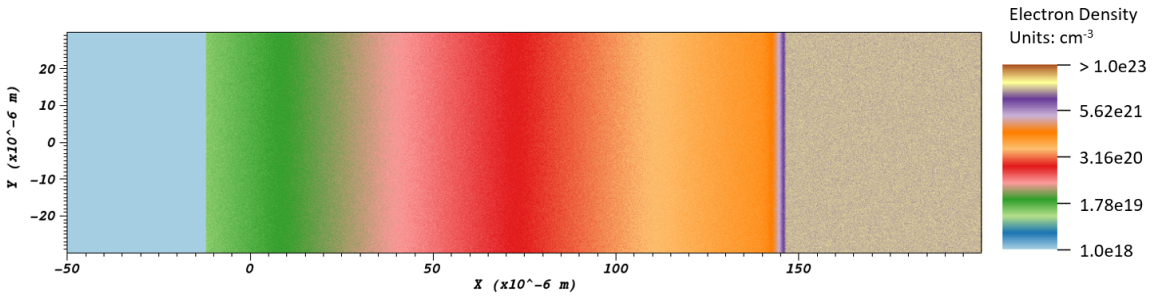

Figure 5.9: Initial simulation box with pre-plasma density profile for 2D simulations plotted by VisIt. Density profile is truncated 160 µm from the target surface to give a region for plasma to expand to and to keep file sizes reasonable while keeping relevant pre-plasma effects.

the outputs from the simulation in 2D is to use the data visualization and plotting software called VisIt. VisIt provides the ability to open and overlay data from several different input source files while correlating them by timestep. Using this to visualize the particle tracking, density and field outputs a clear qualitative picture can be made of what happens in the simulation over time.

When plotting the 150 fs results a few things are readily apparent. First a large degree of self focusing occurs in the pre-plasma, condensing the energy of the beam into a higher intensity spot. Second, when looking at the locations of high energy electrons (those plotted have a $\gamma > 100MeV$) most of the energy gained occurs very close to the critical surface. These electrons appear to also travel just behind the front of the laser pulse before the beam hits the target. These electrons are sent into the target when the beam hits critical density and are injected completely isotropically.

The position and timing of the electrons in this shortest pulse case scenario seem to imply they gain energy by $\mathbf{J} \times \mathbf{B}$ acceleration and vacuum heating rather than the pre-plasma mechanisms outlined in chapter 2. The difference between the case with pre-plasma and without is that the pre-plasma allows the incident beam to self-focus heavily, increasing its intensity. The radius of the beam after self focusing

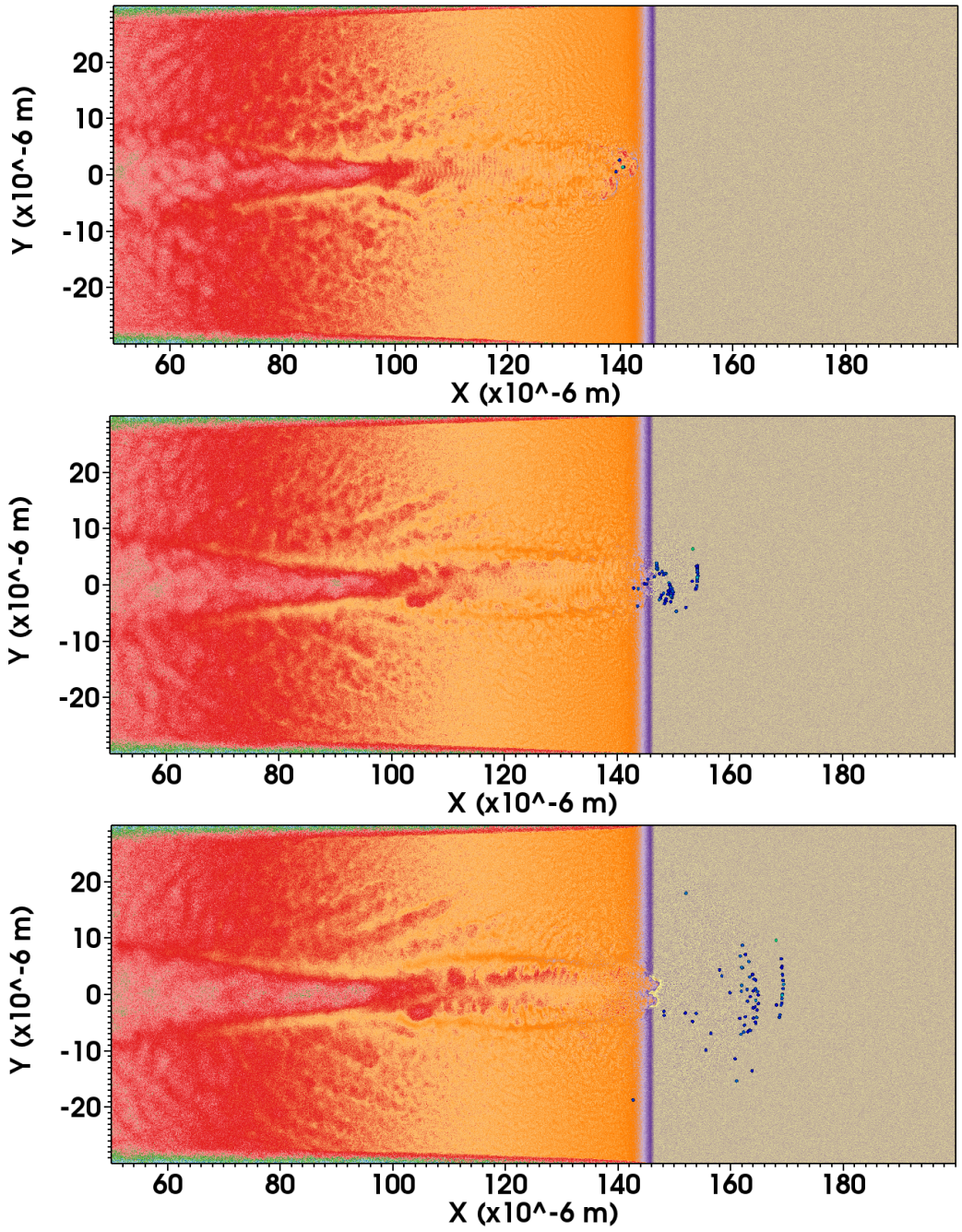

Figure 5.10: Density profile plot over 3 time snapshots with 50 fs between each image. The plotted circles represent electrons with energy greater than 100 MeV. The first sign of these electrons can be seen very close or at the critical density. The beam is filamented into 2 smaller beamlets, when each beamlet impacts the critical surface they generate a batch of high energy electrons isotropically.

appears to decrease by a nearly a factor of 2, increasing the theoretical maximum energy gain for $\mathbf{J}\times\mathbf{B}$ electrons to nearly 200 MeV. However, the conditions required to take advantage of this self focusing are not long lasting and are immediately disrupted when the target surface is distorted. Since these electrons are only generated near the start of the laser pulse it is unlikely that increasing the pulse length would simply increase the number of these initial electrons. Another mechanism must be the source for the super-ponderomotive electron numbers measured for longer pulse lengths.

Plotting 450 fs simulation at similar times confirms this. An initial isotropic blast of electrons is generated at the start of the laser pulse, however in addition a few electrons with over 100 MeV energy are seen far away from the target. As time progresses the number of electrons that stream from this position far away from the target surface increases dramatically. These electrons are clearly accelerated starting at around 50 µm from the target surface and only pick up slightly more energy as the progress towards the target. This heating effect matches the description of direct laser accleration (DLA) electron heating outlined in sections 2.9.3 and 2.10. The electrons that are accelerated are clearly channeled by electrostatic fields that develop from the laser pushing aside electrons when traveling through the pre-plasma and magnetic fields from the hot electron current itself. The trajectory of the heated electrons are directly into the target in the laser direction.

It should be noted that while the exact filamentary nature of the incident beam is exactly reproducible in simulations due to their seeded nature, the filaments on an experiment will vary greatly depending on the structure of the pre-plasma generated and the spot quality of the beam. In the images from the 450 fs case two laser beam filaments can be seen impacting the target in two places. The exact filamentation dynamics may change in an actual experiment due on shot to shot variation, however, the general direction that electrons travel as they pass through this region and the

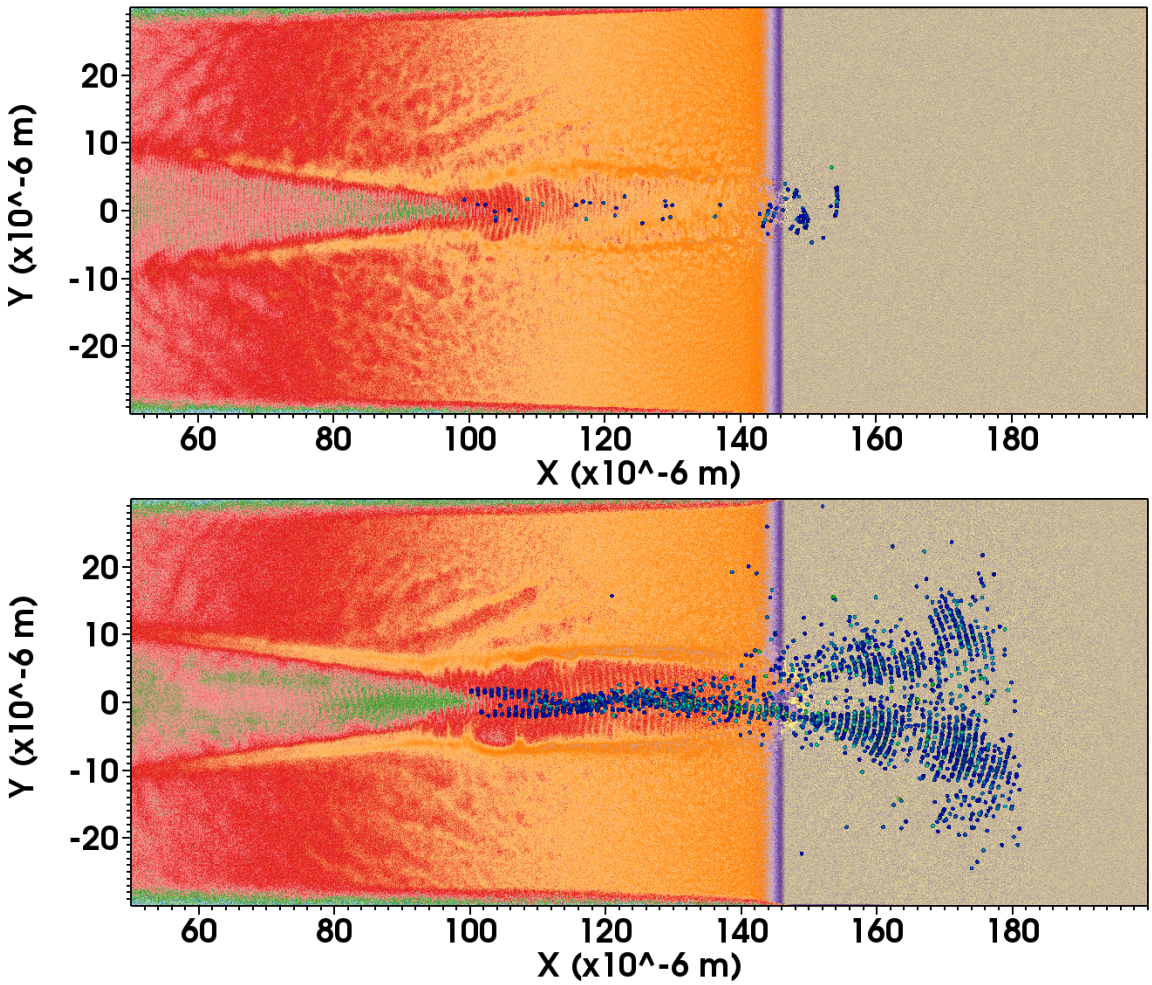

Figure 5.11: 2D EPOCH 450 fs plots with the first image taken at the same time where the second image was taken in the 150 fs plots. It is clear that the original isotropic electrons are still created but new hot electrons are separately heated far from the target surface in the self focused channel. The second image demonstrates that the electrons heated farther back in the channel are the dominant source of super-ponderomotive electrons.

location where they are generated is useful information. Electrons are accelerated up to energies over 100 MeV far away from the target surface and travel along the laser direction straight towards and through the target.

Extending the pulse length to 600 fs changes electron transport once again; streaming electrons accelerated by DLA **later** in time, after 450 fs, are deflected

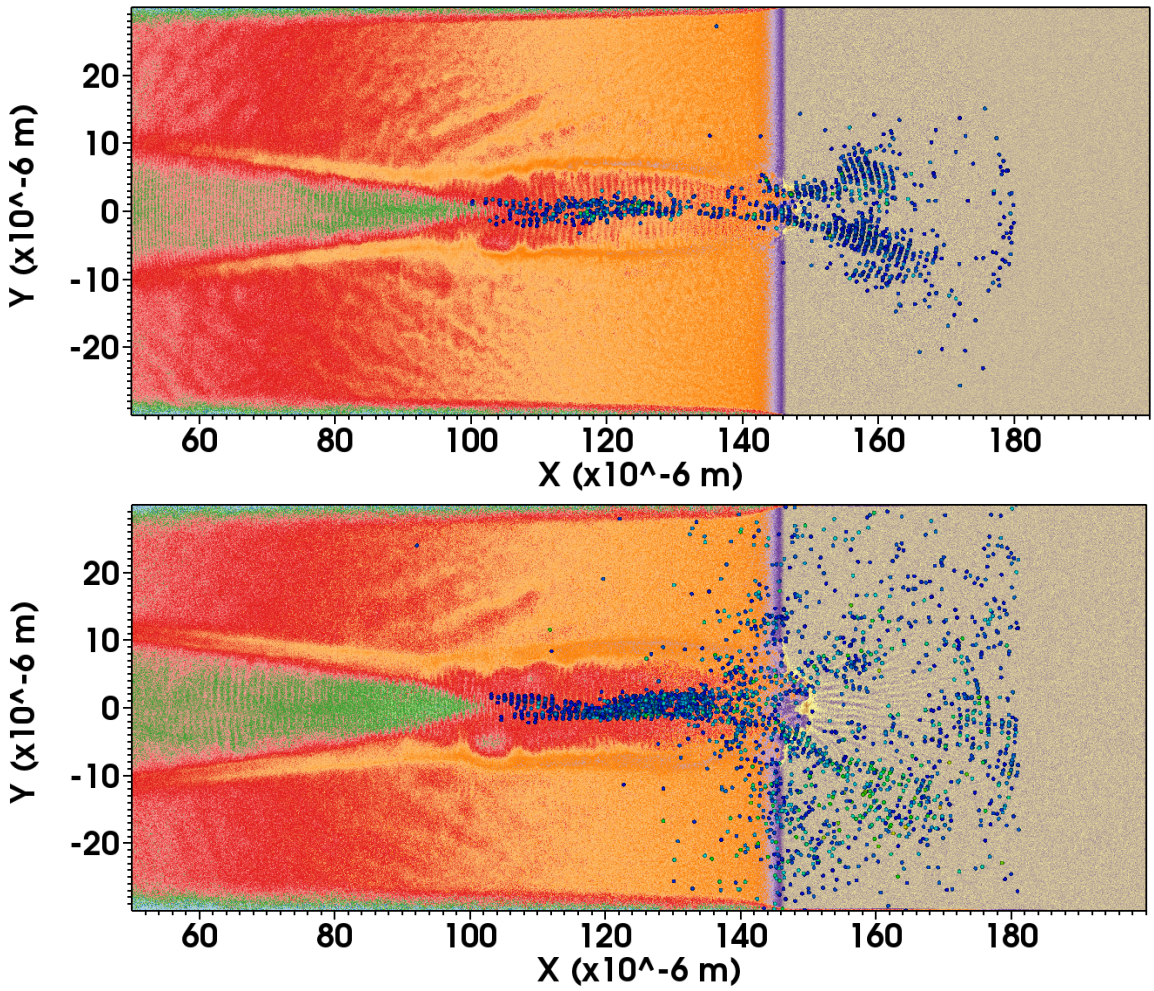

Figure 5.12: 2D EPOCH results for 600 fs, demonstrating the severe deflection of electrons that arrive later in time.

severely away from the forward going direction. This explains why there was very little change between the spectrum for the 450 fs and 600 fs simulations when integrating the number of electrons at the extraction plane at 180 µm. Most of the electrons generated in the extra 150 fs of the laser pulse are deflected so far off course they leave the simulation box before encountering the extraction plane. These electrons would also never be measured on our EPPS diagnostic on experiment.

To help understand the deflection of late timed electrons, field output files are used to construct images of where electromagnetic forces are greatest. First, when

examining the electric field in the y direction (in the polarization direction of the laser) distinct traces of the reflected wave from the target can be seen in the reflection direction. The reflected field is nowhere near as strong as the field of the incident beam but likely could play some role with accelerating electrons via stochastic heating [30]. Using the field output files a map can be created of the Lorentz force encountered by an electron of a given energy in the regions of interest. Electrons traveling towards the target are channeled in the lower density region due to a combination of electrostatic fields created by the beam pushing large quantities of electrons aside as it propagates through the underdense pre-plasma, and a large magnetic field that develops from the large quantities of electrons traveling towards the target. These different components of the Lorentz force, can be visualized by including or excluding the electric field term. Upon reaching the target surface, the Lorentz force on electrons the target surface reverses. The strength the fields creating the reversed Lorentz force appear to increase strongly in time, both in magnitude and in distance. When comparing the strengths of the Lorentz force with and without the magnetic field it is clear that the magnetic field is the dominant effect near the target surface.

The magnetic field that reverses the channeling Lorentz force from the incident beam is somewhat consistent with $\nabla N \times \nabla T$ field orientations. For the upper regions where y > 0, $\nabla N \times \nabla T$ fields are oriented out of the page in the positive z direction. An electron interacting with such fields would be deflected in the positive y direction which is shown in the plots of the Lorentz force. The shape of the magnetic fields generated are not quite consistent with characteristic $\nabla N \times \nabla T$ fields, which usually extend along the target surface in a triangular manner. Another explanation for the creation of such fields would be the development of a large return current opposing the incident electron current. Electrons can be potentially accelerated by the reflected beam away from the surface of the target. As the pulse length increases, the force in

the opposite direction increases and extends further away from the target surface.

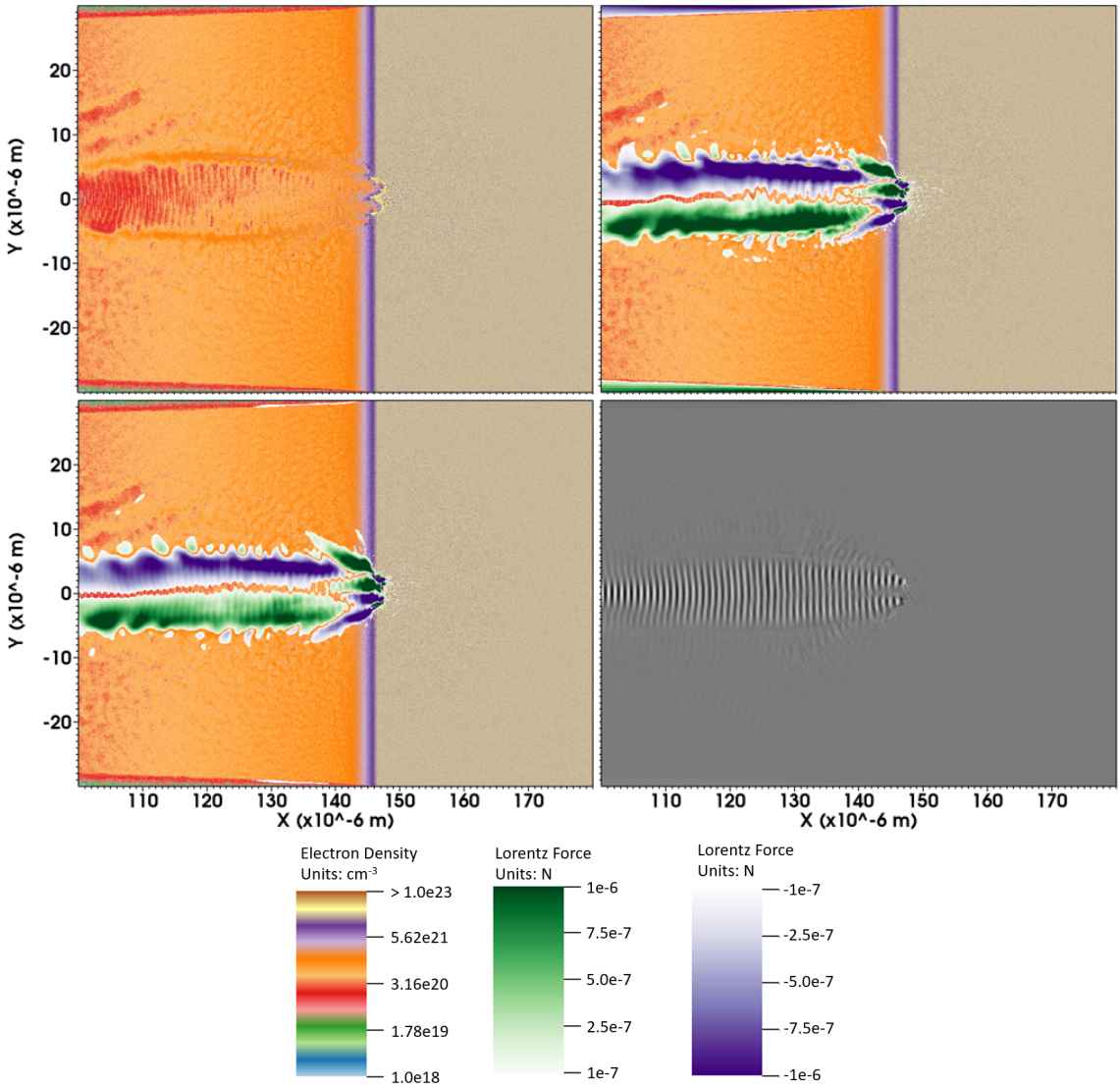

Figure 5.13: 4 different plots taken at the same time step in the 600 fs simulation. Top left: Electron density profile output showing the excavation of a pre-plasma channel by the incident beam. Top right: Density map with the total Lorentz force in the y direction. Force in the positive direction (upwards) is represented by purple and the negative direction is represented by green. Bottom left: Density map with the magnetic Lorentz force only with the same scale. Bottom right: electric field in the y direction which captures the incident and reflected waves.

The overall result from this deflection is curious since it almost directly contradicts the results of the experiment. The simulations showed moving from 450 to

600 fs pulses results in producing nearly the same quantity of super-ponderomotive electrons. In the experiment, super-ponderomotive electrons were not measured in the 450 fs case but simulations predicted that they should be. Super-ponderomotive electrons *were* measured for 600 fs pulses on experiment where simulations predict little difference between the 450 and 600 fs cases. What could account for such a discrepancy between experiment and simulation?

To look for answers, the possible differences between experiments and simulations must be examined. A key difference not accounted for in these simulations, or in previous simulations examining pre-plasma heating, is the effect of the laser incidence angle on the directionality of electrons. To simulate this the density profile is rotated while keeping the incident beam the same. This is achieved by changing the input file to include a density based on rotated coordinates:

$$x_r = (x * cos(\theta_{rot}) - y * sin(\theta_{rot})) \quad y_r = (x * sin(\theta_{rot}) + y * cos(\theta_{rot})$$

The extraction plane probe is defined by a point and a normal vector to the plane. To move and rotate the probe slightly closer to the critical surface to capture more electrons before they leave the simulation box the normal vector was changed to match the rotation of the density profile. The rotation chosen was 22 degrees to match the incidence angle of the laser on the TPW experiment.

When the incidence angle of the beam is changed significant changes in the field structure takes place. The first thing to note in the results from the angled simulations shown in Fig 5.14 is that the initial isotropic batch of electrons and the early electrons accelerated by DLA propagate in the laser direction and not the target normal direction. Second, the magnetic fields that develop near the target surface become extremely asymmetric in time. The opposing magnetic fields in the normal incidence case were completely symmetric and deflected electrons evenly away from the laser propagation direction. In the angled case electrons only see one side of the

field. Electrons accelerated far away from the target and injected along the laser path reach the top side of the magnetic field first due to the angle of the target. The asymmetry and strength of magnetic fields was not previously seen as significant due to the premise that most high energy electrons are generated close to the target surface where the laser meets the critical density. Instead the high energy electrons of interest are generated far away from the surface and are deflected in the positive y direction.

The important message from these 450 fs simulations is that the interaction creates strong deflecting fields at the target surface late in time. These fields disrupt electrons that are accelerated far away from the target, but have a trajectory through the region. While this is occurring, the laser continues to hit the surface and accelerate electrons via $\mathbf{J} \times \mathbf{B}$, vacuum heating and other mechanisms. This can be seen when looking at the location of the laser field as well as when seeing the telltale Weibel instability magnetic fields that are generated at solid density surface (Fig. 5.14). Furthermore, a reverse current is created by the reflecting beam accelerating electrons away from the target surface. This reverse current travels primarily along the reflection direction of the beam and contributes a small magnetic field that also deflects the incoming electrons. In effect the two currents repel each other and the magnetic field between the two counter propagating currents increases substantially. This reflected/reverse current effect has been seen in previous 3D simulations conducted by F. Perez [57].

When the pulse length is extended to 600 fs the electrons created later in time encounter these large fields, which deflect incoming electrons away from the main laser target interaction and in the direction of the target normal. The stream of electrons missing the main region of interaction is important; instead of being deflected in all directions due to the fluctuating fields occurring at the target surface the entire

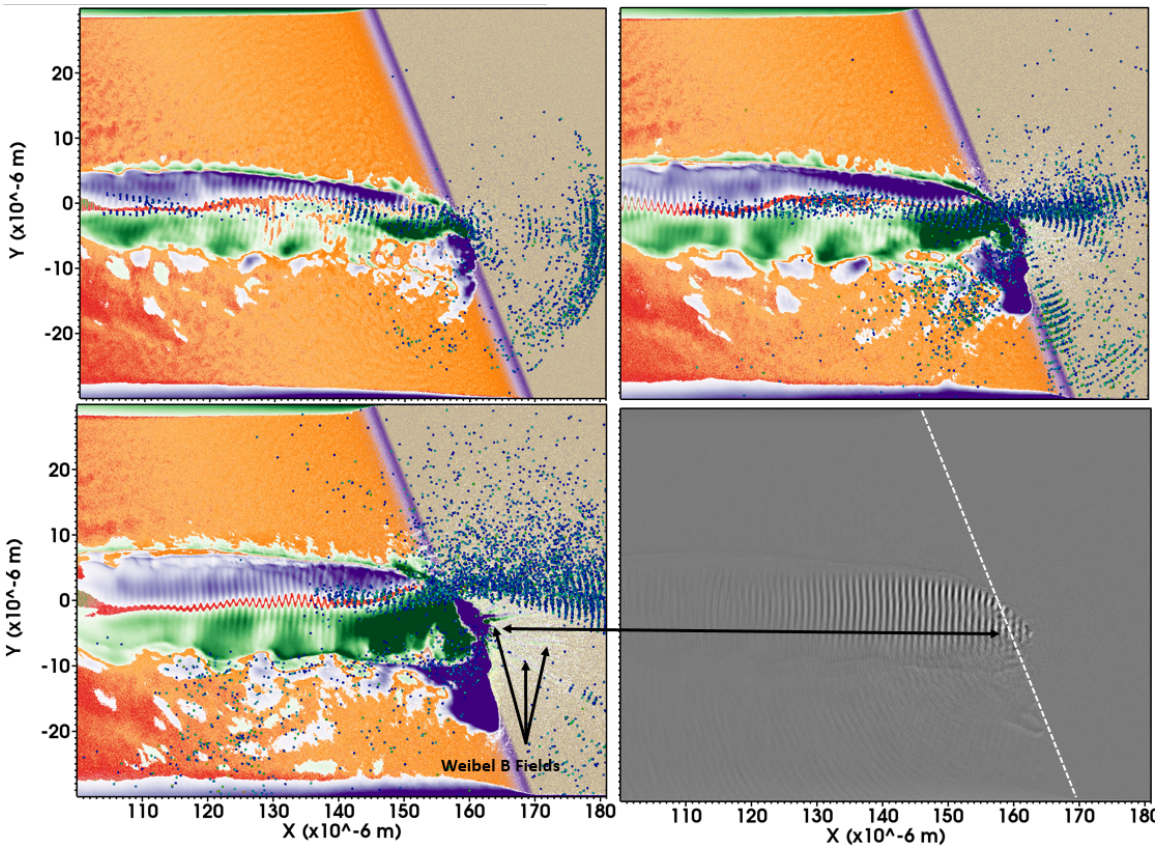

Figure 5.14: 4 plots taken with the 450 fs pulse incident at an angle on the target. The first 3 plots shows electrons with $>$ 100 MeV and the Lorentz force for 3 time steps, each 100 fs apart. Top Left: The initial isotropic blast of electrons propagates forward centered on the laser propagation direction, DLA electrons can be seen further back accelerated as normal. Top Right: DLA electrons most significantly move forward into the target along the direction of laser propagation, not the target normal direction. Electrons are also seen accelerated in the direction of the reflecting beam. Bottom Left: Late DLA electrons begin to be deflected upwards by growing magnetic fields from the laser interacting with the target surface. Bottom Right: Plotting the electric field in the y direction shows the location of the laser's fields as well as the reflected beam. The laser clearly continues to reach the target surface in a different location from where the DLA electrons are deflected.

stream is deflected by one large field and keeps a degree of directionality. This means that in an experiment our diagnostic would see either large quantities of electrons (if the diagnostic is lined up to the electron stream), or almost none at all (if the stream misses the diagnostic).

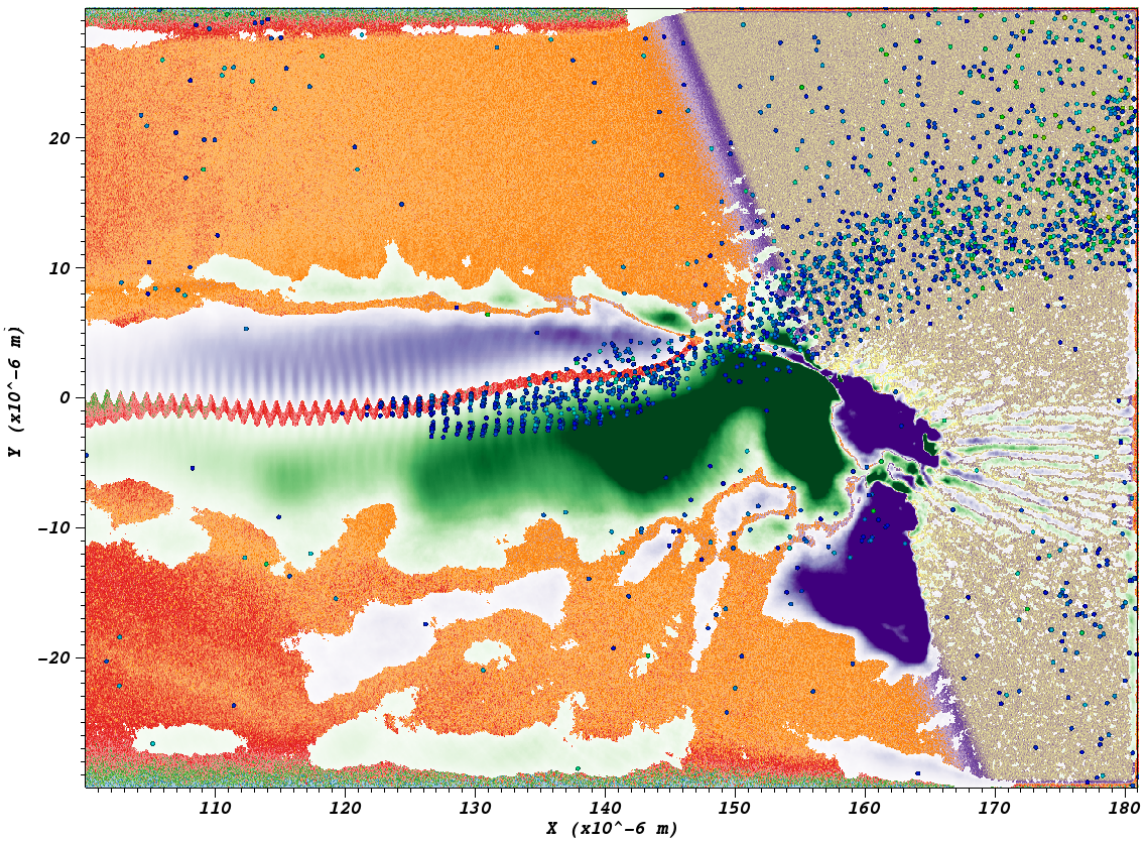

Figure 5.15: Simulation of 600 fs pulse with a snapshot taken later in time. The magnetic field grows large enough to significantly deflect the stream of super-ponderomotive electrons away from the region

When including incidence angle, the simulation results compare much more favorably to the experimental data than the normal incidence cases. To make a comparison to the experimental data, the position of the EPPS, which faces the rear of the target at exactly normal incidence, must be taken into account. This means that electrons that travel along the laser direction will completely miss the diagnostic and not be measured. In the case of ponderomotive scaling electrons this is not a large issue since they tend to spread more isotropically. However, super-ponderomotive electrons are generated far from the target surface and are accelerated via by DLA along the path of the laser in a single direction. The magnetic field is

only established later in time for longer pulse lasers and deflects DLA electrons away from the laser propagation direction. The deflection of such electrons is in the target normal direction and are more likely to be captured by the diagnostic. To show this in the simulation the electron angle is plotted by using their momenta and are color coded to indicate which are closer to being measured.

We can see from the plot that initially electrons have an angle centered 25 or so degrees relative to the target. This makes sense since the incident angle of the beam is 22 degrees and these electrons are accelerated along the laser direction and are not significantly deflected since magnetic fields are not large enough. Later near the tail end of the pulse electrons are deflected and their angles are nearly centered on the direction of the EPPS (represented by 0 degrees). This is a good explanation for the TPW experimental data, which measured no super-ponderomotive electrons at the 450 fs pulse length, but did measure them sporadically for the 600 fs pulse length. It is clear that the regime of 450-600 fs is a transition to a regime where the magnetic field of the laser-target interaction begins to matter.

Another effect verified by experiment is the acceleration of electrons by the reflected wave. As shown in figures 4.15 and 4.16, when pre-plasma was present, hotter electrons were measured in the direction of laser reflection by the second EPPS on the second TPW experiment. In Fig 5.14 the electron beam due to laser reflection is generated very early in time in the pre-plasma over 10 μm from the target surface. In the cases without pre-plasma very few electrons are available to be accelerated by the reflected wave. In the pre-plasma case the reflected wave accelerates electrons and generates fields similar to the incident wave, albeit weaker and in the reverse direction. The simulated data in Fig 5.18 fact shows a much larger disparity between measurements with and without pre-plasma than what was seen on experiment. It is therefore likely that the level of intrinsic pre-plasma in our “no pre-plasma” case on

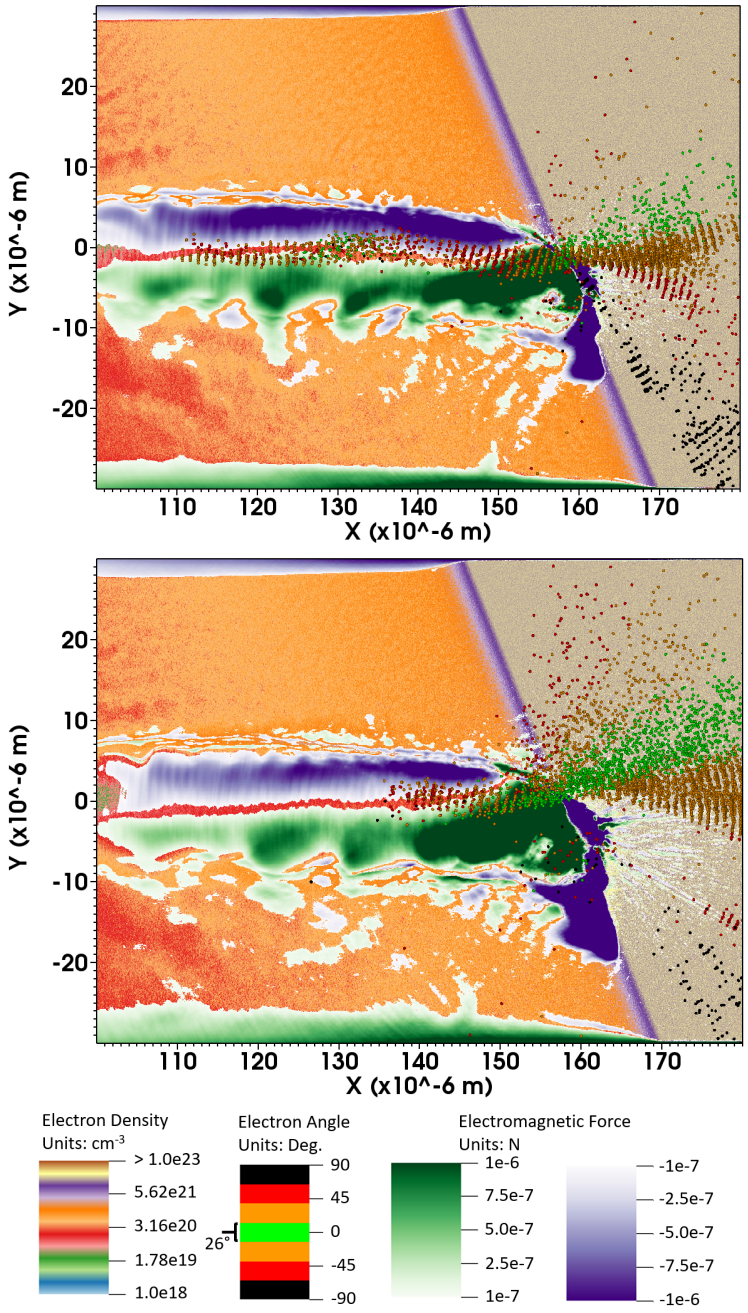

Figure 5.16: Electron ejection angles near the beginning (top) of a 600 fs pulse and near the end (bot). Electron color denotes the angle of the electrons within a +/- 12 degree window adjusted for the target angle. Electrons in green are traveling with the general angle that is measured by the EPPS while the others are outside.

experiment is higher than advertised.

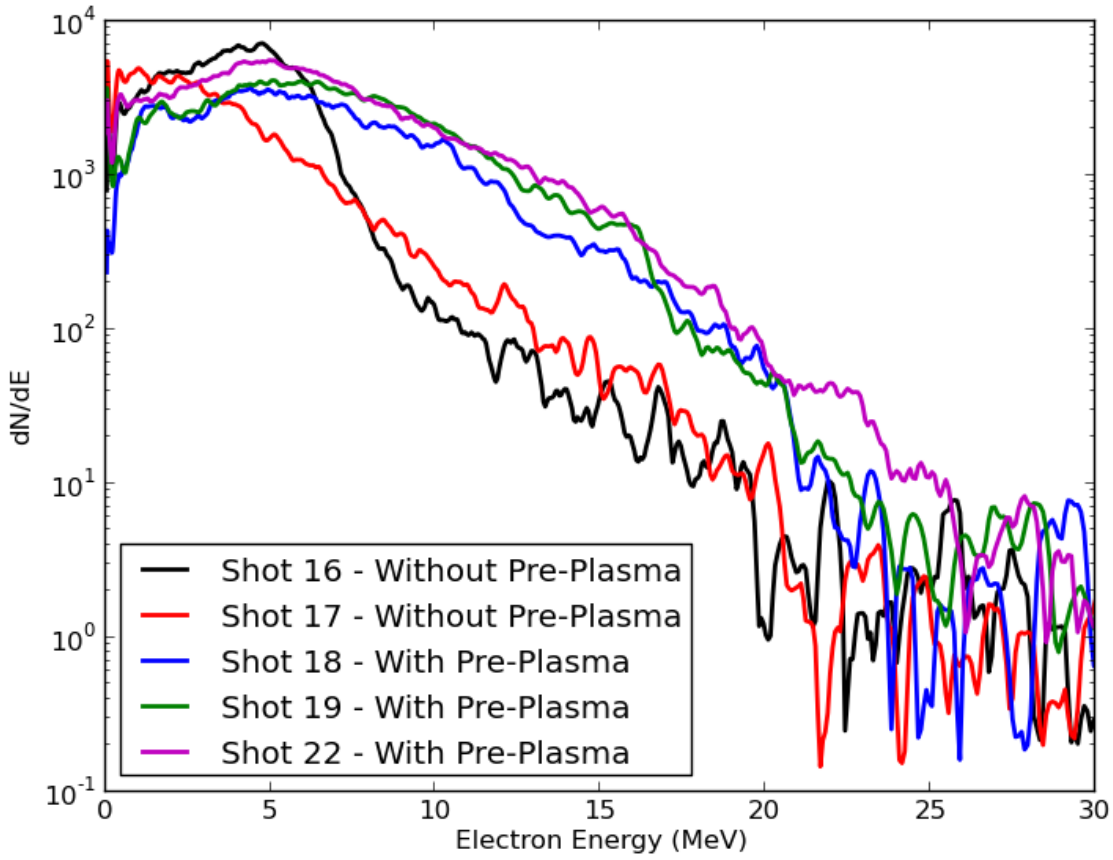

Figure 5.17: Data from the EPPS facing the laser reflection direction. Differences between cases with and without pre-plasma are clear and consistent with nearly an order of magnitude increase in electrons with energy $>$ 10 MeV.

Now that there is confidence that magnetic field deflection of DLA heated electrons is the source of these experimental results, simulations can be performed to look at how changes to various parameters could change the outcome. Since most laser systems of very high intensity do not allow for normal beam incidence on target these could help inform future experiments that wish to use such platforms. Parameters that could likely change between experiments are intensity, overall spot size, amount of pre-plasma and laser incidence angle. Simulations were conducted for each of these while holding the others constant with the 600 fs angled beam full pre-plasma used

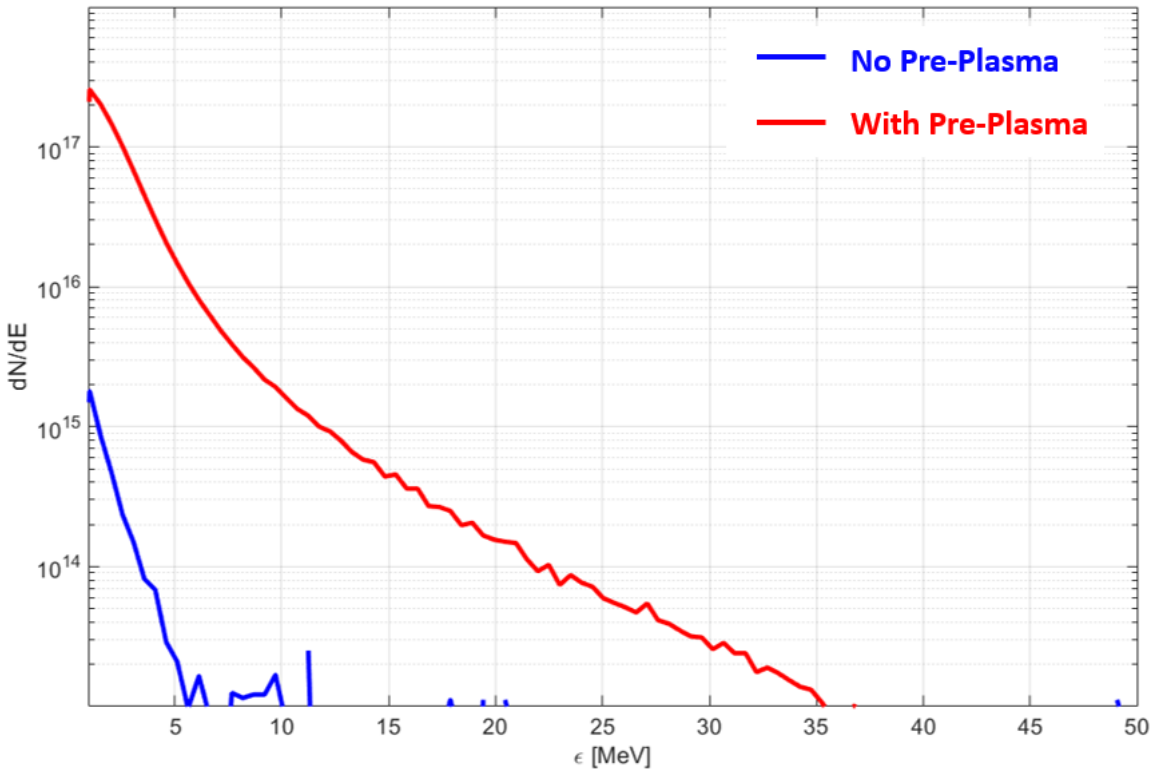

Figure 5.18: Extraction plane outputs in front of the target measuring electrons traveling away from the target. Very few electrons are measured with significant energy in the reverse direction for the no pre-plasma case.

as a guideline.

Changes in spot size resulted in a large change in laser pre-plasma interaction far away from the target surface. A larger spot resulted in a much larger degree of filamentation of the beam prior to reaching critical density. However these filaments appear to push the underdense plasma in a straightforward way, all impacting the target along the same trajectory. These multiple filaments interact with the target surface and coalesce into one large beam quickly. The fields generated in such a case are larger due to the fact that the same intensity is spread over a larger spot. In essence there is more energy in the beam to generate electrons and fields since intensity and duration have been held constant. These electrons behave much like

they do in the small spot case. DLA electrons early in time travel along the beam trajectory, while later electrons are heavily deflected by evolving magnetic fields. This effect in combination with a lower intensity will be expanded upon in simulations of longer pulses.

When reducing the pre-plasma to a lower but still significant level (the second plasma scale length of 30 µm is reduced to 10 µm) a few changes occur. First, very few super-ponderomotive electrons are generated and none originate from the direct laser acceleration region. When comparing to previous results this is understandable since the pre-plasma does not extend significantly in the region where DLA was occurs and it has been shown in previous work that super-ponderomotive electrons scale with pre-plasma scale length [31]. Second, the deflecting fields appear to be just as strong, if not stronger than in the original case. However, no super-ponderomotive electrons are produced far from the target surface, and these strong fields have no electrons to deflect.

The final simulation examined a reduction in incidence angle from 22 to 10 degrees. This produced an extremely surprising result: the electron deflection angle significantly increased to the point where electrons were deflected backwards and perpendicular to the target surface. The area where the magnetic deflection field is significant is not much larger than in the 22 degree case. Rather, the magnitude of the magnetic field in the location of interest has spiked and its position has changed. Since ∇N and ∇T do not change significantly with a 10 degree change of incidence angle the change in electron deflection cannot be attributed to the change in this magnetic field. Instead, the dominant component of the deflecting field comes from the reflecting current. This current, which propagates in the opposite direction to the incident current generates an opposing field which is displaced due to the incidence angle. This displacement causes the opposing fields to overlap constructively rather

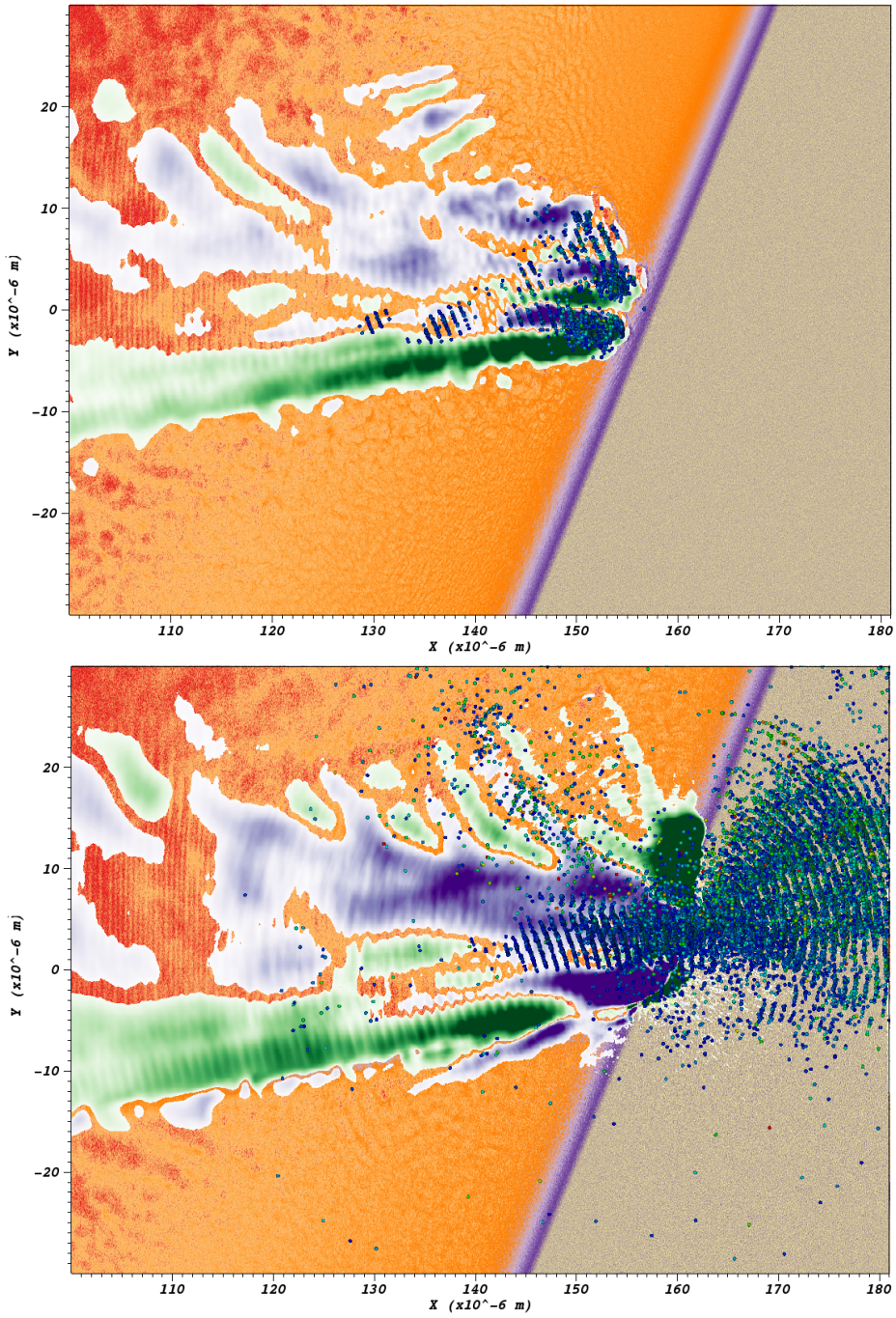

Figure 5.19: Large spot size simulations showing many more electrons, though similar dynamics to the small spot size case. Early in time many filaments can be seen with 3 parallel filaments heading towards the main target.

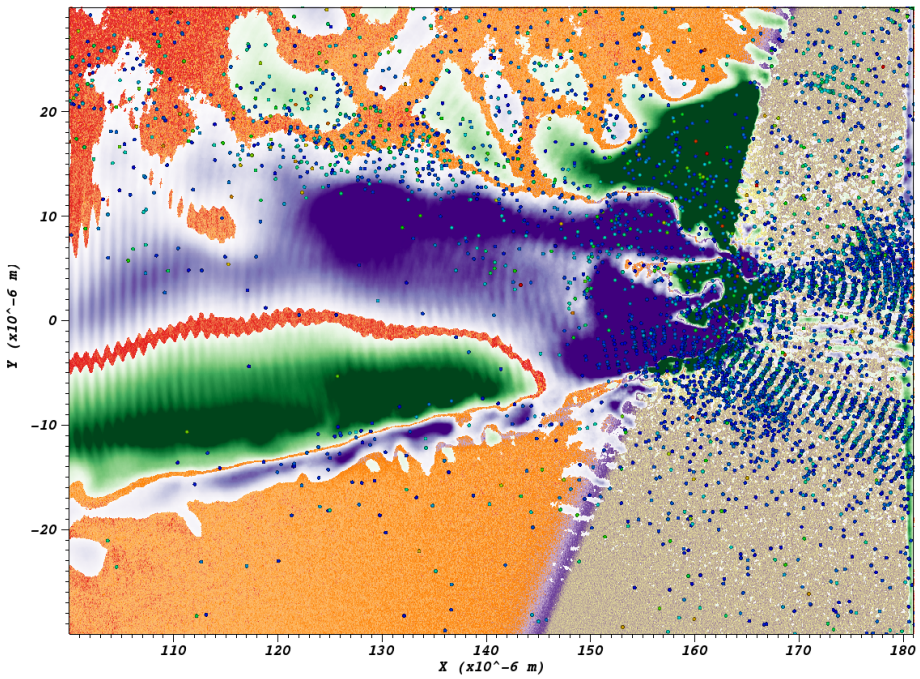

Figure 5.20: Large spot size simulations indicating magnetic field deflection demonstrate that super-ponderomotive electron deflection via magnetic field still occurs similar to the smaller spot size case.

than destructively as seen in the normal incidence case. As the beam approaches normal incidence the reflecting beam size decreases, increasing its effective intensity and condensing the region where electrons are accelerated away from the target. This can be seen by plotting the current for electrons by using their momenta and weight outputs and color coding it by forward or backwards going electrons. A significantly higher reverse current is seen in the small angle case. The end result is an addition deflection based on two opposite currents repelling each other. This effect has a high drop off as the incidence angle increases due to the fact that the reverse current becomes more spread out and is further away from the incident current.

This small angle simulation raises a very important question: what is the primary driver for the large deflection of DLA electrons? Several previous journal articles have attributed the development of a large magnetic field to the Biermann Battery or

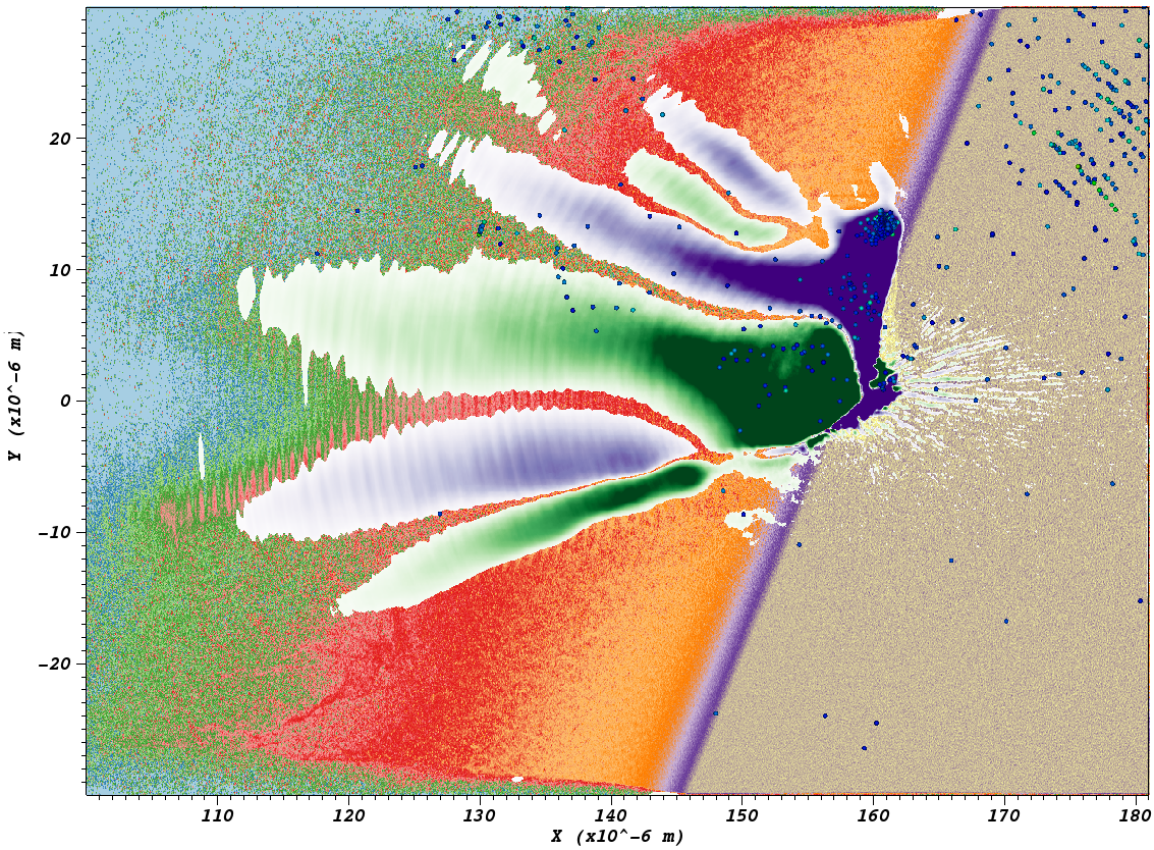

Figure 5.21: Reduced pre-plasma simulation. Almost no super-ponderomotive electrons are registered in the simulation though deflection fields are still significant.

$\nabla N \times \nabla T$ mechanism. In particular M. Borgehsi et al. [55] used Faraday rotation to demonstrate the development of such fields experimentally. Work performed by W. Schumaker [56] also experimentally showed with gas jets the development time of such fields. Each of these attribute the creation of such fields to the Biermann Battery, though do not necessarily show that this is the exact mechanism which generates the strong magnetic fields. F. Perez et al. [57] used 3D PIC simulations to demonstrate that under experimental conditions similar to those on TPW, the reflecting current generates a large magnetic field in the deflecting direction. The two simulations using 10 and 22 degree incidence angles helps shed some light on which mechanisms are dominant in terms of electron deflection.

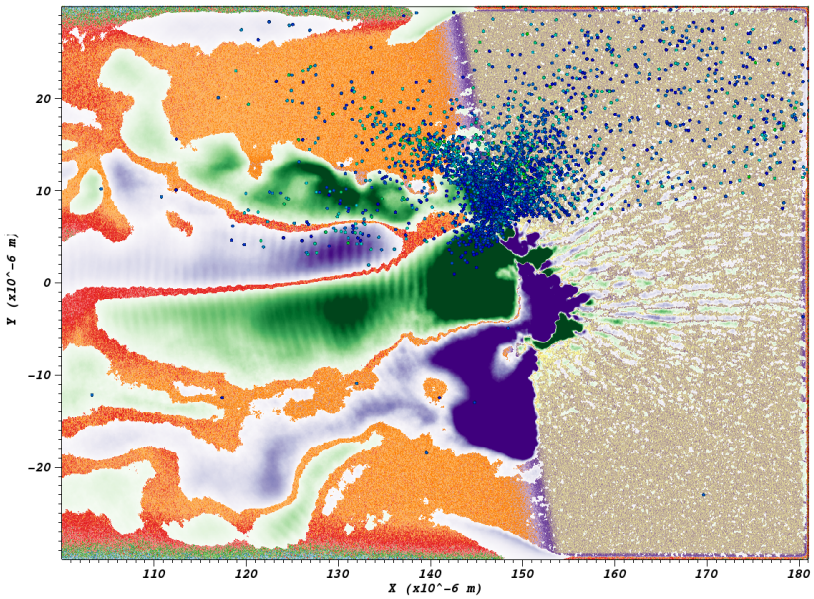

Figure 5.22: Electron trajectories for the small angle case show more severe deflection in the positive y direction for smaller incidence angles. Many electrons are deflected so severely they never enter the target.

To better understand the currents generating the most significant magnetic fields, the absolute value of current density is plotted rather than a directional one. These are overlayed with contours of the magnetic fields shown in previous graphs. The electric field due to charge separation is clearly insignificant compared to the magnetic field in terms of electron deflection and is not included. In the small incidence angle case (shown in Fig 5.24) it is possible to distinguish the different magnetic field components prior to significant electron deflection. The Biermann Battery field is easy to distinguish due to its characteristic triangular shape a position along the target surface, which is a consequence of the density gradient increasing dramatically close to the surface. However inside the region where the beam is interacting with the target the density and temperature gradients are less clear, the fields developing here are the product of the return current from the main interaction.

How do these fields cause such a significant deflection in one direction? Moving

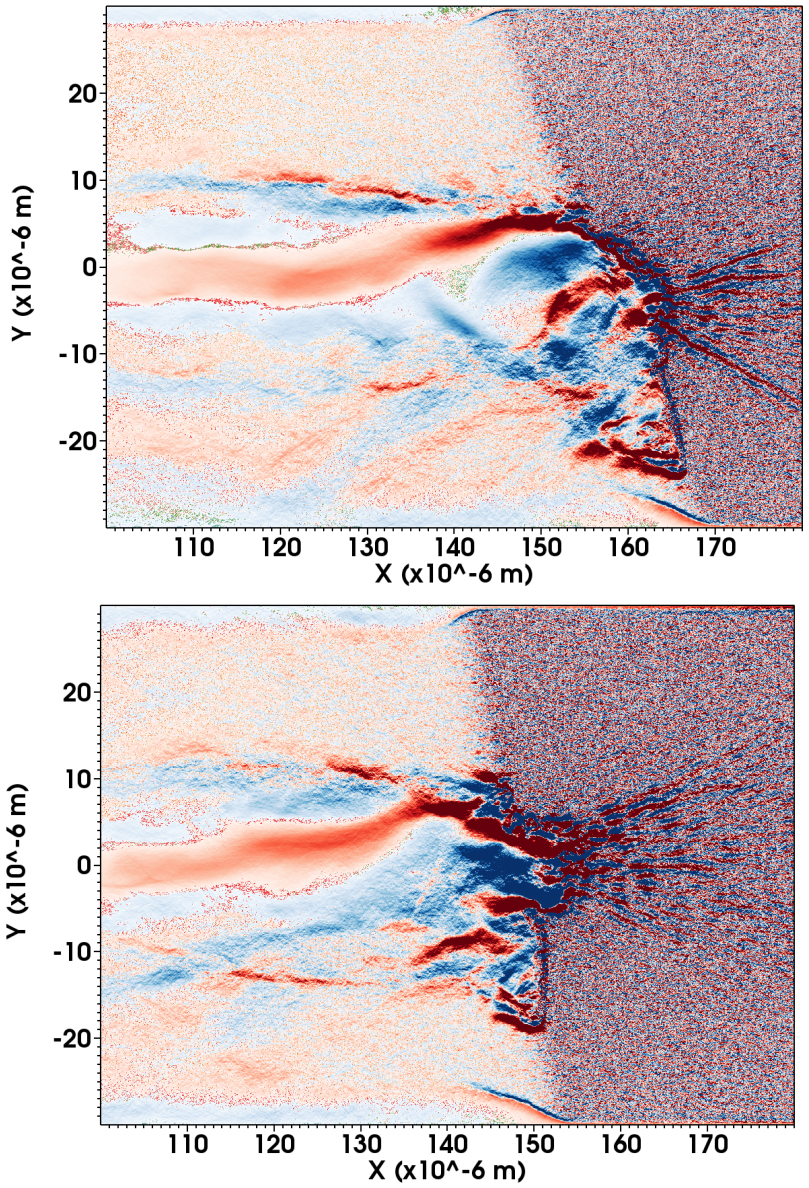

Figure 5.23: Simulation results with a two incidence angles showing current density. The first image shows the large angle case with less severe deflection of electrons. The electrons traveling away from the target (blue) are spread out over a large area. The second image shows the small angle case where the reflected current is more concentrated and travels in close to direct opposition to the beam.

50 fs forward in the simulation (Fig 5.25) it is shown that the positive magnetic fields from the incident and reverse currents join together. DLA electrons traverse this region where the fields join and are severely deflected. Another way to understand

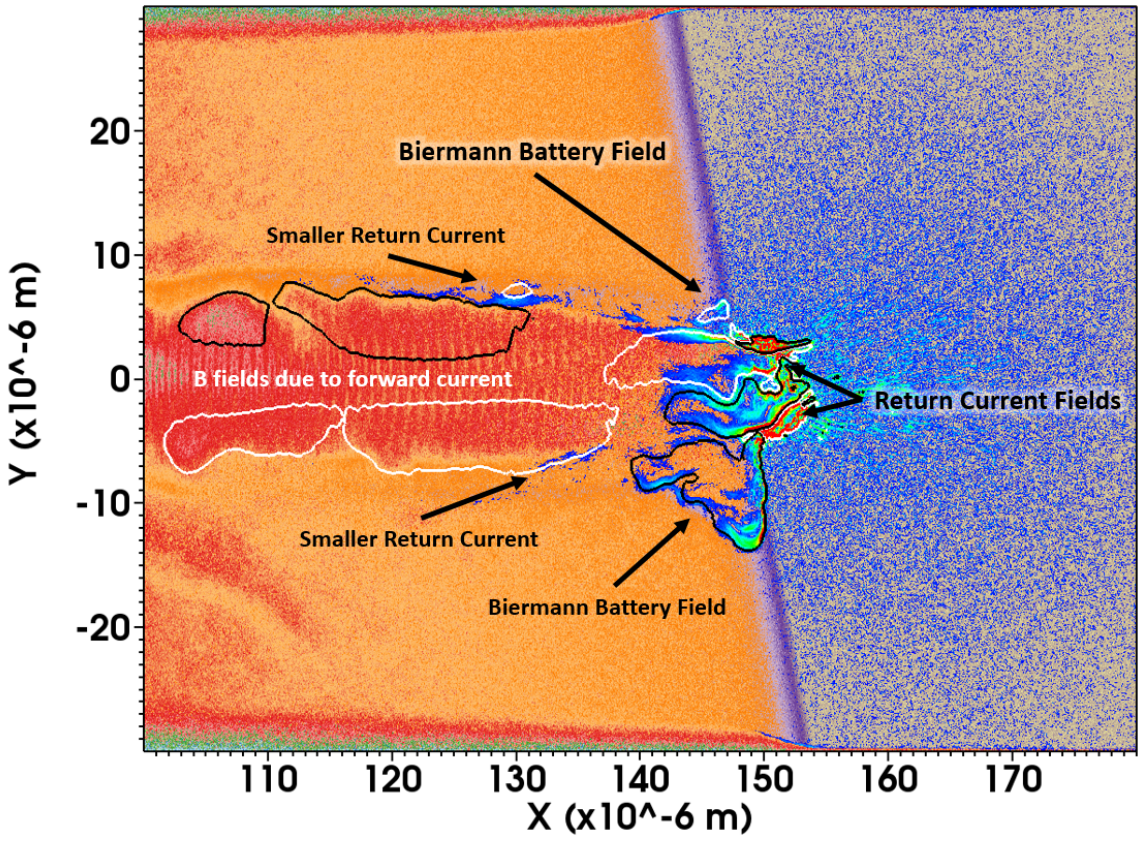

Figure 5.24: Density, absolute value of current density and contours of strong magnetic fields are plotted for the small incidence angle case, just prior to significant electron deflection. Different magnetic field sources can be differentiated due to position and currents in the vicinity. Magnetic fields far from the surface are generated by the forward going electrons. These do not appear in the current density plot as they are spread over a larger area. The asymmetric Biermann Battery fields characterized by their wedge shapes on the sides of the main interaction. These are positioned outside of the region of severe electron deflection. Fields from the return current in the region where the laser impacts the target surface grow, opposing fields from the incident current.

this is to consider it as two counter propagating currents. If the currents head straight at each other they each repel each other to a large degree such as in the small angle case. If the currents are arranged such that they graze each other, the deflection for each is less severe as seen in the large angle case. This preference for deflection degree is determined by the initial angle.

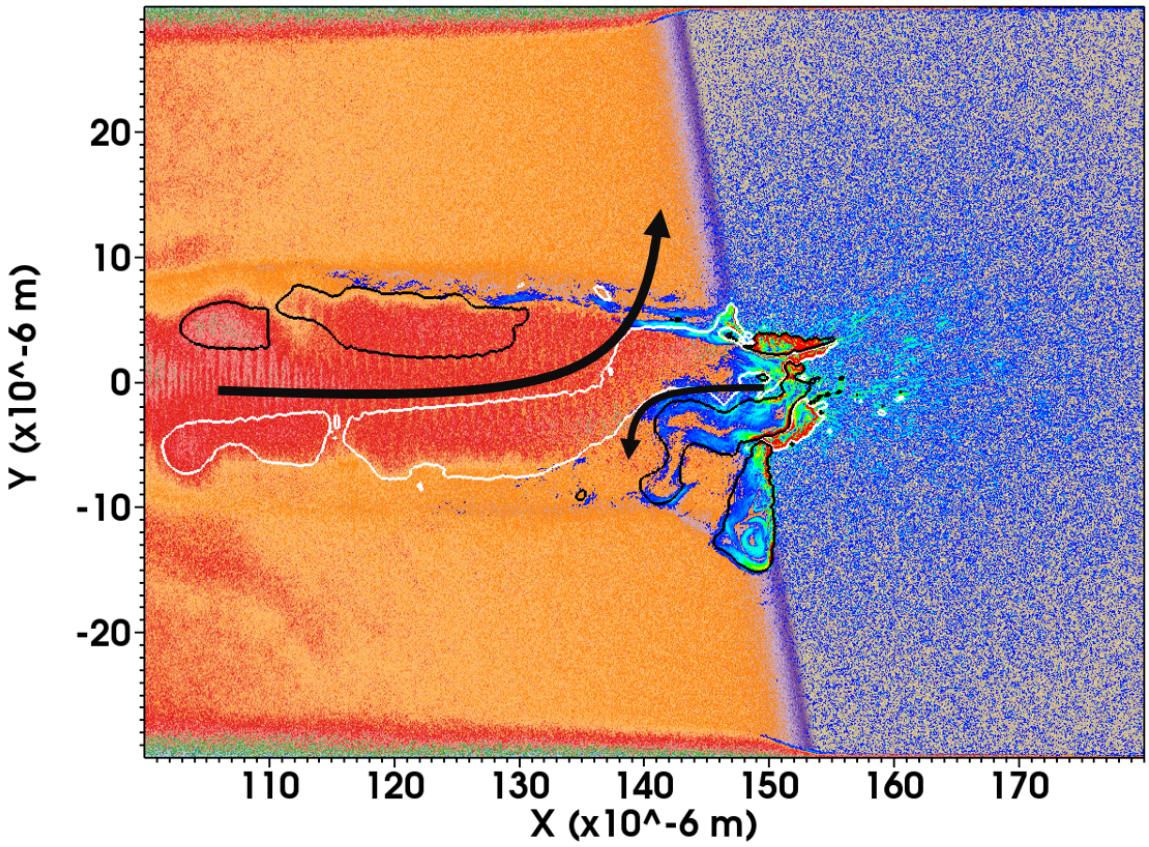

Figure 5.25: Similar plot of fields, density and current taken 50 fs later than the prior image. It is clear that the fields from the return current link with the fields from the incident current forming a kink in the magnetic field. This is the result of two counter-propagating currents interacting with each other nearly straight on.

Does that mean that the Biermann Battery fields has absolutely no impact on the electron deflection? Not quite; the battery fields are in a region far away from where the significant DLA electron deflection takes place. However, the battery fields created do affect the reflected current's trajectory and help keep it close to the incident beam of electrons. As seen in the small angle simulation in figure 5.22, the reflected current is pushed slightly upwards towards the path of incident electrons, away from the direct reflection angle. Lower temperature electrons travel around the Biermann Battery field and exert pressure on the reflected current. Essentially these battery fields collimate and constrain electrons flowing away from the target and help

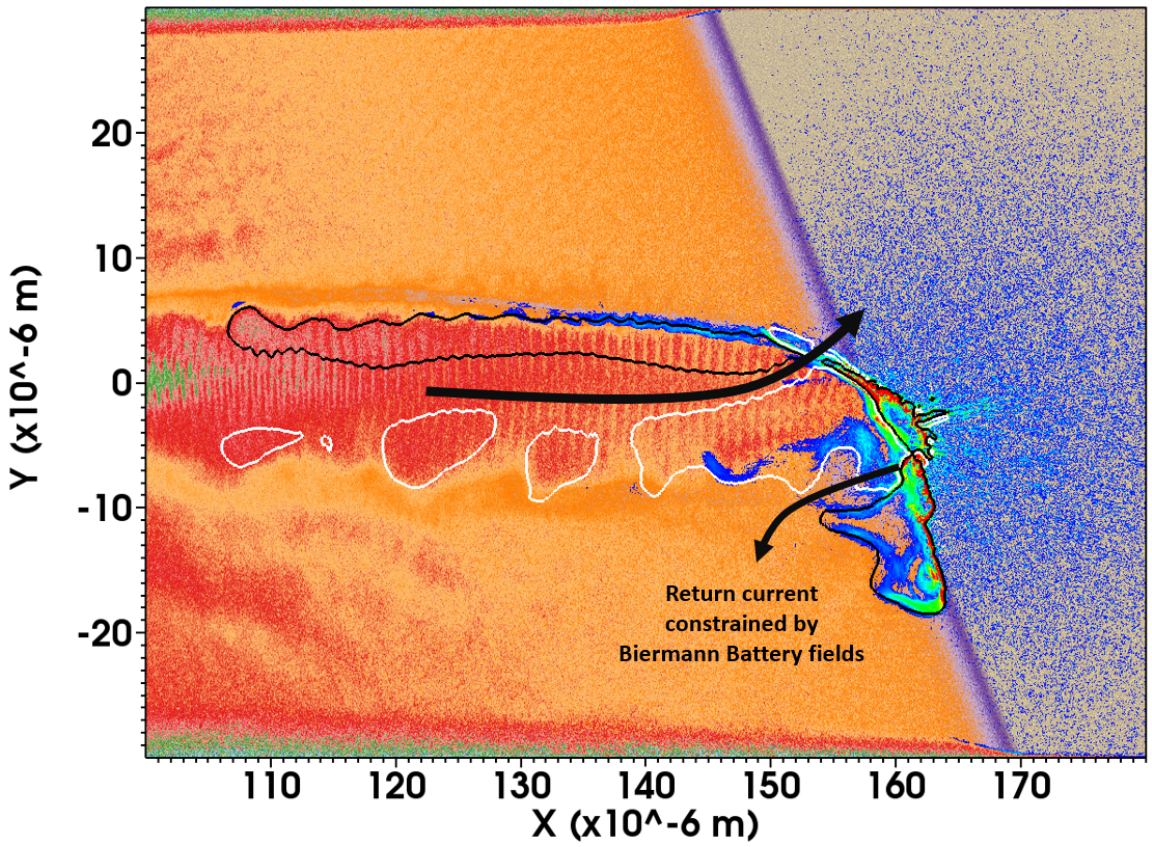

Figure 5.26: Graph of large incidence angle current density and fields; the large angle case helps show the Biermann Battery's effect on the return current. Backwards flowing electrons are held closer to the incoming electrons by the fields close to the target surface. This current diffuses as the Battery field diminishes far away from the target surface.

keep the quantity of backwards traveling electrons concentrated. When the fields of the battery diminish the reflected current becomes more diffuse and deflection of the incident super-ponderomotive electrons decreases. In the case of the large incidence angle shown in figure 5.26, the battery field is displaced from the incident super-ponderomotive electrons, and the reflected current, while still constrained by the battery field is much further away from the incident DLA electrons. The two opposing currents have a glancing interaction rather than a head on crash, leading to a much gentler deflection.

These simulations demonstrate how fickle the magnetic field is based on potential experimental parameters. A different intensity, incidence angle or spot size have varying impact on results. Considering that having a non-normal incidence angle is a requirement on most high power laser systems (in order to prevent severe reflection damage to optics upstream) it is important to consider the effect of magnetic fields at small angles of incidence.

Sections of this chapter are currently being prepared for submission for the publication: "Super-Ponderomotive Electron Generation and Deflection via Self Generated Magnetic Fields", J. Peebles, A. V. Arefiev, S. Zhang, C. McGuffey, J. Park, H. Chen, H.S. McLean, M. Spinks, E.W. Gaul, G. Dyer, B.M. Hegelich, M. Martinez, M. Donovan, T. Ditmire, M. S. Wei, S.I. Krasheninnikov and F.N. Beg, Physical Review Letters (in preparation), (2017). The dissertation author was the primary investigator and author of this material.

Chapter 6
Medium Pulse Length: Titan Laser Experiment

6.1 Titan Experimental Setup

In order to extend the study of pre-plasma electron acceleration to longer pulse lengths an experiment was performed using the Titan laser at Lawrence Livermore National Laboratory, similar to the previous TPW experiment. The Titan laser system features a short pulse beam with a variable pulse length between 700 fs and 10 ps. However, at these pulse lengths the maximum intensity for Titan is much lower than TPW. As such the maximum pulse length was limited to 5 ps in order to maintain an intensity of above 10^{18} W/cm^2. 3 pulse lengths were chosen for this experiment: 0.7, 3.0 and 5.0 ps. While an effort was made to maintain the same intensity for all 3 pulse lengths, energy levels on the laser did not keep pace with the pulse length as well as they did on TPW. This reduction in energy lead to different intensities for each pulse length with approximately $2 \times 10^{19}, 1 \times 10^{19}, 5 \times 10^{18}$ W/cm^2 for each pulse length respectively. The lower intensities of Titan result in the maximum energy of ponderomotive scaling electrons being reduced to around 3.5 MeV. This is much lower than the 50 MeV ponderomotive scaling electrons seen on TPW, and means that EPPS and BMXS will both measure components from the ponderomotive and super-ponderomotive parts of the electron spectrum.

A large change from the TPW experiments at Titan was the capabilities of the long pulse beam, used as a controlled injected pre-pulse. The beam itself has a capability of several hundred joules for up to 20 ns, far more than is required to generate the low density pre-plasma needed for super-ponderomotive electron acceleration. The spot size of the beam was adjusted by placing a 200 µm phase plate

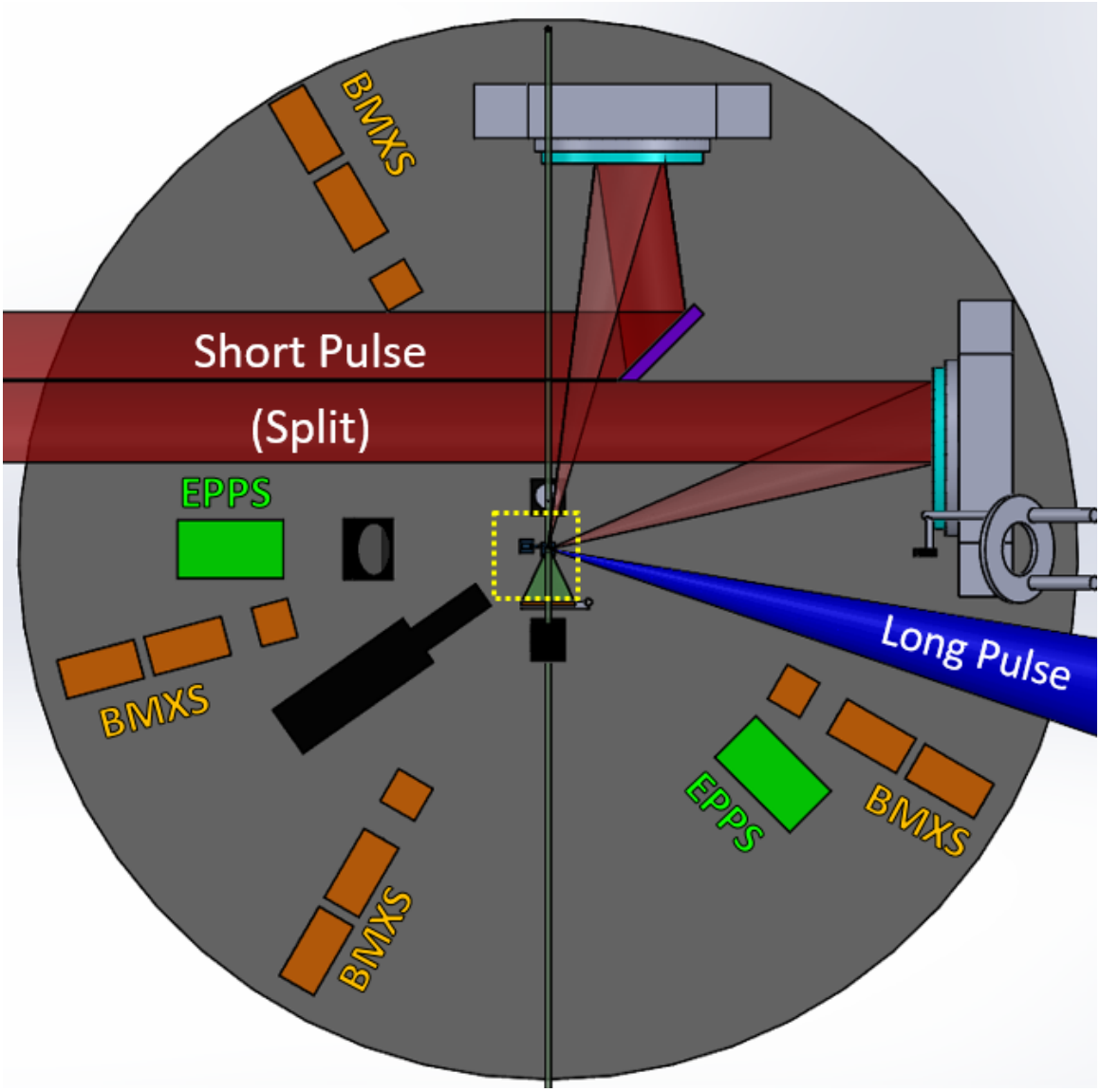

Figure 6.1: Titan chamber experimental layout showing the split short pulse beam along with long pulse beam injection.

in the unfocused beam resulting in a large uniform spot size. The beam energy was adjusted to be much lower than maximum, with a variable energy between 0-150 J. As before, the beam was focused on the same spot as the short pulse, high intensity beam, though unlike at TPW, a secondary parabola was used. The pulse length chosen was 3 ns and was injected 3 ns prior to the short pulse resulting in zero time

delay between the beams.

	Azimuthal Angle (deg)	Polar Angle rel to Target (deg)	Polar Angle rel to Laser (deg)	Distance (cm)	Pixel Size	IP Type
SCI	39 +/-1, 2.7 +/- 0.1	0	-14	29.5 (crystal)	25um	BAS-MS (white)
EPPS1	0	0	-14	43.5	100um	SR (blue)
EPPS2	0	140	126	41.5		
BMXS1	0	-45	-59	85.5	100um	BAS-MS (white)
BMXS2	0	9	-5	86		
BMXS3	0	39	25	86		
BMXS4	0	134	120	85		
RCF	0	90	76	5		

Figure 6.2: Diagnostic positions for the Titan experiment.

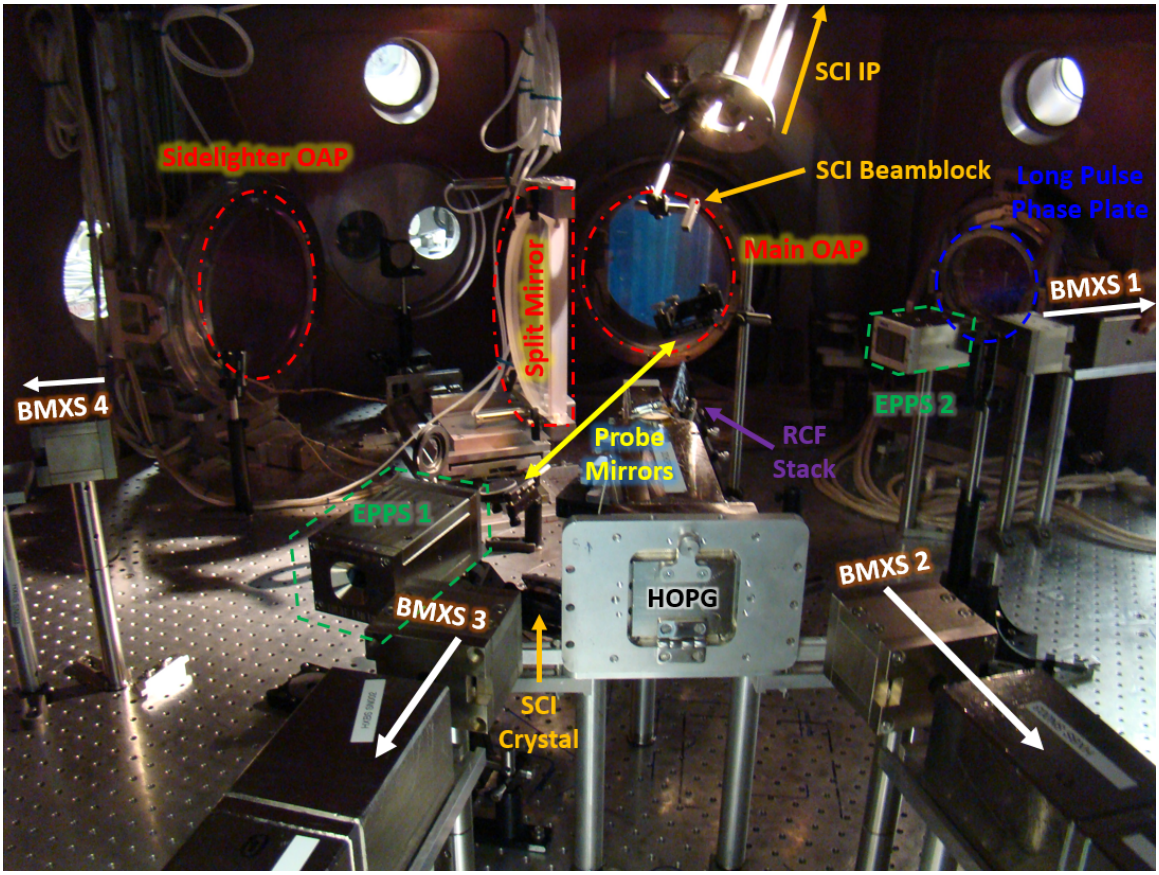

Figure 6.3: Photograph image of Titan chamber with several diagnostics shown.

In addition to the EPPS, BMXS, proton radiography and SCI that were fielded on TPW, new diagnostics such as HOPG and interferometry were implemented on Titan. Implementation of proton radiography on Titan was slightly different than

TPW. Advantage was taken of the ability to split the Titan laser in the laser bay. A hemispherical pick off mirror and secondary parabola were provided and allowed for the accurate and independent alignment of the secondary proton generation beam. These beams were timed via streak camera with timing changed via trombone stage in the laser bay. To use the streak camera a special twin fiber alignment target was constructed with 10 µm wires placed at the locations of the two targets. These wires were coated in a small layer of whiteout, which shines and reflects incident laser light brightly. The OPCPA was sent to the two targets and the bright flashes that resulted were timed via the streak camera to sub picosecond precision. This allowed for much more accurate timing of the radiography beam prior to shooting.

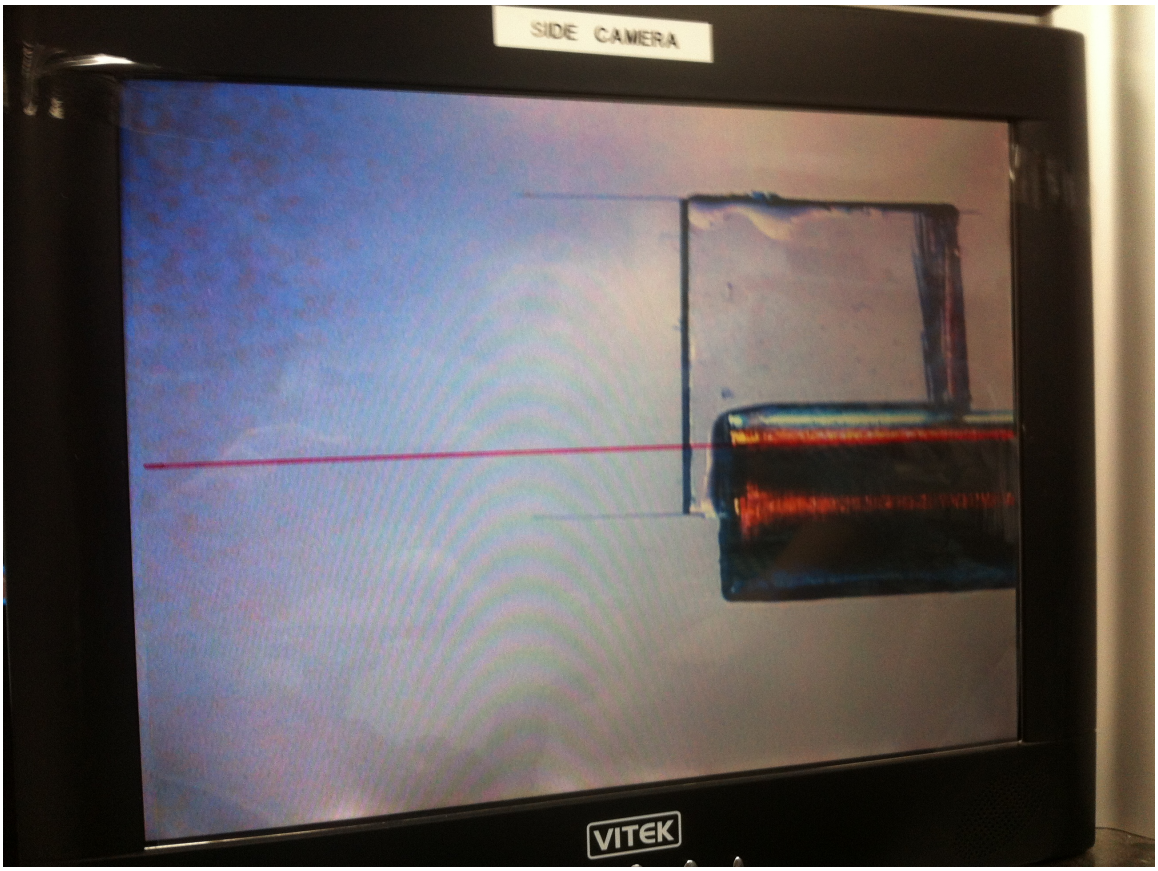

Figure 6.4: Double wire alignment target for sidelighter beam timing and beam alignment.

HOPG (Highly Oriented Pyrolytic Graphite) is a diagnostic named for the HOPG crystal it uses, and is very similar to the SCI in that it uses the Bragg angle to measure K shell x-ray emission. The HOPG sacrifices the spatial resolution of SCI in order to cover an x-ray spectrum much wider than the SCI. The HOPG's primary use is to gauge difference between different spectral lines which can be used to infer target temperature and electron coupling. Unfortunately, on the experiment the introduction of the long pulse injected pre-plasma beam increased the noise on the image plates of the HOPG and the SCI to such an extent that any data became unreadable.

The interferometry capability allowed us to verify the creation of a pre-plasma with the long-pulse beam and gave us the ability to characterize it. Analysis of the interferometry images was performed by P. F. Colleoni and showed good agreement with subsequent 1 and 2D rad-hydro simulations of the pre-plasma density profile. The interferometry capability close to the target is somewhat hampered by the self emission of the target, which is bright enough to overpower the fringes produced by the interferometer probe. Therefore the interferometry probe did not measure pre-plasma densities very close to the target surface. Interferometry was aligned with a vertical angle relative to the target and diagnostic plane in order to not impede the vision of other diagnostics.

6.2 Titan Experimental Results

Titan's EPPS results appear to build directly on TPW's results, despite the intensity of the laser dropping by an order of magnitude. When a long pulse is added the EPPS measures a super-ponderomotive electron component, seen in both the change in spectra shape and spike in HMIE values. For 0.7 ps shots this feature is still inconsistent, however slightly less inconsistent than at TPW. A clear hot electron tail was registered on 3 out of 6 shots with significant long pulse energy. When examining

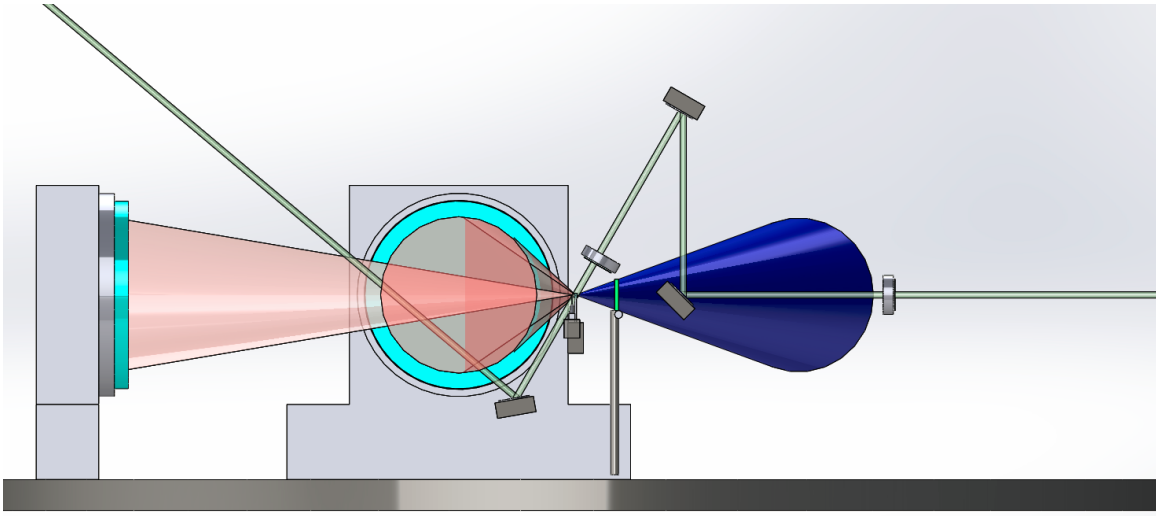

Figure 6.5: Setup for the 2ω probe beam interferometry system. The probe was sent in from above the target at an angle in order to not impede the vision of other diagnostics or beams.

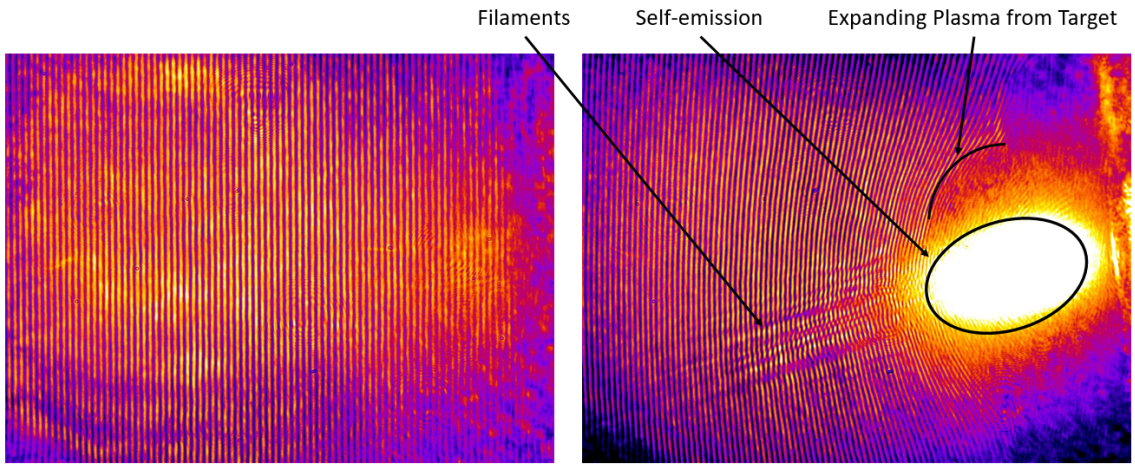

Figure 6.6: Interferometry images with a reference image (left) compared with the image taken on shot (right). Many features can be made out including the filamentation of the beam and the expanding plasma from target surface.

the spectra directly these hot electron tails are extremely clear and help distinguish the differences between ponderomotive and super-ponderomotive electrons. The raw dN/dE spectra also demonstrate the difficulties in using a slope temperature to fit the data when their shape is "humped" rather than sloping. Another difference be-

tween the spectra on the Titan and TPW experiments is that there is no obvious suppression of lower energy electrons when super-ponderomotive electrons are measured. However, this could potentially be a result of the fact that the EPPS is only reliable at measuring electrons with energy greater than 5 MeV, and any suppression of low energy electrons is lost in the noise.

Increasing the pulse length to 3.0 ps, the super-ponderomotive electron component was measured on EPPS nearly 100% of the time. This suggests that the Titan results are following the trend from TPW, but the intensity of the Titan experiment is an order of magnitude lower, and the level of pre-plasma is much higher. The deflections from magnetic fields seen in the previous TPW PIC simulations may not hold for Titan's parameters. Another possibility for the sudden consistency of EPPS results may be that so many more hot electrons are created in every direction for longer pulse lengths that it can be consistently measured, even if significant portions of the electron spectrum are deflected. It is also important to remember that Titan has a significant amount of intrinsic pre-pulse, which helps explain why the EPPS measured some electrons with energy much higher than the maximum ponderomotive scaling energy without the injected pre-plasma. However, the number and energy of these electrons are much lower than in the larger injected pre-plasma cases. This further supports previous simulations that showed super-ponderomotive electron energy scales with level of pre-plasma cite. This conclusion is also supported by the fact that with the exception of one data point, the HMIE value consistently increases as the amount of pre-plasma increases, in the 3.0 ps case.

Because Titan has lower intensity compared to TPW, the BMXS becomes much more useful in this regard. We can see from the EPPS that much of the super-ponderomotive portion electron spectrum is in range to be captured by the BMXS. The BMXS will be able to measure both x-rays generated from both components

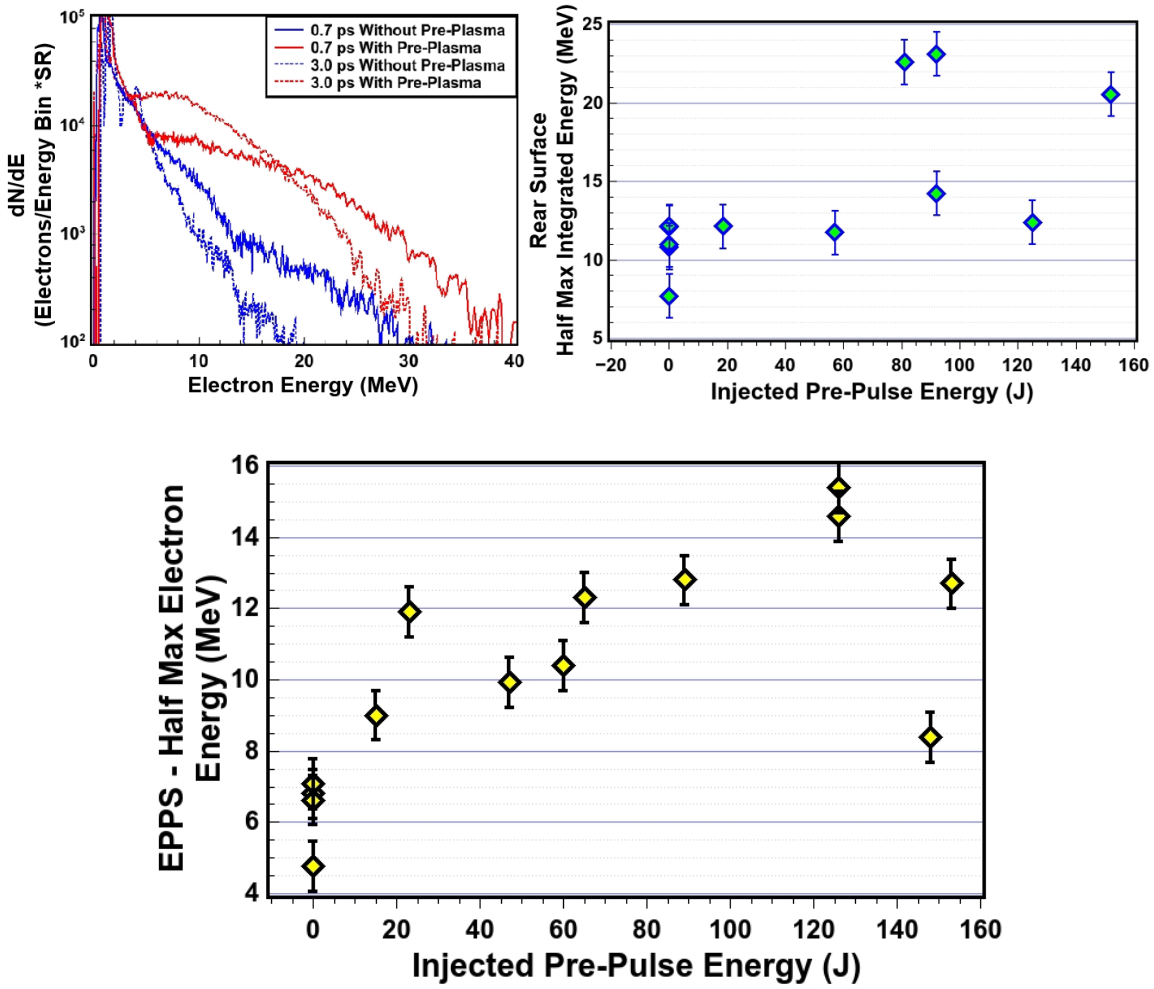

Figure 6.7: Left: Electron spectra from EPPS for 0.7 and 3.0 ps shots with and without pre-plasma. It is clear that the inclusion of injected pre-pulse causes a new secondary component of electrons to arise. The hump that forms from these spectra render slope temperature measurements meaningless as the slope will greatly change depending on where along the spectrum it is measured. Right: HMIE results from EPPS for 0.7 ps shots. We see that similar to TPW at 600 fs, only a fraction of shots measured the hot electron tail. Bottom: HMIE results for 3.0 ps shots. Here the hot electron tail becomes 100% consistent and is measure on all shots with a long pulse.

of the electron spectrum. In order to use the BMXS to gather information from the main interaction, bremsstrahlung from the proton radiography target spraying electrons into the main target must be accounted for. To do this the entire target setup was simulated in ITS from 2 perspectives, the main target and the side lighter

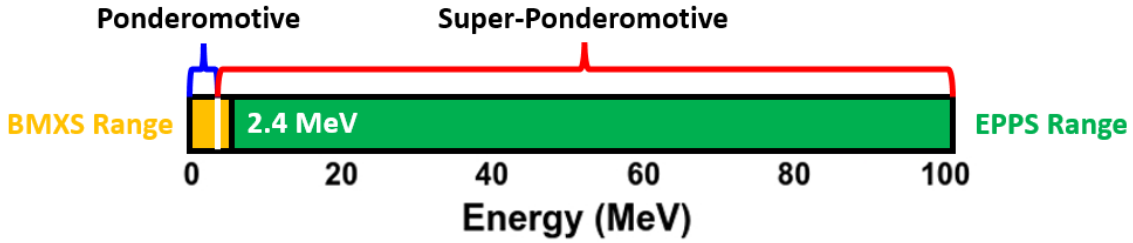

Figure 6.8: Diagnostic energy ranges compared to heating mechanisms for maximum Titan intensities.

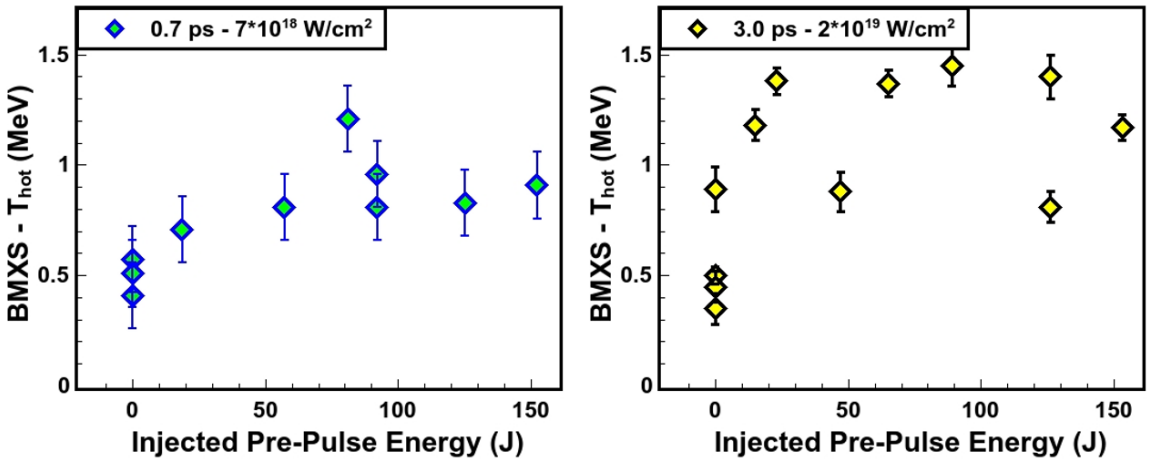

Figure 6.9: Left: BMXS slope temperature for the "hot" component of the 2 temperature spectrum for the main target with 0.7 ps pulse length. Right: The same for the 3.0 ps pulse length.

target. Electron spectra generated for each target had 2 temperature components, with different degrees of electron divergence and conversion efficiencies for each. Two of the BMXSes around the chamber faced primarily towards the back of the main target and less towards the side lighter were used to help distinguish bremsstrahlung generated by electrons from each target. This task was made easier through the use of reference shots, which included measurements of BMXS signal with the sidelighter beam only and the main beam only. These references showed that signal on the higher energy channels of BMXS 2 and BMXS 3 were dominated by the main interaction. Using these channels to constrain one of the temperature components of the main

interaction helped reduce the complexity of the fitting routine described in Section 3.2.4.

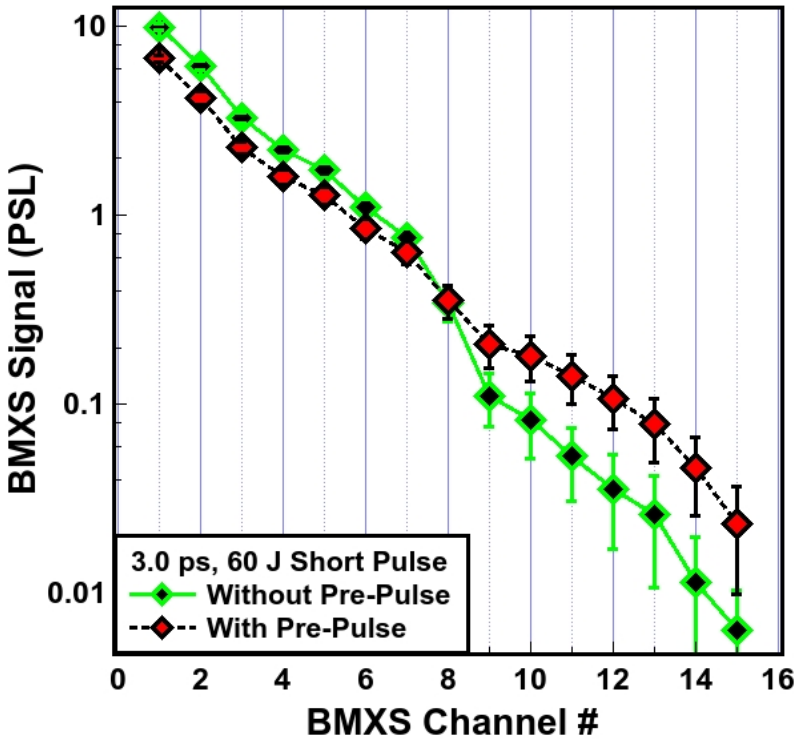

Figure 6.10: Raw PSL values for all 15 channels compared between a shot with and without pre-plasma. The injected pre-plasma decreased x-ray signal for low energy channels (1-7) while increasing x-ray signal for the high energy ones (9-15)

It is clear that even in the 0.7 ps case there is a notable increase in inferred slope temperature of the hotter temperature electron component. In every shot with a long pulse beam a hotter spectrum is measured by the BMXS. In terms of raw data this translated to an increase in signal for the higher energy channels. This increase was also met by a decrease in signal for the lower energy x-ray channels. This suggests that in the 0.7 ps case that the hot electron tail is actually consistently generated. The consistency of the BMXS data suggests that hotter electrons are generated every shot with injected pre-plasma, but are missed by EPPS on several

shots. This consistency supports the simulations in the chapter 5, which also suggested that super-ponderomotive electrons are consistently generated in pre-plasma, but are highly directional.

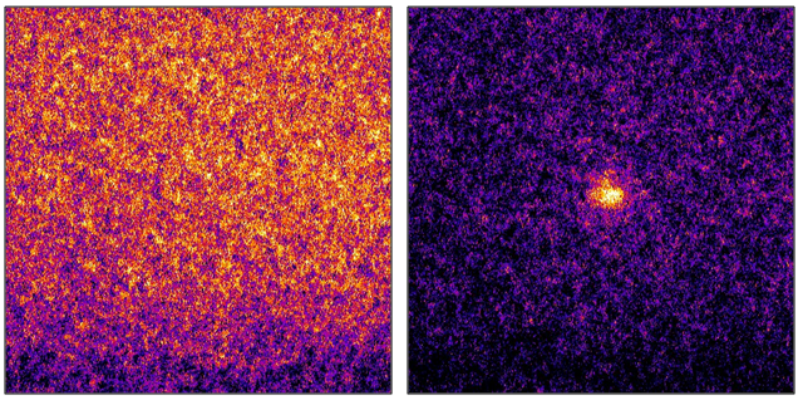

Figure 6.11: SCI data taken with (left) and without (right) the long pulse beam on the same color scale. Large increases in background signal occurred with the long pulse beam. The background on these shots with injected pre-plasma was of the same order of magnitude as the main signal measured on shots without injected pre-plasma. Since injected pre-plasma usually decreases the peak Cu-K/*alpha* signal it is unsurprising that most shots with an injected pre-plasma did not have enough signal to measure over the noise.

Ideally SCI could be used to further gauge some change in directionality, which could be used to verify this theory and validate EPPS data. However, the functionality of the SCI was disrupted by the introduction of the long pulse beam. The long pulse beam produced such a large background signal on the SCI that it overrode any Kα information. Similarly due to issues with beam placement and spot size EPPS was not fielded on this experiment looking at the front surface of the target.

When extending the pulse length to 5.0 ps it was expected that the hot electron tail would continue to be measured consistently like in the 3.0 ps case. However, EPPS results show completely inconsistent trends for the longer pulse length. A new development is that hot electron tails were observed for some shots without an injected pre-pulse and there were some shots observed with hot electron tails with

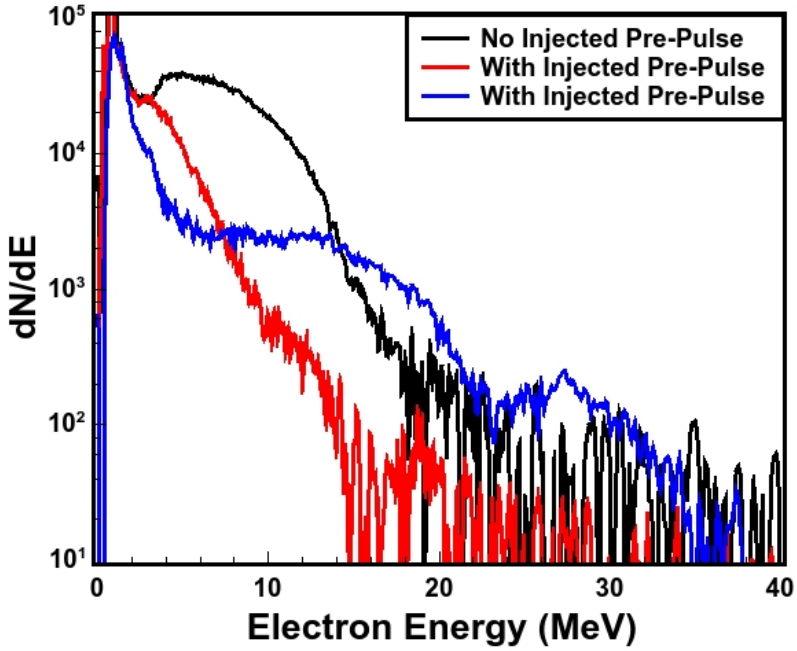

Figure 6.12: 3 seemingly contradictory spectra from 5.0 ps shots on Titan. In black we see a hot electron tail generated without an injected pre-pulse. In red we see the opposite case, an injected pre-pulse results in no significant hot tail. In blue we see a case where the hot tail is generated with pre-pulse but there is a large dip at around 25 MeV.

large gaps in portions of the spectrum. Once again, hot electron tail measurement was inconsistent with pre-plasma, however in a departure from previous data, super-ponderomotive electrons were measured without an injected pre-pulse.

Since the pulse was extended to 5.0 ps the intensity dropped down to 5×10^{18} W/cm^2 and it was thought that these strange results were caused by inconsistencies in the beam at such low intensities. Similarly, it was impossible to have an accurate BMXS temperature on several of these shots since the electron temperatures dropped so significantly on some shots only a few channels on the spectrometers had any signal. The lack of channels in conjunction with the signal from the secondary side lighter interaction made it much more difficult to analyze the BMXS data. It was

clear that further exploration into longer pulse lengths would require a beam with more energy and consistency. PIC simulations were used to try and explain these results, and are shown in chapter 9.

Sections of this chapter are currently being prepared for submission for a publication authored by J. Peebles, C. M. Krauland, C. McGuffey, P. Forestier-Colleoni, S. Zhang, R. Hua, J. J. Santos, H. Sio, J. Park, H. Chen, H. S. McLean, M. S. Wei, S. I. Krasheninnikov and F. N. Beg. The dissertation author was the primary investigator and author of this material.

Chapter 7
Titan Proton Radiography Results

The proton radiography results are separated in this section from the rest of the results from the Titan experiment for a few reasons. First, the dynamics of the laser pre-plasma interaction that are seen in PIC simulations are difficult to resolve consistently with the spatial and time resolution of the proton radiography setup used on this experiment. The entire short pulse laser has a duration of 1-5 ps, while the best time resolution between radiography frames is 1.5 ps (with the worst being nearly 100 ps). The spatial resolution of the radiographs was around 10 µm which is also on the order of the laser spot size. While some information can be gleaned from radiographs about the short pulse interaction, it is difficult to make definitive, quantitative measurements based on single frames and pixels. The second reason this section is separated is because the radiographs contained significant results that were completely unanticipated but also somewhat unconnected from the generation of super-ponderomotive electrons.

To start, blank radiographs were taken which only had signal from the proton generating (side lighter) interaction. Other diagnostics were placed in order to measure the signal that the sidelighter target generated by itself. This was partly due to concerns from the earlier TPW experiment, where the sidelighter target signal dominated the main interaction signal on some diagnostics. It was found that the EPPS facing the side lighter target received most of its signal from this source as expected. The other diagnostics showed some contribution from the sidelighter target, but nothing so strong it would dominate the main interaction.

These blank radiographs confirmed that some features seen in radiographs are due to structures in the proton beam spatial distribution. One feature that was

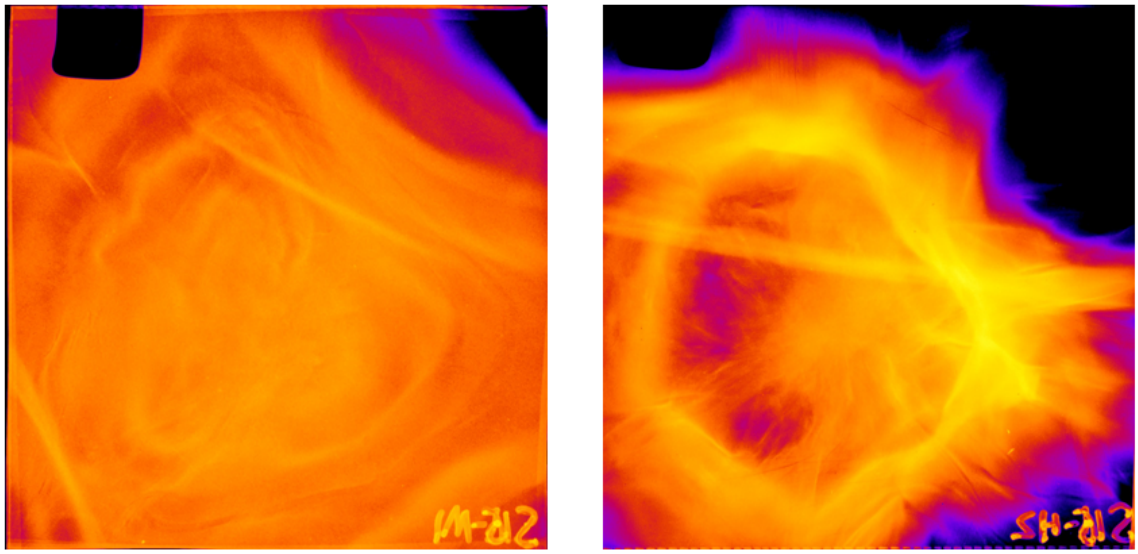

Figure 7.1: Sidelighter only radiography reference shots with out any main target or main beam. On the left an earlier frame (M1) corresponds to 8.9 MeV protons, is compared to a later frame (H2), which correspond to 3.35 MeV protons. On both frames several vague features can be seen that are structures in the proton beam. A consistent feature on low energy films was seen, which consisted of a horizontal band across the entire film.

consistent was the creation of a horizontal band on lower energy, later time films. These could be the product of either protons or electrons and are hypothesized to originate from the edges and corners of the sidelighter foil, based on the angle of the line relative to the target. Further "blank" radiographs were taken where the main target was inserted, but not shot with the main beam. These shots were performed to ensure that the sidelighter interaction did not interfere with the main interaction and to check whether charged particles from the sidelighter hitting the reference mesh would cause any noticeable charge to gather, in which case the image around the mesh wires would expand or contract.

The mesh reference target can be used to gauge the spatial scale of several features seen on the proton radiography. These features can also be compared less precisely against the main target size (1 mm) when the targets are properly aligned.

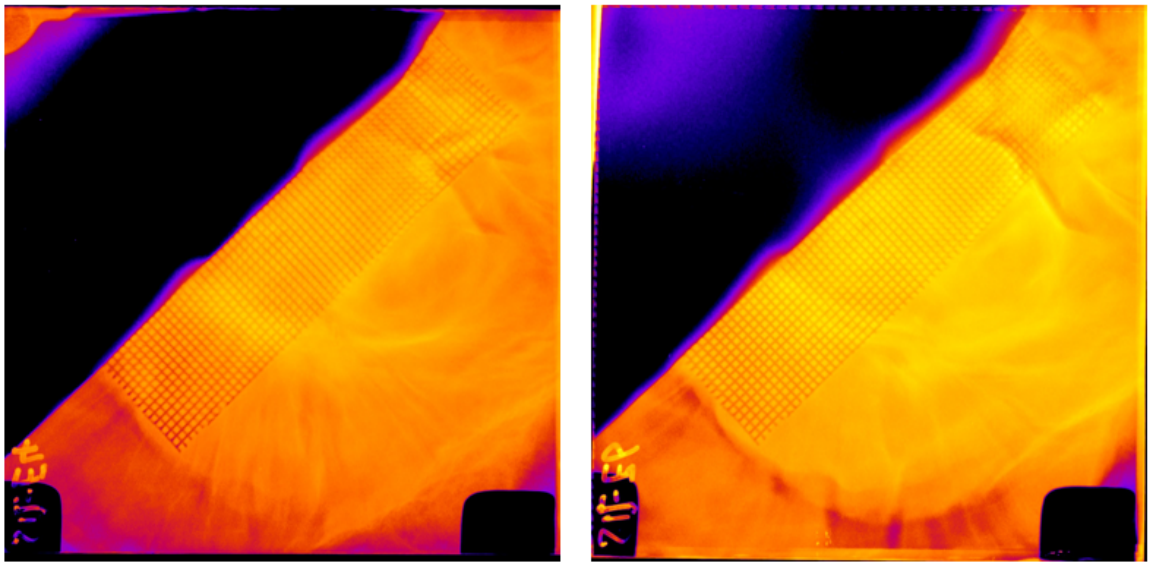

Figure 7.2: Sidelighter only shots with a main target and reference mesh in place. Some slightly random proton beam structure is seen but no significant charge on target or mesh was measured. Looking at the image it is possible to see that the main target had a small angular misalignment where the plastic juts out in front of the metal foil target. This effect can occur with a roughly 2 degree angular misalignment.

Since the mesh's position relative to the targets cause it to be magnified twice as large as objects imaged at the main interaction, each mesh grid, which is 25 µm in reality, represents 50 µm in the target plane.

These reference shots give confidence in the determination of which certain features are caused by fields or density perturbations from the main high intensity interaction. Looking first at the radiographs for a shot without the injected pre-pulse beam we find features which are extremely reproducible. Due to the fast expulsion of electrons from the main target a large electrostatic sheath field forms, which is partially determined by the shape and material of the target. This sheath field has been well documented in previous experiments and occurs when the entire target and apparatus become charged. Some structure can be seen inside the hemispherical bubble sheath that appear to be lines directed towards the point of focus. It is difficult to say with certainty what these structures are since the bubble sheath pushes so

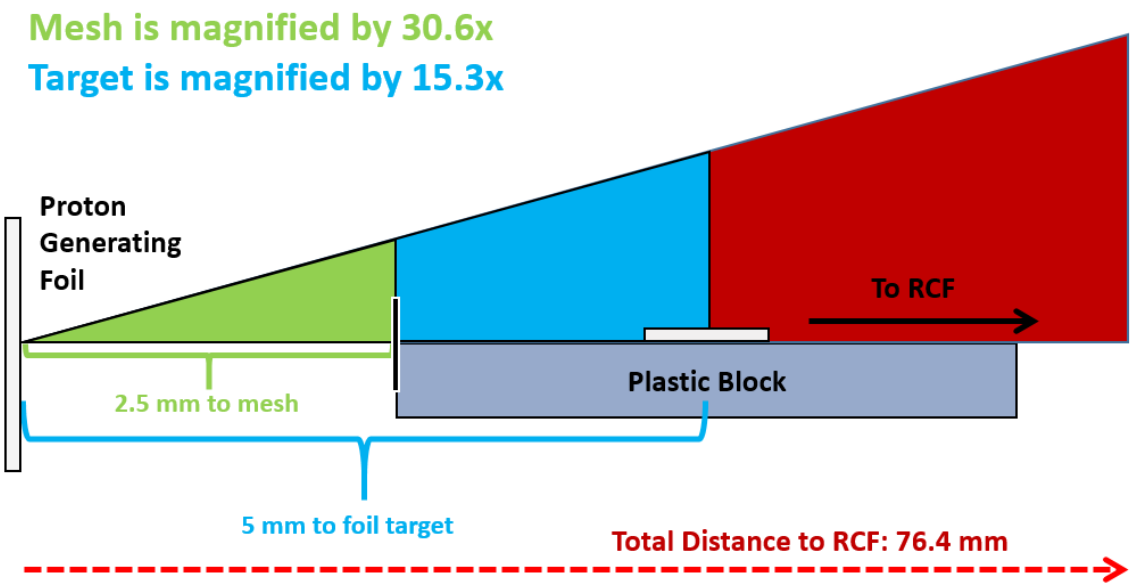

Figure 7.3: Magnification guide with a view of main target, side target and mesh relative positions. Note that interactions from the main target have a different level of magnification than the mesh.

many protons away that there is barely any signal inside the bubble. This effect was recorded without fail for every single 0.7 and 3.0 ps shot with the high intensity beam without the injected pre-plasma.

When the injected pre-plasma is introduced in the form of the long pulse beam both of these features are removed and a host of other features can be seen and characterized. All of these features have some dependency on the amount of energy delivered in the long pulse beam, though they are not nearly as consistent as the main beam only features. These features are divided and named into the following groups for quick identification: tomato feature, laser channel, wing feature and wave-post-soliton.

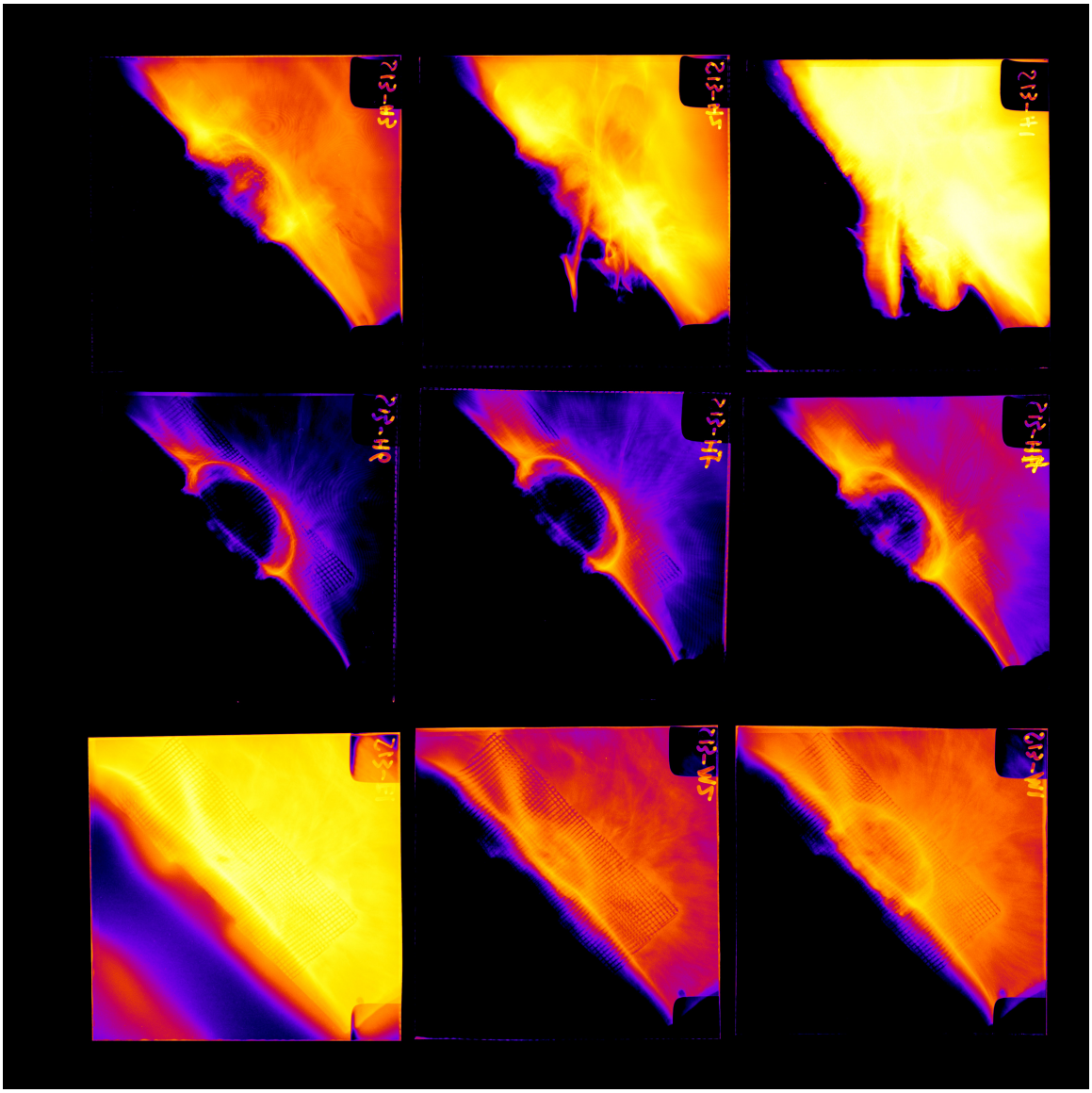

Figure 7.4: Final 9 frames of the RCF stack after the short pulse laser has arrived, with the earliest frame in the bottom left and the latest frame in the top right. 2 strong field features arise, an overall planar sheath field on the entire plastic structure and a more specific hemispherical field that forms right over the metal foil target. The earliest frame shows the position of the metal foil relative to the plastic block.

7.1 The Tomato Feature

This feature seen on multiple shots was called "Tomato feature" in order to separate from the other features seen on RCF and gains its name due to its unique

tomato like shape which makes it easily identifiable. This feature has several characteristics which are reproducible and consistent. We can define the feature by these qualities:

- The feature primarily arises on radiography frames that occur earliest in time. The frames where the feature is most prominent are E6-E9.
- Switching film types from E to M or H decreases the feature's intensity compared to other features on the radiograph.
- The size of the feature appears to increase with energy in the long pulse beam, although the increase may not be linear.
- The feature appears to be independent of other sources of protons. Other features that are seen on radiographs will arrive, appear to overlap and be unaffected by the presence of the tomato feature.
- Signals in and around the feature do not appear to backlight the mesh grid like other proton signals do.
- The feature appears constant and unchanging over a long period of time.
- No tomato feature was seen on reference shots were performed with the main target only with an injected pre-plasma and no side lighter.

This information was collected over dozens of shots and when put together, some conclusions about the origin of this feature can be reached. First, reference shots without the sidelighter at all confirm that this feature **requires** the sidelighter interaction to be present. However, we can say with some degree of certainty that this feature is **not due to protons**. It appears to be completely independent of other proton signals where dark regions of the "tomato" will suddenly be breached by the

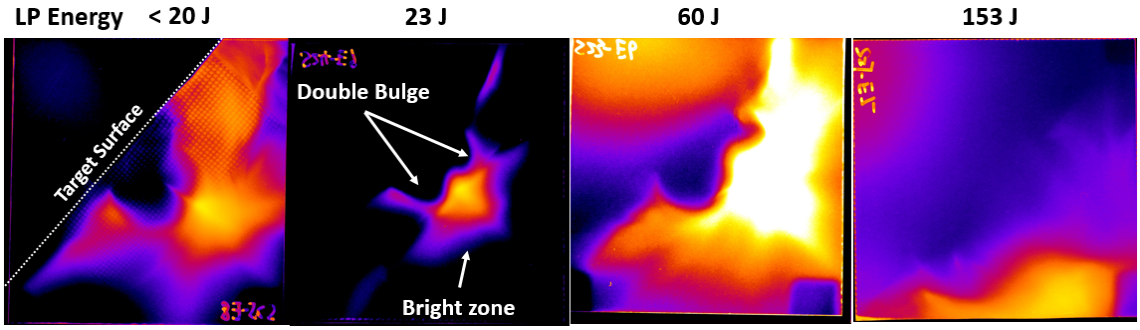

Figure 7.5: Tomato feature on 4 separate shots with injected pre-plasma with long pulse energies for each shot listed above. The feature clearly grows in size as energy in the long pulse increases and is characterized by a double bulge above the main target with a bright patch sprouting between them. No reference mesh can be seen in the middle two frames when it should be visible.

arrival of a bright proton signal. Further support of this is that the bright feature at the top of the tomato does not appear to resolve the reference mesh. This likely means that the signal is being generated on the main target side of the mesh.

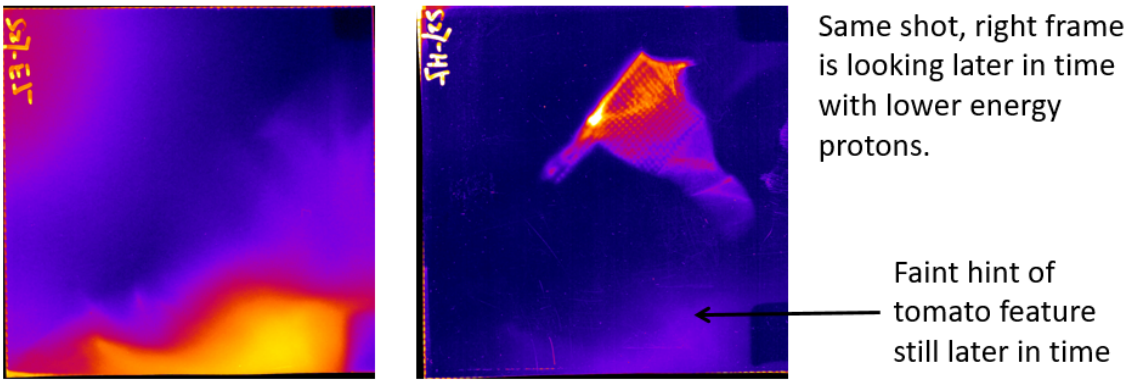

Figure 7.6: Two frames from a single shot with the earlier time shown on the left. The tomato feature is clear in the early time frame but can still be seen on the later time radiograph. However a second signal, clearly comprised of protons (since the mesh is visible and distorted) appears deep in the dark zone of the "tomato".

It seems safe to say that this feature is the result of electrons or x-rays from the side lighter target interacting with the underdense plasma on the front surface of

the target. This interaction could be heavily dependent on the underdense plasma density. This would explain several of the characteristics of the feature:

- The feature appears at an "early time", independent of proton signal because it is caused by electrons or x-rays which do not have the same Bragg peak in the RCF stack as the protons. For the same reason the feature would appear to be unchanging over time. Essentially, electrons and x-rays do not follow the same time resolution rules on the RCF stack as protons.

- For the same reason changing film types has a different impact on relative signal of the tomato feature because it is not caused by protons.

- The feature changes with long pulse beam energy as the level of underdense plasma increases and moves further away from the target surface. The resulting signal must therefore be dependent on the interaction between the sidelighter and the pre-plasma created.

7.2 The Laser Channel

The laser channel is a feature that appears on the proton radiographs for shots with injected pre-plasma and is readily explained. As the laser passes through the underdense plasma the ponderomotive pressure pushes the plasma aside, forming a laser channel. When the plasma is pushed away the electrons move faster than the ions and a charge imbalance occurs creating electrostatic fields around the region of the laser. This can be seen in the simulations in chapter 5.

The extensive pre-plasma created in the Titan case extends millimeters from the target and can have higher densities than the injected pre-plasmas seen on the TPW experiments. The radiographs showing the laser channel also show heavy filamentation long before the beam hits the target surface. The laser channel's total size

appears to roughly match the predicted size of the beam further away from the target when using the Titan parabola's f number of 1/3. These results are somewhat similar to those seen by L. Willingale et al. on experiments performed on an extremely large underdense plasma [40].

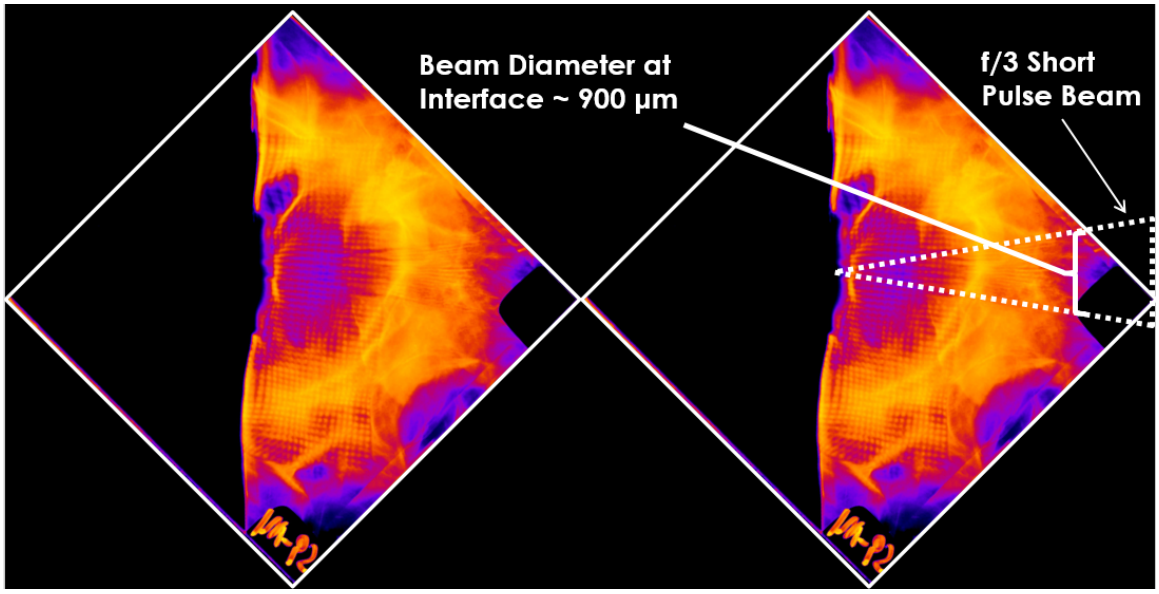

Figure 7.7: Proton radiograph showing the channel feature with an overlay of the approximate width of the beam using the Titan laser parabola's focusing power. Individual channels from filamentation of the beam can be seen in the underdense plasma as striations across the entire channel.

It is difficult to measure effects close to the target seen in the PIC simulations shown in chapter 5 due to the resolution and size difference of the radiographs. As noted before, each mesh grid is roughly 50 µm in size at the image plane. Looking carefully at the region where the beam hits the target there is a great deal of disturbance that extends several mesh grids in distance. The fields generated close to the target surface in simulations are shown to be on the 10 µm scale. Resolving any sort of beam self focusing effect on the scale of a single grid size would be extremely difficult to impossible. However, confirming rough beam propagation, alignment and focusing in the underdense plasma is still a benefit.

7.3 The Wing Feature

The wing feature is best described by a region of high proton deflection above and below the focal point of the short pulse beam. The characteristics of this feature that are consistent when it is observed are:

- The "winged", triangular shape region is bordered by a proton focusing field, especially on the sides away from the target. The region can be hundreds of microns in size.
- The area inside the region is magnified significantly in all directions by several times, which can be measured using the reference mesh. The maximum magnification is unknown due to magnification being so high that the reference mesh is unresolvable.
- The size of the wings is on the order of a millimeter on some shots and a wing is often formed on each side of the beam focus.
- The wing on the top side of the short pulse beam location is always larger than the wing on the bottom side. On occasion the wing on the top will be the only one visible.
- The wing is only seen on shots with the injected pre-plasma (long pulse beam).
- On shots with extremely high energy in the long pulse beam it was often the *only* feature recorded on the RCF.
- The size of the wing feature did not appear to vary with long pulse energy upon initial inspection. However when ranking the size of the feature and comparing the energies it is possible that the size of the feature may indeed scale with the long pulse energy.

- 9 shots with the largest features had an average long pulse energy of 110.25 J, 9 shots with medium sized features had 82.2 J and the 5 cases where the feature was small or non existent had long pulse energies averaging 69.64 J.

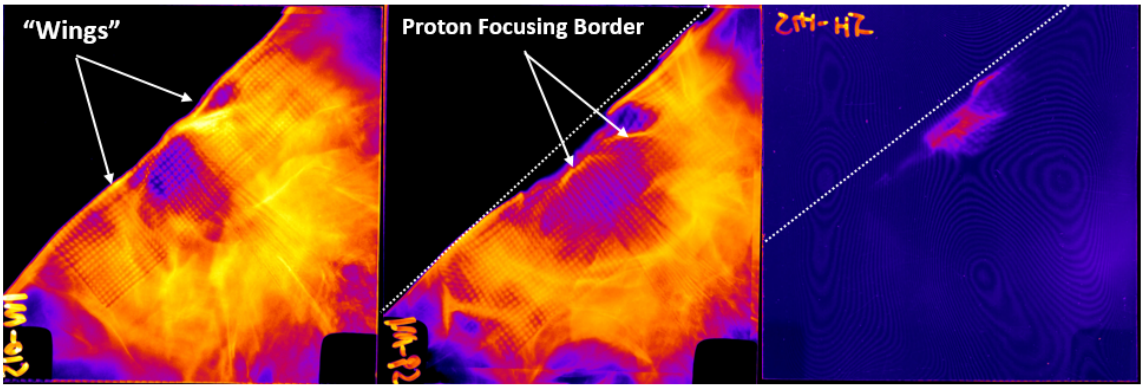

Figure 7.8: 3 RCF frames from different shots showing the wing feature. In all 3 cases it is clear the top-right wing (which is above the beam focal spot) is much more defined. In the center frame, perfect angular alignment shows the bulge of the metal foil target in front of the plastic block it's placed on. This alignment also shows that the proton focusing border region is connects the top and bottom wings across the short pulse beam. The right frame is a shot with one of the largest energy injected pre-plasmas and the only feature seen was the wing.

There are a few conclusions that we can draw about the origin of this feature. First this feature must be captured by protons from the sidelighter being deflected by fields in the interaction region on the surface of the target. This is proven by the fact that the mesh is resolved indicating that the sidelighter target is the source and the mesh is distorted indicating the particles were deflected. The feature appears to change as radiochromic film layers change instead of being constant like the tomato feature, which suggest that the signal is from protons, not electrons. The field appears on the surface of the metal foil, but the region of deflection is extremely large, with a size on the order of a millimeter.

What sort of field could possibly create such a feature? The $\nabla \mathbf{N} \times \nabla \mathbf{T}$ magnetic field that occurs for long pulse laser interactions was described in Chapters 2

and 5, and appears to match the vague shape and position seen on the radiograph. At first glance there are a few problems with this theory: first the direction of such a magnetic field is toroidal. The toroidal field above the laser will actually be parallel with the radiograph protons resulting in minimal deflection. The field components that are not parallel will produce alternating deflection forces which would not produce the magnification effect seen on the radiographs. However it has been shown in both previous simulations and experiments that electrons on the surface of the target flow around the edges of these strong magnetic fields forming a strong current. This current flow circulating around the target would certainly lead to the proton focusing lines around the regions of mesh magnification.

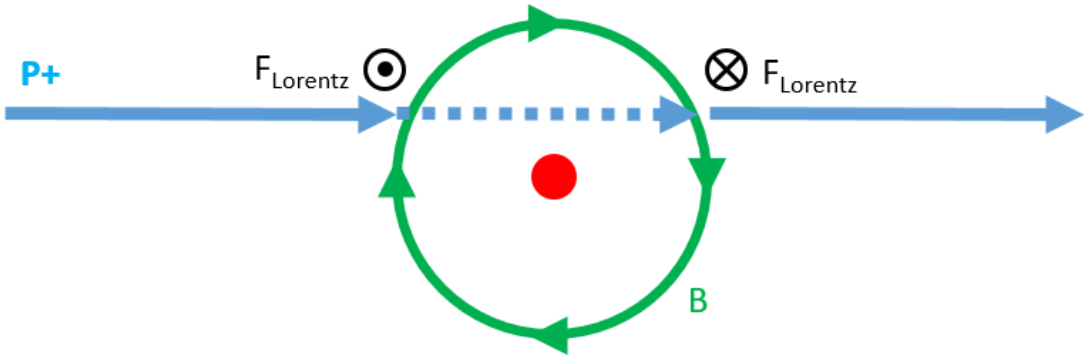

Figure 7.9: Cartoon demonstrating how a toroidal magnetic field will shift a proton from the sidelighter.

It is likely that this large field structure is due to the long pulse rather than the short pulse as these features are seen very early in time, prior to when the short pulse beam affects the pre-plasma in the region. The scale of the size of these features also suggests that the long pulse interaction is the cause, since such fields in short pulse simulations only extend to tens of μm in size. The long pulse, with its 200 μm sized beam and large energy would create fields that extend further from the target. An attempt was made to have a reference shot with a long pulse beam only

with radiography to verify this, however the energy in the long pulse was too high, resulting in no radiograph images.

7.4 Waves and Post Solitons

The final feature discussed is likely the most complicated and can be divided into a two step process. It appears that as the beam enters the very low density plasma far away from the target surface it excites a group of waves, which travel behind the beam. These waves begin bunched up but propagate at different speeds and eventually separate from each other as they propagate towards the target. In their wake the beam channel appears to be heavily disrupted and turbulent features are formed behind the waves, which are called post solitons. The spatial and time scales of these features are so large that designing a PIC simulation to understand them is a large undertaking. Several unique characteristics of these waves are listed below:

- The waves are the first direct indication of the laser hitting the underdense plasma. In prior frames the radiograph shows a uniform proton signal that is similar to reference shots.
- The first indication of the waves is a single shock like front which appears to narrow in later frames. These occur nearly 3 mm away from the target surface.
- The wave either splits into multiple waves with differing velocities, or additional waves are stacked upon the original. These travel towards the target but their relative separation increases.
- As time progresses the overall edge of the entire underdense plasma becomes more defined on the radiograph creating a distinctive 2.5-3 mm radius semicircle.

- Waves continue to travel towards the target, waves that are faint in earlier radiography frames become clearer as film type changes for later frames.
- After about 50 ps the first wave stops near the target surface, several hundred microns away. Later waves stack near the surface in the same location later in time.
- A turbulent structure (also called post solitons) develops behind the last wave which appears to be the result of the laser channels breaking through the varying wavefronts.
- This feature was consistently reproducible for the specific long pulse energy range of 10 - 50 J. Very few protons were recorded on shots with higher long pulse energies where the wing feature was often the only notable result in these cases.
- The velocity of the leading wave front was extremely fast, nearly 0.3c in some cases. The following waves are somewhat slower than the initial wave.

The source of the waves shown in the RCF images is unexplained. The largest obstacle to be overcome is setting up a simulation that can accurately capture the effects on such a large scale. Ideally to ease the requirements for simulating the experiment we should make the box as small as possible. In this simulation we would like to capture the initial creation of waves which we can then assume will move through the underdense plasma. Therefore the simulation box will contain a wide beam laser 2500-3000 µm away from the target surface and the simulation time must be at least 10 ps.

Using 2D rad-hydro simulations we can show that the ideal simulation parameters would include a box wide enough to contain the beam with an intensity

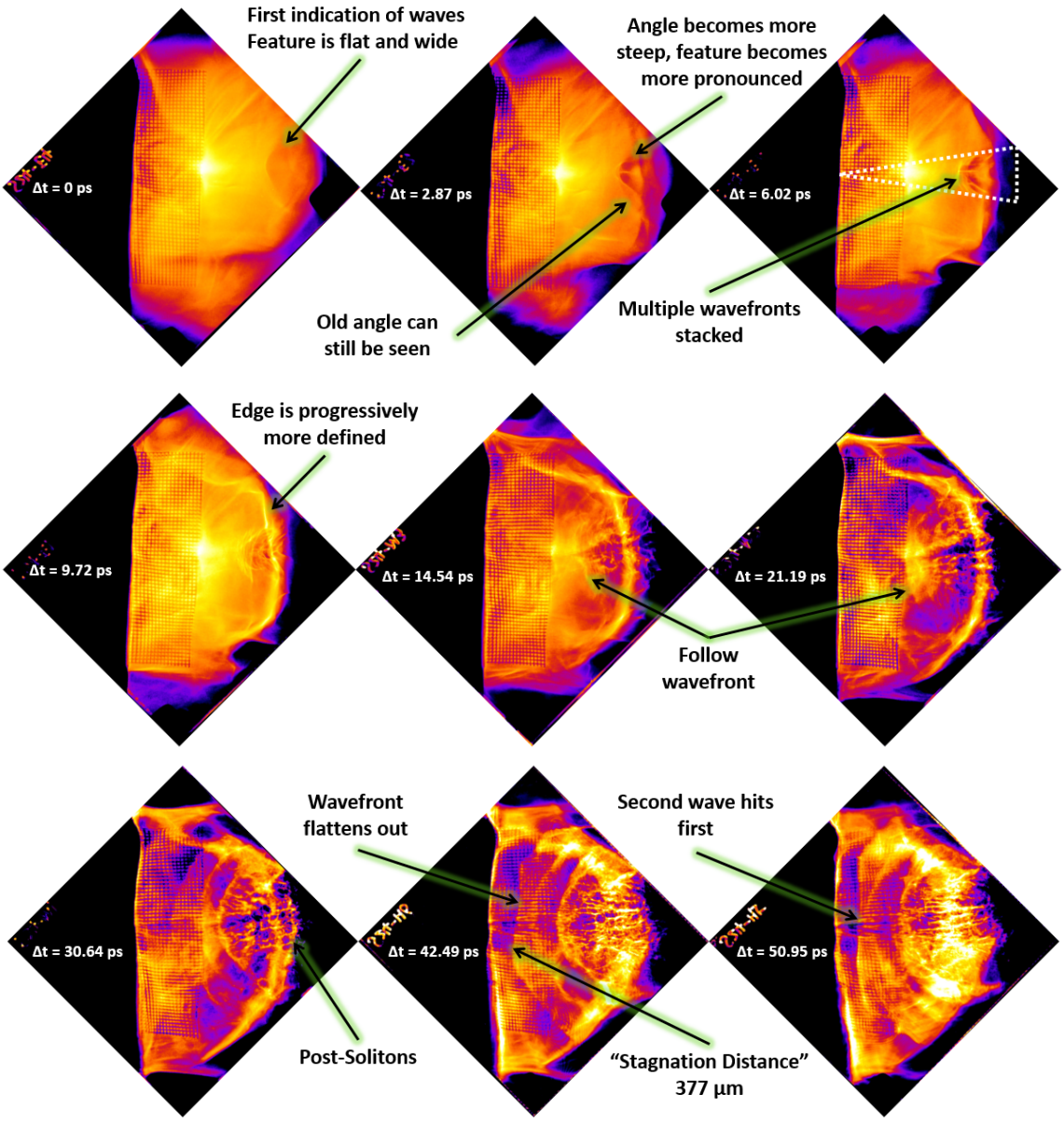

Figure 7.10: 9 frames from proton radiography taken on the same shot cataloging the creation and propagation of large wave features and subsequent post-solitons. It should be noted that the time between frames accelerates, with over 8 ps separating the final two frames. The distance between the target surface (on the left) and the edge of proton signal is estimated at nearly 3000 µm

of 10^{16} W/cm^2 impacting a plasma with a significant velocity in the opposite direction of the beam. This box would need to be several hundred microns in length and might require tens of picoseconds to run. Future simulations with greater computing

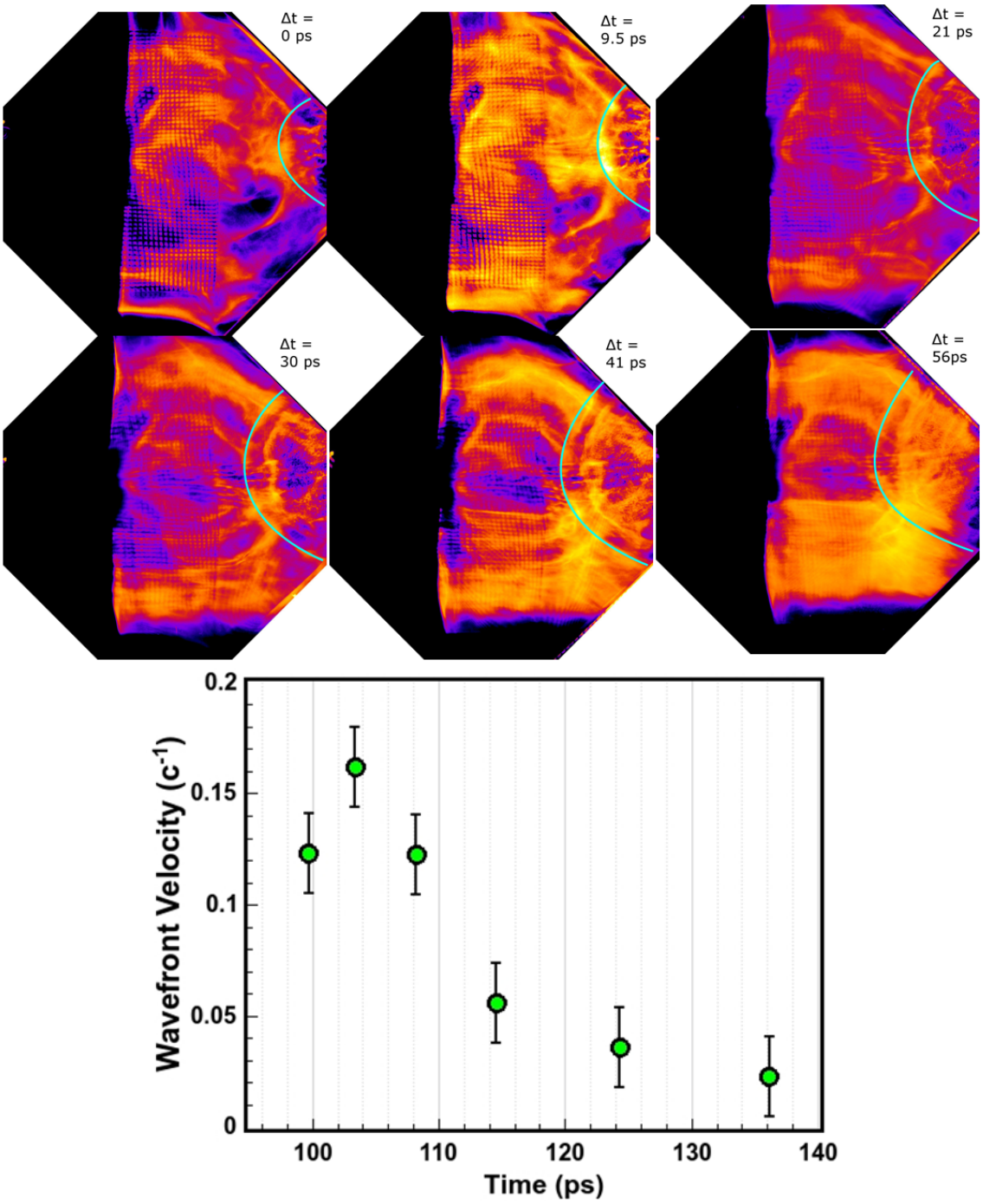

Figure 7.11: Another shot with fewer slower moving waves, the wave at the front is highlighted in blue. It was easier to capture the velocity (plotted below) of the wave consistently between frames. Even these slower moving waves appear to be moving at relativistic speeds.

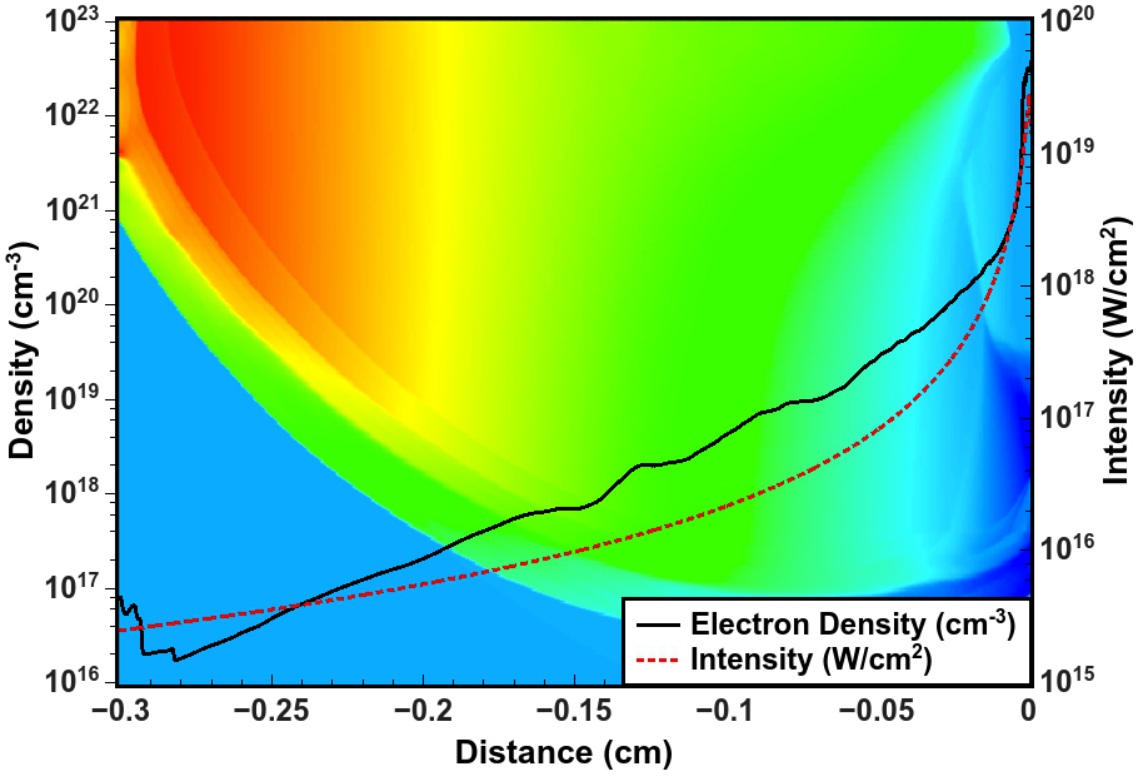

Figure 7.12: Color map and density outputs from 2D FLASH simulations of the pre-plasma density profile seen on experiment for the entire region. The color map corresponds to the velocity of the plasma away from the target. It is clear that 3000 µm away from the target surface the beam is defocused and has a large 900 µm diameter.

resources may shed further light on this feature.

Sections of this chapter are currently being prepared for submission for a publication authored by J. Peebles, C. M. Krauland, C. McGuffey, P. Forestier-Colleoni, S. Zhang, R. Hua, J. J. Santos, H. Sio, J. Park, H. Chen, H. S. McLean, M. S. Wei, S. I. Krasheninnikov and F. N. Beg. The dissertation author was the primary investigator and author of this material.

Chapter 8
Longest Pulse Length Case: OMEGA-EP Laser

8.1 Experimental Parameters

The OMEGA-EP laser systes features four beams, two of which have been compressed to give high intensities at shorter pulse lengths. These beams have a peak intensity of $I_{peak} \sim 4 \times 10^{19}$ W/cm^2 with 80 percent of the total energy (1.25-1.5 kJ for a 10 ps pulse) contained in a roughly 15-20 µm radius spot. OMEGA-EP is unique in the ability to provide a high intensity pulse, for longer pulse lengths.

OMEGA-EP was therefore used to continue pre-pulse experiments into the 5-10 ps pulse length regime. To do this, two experiments were conducted; the first experiment varied pulse length between 1, 3 and 10 ps while scaling energy to keep intensity consistent between pulse lengths. A major drawback of these initial experiments is that there was a significant level of **intrinsic** pre-pulse. The low contrast beam had a pre-pulse with energies of 5, 20 and 120 mJ for pulse lengths of 1.0, 3.0 and 10 ps respectively. This intrinsic pre-pulse had most of its energy contained in a 30 x 45 µm spot present in a 2 ns long pedestal that arrived prior to the main beam. This experiment compared the effect of pre-plasma before and after a high contrast upgrade to the laser, which removed the intrinsic pre-pulse.

The short pulse beam was incident normally onto a multilayer foil target, composed of a 135 µm layer of aluminum, 20 µm layer of copper for Cu-Kα imaging, an additional 20 µm layer of aluminum and a 1 mm thick layer of plastic. These targets were very similar to those in previous experiments, though with slight changes to the material thickness to accommodate the higher energy delivered on target.

A second experiment was conducted on OMEGA-EP to further examine hot

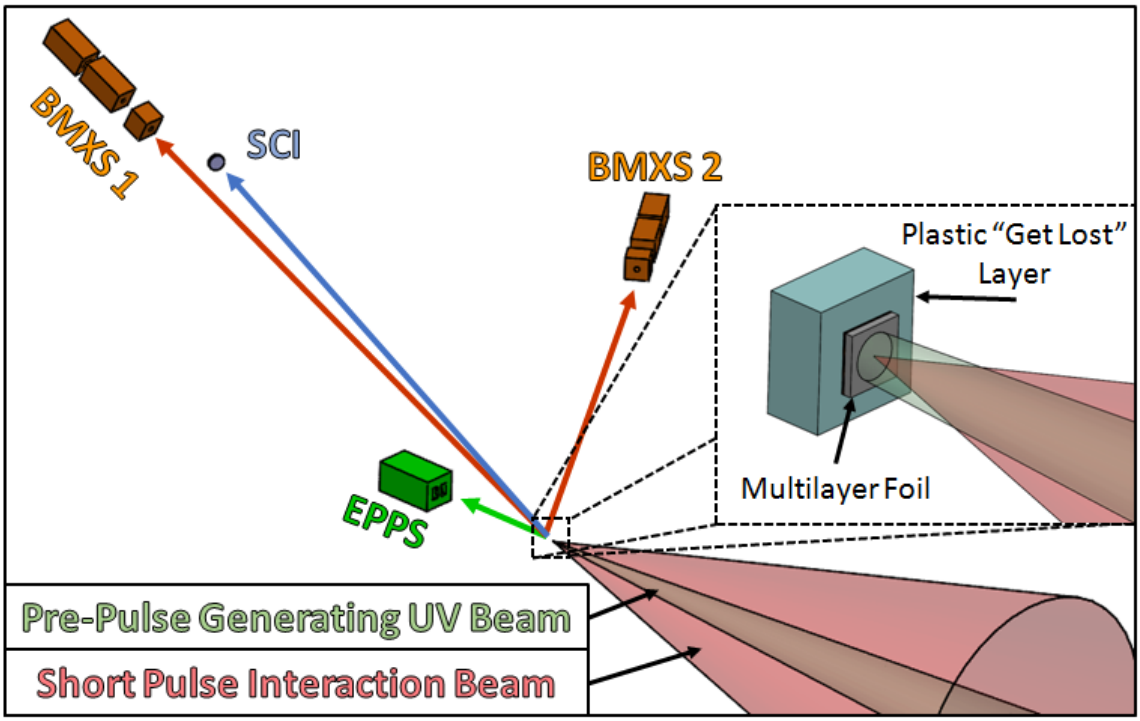

Figure 8.1: Experimental setup demonstrating the UV beam overlay used to generate controlled injected pre-plasma. The EPPS was placed directly behind the target while the BMXSes were placed facing the rear of the target at different angles.

electrons generated in pre-plasma, this time with a greater emphasis for longer pulse lengths (all shots used a 10 ps pulse length). Since the first experiment had uncontrolled pre-plasmas that scaled with pulse length, it was difficult to fully separate the impact different scale lengths of pre-plasma had on electrons from the impact of pulse length. For example, an increase in electron temperature when changing the pulse length from 1 to 10 ps may be a result of larger quantities of pre-plasma, or it could be caused by the increase in pulse length. Furthermore, pre-plasmas in this case are generated in a region which is on a similar size scale as the laser. 2D effects that arise from a smaller pre-pulse spot introduce inconsistencies which make it difficult to ascertain its impact. Therefore all shots taken in the second experiment used a beam with the high contrast upgrade, which effectively eliminated the intrinsic pre-plasma. Instead, a controlled, 1D **injected pre-plasma** was generated, similar to

those created in the TPW and Titan experiments, in lieu of the large uncontrollable intrinsic pre-pulse. To produce a controlled pre-plasma for the second experiment, a UV beam with an energy of 20 J in 1 ns square pulse, with a large 750 µm spot, was delivered on target. The amount of pre-plasma generated was controlled by changing the delay between the UV and short pulse beams, with a full 1 ns delay corresponding to the maximum controlled pre-plasma case.

BMXSes were placed around the chamber 1900 cm from the target at 25° (BMXS1) and 65° (BMXS2) angles with respect to the rear normal of the target (Fig. 8.1). For the second experiment a single EPPS was added, placed facing the rear surface of the target similar to previous experiments. Finally the SCI was fielded facing the back of the target, and generated an image with a magnification of 9.63 and resolution of 25 µm. All image plates were scanned 25 minutes after each experiment and previous calibrations of both the scanners and image plates enabled us to account for any loss of signal due to time between shot and scan.

8.2 Experimental Results

The results from the first experiment examined the impact of different levels of uncontrolled pre-pulse and changing pulse length. Two clear trends arise from electron temperatures inferred by the BMXS shown in Fig. 8.2. First, improving the contrast between the two sets increased the temperature of the electrons measured by BMXS by 1.0 MeV for several shots. However, it is noticeable that 3 high contrast shots had temperatures almost identical to their low contrast counterparts. When examining these shots more closely it was determined that the temperature drop correlates to shots with lesser focal spot quality (Fig. 8.2 (bottom)). While the overall spot size was only marginally larger for these shots, the focus and peak intensity were split somewhat between two spots resulting in less intensity. The second notable trend was that electron temperature increased as pulse length increased, while intensity

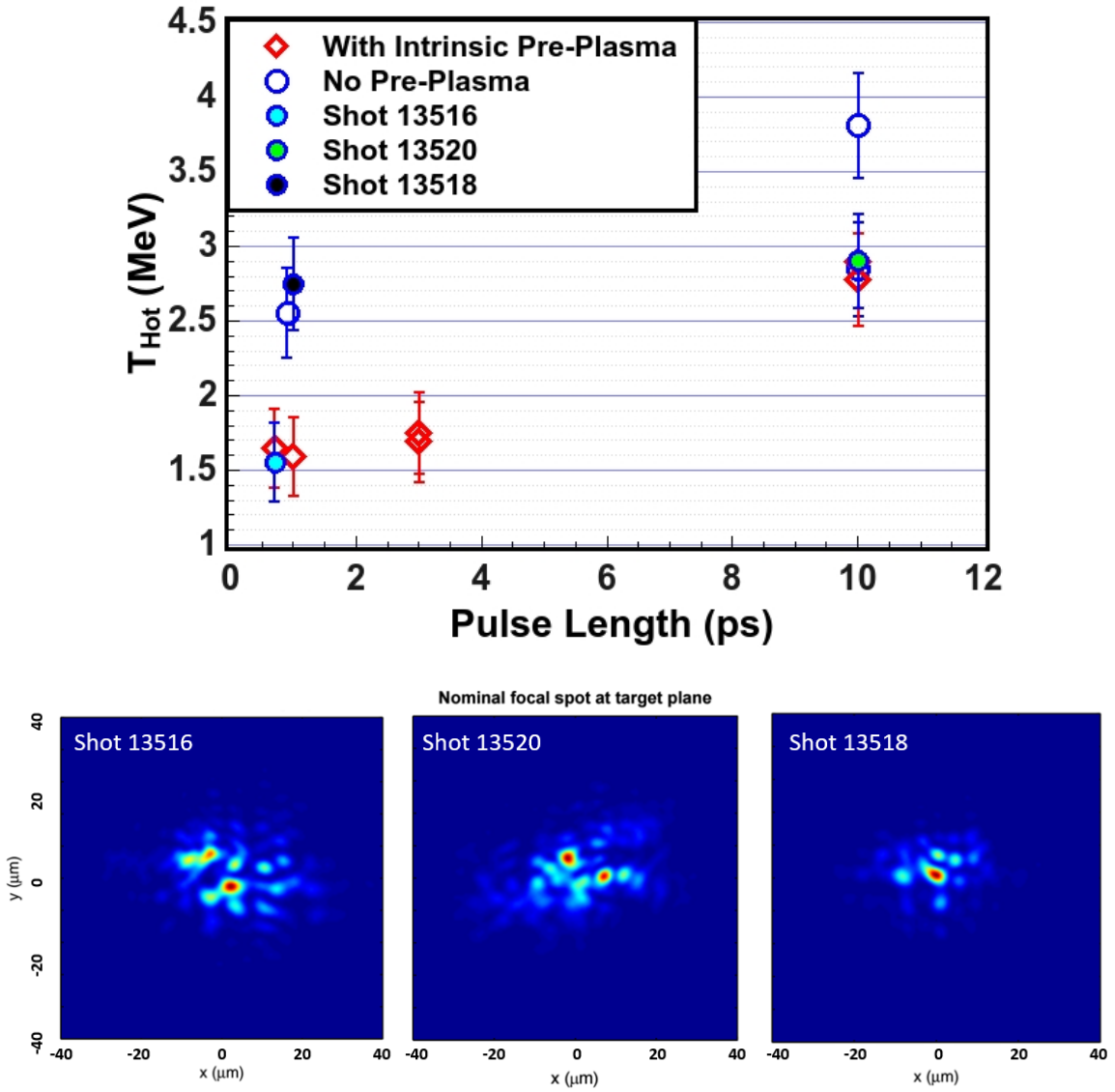

Figure 8.2: BMXS inferred T_{Hot} from individual shots with and without intrinsic pre-plasma shows a significant increase in temperature for ponderomotive scaling electrons when pre-plasma was reduced and pulse length was increased. Focal spot quality analysis shows that on several high contrast shots (13516, 13520) the bulk of energy was split 2 lower intensity spots resulting in the reduced BMXS temperature. Shot 13518 is an example of a shot with a single higher intensity spot, which in conjunction with the higher contrast, increases electron temperatures.

was kept constant. The increase in temperature when going from 3 ps to 10 ps is substantial, nearly another 1 MeV in electron temperature.

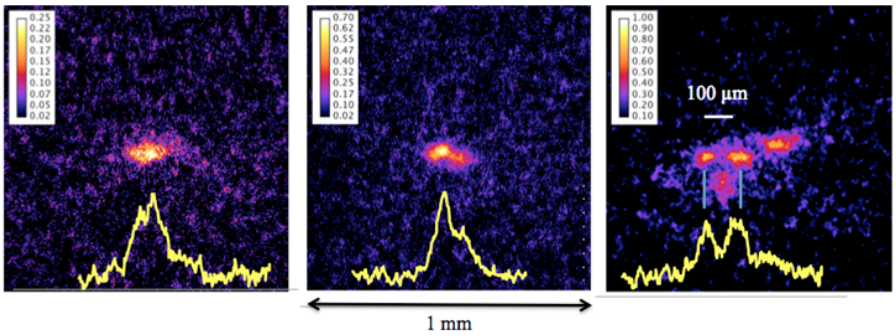

Figure 8.3: SCI images for 1, 3 and 10 ps shots respectively on the first OMEGA-EP experiment. These demonstrated that as pulse length increased, degree of filamentation in the electron beam also increased. It is unclear whether this is due to changing dynamics over the 10 ps pulse, or the increase in intrinsic pre-plasma for the longer shots which contained proportionally more energy.

It is also interesting to note that the electrons generated at the 10 ps time scale become less directionally consistent. The SCI data taken on these shots (Fig. 8.3) shows that as pulse length increases, the amount of electron beam filamentation increases. At 1-3 ps the traced electrons in the copper layer show a single spot, with perhaps slightly more divergence in the 3 ps image. At 10 ps however we see that the electron beam diverges into 4 separate smaller spots emitted in different angles. The divergence angles between these beams can be estimated from the travel distance to the copper layer and transverse distance of the beam spot, which results in at least a 20° half angle difference spread between electron filaments. These differences are difficult to gauge with the BMXS diagnostic as the differences in the total bremsstrahlung emission from these separate filaments are not great enough to be spatially resolved. While the beam divergence in these shots is a clear trend, it is unclear from this data alone whether this is caused by the increase in interaction time by the short pulse beam, or the increase in amount of initial pre-plasma, which scaled with the short pulse length in this data set.

Since it is difficult to say with confidence whether the increase in electron

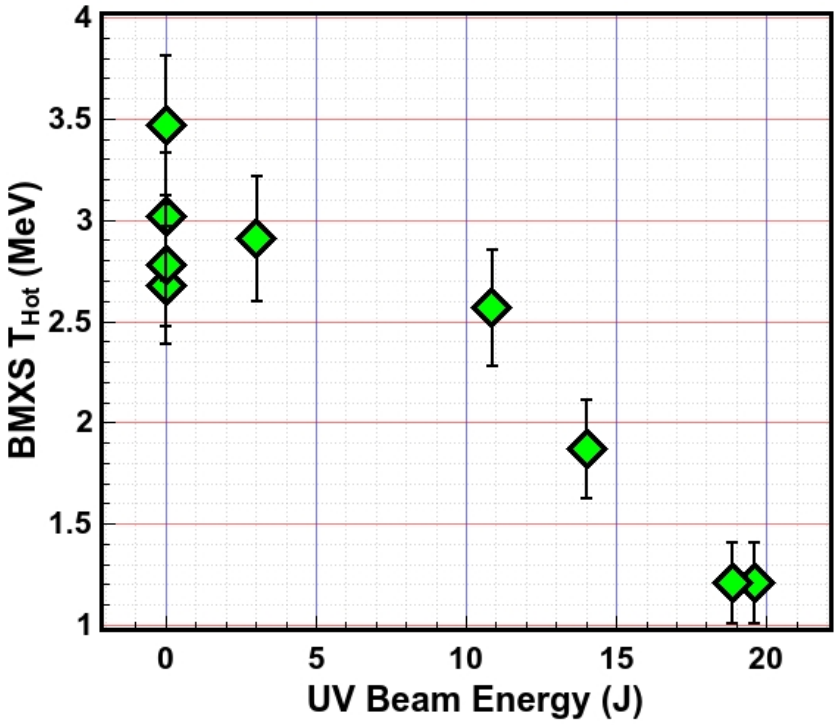

Figure 8.4: BMXS inferred temperature from the main experiment (10 ps only) shows that the significant decrease in temperature of bremsstrahlung generating electrons scales with the amount of pre-plasma.

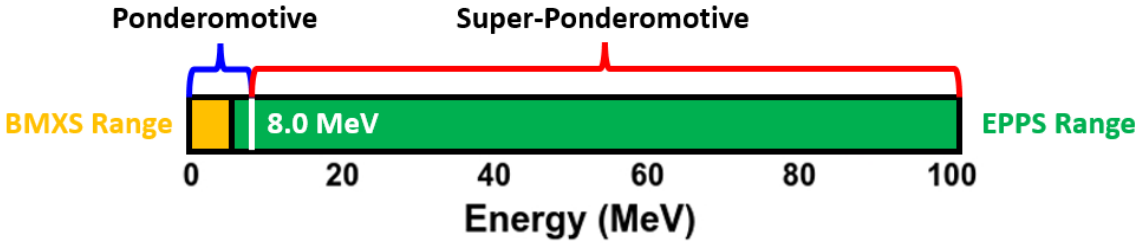

Figure 8.5: Diagnostic energy ranges compared to heating mechanisms for OMEGA-EP intensities.

temperature and divergence of the electron beams is due to simply increased pulse length, increased pre-plasma or a combination of both, a second experiment separated the two by removing the scaling intrinsic pre-plasma nearly entirely. Using the BMXS with a controlled injected pre-plasma and a fixed 10 ps pulse duration, the BMXS

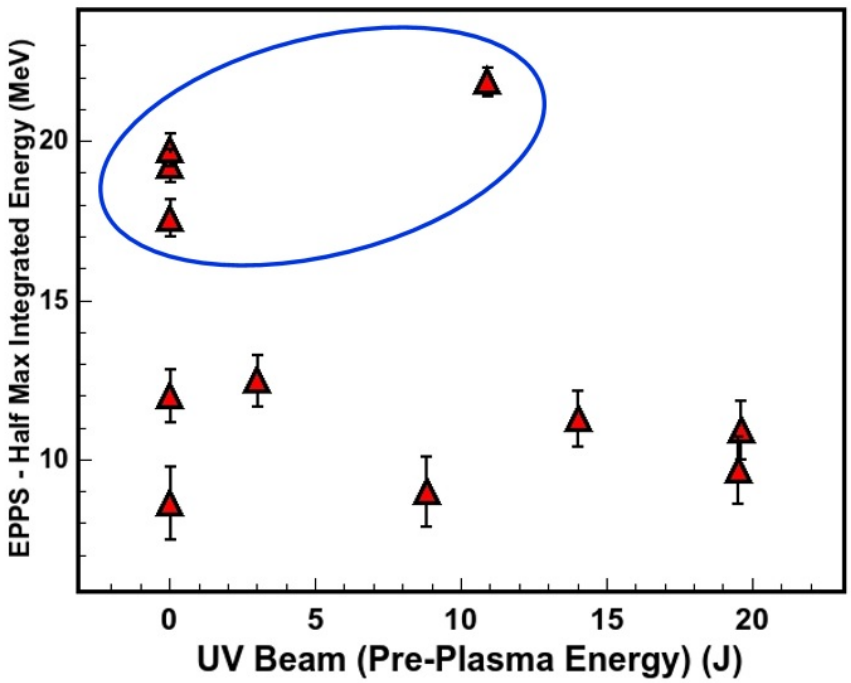

Figure 8.6: The EPPS characteristic half max integrated energy (HMIE) for all shots taken in the main experiment shows that the measured hot electron tail (circled in blue) does not correlate to increased injected pre-plasma via UV beam.

results from the first experiment were validated. By carefully controlling the injected pre-pulse it becomes much clearer that the presence of pre-plasma is what reduces the characteristic temperature of sub 5 MeV electrons measured by BMXS (Fig. 8.4). As the level of pre-plasma increases, the inferred electron temperature steadily decreases. In the case of the maximum level of pre-plasma, the temperature drops by nearly 1.5 MeV to 1 MeV, a similar drop to what was measured with the uncontrolled pre-pulse. The temperature of the shots without pre-plasma in this data set is slightly lower than in the initial experiment due to the slight decrease in energy and intensity between the two experiments.

A unique difference between the conditions on the OMEGA-EP experiment compared to the Titan experiment was the energy range of ponderomotive scaling electrons with respect to the diagnostics. At intensities of 4×10^{19} W/cm^2 ponderomotive

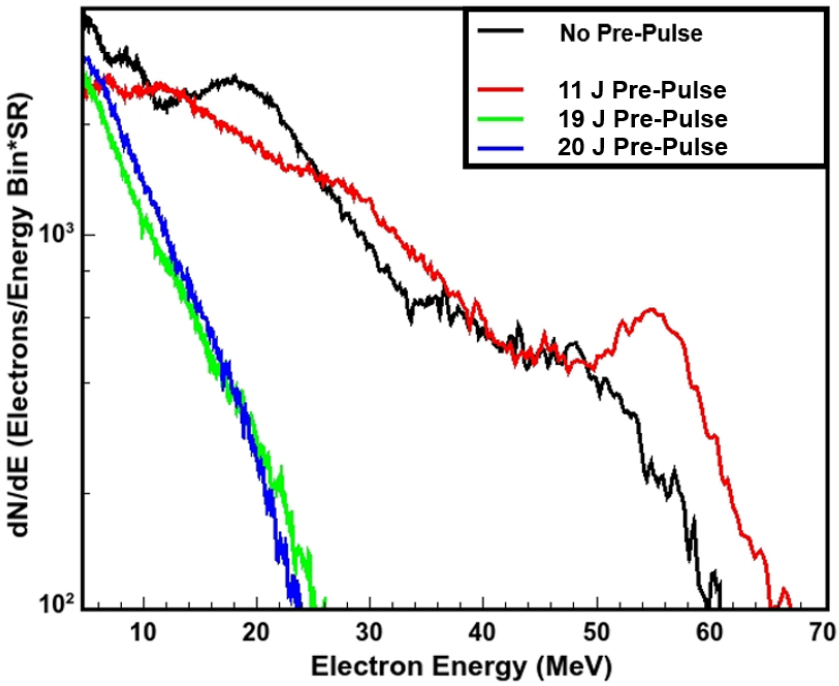

Figure 8.7: EPPS spectra for 4 shots with and without injected pre-plasma. Here we see 2 shots with clear hot electron tails, however one does not have any injected pre-plasma. As seen in both shots the spectra are much bumpier than their non hot tail cousins. The shots in green and blue did not generate a hot electron tail despite having an initial pre-plasma.

scaling electrons dominate all channels of the BMXS while the super-ponderomotive electrons dominate nearly the entire range for EPPS (Fig. 8.5). This means that the two diagnostics are essentially looking at separate electron populations, unlike on Titan where the BMXS was looking at contributions from both electron populations.

When examining the HMIE results from EPPS in the second experiment, seen in Fig. 8.6, there is a clear group with significantly higher HMIE temperature representative of the hot tail. However, it is interesting that not only were **hot electron tails observed for shots without injected pre-plasma, they were observed more often**. This is contrary to what was seen in previous shorter pulse length experiments and simulations. This can be seen in Fig 8.7, which shows 4 electron

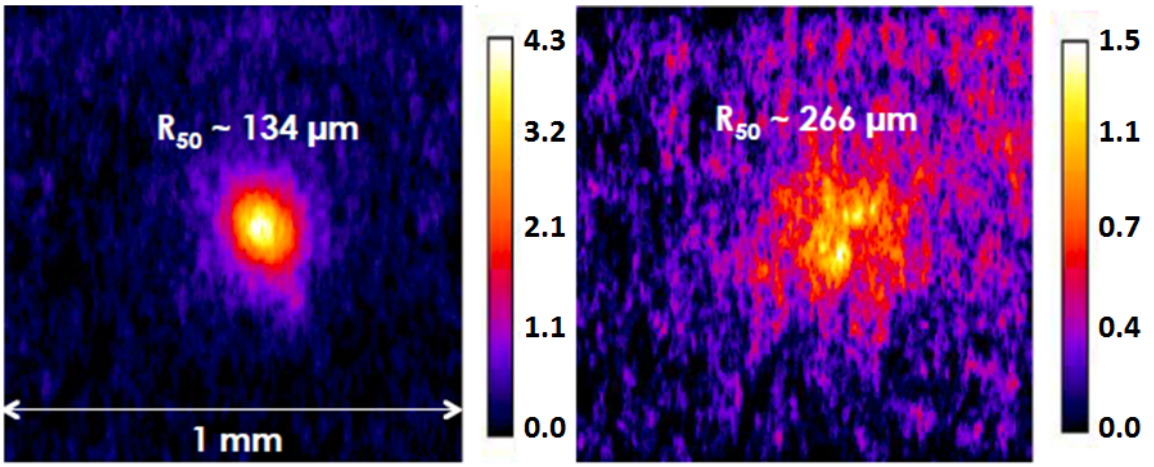

Figure 8.8: SCI data from 10 ps shots shows that cases with a cleaned pre-plasma (left) are less likely to diverge than with the with a large pre-plasma (right). When a controlled pre-plasma is introduced at the maximum level we can see that the electron beams become diffuse, indicating filamentation of the laser in the pre-plasma.

spectra from the second OMEGA-EP experiment. Of the three shots displayed with a large quantity of injected pre-plasma, only one contained significant quantities of super-ponderomotive electrons.

The SCI diagnostic helps explain some of the inconsistent measurements from EPPS. As seen in Fig. 8.8, the introduction of a significant pre-plasma results in a "scattering" of the generated electrons when passing through the copper tracer layer. The reduction of spot intensity and speckled pattern of the spot is likely due to the laser beam splitting into multiple filaments reducing it's effective intensity. This corroborates the information from the BMXS, which showed a decrease in the temperature of ponderomotive scaling electrons. This is understandable as J $\times$ B acceleration depends on the intensity of the laser. The long interaction region with the large volume of pre-plasma also contributes to the spread of the electron beam. Since the EPPS has a small acceptance angle and can only measure electrons emitted out of a 0.2° cone, the large degree of filamentation would lead many electrons to miss the EPPS pinhole. However, since the SCI traces nearly all electrons regardless of their temperature it is important to verify whether or not the high energy electrons

are affected by this filamentation as much as the rest of the electron population. 1 and 2D simulations presented in the following section verify these effects.

This chapter contains some material and figures from "Investigation of Laser Pulse Length and Pre-Plasma Scale Length Impact on Hot Electron Generation on OMEGA-EP", J. Peebles, M. S. Wei, A. V. Arefiev, C. McGuffey, R. B. Stephens, W. Theobald, D. Haberberger, L. C. Jarrott, A. Link, H. Chen, H. S. McLean, A. Sorokovikova, S. Krasheninnikov, F. N. Beg, New Journal of Physics **19**, 023008 (2017). The dissertation author was the primary investigator and author of this paper.

Chapter 9
Understanding Titan and OMEGA-EP Results Using 2D PIC Simulations

While it appears that Titan and TPW experimentally share many similarities, the experimental conditions from Titan and OMEGA-EP are actually more similar to each other and very different from TPW. Both have intensities of around 10^{19} W/cm^2, both have larger spot sizes than TPW and both cases had larger quantities of injected pre-plasma. On TPW the limited energy of the probe beam restricted the amount of pre-plasma generated severely. This meant that when injected pre-plasmas were created on Titan and OMEGA-EP with much more energetic beams, the quantity of injected pre-plasma was greater.

The difference in the regimes between the TPW and Titan experiments is extremely noticeable when conducting a 2D EPOCH simulation. These simulations are nearly the same as the ones for TPW for 600 fs pulses except certain key values are changed. The intensity is decreased by an order of magnitude and the incidence angle is slightly less severe (14 degrees). In addition, the pre-plasma is much larger in the Titan case, and a conservative injected pre-plasma best expressed by a triple scale length of:

$$n_e = \frac{7.85e23}{1 + exp(-(x-150)/1)} + \frac{2.0e21}{1 + exp(-(x-150)/50)} + \frac{1.5e20}{1 + exp(-(x-150)/100)} \tag{121}$$

This estimate was created by 2D FLASH [58] (an open source radiation-hydrodynamics code) simulations conducted by S. Zhang. A lineout was taken of these simulations and extrapolated/fit into the scale length equation format. It is immediately clear that the level of injected pre-plasma has the potential to be much

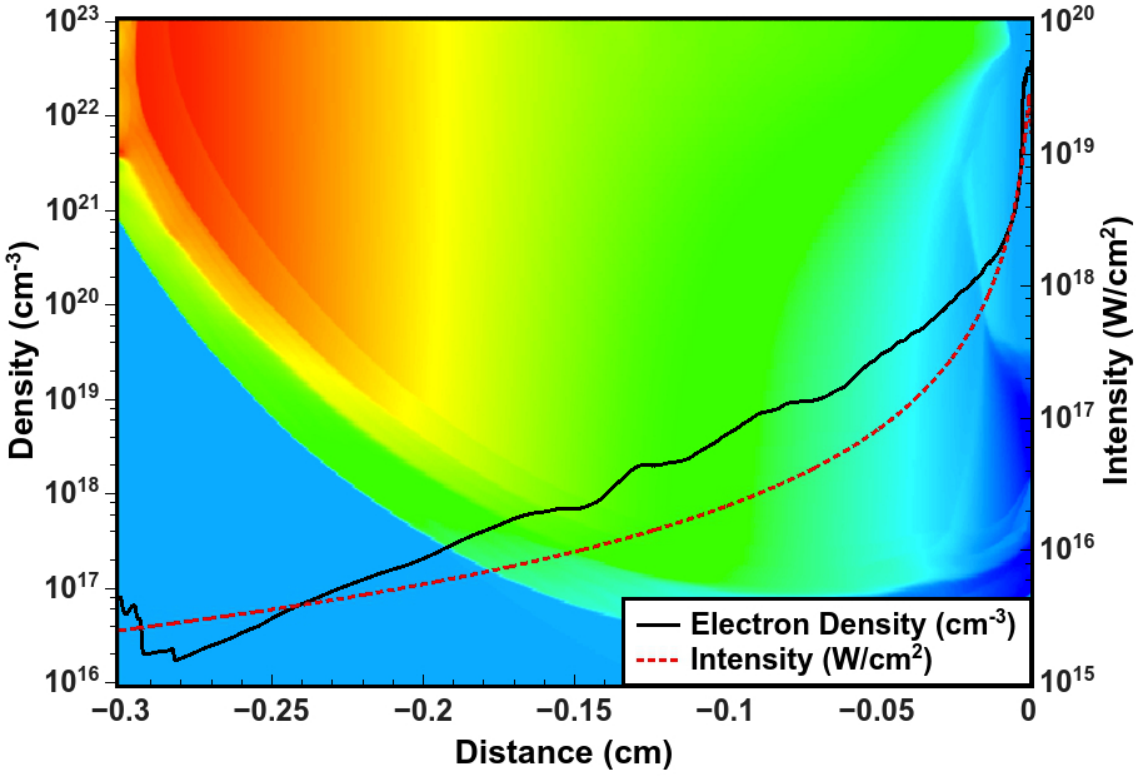

Figure 9.1: Left: 2D FLASH simulations used to estimate the level of pre-plasma created in a medium injected pre-plasma case on Titan. Relative beam intensities and a density lineout are plotted over the mapping of electron velocity away from the target.

greater on Titan and OMEGA-EP than on TPW since the maximum energy used in the Titan long pulse is 150 J and in TPW the maximum was barely 150 mJ. On TPW this was compensated for by making the spot size of the pre-plasma generation beam smaller, but still larger than the size of the high intensity beam's spot. On Titan and OMEGA-EP the long pulse injected pre-plasma beams had energy to spare much larger spot sizes were used to compensate and keep intensity low (200 and 750 µm respectively). Even with the larger spot size, the intensity of the injected pre-plasma beams for the Titan and OMEGA-EP experiments were an order of magnitude larger.

The results from the simulations using the pre-plasma and laser conditions

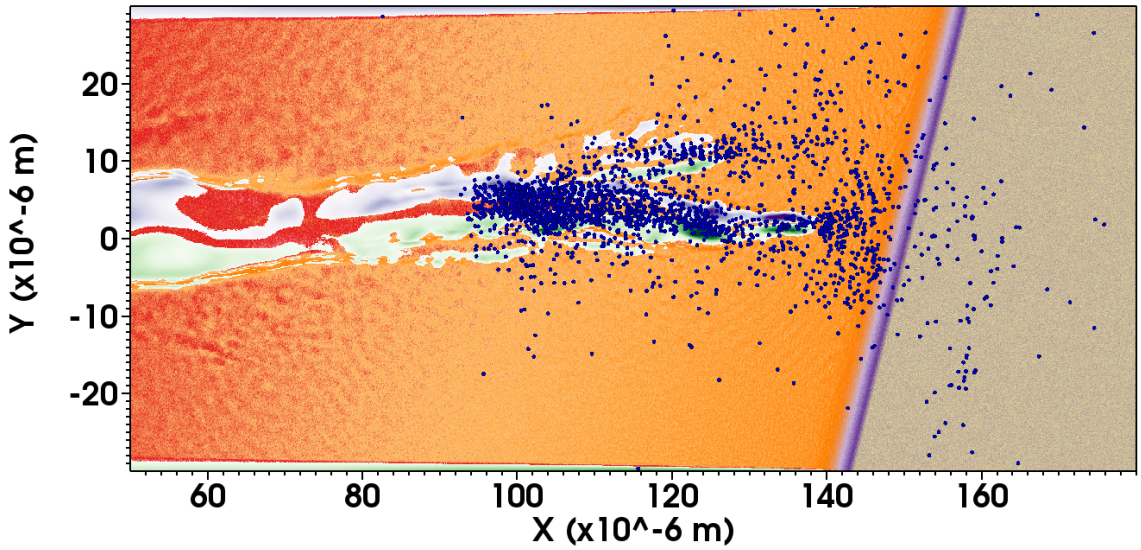

Figure 9.2: Late time image of a 2D EPOCH simulation of a 0.7 ps shot on Titan showing electromagnetic force (purple and green), density and super-ponderomotive (15 MeV) electrons. The pre-plasma is so immense and the beam intensity is so much lower than the main beam never reaches the actual target surface in the simulation. Filamentation is extremely heavy causing the electrons to spread more isotropically than in the TPW simulations.

seen on the Titan experiment are completely different than those in the TPW case:

There are a few things that are immediately clear when looking at the outputs from the new Titan simulations. The most noticable result is that **the beam does not even reach the solid surface of the target**. This is due to a combination of three factors. First, the beam is less intense (2×10^{19} W/cm^2) and therefore does not exert as much ponderomotive pressure on the underdense plasma as the TPW beam (3×10^{20} W/cm^2). Second, the increased level of pre-plasma means that the reduced intensity beam has more mass to push aside. Third, the increased spot size directly corresponds to an increase in the number of filaments as the beam has more opportunities to become unstable.

The ramifications of these effects on generated electrons is two-fold. Super-ponderomotive electrons are once again accelerated far away from the target surface in the laser channel. However, the filamentation of the beam results in the formation

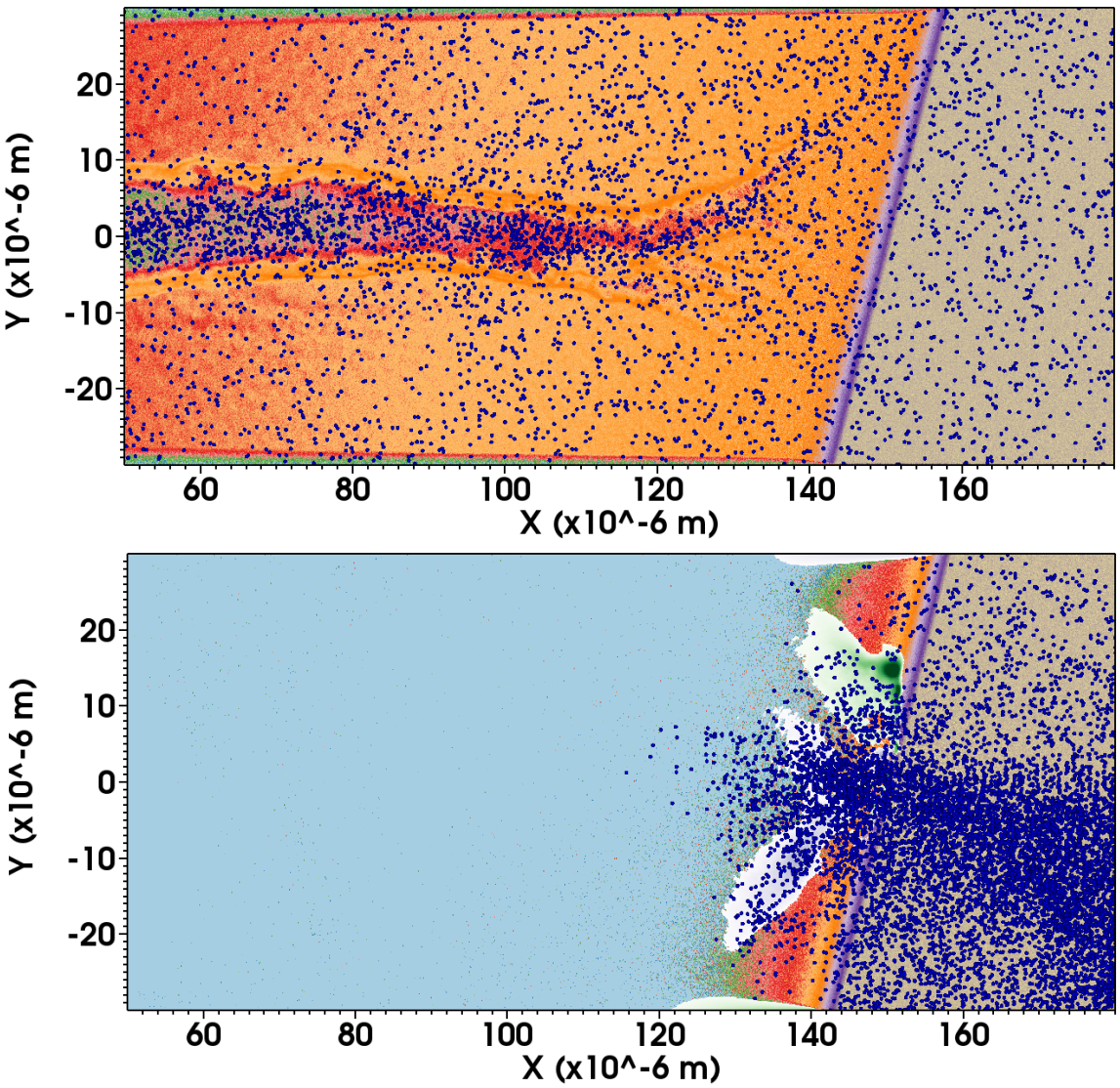

Figure 9.3: Low energy (1.5 MeV) electrons generated in cases with (top) and without (bottom) injected pre-pulse. These results show that low energy electrons become much more diffuse in the injected pre-plasma case.

of several laser channels with different directions. The mixture of fields due to the splitting of the beam causes the forward going super-ponderomotive electrons to enter the target more isotropically rather than being collimated in a single beam as seen in the TPW simulations. Furthermore, there are no significant deflecting fields on the target surface since the beam does not interact with the target surface at all.

Ponderomotive scaling electrons are also greatly impacted; the increase in

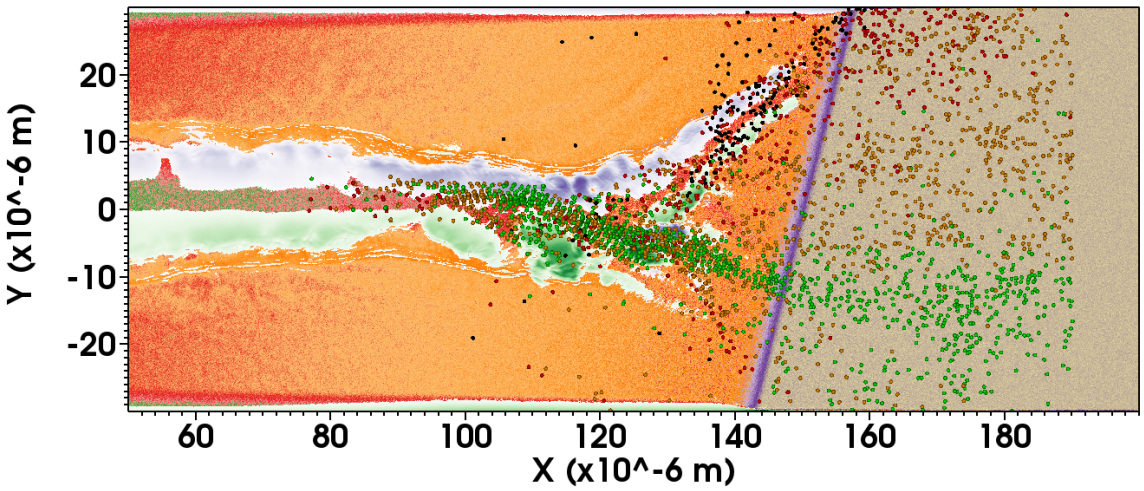

Figure 9.4: Super-ponderomotive (30 MeV) electrons plotted in the 3.0 ps simulation. Angle relative to the EPPS diagnostic (placed at target normal) are shown via color of electrons with green in an acceptance angle window. The isotropic nature of the 0.7 ps simulations extends to the 3 ps case.

filamentation and distance between the target and position where electrons are accelerated results in reducing the quantity of lower temperature electrons that make it into the target. Furthermore, the filamentation of the beam results in beamlets that have less intensity than the original single beam. This change in low energy electron propagation can be most readily seen when plotting 1.5 MeV electrons in simulations with and without the injected pre-plasma (Fig. 9.3).

These effects continue when extrapolated to conditions seen for the 3.0 ps shots on Titan. Intensity is further reduced to 1×10^{19} W/cm^2 and even after 3.0 ps, roughly 4 times the previous pulse length, the beam does not fully impact the target surface (Fig 9.4).

With respect to our Titan experimental results these simulations demonstrate that the inconsistency of measuring super-ponderomotive electrons in the 0.7 ps case are a result of beam filamentation in the pre-plasma rather than fields generated on the target surface by a counter propagating electron current. As the pulse length (and energy) increases more filaments are generated and tend to spread out. As the number

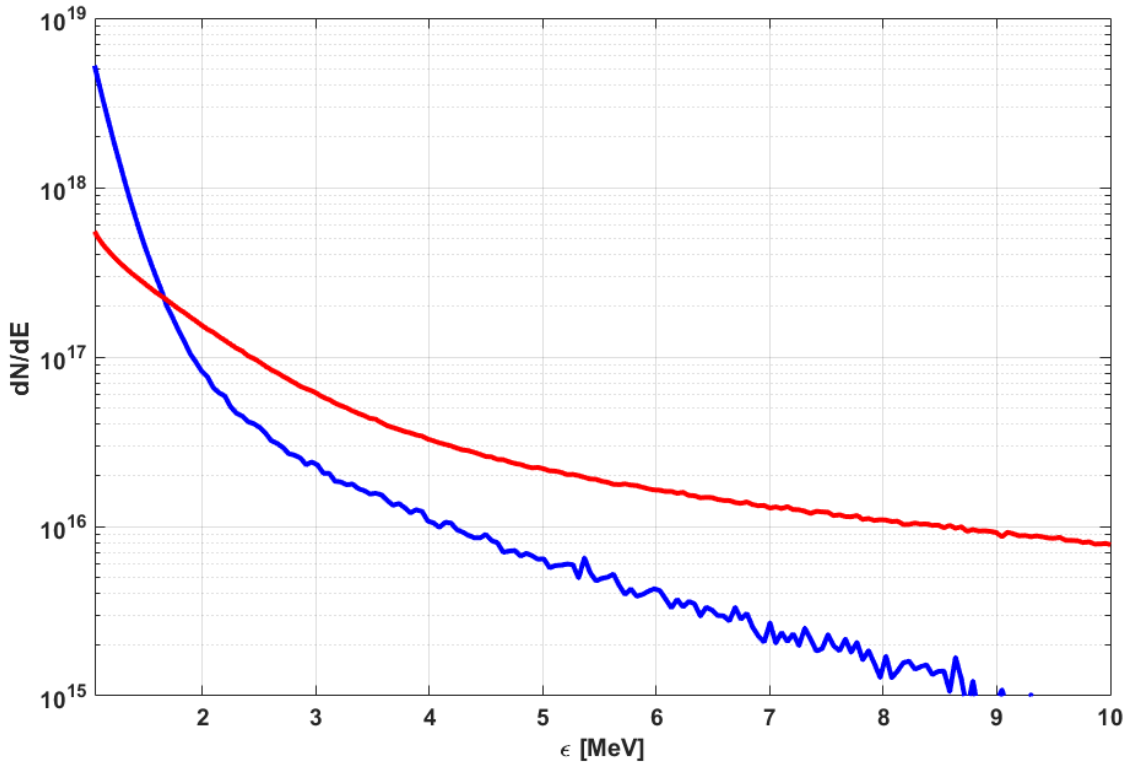

Figure 9.5: Electron spectrum calculated from an extraction plane inside the target, which collected all electrons penetrating 10 µm into the solid target. The cases shown are with a moderate level of injected pre-plasma shown in red and no injected pre-plasma shown in blue. Nearly an order of magnitude more low temperature, ponderomotive scaling electrons make it to the extraction plane when minimal pre-plasma is present.

of filaments increases with pulse length, so too does the chance of measuring super-ponderomotive electrons accelerated in these filaments by the EPPS. This is how a 3.0 ps data set becomes nearly 100% consistent in measuring the super-ponderomotive electron component.

The low energy electron simulations results also corroborate results seen on prior experiments with lower intensity beams incident on pre-plasma [34], [59], [35]. The quantity and temperature of ponderomotive scaling electrons that reach the target drop significantly as pre-plasma increases. A similar result can be seen in the Titan BMXS data in figure 6.10. When integrating the total spectrum crossing into the target region we can see the disparity between ponderomotive and super-

ponderomotive electrons quite clearly in figure 9.3

The EPPS data from OMEGA-EP and 5.0 ps shots on Titan raised two questions that needed to be addressed. First, why are super-ponderomotive electrons rarely generated or measured with an initial pre-plasma for 5 - 10 ps pulse lengths? The 3.0 ps Titan shot data clearly demonstrated that increasing the pre-plasma pulse length to 3.0 ps caused super-ponderomotive electrons to be measured very consistently. Second, why are super-ponderomotive electrons generated more often, or at all without pre-plasma? Once again we turn to 1 and 2D simulations using 2D rad-hydro estimates of pre-plasma density to understand the results.

2D HYDRA [60] simulations of the pre-plasma density profile for OMEGA-EP using the UV beam characteristics show that ns scale pre-pulses result in plasmas that extended hundreds of microns off the surface of the target, similar to that in the Titan case (Fig 9.6). The OMEGA-EP platform provides a unique density measurement diagnostic called the AFR (angluar filter refractometry) which can measure densities very close to the target surface. This allows for extremely accurate density calculations which can be compared to the rad-hydro simulations [53]. The 2D HYDRA simulations were shown to be in good fit with the AFR data which verifies its use in pre-plasma estimates for the other experiments. In the case of OMEGA-EP a fit to the AFR density profile was used for all simulations with a pre-plasma (since it's more accurate to use what density was measured on experiment than what is theoretically supposed to be generated). In the OMEGA-EP experiment there was more injected pre-plasma than on TPW, but less than on Titan. For cases without injected pre-plasma a single scale length of 1 μm was used.

Initial comparisons between electrons generated in the pre-plasma vs no pre-plasma case were performed in 1D since the simulation length of the OMEGA-EP experiment was nearly 100 times longer than the best compression TPW experiment.

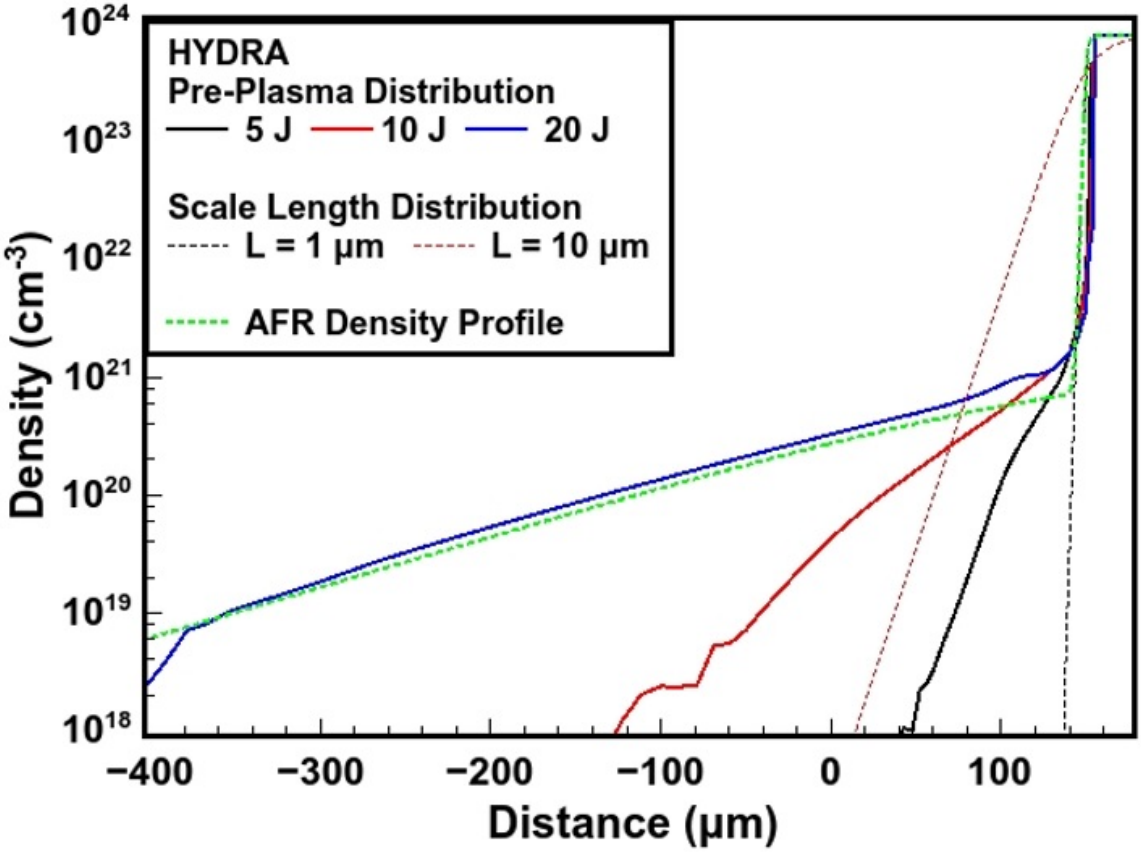

Figure 9.6: HYDRA simulated density profiles of pre-plasma. Single exponential profiles underestimate the distance that underdense plasma extends from the target. The AFR estimated density profile from a maximum injected pre-pulse shot (18.85 J in the UV beam) is shown in dotted green and is in good agreement with the 20 J HYDRA case. For PIC simulations with pre-plasma the AFR curve was used as an initial pre-plasma density profile.

These simulations were conducted for 1, 3, 5 and 10 ps pulse lengths with a simulation box 800 μm long, containing 80 cells per μm with 1000 and 100 particles per cell for electrons and ions respectively. The corresponding time step allows us to correctly resolve the dynamics of the accelerated electrons. Forward going electrons were extracted 30 μm inside the target. As Fig. 9.7 shows, even in the case without pre-plasma, measurable quantities super-ponderomotive electrons were consistently generated for 10 ps pulses. In the 3 ps no pre-plasma case, electrons have temperatures closer in line with ponderomotive scaling predictions, with a cutoff around 20

MeV. With pre-plasma, both 3 and 10 ps pulses generate super ponderomotive electrons as expected with comparable temperatures. Examining time evolving density helps explain why shots with longer pulse lengths without any initial pre-plasma still produce spectra containing significant quantities of super-ponderomotive electrons. It is apparent that self heated plasma expansion takes place over the first 5 ps of the 10 ps pulse (Fig. 9.8). After 5 ps the density profile of the target is remarkably similar to a 10 µm scale length pre-plasma. The plasma that expands functions much as an initial pre-plasma does, allowing an electrostatic potential well to form and accelerate electrons as shown in previous work [43]- [47].

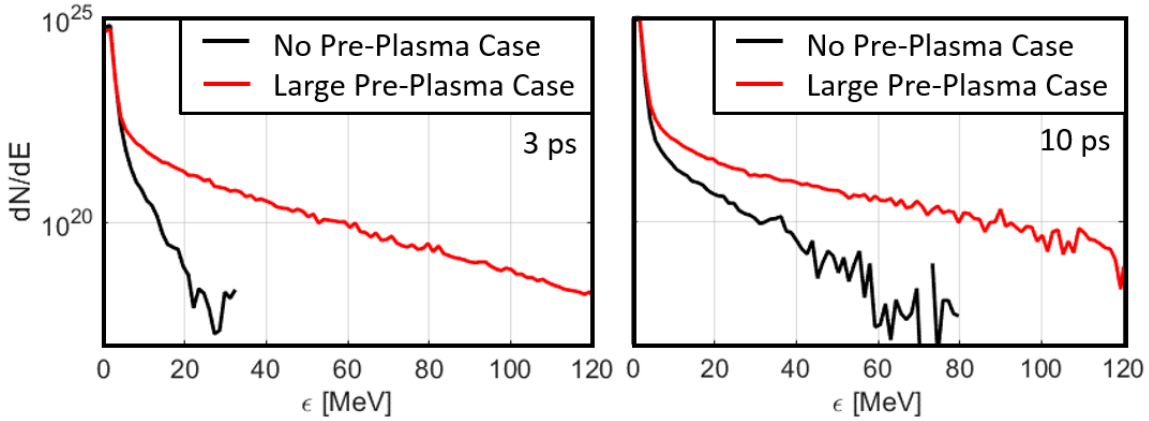

Figure 9.7: 1D EPOCH simulations comparing cases with and without a large pre-plasma for 3 and 10 ps pulses (left and right respectively). The 10 ps case clearly demonstrates the development of super-ponderomotive electrons despite the lack of initial pre-plasma. This is in contrast to the 3 ps case where no super-ponderomotive electrons were seen on a shorter time scale.

While these simulations help explain why a hot electron tail is seen without injected pre-pulse, they do not provide an explanation as to why the hot tail was missing on several shots with pre-pulse. As the SCI data showed in the previous section, large amounts of initial pre-plasma results in significant scatter in the generated electron beam. To resolve this effect 2D simulations are required, however the hundreds of microns of pre-plasma is computationally expensive to simulate in 2D. We therefore simulated 1 and 5 ps pulses with a shorter simulation box, in this case

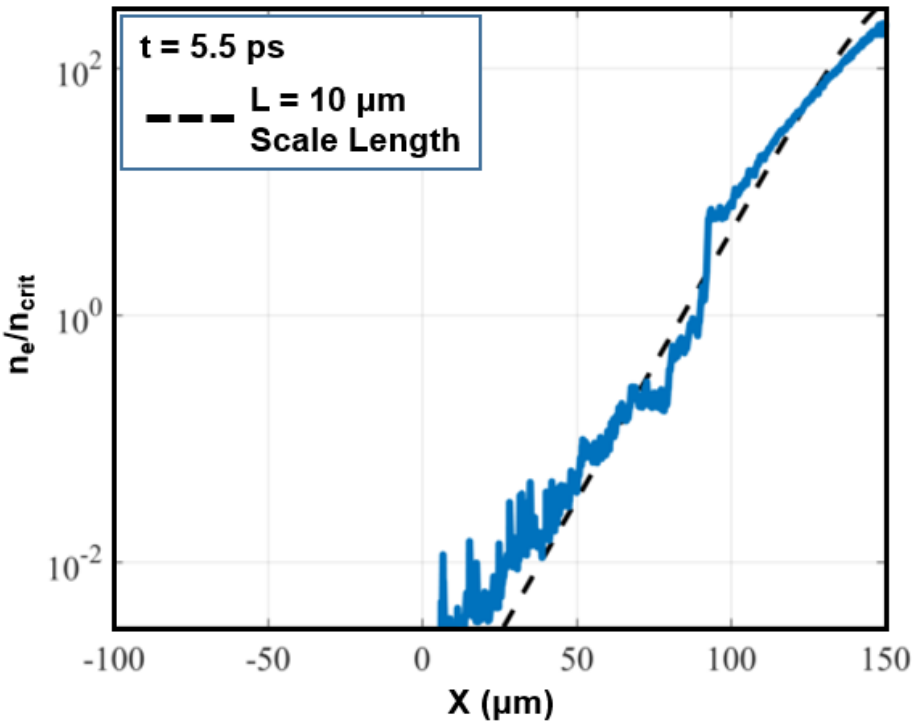

Figure 9.8: Density output at 5.5 ps in a 10 ps simulation with no initial pre-plasma. An underdense plasma expands from the surface and forms a density profile reminiscent of a large scale length pre-plasma, which then allows super-ponderomotive electrons to be trapped and heated later in time.

extended 200 μm along the laser axis and 120 μm in the transverse direction. The resolution for these 2D simulations were 20 and 10 cells per μm for the x and y directions respectively, with 20 and 10 particles per cell for electrons and ions respectively. The same density profiles from the 1D cases are extended to the 2D simulations. The 2D simulations only capture a portion of the significant pre-plasma, as the HYDRA and AFR show that pre-plasma can extend for over 500 μm. However the amount used is still significant enough to demonstrate its effects on generated electrons.

Upon extracting the propagating electrons 30 μm in the target several conclusions can be drawn. Integrating the forward going electron spectra in the 5 ps case demonstrates that the super-ponderomotive electron generation mechanism seen in 1D simulations is preserved in the 2D simulations (Fig. 9.9 (left)), which was also

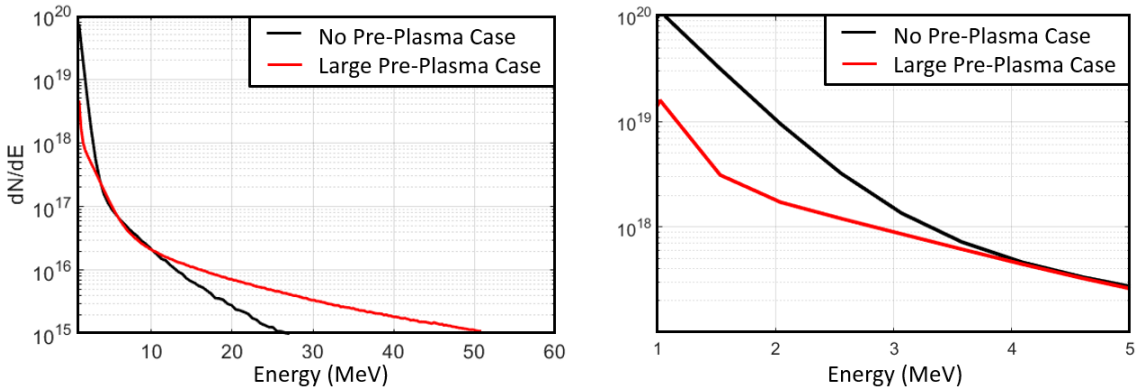

Figure 9.9: Electron spectra outputs for 5 ps pulses with and without pre-plasma. When examining higher energy electrons (left) we can see that the hot electron tail effect is still preserved in these 2D simulations. The low energy portion of the electron energy spectrum (right) demonstrates that the filamentation of the beam caused by the presence of pre-plasma reduces the number of 1-3 MeV, ponderomotive scaling electrons.

seen in work performed by A. Sorokovikova et al. [50]. The measured hot tail is less energetic than in the 1D case, but still present. When examining only the lower energy part of the spectrum, ponderomotive scaling electrons are significantly reduced by the presence of pre-plasma. The filamentation shown in the 2D simulations show the energy is split into two or more beams, effectively reducing their intensity and reducing the quantity of lower energy electrons able to reach the target. As demonstrated in Fig. 9.9 (right), the amount of low energy electrons drop by an order of magnitude. It is also likely that extending these simulations to 3D would enhance this filamentation effect. These results validate those found in the experiment by the BMXS, which shows an effective reduction in temperature for bremsstrahlung generating electrons with pre-plasma was increased. The filamentation of the beam has a similar effect to the poor spot quality seen in the intrinsic pre-plasma experiment. In both cases the beam's energy was split into multiple spots which resulted in a significant drop of lower temperature ponderomotive electrons.

While the super-ponderomotive electrons generated in the 1 ps case were very isotropic with little structure or divergence, the ones generated in the 5 ps case with

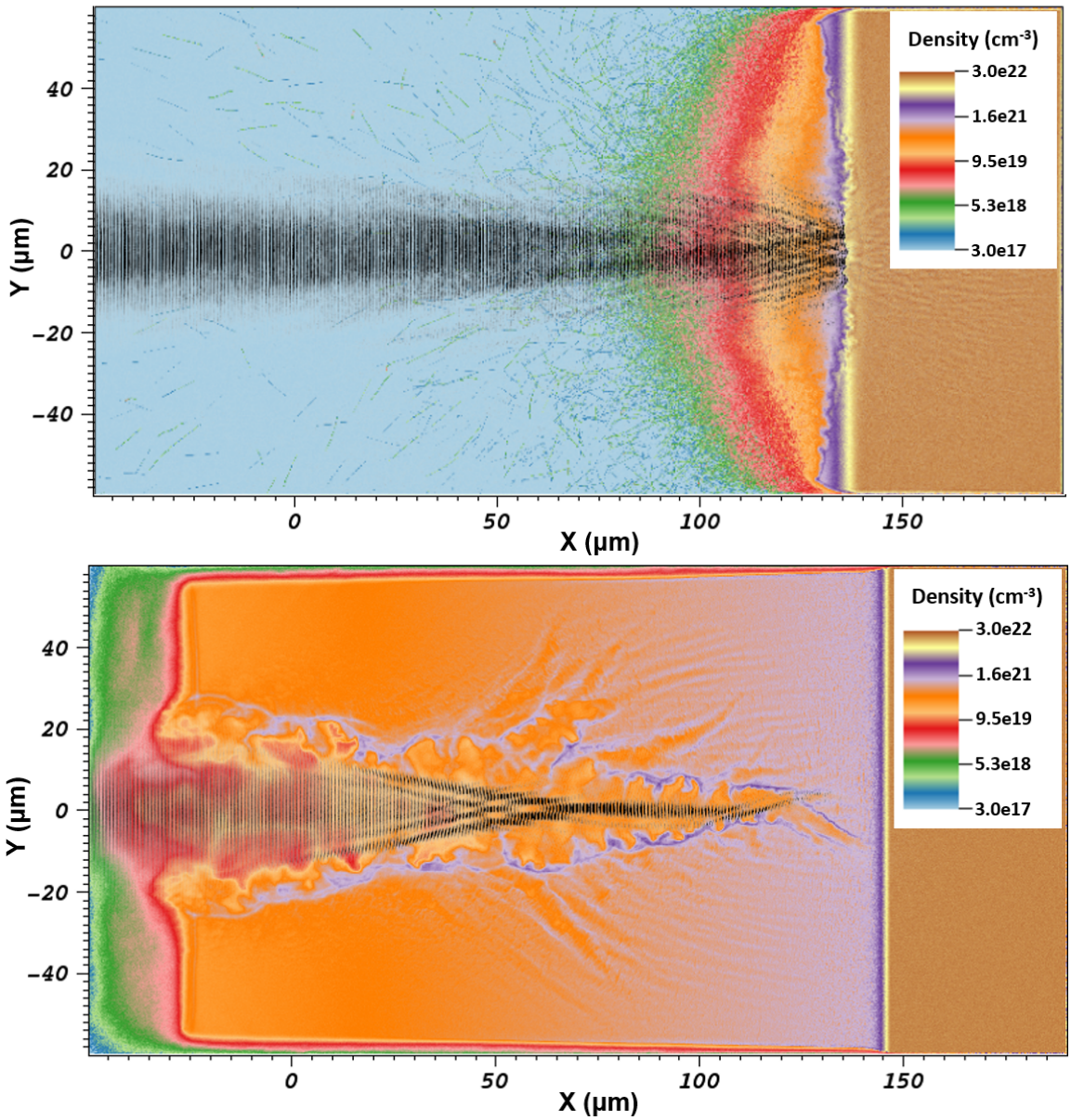

Figure 9.10: Density and electric field snapshot of a 2D EPOCH simulations of a 5 ps pulse with (bottom) and without (top) pre-plasma. Clear relativistic self focusing occurs nearly 100 μm from the critical surface causing the beam to focus and then diverge into multiple filaments prior to generating electrons. A fiducial at 3 ps shows that high energy electrons are generated earlier in time when an initial pre-plasma is present.

pre-plasma were splintered into filaments that evolve over time. By plotting the angle of super-ponderomotive electrons inside the target with respect to time we can see how the electron beam evolves. As shown in Figure 9.11, in our simulations super-

ponderomotive electrons are primarily contained in a single filament that changes angle over time. Electrons begin with an angle of around 20 degrees but increase over time. This process is extremely random the direction and quantity of the laser filaments that accelerate electrons is greatly dependent on the initial pre-plasma and laser spot conditions. Concerning lower energy electrons, the filamentation and push-back of the critical density regions helps explain our SCI data, which showed that the speckled electron trace images were a product of pre-plasma and longer pulse lengths. This also means that the laser energy is split into multiple beams prior to interacting with the critical surface as shown in Fig. 9.10. This result is similar to those seen in previous experiments performed by L. Willingale et al. [40] and in high Z cone pre-plasma simulations discussed by A. G MacPhee [41], which demonstrate this filamentary effect in detail. Finally it is notable that there are quite a few super-ponderomotive electrons generated in the 5 ps case without pre-plasma. The bulk of these are generated and measured at 4 ps into the 5 ps pulse, after an underdense expanding plasma has been established. In Fig. 9.11 we can see in the pre-plasma case, the bulk of high energy electrons are generated nearly 1 ps earlier, since a low density plasma is established prior to the pulse's arrival. This supports the findings of the 10 ps 1D simulations in Fig. 9.7, which show that this underdense expanding plasma can significantly increase super ponderomotive electron production on longer time scales, even without an initial pre-plasma. The super-ponderomotive electrons in the no pre-plasma case are much more isotropic than in the case with an initial pre-plasma; this is likely due to the fact that the laser does not initially filament during the interaction. The underdense plasma that develops is smaller than the injected pre-plasma created by the UV beam and therefore does not provide a large enough region for significant filamentation to occur.

These results shed some light on why there is a greater chance of measuring a

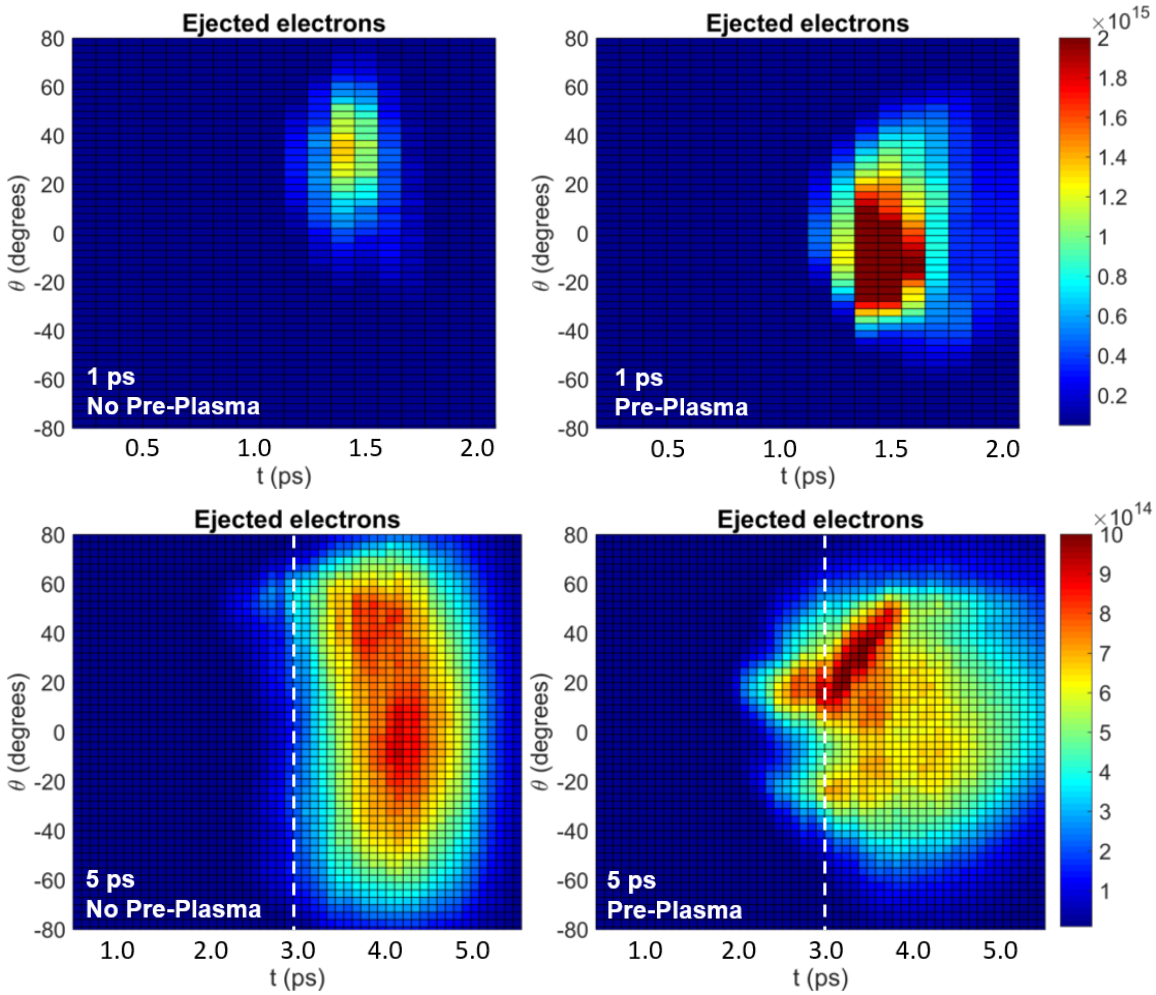

Figure 9.11: Divergence angle of > 5 MeV electrons vs time for 1 (top) and 5 ps (bottom) simulations with (right) and without (left) pre-plasma. Beam filamentation developing over time leads to the higher energy electrons being more divergent and less likely to be measured by EPPS. The cases without pre-plasma shows electrons are generated in a uniform single spot.

hot electron tail with EPPS when there is no initial pre-plasma. In cases with heavy pre-plasma the laser filaments away from the axis (and the spectrometer) and the bulk of hot electrons miss the diagnostic entirely. Ponderomotive scaling electrons are more isotropic and can be consistently measured resulting in green and blue spectra seen in Fig 8.7. As the 1 and 2D simulations show, generating a hot electron tail is possible without an initial pre-plasma for long pulse lengths. However since the filamentation effect scales with level of initial pre-plasma it will be more likely to be measured in

cases without pre-plasma, which is what was observed on the experiment. It is likely that extending these simulations to 3D or increasing the simulation box length to include more pre-plasma would enhance this filamentation effect further resulting in larger temperature drops for ponderomotive electrons and greater angular divergence.

This chapter contains some material and figures from "Investigation of Laser Pulse Length and Pre-Plasma Scale Length Impact on Hot Electron Generation on OMEGA-EP", J. Peebles, M. S. Wei, A. V. Arefiev, C. McGuffey, R. B. Stephens, W. Theobald, D. Haberberger, L. C. Jarrott, A. Link, H. Chen, H. S. McLean, A. Sorokovikova, S. Krasheninnikov, F. N. Beg, New Journal of Physics **19**, 023008 (2017). The dissertation author was the primary investigator and author of this paper.

Chapter 10
Conclusions and Future Work

10.1 Conclusions

In conclusion, multiple experiments were conducted across 3 laser platforms to examine the impact of pulse length and pre-plasma scale length on super-ponderomotively accelerated electrons.

Experiments and supporting simulations found that super-ponderomotive electrons require a high intensity laser to have a pulse length of at least 400 fs in order to be accelerated. It was demonstrated via PIC simulations that many of these electrons are accelerated far away from the target in the pre-plasma and travel towards the target along the trajectory of the laser. Experiments and simulations showed electrons accelerated by the reflected beam form a counter propagating current which creates a deflecting magnetic field. The degree of electron deflection is highly dependent on the incident angle of the beam, amount of pre-plasma and beam intensity. If the beam channels through the pre-plasma and makes it to the target, large deflecting magnetic fields develop. If the beam filaments and splits into multiple less intense filaments due to an abundance of pre-plasma they are less likely to reach the target and super-ponderomotive electron trajectory will be dominated by the trajectory of the filamenting beams. This regime of filamentation dominance was seen on experiments with longer pulse lengths, larger pre-plasmas and lower intensity beams (Titan and OMEGA-EP).

Results from 5 ps Titan and 10 ps OMEGA-EP interactions also demonstrated that super-ponderomotive electrons can be generated without an initial scale length pre-plasma. This is likely due to self heated plasma expansion which forms an underdense plasma similar to a pre-plasma. Electrons are accelerated in this underdense

plasma in the latter part of the longer laser pulse and achieve energies similar to cases with an initial pre-plasma present. The trajectories for super-ponderomotive electrons in these two cases is extremely different. In the case of an initial underdense plasma, electron trajectory is determined by the direction of the filaments traveling through underdense plasma. In the case of an underdense plasma that develops over the course of the laser pulse, super-ponderomotive electrons tend to be more uniform since the beam does not undergo severe filamentation. Ponderomotive scaling electrons behave more simply; on all experiments regardless of pulse length large quantities of pre-plasma reduce the temperature and quantity of these ponderomotive scaling electrons.

What does this all mean? Well it depends greatly on which electrons are of interest. From a fast ignition stand point, the results from experiments using the longer 10 ps pulses are not entirely encouraging. Any quantity of initial pre-plasma will significantly inhibit generation 1-3 MeV electrons which are used to deposit energy into the compressed hot spot. Furthermore, laser energy will be effectively wasted accelerating super-ponderomotive electrons in the pre-plasma. Even with the initial pre-plasma entirely removed, self heated underdense plasmas form in front of the target for the longer pulse lengths used on full scale fast ignition experiments. At later times in longer pulses fewer 1-3 MeV electrons are created due to the increase in underdense plasma while more energy is dumped into accelerating higher energy electrons which will not couple to the compressed fuel.

From a particle acceleration standpoint the short pulse length experiments show a somewhat promising result. Super-ponderomotive electrons, which scale very well with laser intensity, can be generated in large quantities with short pulses. However, future experiments which use a pre-plasma to accelerate electrons must be extremely careful with all aspects of experimental setup. Magnetic fields from the laser

impacting the target surface can significantly deflect the electrons generated in the pre-plasma which pass nearby. Small changes in laser incidence angle can result in massive changes to electron trajectory. This is an important consideration since many high intensity laser platforms do not allow for a normal incidence beam on target due to potential for equipment damage due to reflected light. Level of pre-plasma, spot size and beam intensity all affect the degree of filamentation and can be dominant effects if not accounted for.

10.2 Future Work: Particle Acceleration in an External Magnetic Field

The trajectory for high energy electrons has been shown to be very important for the development of a strong electrostatic sheath field used to accelerate ions and protons [12]. While protons are heavy and difficult to contain with a magnetic field, electrons which comprise the sheath are more easily manipulated. 2D EPOCH simulations show that a large axial magnetic field significantly collimates electrons in a high-intensity interaction, altering the geometry of the sheath field. The magnetic field severely limits lateral electron movement changing the topology of the electric sheath field on the rear surface of the target.

Previously, platforms to explore interactions in an externally applied magnetic field were very difficult to carry out, often utilizing pulsed power devices with sustained magnetic fields of up to 10 T [61]. These magnetic fields are found to be too weak in order to impact electron trajectories or energies significantly. A new type of platform called a "laser driven coil" shows much promise in the generation of > 100 T fields sustained for over a nanosecond [62]. These coils use the sheath field that develops in a laser plasma interaction that is not dissimilar to the one seen in TNSA. When a laser forms plasma on a solid target, electrons leave the target more readily than the heavier ions, which lag behind, leading to a charge imbalance and current

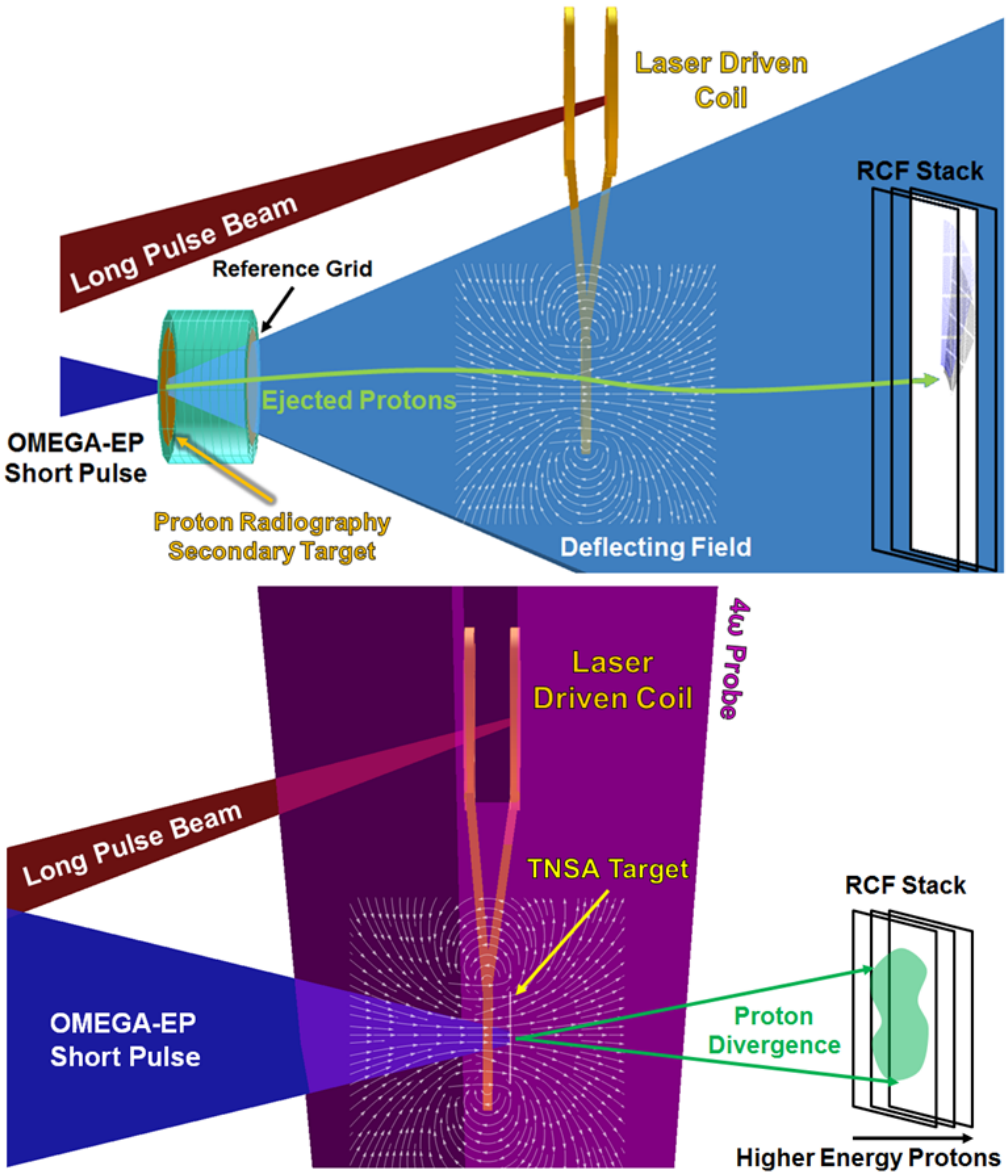

Figure 10.1: Schematic of future experimental setup for interactions with an externally applied magnetic field. (Top) proton probing down the axis of the coil along the measures the magnetic field by looking at its radial component. This field causes the protons to rotate about the axis whereas an electric field will focus or defocus protons. (Bottom) A target is placed in the external field and hit with a short pulse high intensity laser; changes in the electron and proton energies and trajectories will be measured and compared with different levels of field.

flow. This current flow can be utilized by designing a target such that the current flows in a loop near the region of interest, creating an axial magnetic field. This current has been used to generate magnetic field in a number of experiments, though measuring the field on these experiments has had mixed and confusing results [63]-[65]. Placing crystals for Faraday rotation measurements and B-dot probes near the region of interest results in their destruction due to the hostile environment of the interaction. Therefore measurements using these tools have almost always been of fringe fields, which are then extrapolated. This extrapolation technique leads to a large variance in reported results (100T to 1.5 kT!) Proton radiography has also been a tool used to measure the magnetic field, however the electric field from the target charging causes a large degree of error in this measurement.

Future experiments will be designed to first characterize the laser driven coils, then use them to magnetize a secondary high intensity interaction. Using a facility such as OMEGA-EP or Titan, future experimental designs are shown in figure 10.1. These experiments will utilize proton probing along the axis of the coil to characterize magnetic and electric fields. When the secondary high intensity interaction is placed in the magnetic field, TNSA protons will be measured via a radiochromic film pack and electrons will be measured via multiple magnetic electron spectrometers. It is anticipated that the addition of the magnetic field will decrease both electron and proton divergence and increase the TNSA proton energy.

10.3 Future Work: Super-Ponderomotive Electrons

Throughout the course of the experiments outlined in this dissertation it is clear that diagnostics for measuring high energy electrons are extremely limited in two ways. The first way, indicated by the EPPS's small pinhole, is that high energy electron diagnostics have a very limited acceptance angle for measurement. The EPPS measurement is a small sample of the electrons that leave the target, and unless

electrons behave isotropically, they are easily missed by the EPPS. A new diagnostic that captures a much wider solid angle measurement could be extremely useful in understanding how electrons behave on experiments. This could potentially be done by using a slit spectrometer rather than a pinhole one, similar to the iWASP (ion Wide Angled Spectrometer) which is used for proton spectroscopy [67]. A further capability that has some interest is the development of a time resolved electron spectrometer with picosecond resolution, which could help confirm the times at which electrons are generated in the interaction. Currently *x-ray* framing cameras have a resolution of around 10 ps [66] and could be potentially used with Kα imaging systems to have a time resolved trace of electrons. However, such a system would not be able to distinguish different electron energies. In particular measuring super-ponderomotive electrons, which are fewer in number compared to ponderomotive scaling electrons, with such a system would be difficult.

Such diagnostics could allow future experiments to be more easily compared to simulation results. Follow up experiments on high intensity lasers such as TPW could change beam incidence angle, target material and levels of pre-plasma while using these diagnostics to measure changes in the directionality of the super-ponderomotive electron component of the spectrum. Further useful experiments can still be conducted using current diagnostics; it would be difficult, but possible, to conclusively verify the magnetic field deflection effect by placing several EPPSes facing the rear surface of the target. At least one of these should be placed in the laser direction and another in the target normal direction. On this experiment beam incidence angle can be changed to verify the changes in electron deflection seen in section 5. Multiple spectrometers placed around the rear surface of the target would also verify that the super-ponderomotive electron beam is more collimated rather than isotropic. Some easy modifications can be performed on the EPPS in order to improve its collection

capability. Moving the diagnostic closer to the target and expanding the pinhole slightly will greatly expand the solid angle measured by the diagnostic at the cost of increased x-ray noise. Future experiments on high intensity facilities such as TPW should also use spectrometers with stronger magnetic fields since on several shots electrons were detected past the end of the spectrometer.

10.4 Future Work: Unexplained TPW Results

The results from the second TPW experiment has one large unanswered question: why is it that when super-ponderomotive electrons are measured, ponderomotive scaling electrons are greatly reduced? At first this appears to be in line with other results, where ponderomotive electrons are reduced in temperature and quantity when a pre-plasma is present. However, there were several shots on TPW where pre-plasma was present and no super-ponderomotive electrons were measured. In these cases the electron spectra were very similar to the no pre-plasma result. This means that it is likely that the drastic change in the lower energy electron spectrum may not be due to the pre-plasma impeding $\mathbf{J} \times \mathbf{B}$ acceleration. Rather it implies that super-ponderomotive electrons disrupt lower energy electrons from being measured by the EPPS diagnostic.

An explanation for this behavior may be found in the rear target surface, where a strong electrostatic sheath field develops from electrons leaving. Depending on when and where electrons leave the rear target, and their temperature, lower energy electrons may be inhibited by a strong electrostatic field, preventing a significant number of them from being measured by EPPS. Verifying the formation and strength of such a sheath field for our experimental setup is extremely difficult, since including the entire target increases the simulation box by over a millimeter along the laser direction. A potential way to overcome this is to extract electrons as they enter

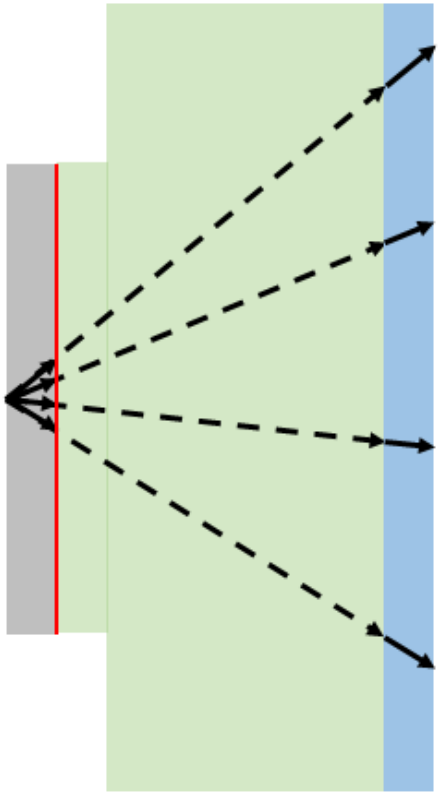

Figure 10.2: Cartoon of proposed simulation setup. In gray the original simulation produces electrons with trajectories measured by the extraction plane shown in red. These are extrapolated over the majority of the target (green) until just before the rear surface. A second simulation of the rear surface (blue) is conducted using electrons injected with the extrapolated position and trajectory.

the target and assume they are ballistic. Once their trajectories are known, their position after traveling a millimeter inside the target can be extrapolated and a second simulation can simulate them leaving the rear surface.

10.5 Future Work: Waves and Postsolitons from Titan's Proton Radiography

While several features seen in the proton radiographs on the Titan experiment have satisfactory explanations, the wave and postsoliton feature does not. Typically

PIC simulations are used to help explain features similar to this. However, constructing a 2D or 3D simulation that can capture the developing wave features seen on experiment on the spatial and time scales that they occur is an extremely difficult computation problem. Shown in Fig 7.12 are the relevant parameters outputted from a 2D rad-hydro simulation for use in a PIC simulation. The region where waves were generated is shown to be roughly 2.5 mm away from the target surface, or where the intensity is around 4×10^{15} W/cm^2, density is roughly $6 \times 10^{15} cm^{-3}$ and the electrons have a velocity significant velocity in the negative x direction. 1D simulations using the intensity and density have been run for 30 ps and show no discernible wave formation.

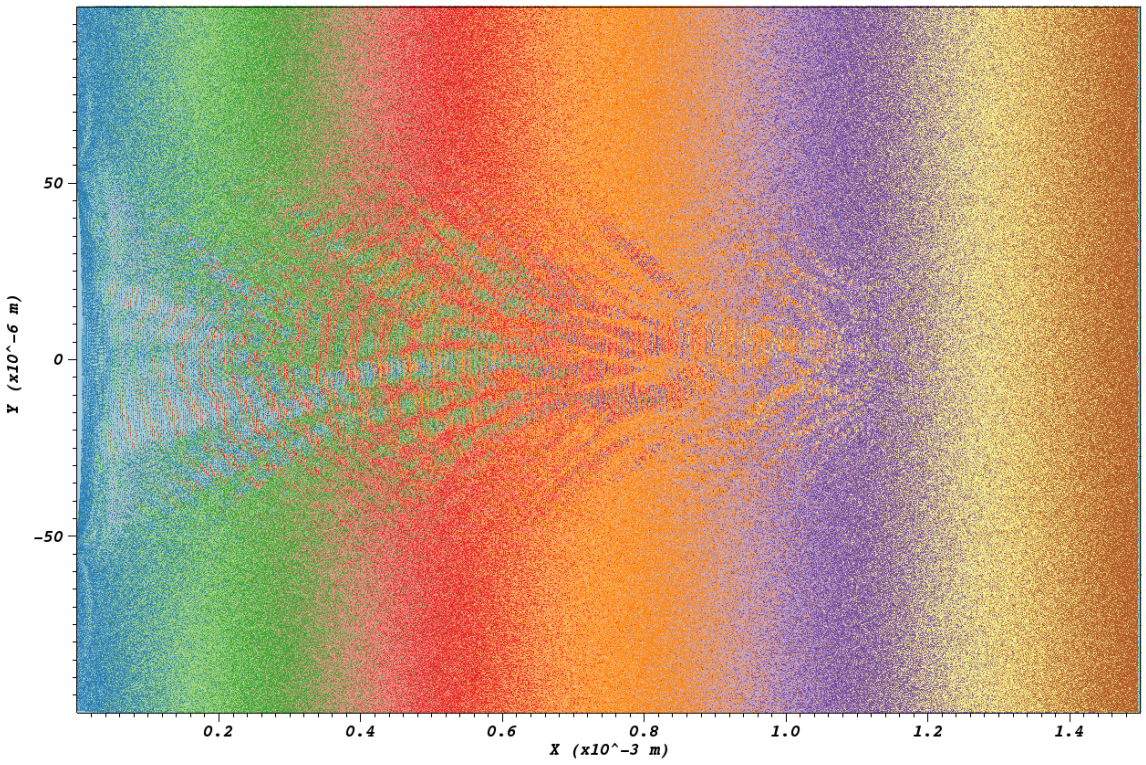

Figure 10.3: Initial 2D PIC simulations of conditions on Titan experiment in the region of underdense plasma. Some rippling of the electron density is seen which grows with time. However, current simulations do not correctly show the development of *propagating* waves.

Since the size of the beam is on the same scale length as the waves near the point where the waves are generated 2D effects may play a large role. The flat 1D portion of the wave fronts are much smaller compared to the size of the low intensity beam. Furthermore, the 1D simulations did not test the impact of giving the electron plasma a large initial velocity. In the region where waves were generated the velocity of the expanding plasma was highest.

2D simulations are currently being performed using EPOCH with these parameters. Since it is unclear which parameters impact wave generation, scaling certain parameters to reduce computation burden may inadvertently prevent them from being formed and observed. Therefore a range of simulations will be conducted over tens of picoseconds.

REFERENCES

[1] M. D. Rosen,"The physics issues that determine inertial confinement fusion target gain and driver requirements: A tutorial," Physics of Plasmas, **vol. 6, no. 5**, 1690 (1999);

[2] J. Lindl, "Development of the indirect-drive approach to inertial confinement fusion and the target physics basis for ignition and gain," Physics of Plasmas, **2**, 3933 (1995);

[3] R. Betti, V. N. Goncharov, R. L. McCrory, and C. P. Verdon, "Growth rates of the ablative RayleighTaylor instability in inertial confinement fusion," Physics of Plasmas **5**, 1446 (1998);

[4] M. Tabak, J. Hammer, M. E. Glinsky, W. L. Kruer, S. C. Wilks, J. Woodworth, E. M. Campbell, M. D. Perry, and R. J. Mason, "Ignition and high gain with ultrapowerful lasers", Physics of Plasmas, **1**, pp. 1626-1634, (1994);

[5] S. Atzeni, "Inertial fusion fast ignitor: Igniting pulse parameter window vs the penetration depth of the heating particles and the density of the precompressed fuel", Physics of Plasmas, **6**, 3316 (1999);

[6] M. Roth, T. E. Cowan, M. H. Key, S. P. Hatchett, C. Brown, W. Fountain, J. Johnson, D. M. Pennington, R. A. Snavely, S. C. Wilks, K. Yasuike, H. Ruhl, F. Pegoraro, S. V. Bulanov, E. M. Campbell, M. D. Perry, and H. Powell, "Fast Ignition by Intense Laser-Accelerated Proton Beams," Physical Review Letters **86**, 436 (2001);

[7] Y. Mori, Y. Nishimura, R. Hanayama, S. Nakayama, K. Ishii, Y. Kitagawa, T. Sekine, N. Sato, T. Kurita, T. Kawashima, H. Kan, O. Komeda, T. Nishi, H. Azuma, T. Hioki, T. Motohiro, A. Sunahara, Y. Sentoku, and E. Miura, "Fast Heating of Imploded Core with Counterbeam Configuration," Physical Review Letters **117**, 055001 (2016);

[8] S. Hatchett and M. Tabak, Cone focus geometry for Fast Ignition, presented at the 30th Annual Anomalous Absorption Conference, Ocean City, MD (April 2000);

[9] M. H. Key, J. C. Adam, K. U. Akli, M. Borghesi, M. H. Chen, R. G. Evans, R. R. Freeman, H. Habara, S. P. Hatchett, J. M. Hill1, A. Heron, J. A. King, R. Kodama, K. L. Lancaster, A. J. MacKinnon, P. Patel, T. Phillips, L. Romagnani, R. A. Snavely, R. Stephens, C. Stoeckl, R. Town, Y. Toyama, B. Zhang, M. Zepf, and P. A. Norreys, "Fast ignition relevant study of the flux of high intensity laser-generated electrons via a hollow cone into a laser-imploded plasma," Physics of Plasmas **15**, 022701 (2008);

[10] R. Kodama, Y. Sentoku, Z. L. Chen, G. R. Kumar, S. P. Hatchett, Y. Toyama, T. E. Cowan, R. R Freeman, J. Fuchs, Y. Izawa, M. H. Key, Y. Kitagawa, K. Kondo, T. Matsuoka, H. Nakamura, M. Nakatsutsumi, P. A. Norreys, T. Norimatsu, R. A. Snavely, R. B. Stephens, M. Tampo, K. A. Tanaka and T. Yabuuchi, "Plasma devices to guide and collimate a high density of MeV electrons,," Nature **432**, 1005-1008 (23 December 2004);

[11] S. C. Wilks, A. B. Langdon, T. E. Cowan, M. Roth, M. Singh, S. Hatchett, M. H. Key, D. Pennington, A. MacKinnon, and R. A. Snavely, "Energetic proton generation in ultra-intense laser-solid interactions", Physics of Plasmas **8**, 542 (2001);

[12] A. Arefiev, T. Toncian, G. Fiksel, "Enhanced proton acceleration in an applied longitudinal magnetic field," New Journal of Physics **18**, 105011 (2016);

[13] W. Bambynek, B. Crasemann, R. Fink, H.-U. Freund, H. Mark, C. Swift, R. Price, and P. V. Rao, "X-ray fluorescence yields, auger, and coster-kronig transition probabilities", Reviews of Modern Physics, **vol. 44, no. 4**, 716, (1972);

[14] I. Pomerantz, E. McCary, A.R. Meadows, A. Arefiev, A.C. Bernstein, C. Chester, J. Cortez, M.E. Donovan, G. Dyer, E. W. Gaul, D. Hamilton, D. Kuk, A.C. Lestrade, C. Wang, T. Ditmire, and B.M. Hegelich, "Ultrashort Pulsed Neutron Source," Physical Review Letters **113**, 184801 (2014);

[15] H.-S. Park, D. M. Chambers, H.-K. Chung, R. J. Clarke, R. Eagleton, E. Giraldez, T. Goldsack, R. Heathcote, N. Izumi, M. H. Key, J. A. King, J. A. Koch, O. L. Landen, A. Nikroo, P. K. Patel, D. F. Price, B. A. Remington, H. F. Robey, R. A. Snavely, D. A. Steinman, R. B. Stephens, C. Stoeckl, M. Storm, M. Tabak, W. Theobald, R. P. J. Town, J. E. Wickersham and B. B. Zhang, "High-energy K radiography using high-intensity, short-pulse lasers," Physics of Plasmas **13**, No. 5, 056309 (2006);

[16] C. Courtois, A. Compant La Fontaine, O. Landoas, G. Lidove, V. Mot, P. Morel, R. Nuter, E. Lefebvre, A. Boscheron, J. Grenier, M. M. Alonard, M. Gerbaux, F. Gobet, F. Hannachi, G. Malka, J. N. Scheurer and M. Tarisien, "Effect of plasma density scale length on the properties of bremsstrahlung x-ray sources created by picosecond laser pulses," Physics of Plasmas **16** No. 1, 013105 (2009);

[17] W. Theobald, K. Akli, R. Clarke, J. A. Delettrez, R. R. Freeman, S. Glenzer, J. Green, G. Gregori, R. Heathcote, N. Izumi, J. A. King, J. A. Koch, J. Kuba, K. Lancaster, A. J. MacKinnon, M. Key, C. Mileham, J. Myatt, D. Neely, P. A. Norreys, H.-S. Park, J. Pasley, P. Patel, S. P. Regan, H. Sawada, R. Shepherd, R. Snavely, R. B. Stephens, C. Stoeckl, M. Storm, B. Zhang and T. C. Sangster, "Hot surface ionic line emission and cold K-inner shell emission from petawatt-laser-irradiated Cu foil targets," Physics of Plasmas **14** No. 4, 043102 (2006);

[18] John David Jackson. Classical Electrodynamics, 2nd Edition. John Wiley & Sons, Inc., (1975);

[19] S. V. Bulanov, T. Z. Esirkepov, F. F. Kamenets, Y. Kato, A. V. Kuznetsov, K. Nishihara, F. Pegoraro, T. Tajima, and V. S. Khoroshkov, "Generation of high-quality charged particle beams during the acceleration of ions by high-power laser radiation", Plasma Physics Reports **28**, 975 (2002);

[20] D. Wagenaar (1995) "7.1.3 The Bragg Curve", **Radiation Physics Principles**, Archived from the original on 1 March 2016. Retrieved 27 January 2016;

[21] S. P. Hatchett, C. G. Brown, T. E. Cowan, E. A. Henry, J. A. Koch, A. B. Langdon, B. F. Lasinski, R. W. Lee, A. J. Mackinnon, D. M. Pennington, M. D. Perry, T. W. Phillips, M. Roth, T. C. Sangster, M. S. Singh, R. A. Snavely, M. A. Stoyer, S. C. Wilks and K. Yasuike, "Electron, photon, and ion beams from the relativistic interaction of Petawatt laser pulses with solid targets," Physics of Plasmas, **7**, 2076 (2000);

[22] T. Tajima and J. M. Dawson, "Laser Electron Accelerator," Physical Review Letters, **Vol 43, No 4**, (1979);

[23] S. C. Wilks, W. L. Kruer, M. Tabak, and A. B. Langdon, "Absorption of ultra-intense laser pulses," Physical Review Letters **69**, 1383 (1992);

[24] F. Brunel, "Not-so-resonant, resonant absorption," Physical Review Letters, **vol. 59, p. 52**, 1987;

[25] V. L. Ginzberg, *The Properties of Electromagnetic Waves in Plasma.* Pergamon, New York, 1964;

[26] A. D. Krumbein, Y. Shima, and H. Yatom, "Inverse bremsstrahlung energy absorption in laserirradiated plasmas," Journal of Applied Physics **6167**, (1978);

[27] S. Keppler, A. Savert, J. Korner, M. Hornung, H. Liebetrau, J. Hein and M. C. Kaluza, "The generation of amplified spontaneous emission in high-power CPA laser systems," Laser and Photonics Reviews **10**, 264-277 (2016);

[28] L. Biermann, Z. Naturforsch.,"Uber den Ursprung der Magnetfelder auf Sternen und im interstellaren Raum," 5a, 65 (1950);

[29] A. J. Kemp, Y. Sentoku and M. Tabak, "Hot-electron energy coupling in ultraintense laser-matter interaction," Physical Review E **79**, 066406 (2009);

[30] Z.-M. Sheng, K. Mima, Y. Sentoku, M. S. Jovanović,1 T. Taguchi, J. Zhang, and J. Meyer-ter-Vehn, "Stochastic Heating and Acceleration of Electrons in Colliding Laser Fields in Plasma," Physical Review Letters, **Vol 88 No 5**, (2002);

[31] B. S. Paradkar, M. S. Wei, T. Yabuuchi, R. B Stephens, M. G. Haines, S. I. Krasheninnikov, F. N. Beg, "Numerical modeling of fast electron generation in the presence of preformed plasma in laser-matter interaction at relativistic intensities," Physical Review E **83**, 046401 (2011);

[32] B. S. Paradkar, S. I. Krasheninnikov, and F. N. Beg, "Mechanism of heating of pre-formed plasma electrons in relativistic laser-matter interaction," Physics of Plasmas **19**, 060703 (2012)

[33] A. P. L. Robinson, A. V. Arefiev and D. Neely, "Generation of 'Super-Ponderomotive' Electrons due to a non-Wakefield interaction between a Laser Pulse and a Longitudinal Electric Field," Physical Review Letters **111**, 065002 (2013);

[34] T. Ma, H. Sawada, P. K. Patel, C. D. Chen, L. Divol, D. P. Higginson, A. J. Kemp, M. H. Key, D. J. Larson, S. Le Pape, A. Link, A. G. MacPhee, H. S. McLean, Y. Ping, R. B. Stephens, S. C. Wilks, and F. N. Beg, "Hot Electron Temperature and Coupling Efficiency Scaling with Prepulse for Cone-Guided Fast Ignition," Physical Review Letters **108**, 115004 (2012);

[35] K. A. Tanaka, R. Kodama, H. Fujita, M. Heya, N. Izumi, Y. Kato, Y. Kitagawa, K. Mima, N. Miyanaga, T. Norimatsu, A. Pukhov, A. Sunahara, K. Takahashi, M. Allen, H. Habara, T. Iwatani, T. Matusita, T. Miyakosi, M. Mori, H. Setoguchi, T. Sonomoto, M. Tanpo, S. Tohyama, H. Azuma, T. Kawasaki, T. Komeno, O. Maekawa, S. Matsuo, T. Shozaki, Ka Suzuki, H. Yoshida, T. Yamanaka, Y. Sentoku, F. Weber, T. W. Barbee Jr., and L. DaSilva, "Studies of ultra-intense laser plasma interactions for fast ignition," Physics of Plasmas **7**, 2014 (2000);

[36] H-B. Cai, K. Mima, A. Sunahara, T. Johazaki, H. Nagatomo, S-P. Zhu and X. T. He, "Prepulse effects on the generation of high energy electrons in fast ignition scheme," Physics of Plasmas **17**, 023106 (2010);

[37] T. Yabuuchi, B. S. Paradkar, M. S. Wei, J. A. King, F. N. Beg, R. B. Stephens, N. Nakanii, M. Hatakeyama, H. Habara, K. Mima, K. A. Tanaka, and J. T. Larsen, "Transport study of intense-laser-produced fast electrons in solid targets with a preplasma created by a long pulse laser," Physics of Plasmas **17**, 060704 (2010);

[38] K. A. Ivanov, S. A. Shulyapov, P. A. Ksenofontov, I. N. Tsymbalov, R. V. Volkov, A. B. Savel'ev, A. V. Brantov, V. Yu. Bychenkov, A. A. Turinge, A. M. Lapik, A. V. Rusakov, R. M. Djilkibaev, and V. G. Nedorezov, "Comparative study of amplified spontaneous emission and short pre-pulse impacts onto fast electron generation at sub-relativistic femtosecond laser-plasma interaction," Physics of Plasmas, **21**, 093110, (2014);

[39] C. Gahn, G. D. Tsakiris, A. Pukhov, J. Meyer-ter-Vehn, G. Pretzler, P. Thirolf, D. Habs, and K. J. Witte, "Multi-MeV Electron Beam Generation by Direct Laser Acceleration in High-Density Plasma Channels," Physical Review Letters, **Vol 83 No 23**, (1999);

[40] L. Willingale, P. M. Nilson, A. G. R. Thomas, J. Cobble, R. S. Craxton, A. Maksimchuk, P. A. Norreys, T. C. Sangster, R. H. H. Scott, C. Stoeckl, C. Zulick, and K. Krushelnick, "High-Power, Kilojoule Class Laser Channeling in Millimeter-Scale Underdense Plasma," Physical Review Letters **106**, 105002 (2011);

[41] A. G. MacPhee, K. U. Akli, F. N. Beg, C. D. Chen, H. Chen, L. Divol, D. S. Hey, R. R. Freeman, M. Henesian, A. J. Kemp, M. H. Key, S. Le Pape, A. Link, T. Ma, A. J. Mackinnon, V. M. Ovchinnikov, P. K. Patel, T. W. Phillips, R. B. Stephens, M. Tabak, R. Town, L. D. Van Woerkom, M. S. Wei, S. C. Wilks, "Limitation on Prepulse Level for Cone-Guided Fast-Ignition Inertial Confinement Fusion," Physical Review Letters **104**, 055002 (2010);

[42] A. J. Kemp and L. Divol, "Interaction Physics of Multipicosecond Petawatt Laser Pulses with Overdense Plasma," Physical Review Letters **109**, 195005 (2012);

[43] A. G. Krygier, D. W. Schumacher, and R. R. Freeman, "On the origin of superhot electrons from intense laser interactions with solid targets having moderate scale length preformed plasmas," Physics of Plasmas **21**, 023112 (2014);

[44] A. Arefiev, V. Khudik, A. P. L. Robinson, G. Shvets, L. Willingale, and M. Schollmeier, "Beyond the ponderomotive limit: direct laser acceleration of relativistic electrons in sub-critical plasmas," Physics of Plasmas **23**, 056704 (2016);

[45] T. J. M. Boyd and J. J. Sanderson, "The Physics of Plasmas," Cambridge University Press , Cambridge, England (2003)

[46] H. Chen, A. J. Link, R. V. Maren, P. K. Patel, R. Shepard, S. C. Wilks and P Beiersdorfer, "High performance compact magnetic spectrometers for energetic ion and electron measurement in ultraintense short pulse laser solid interactions," Review of Scientific Instruments **79**, 10E533 (2008);

[47] C. D. Chen, J. A. King, M. H. Key, K. U. Akli, F. N. Beg, H. Chen, R. R. Freeman, A. Link, A. J. Mackinnon, A. G. MacPhee, P. K. Patel, M. Porkolab, R. B. Stephens, and L. D. Van Woerkom, "A Bremsstrahlung spectrometer using kk-edge and differential filters with image plate dosimeters," Review of Scientific Instruments **79**, 10E305 (2008);

[48] J. R. Davies, R. Betti, P. M. Nilson, and A. A. Solodov, "Copper K-shell emission cross sections for lasersolid experiments," Physics of Plasmas **20**, 083118 (2013);

[49] J. A. Koch, Y. Aglitskiy, C. Brown, T. Cowan, R. Freeman, S. Hatchett, G. Holland, M. Key, A. MacKinnon, J. Seely, R. Snavely, R. Stephens, "4.5- and

8-keV emission and absorption x-ray imaging using spherically bent quartz 203 and 211 crystals (invited)," Rev. Sci. Instrum. **74**, 2130 (2003);

[50] E. Martinolli, M. Koenig, S. D. Baton, J. J. Santos, F. Amiranoff, D. Batani, E. Perelli-Cippo, F. Scianitti, L. Gremillet, R. Mlizzi, A. Decoster, C. Rousseaux, T. A. Hall, M. H. Key, R. Snavely, A. J. MacKinnon, R. R. Freeman, J. A. King, R. Stephens, D. Neely, and R. J. Clarke, "Fast-electron transport and heating of solid targets in high-intensity laser interactions measured by Kα fluorescence," Physical Review E **73**, 046402 (2006);

[51] T. D. Arber, K. Bennett, C. S. Brady, A. Lawrence-Douglas, M. G. Ramsay, N. J. Sircombe, P. Gillies, R. G. Evans, H. Schmitz, A. R. Bell and C. P. Ridgers, "Contemporary particle-in-cell approach to laser-plasma modelling," Plasma Physics and Controlled Fusion **57**, 1-26 (2015).

[52] A. Sorokovikova, A. V. Arefiev, C. McGuffey, B. Qiao, A. P. L. Robinson, M. S. Wei, H. S. McLean, and F. N. Beg, "Generation of Superponderomotive Electrons in Multipicosecond Interactions of Kilojoule Laser Beams with Solid-Density Plasmas," Physical Review Letters **116**, 155001 (2016).

[53] D. Haberberger, S. Ivancic, S. X. Hu, R. Boni, M. Barczys, R. S. Craxton, and D. H. Froula, "Absorption of ultra-intense laser pulses," Physics of Plasmas **21**, 056304 (2014);

[54] T. Ditmire, Overview of Activities in the Center for High Energy-Density Science, SSAP 2016 Conference, (2016);

[55] M. Borghesi, A. J. Mackinnon, R. Gaillard, O. Willi, A. Pukhov and J. Meyer-ter-Vehn, "Large Quasistatic Magnetic Fields Generated by a Relativistically Intense Laser Pulse Propagating in a Preionized Plasma," Physical Review Letters, **Vol 80 No 23**, (1998);

[56] W. Schumaker, N. Nakanii, C. McGuffey, C. Zulick, V. Chyvkov, F. Dollar, H. Habara, G. Kalintchenko, A. Maksimchuk, K. A. Tanaka, A. G. R. Thomas, V. Yanovsky and K. Krushelnick, "Ultrafast Electron Radiography of Magnetic Fields in High-Intensity Laser-Solid Interactions," Physical Review Letters, **110** 015003, (2013);

[57] F. Pérez, A. J. Kemp, L. Divol, C. D. Chen and P. K. Patel, "Deflection of MeV Electrons by Self-Generated Magnetic Fields in Intense Laser-Solid Interactions," Physical Review Letters, **111** 245001, (2013);

[58] B. Fryxell, K. Olson, P. Ricker, F. X. Timmes, M. Zingale, D. Q. Lamb, P. MacNiece, R. Rosner, J. W. Truran and H. Tufo, "FLASH: An Adaptive Mesh Hydrodynamics Code for Modeling Astrophysical Thermonuclear Flashes," The Astrophysical Journal Supplement Series, 131:273-334, 2000 November

[59] D. P. Higginson, A. Link, H. Sawada, S. C. Wilks, T. Bartal, S. Chawla, C. D. Chen, K. A. Flippo, L. C. Jarrott, M. H. Key, H. S. McLean, P. K. Patel, F. Prez, M. S. Wei, and F. N. Beg, "High-contrast laser acceleration of relativistic electrons in solid cone-wire targets," Physical Review E **92**, 063112 (2015);

[60] F. R. Pearce, H. M. P. Couchman, "Hydra: a parallel adaptive grid code," New Astronomy, **Volume 2 Issue 5**, 411-427 (1997).

[61] O. V. Gotchev, J. P. Knauer, P. Y. Chang, N. W. Jang, M. J. Shoup III, D. D. Meyerhofer, and R. Betti, "Seeding magnetic fields for laser-driven flux compression in high-energy-density plasmas," Review of Scientific Instruments **80**, 043504 (2009);

[62] H. Daido, F. Miki, K. Mima, M. Fujita, K. Sawai, H. Fujita, Y. Kitagawa, S. Nakai, and C. Yamanaka, "Generation of a strong magnetic field by an intense CO2 laser pulse," Physical Review Letters **56**, 846 (1986);

[63] S. Fujioka, Z. Zhang, N. Yamamoto, S. Ohira, Y. Fujii, K. Ishihara,T. Johzaki, A. Sunahara, Y. Arikawa, K. Shigemori, Y. Hironaka, Y. Sakawa, Y. Nakata, J. Kawanaka, H. Nagatomo, H. Shiraga, N. Miyanaga, T. Norimatsu, H. Nishimura and H. Azechi, "High-energy-density plasmas generation on GEKKO-LFEX laser facility for fast-ignition laser fusion studies and laboratory astrophysics," Plasma Physics and Controlled Fusion **54**, 124042 (2012)

[64] J. J. Santos, M. Bailly-Grandvaux, L. Giuffrida, P. Forestier-Colleoni, S. Fujioka, Z. Zhang, P. Korneev, R. Bouillaud, S. Dorard, D. Batani, M. Chevrot, J. E. Cross, R. Crowston, J-L Dubois, J. Gazave, G. Gregori, E. d'Humieres, S. Hulin, K. Ishihara, S. Kojima, E. Loyez, J-R Marques, A. Morace, P. Nicolai, O. Peyrusse, A. Poye, D. Raffestin, J. Ribolzi, M. Roth, G. Schaumann, F. Serres, V. T. Tikhonchuk, P. Vacar and N. Woolsey, "Laser-driven platform for generation and characterization of strong quasi-static magnetic fields," New Journal of Physics **17**, 083051 (2015)

[65] L. Gao, H. Ji, G. Fiksel, W. Fox, M. Evans and N. Alfonso, "Ultrafast proton radiography of the magnetic fields generated by a laser-driven coil current," Physics of Plasmas **23**, 043106 (2016)

[66] S. R. Nagel, T. J. Hilsabeck, P. M. Bell, D. K. Bradley, M. J. Ayers, K. Piston, B. Felker, J. D. Kilkenny, T. Chung, B. Sammuli, J. D. Hares and A. K. L. Dymoke-Bradshaw, "Investigating high speed phenomena in laser plasma interactions using dilation x-ray imager (invited)," Review of Scientific Instruments **85**, 11E504 (2014)

[67] D. Jung, R. Horlein, D. C. Gautier, S. Letzring, D. Kiefer, K. Allinger, B. J. Albright, R. Shah, S. Palaniyappan, L. Yin, J. C. Fernandez, D. Habs and B. M. Hegelich, "A novel high resolution ion wide angle spectrometer," Review of Scientific Instruments **82**, 043301 (2011)

[68] M. Schollmeier, A. B. Sefkow, M. Geissel, A. V. Arefiev, K. A. Flippo, S. A. Gaillard, R. P. Johnson, M. W. Kimmel, D. T. Offermann, P. K. Rambo, J. Schwarz and T. Shimada, "Laser-to-hot-electron conversion limitations in relativistic laser matter interactions due to multi-picosecond dynamics," Physics of Plasmas **22**, 043116 (2015);

[69] A. Arefiev, B. Breizman, M, Schollmeier, and V. Khudik, "Enchancement of laser-driven electron acceleration in preplasma via parametric resonance," Physical Review Letters **108**, 145004 (2012);